UniS

Liquid Recirculation & Mass Transfer Beneath Ventilated Cavities in Vertical Two-Phase Downflows

by

Athanasios Aimiliou Sotiriadis

Submitted for the degree of Doctor of Philosophy in Chemical Engineering

Fluids Research Centre
School of Engineering
University of Surrey

August 2005

To my parents Emil & Vassiliki

DECLARATION

No portion of the work referred to in the thesis has been submitted in support of an application for another degree of qualification of this or any other university, or other institution of learning. The length of this dissertation, including appendices, bibliography, footnotes and equations contains no more than 65,000 words and 150 figures.

Signed: 

Date: 30/8/2005

ABSTRACT

This dissertation examines the hydrodynamic characteristics of large ventilated cavities attached to air spargers in downflowing liquids in vertical pipes. Also it presents an investigation on slug bubbles in both cocurrent upward and downwards vertical two-phase flow. This work is a continuation of the research carried out by Bacon (1995) and Lee (1998) at the University of Cambridge.

The turbulent flow fields behind a cylindrical bluff body shaped like a Taylor bubble in single phase flow and beneath two ventilated cavities attached to a central sparger in two-phase flow are investigated in a 0.105 m id pipe. The results for the time-averaged velocity reveal the formation of a similar toroidal vortex below the bluff body and the ventilated cavities. The bottom boundary of the vortex is defined to be the position of the stagnation point on the centreline, which is found at around $z \simeq 1.32D$ for all cases. The following implied predictions of the model of Thorpe et al. (2001) are confirmed by the experiments; that the geometry (i.e. size) of the vortex does not depend on the liquid volumetric flow rate or the speed of the vortex. On the other hand, the speed of the vortex is directly proportional to the film velocity at the base of the bluff body or the cavities. The falling film velocity determines the velocity field in the near wake and is the driving force of the vortex. Beneath the vortex the bubbles tend to flatten the velocity profile.

The model of Thorpe et al. (2001) gives good predictions for the velocity distribution in the centre of the vortex ring against the LDV results of the cylindrical bluff body and the ventilated cavities and the PIV results for a Taylor bubble of Van Hout et al. (2002).

The local average bubble size in the bulk two-phase flow region below the ventilated cavity has been determined using photography for a horizontal sparger (HS) (industrial design), a central sparger (CS), a peripheral sparger (PS) and a plunging jet sparger (PJS). The results show that the bubble size produced depends on the gas and liquid volumetric flow rates and the sparger design. The average bubble size at fixed flow rates is essentially the same (differences within 10%) for the PS, CS and HS. The PJS is the most effective way of distributing gas in the downcomer pipe since it creates smaller bubbles than all the other spargers and does not allow the formation of ventilated cavities.

The effect of sparger type on the volumetric mass transfer coefficient $k_L a$ was also measured using a dynamic method. The results confirm the apparent superiority of PJS over the other spargers. The $k_L a$ is observed to be larger by 19% when the PJS is used instead of the HS. The CS and PS have similar $k_L a$ values again to that of the HS. However, the particular design of PJS used in this work, has a higher energy consumption than HS. When the 19 % average enhancement in $k_L a$ produced by the PJS is corrected for power consumption, then the PJS and HS have the same mass transfer performance.

In a somewhat separate piece of work, the characteristics of gas slugs in co-current and downward flow, only briefly reported in the literature, have been investigated more extensively and more precisely than before for four different test liquids (water, 2% and 8% w/w aqueous solutions of isopropanol and 3.5% w/w aqueous solution of sodium chloride) and two different

pipe diameters (0.05 m id & 0.105 m id). For very low downward liquid velocities the slugs rose near to the pipe centre (central slugs) and so their drift velocity is close to that predicted by the well-established correlation for an upward co-current slug. On the other hand, at higher downward liquid velocities the slugs did not propagate along the axis of the pipe but instead ascended or descended close to the pipe wall (wall slugs). The velocity of these slugs is dependent on the pipe diameter and surface tension; a reduction of the surface tension or an increase in the pipe diameter increases their speed. A transition region with respect to the slug velocity from central to wall slug behaviour is for the first time reported. This transitional behaviour is because the stabilising effects of surface tension on the shape of the slugs are overcome, which causes the slugs to migrate towards the pipe wall. A constant Weber number accurately describes the onset of wall slugs for each pipe diameter.

ACKNOWLEDGEMENTS

I would like to express my greatest appreciation and admiration to my research supervisor Professor R. B. Thorpe for his valuable guidance, encouragement, and most of all, inspiration throughout this research. I believe I have been really lucky I was given the opportunity to work under his supervision.

I would also like to express my deepest gratitude to Professor J. M. Smith and Dr N. F. Kirkby for their generous support, help and advice in specific problems I had encountered during the experimental programme.

The experiments reported here in this thesis would not have been possible without the help of the technicians of the Chemical Engineering Discipline, Mr D. Hawkins and Mr D. Arnall. Also I would like to express my special thanks to Dr A. Tate for his valuable advice concerning the high-speed photography experiments and for allowing me to access the various computer facilities of the School of Engineering. I am very grateful to Mr B.Underwood for his advice on the safety issues associated with this research. I gratefully acknowledge all four of them for their solidarity and professional manner in dealing with problems.

I am very grateful to Dr A. Walker from the EPSRC Engineering Pool for the generous loan of the Laser Doppler Velocimetry (LDV) instrument and to Dr M. Hyde from TSI Inc. for the technical support he provided during the LDV measurements.

Former students of the Chemical Engineering Discipline, to whom I am especially indebted for making the life in Guildford easier and the long hours in the lab pleasant despite the hard work, are Dr A. Papadopoulos, Dr V. Ashley, Mr S. Chilukuri, Mr N. Fontaine, Mr J. Noble, Mr K. Cheung, Dr R. Rondriguez, Mr D. Montolio, Mr C. Antonis, Mr J. Anagnostopoulos, Miss E. Duzgun.

At this point, I also want to thank my friends Dr G. Biskos, Dr D. Potoglou, Dr A. Kounadis, Dr D. Papanastasiou and Dr D. Haralampopoulos for their support, criticism and remarks throughout this research. I am sure I will be able to see them more often in the future.

Many thanks sincerely belong to my family for their love and constant spiritual support; especially to my parents Emil and Vassiliki, my brother Tom, my sister-in-law Marina and my late grandmother Despina who I greatly miss. Without their constant spiritual support, even though they were far away, my studies would not have been carried through.

I am eternally grateful to my partner in life, my fiancée Maria Frantzeskaki, for her love, support and understanding throughout the last almost four years. She is an amazing source of energy that constantly motivates me in my life. I would like to believe that the completion of this thesis makes her efforts feel worthy.

Finally I wish to express my genuine gratitude for the financial support by the EPSRC through grant GR/P 00079 that enabled this research to become a reality.

A. A Sotiriadis

Guildford, Surrey,

August 2005

CONTENTS

LIST OF FIGURES

LIST OF TABLES

NOMENCLATURE

Symbol	Description	Units
A	Area	(m^2)
a	Radius (half the lateral size) of the Hill's vortex	(m)
B	Parameter that is related to the vorticity ω of the flow since $\omega = Br$	(m^{-1} s^1)
b	Jet to column cross-sectional area ratio	(Dimensionless)
b_p	Thickness of perspex water box	(m)
c	Speed of light	($m\ s^{-1}$)
C	Dissolved oxygen of percentage saturation (%)	(Dimensionless)
C_T	Dissolved oxygen of percentage saturation (%) in the tank	(Dimensionless)
C_P	Dissolved oxygen of percentage saturation (%) at the point of measurement	(Dimensionless)
C_E	Dissolved oxygen of percentage saturation (%) leaving the downcomer	(Dimensionless)
C_D	Dissolved oxygen of percentage saturation (%) before the sparger	(Dimensionless)
$C(t)$	Dissolved oxygen of percentage saturation (%) at time t	(Dimensionless)
C_c	Contraction coefficient	(Dimensionless)
C_f	Wall friction factor $\left(0.079\,\mathrm{Re}^{-0.25}\right)$	(Dimensionless)
C_1	Drift velocity coefficient	(Dimensionless)
C_0	Flow distribution parameter	(Dimensionless)
D	Pipe diameter	(m)
D_N	Nozzle diameter	(m)
D_j	Jet diameter at the plunging point	(m)
$d_{\varsigma^{-2}}$	Diameter of focused laser beam at the waist	(m)
d_h	Horizontal sparger hole diameter	(m)
d_b	Bubble mean diameter	(m)
d_1	Major axis of the bubble	(m)

Symbol	Description	Units
d_2	Minor axis of the bubble	(m)
d_{32}	Sauter mean bubble diameter	(m)
d'_{32}	Sauter mean bubble diameter adjusted for power consumption	(m)
$d_{\max}$	Observed maximum bubble diameter	(m)
$d_{99.9}$	Bubble diameter that is greater than 99.9 % of all the diameters in the cumulative distribution	(m)
E	Ratio of instantaneous mass transfer rate to the maximum possible rate of mass transfer $\left(\frac{C_L - C_o}{C^* - C_o}\right)$	(Dimensionless)
E_k	Relative kinetic energy flux as defined by Su (1995) $\left(\delta V_F^3\right)$	($m^4\ s^{-3}$)
Eo_D	Eotvos number $\left(\frac{gD^2\left(\rho_L - \rho_G\right)}{\sigma}\right)$	(Dimensionless)
$Eo_{d_{32}}$	Eotvos number $\left(\frac{gd_{32}^2\left(\rho_L - \rho_G\right)}{\sigma}\right)$	(Dimensionless)
e	Average energy dissipation rate per unit volume	($kg\ m^{-1}\ s^{-3}$)
e'	Average energy dissipation rate per unit mass	($m^{-2}\ s^{-3}$)
F_a	Focal distance of lens in air	(m)
F_w	Actual focal distance of lens (in water)	(m)
$Fr_{G,\max}$	Froude number at the maximum entrainment rate $\left(\frac{Q_{G,\max}}{\sqrt{(gD)^5}}\right)$	(Dimensionless)
Fr_L	Liquid flow Froude number $\left(\frac{Q_L}{\sqrt{(gD)^5}}\right)$	(Dimensionless)
Fr	Froude number $\left(\frac{j_L}{\sqrt{gD}}\right)$	(Dimensionless)
f	Exponent – Chapter 2	(Dimensionless)
f_D	Doppler frequency	(Hz)
g	Acceleration due to gravity	($m\ s^{-2}$)

Symbol	Description	Units
H_N	Distance from the nozzle exit to the receiving pool	(m)
H_1	Distance from the base of the bluff body or the ventilated cavity to the center of the Hill's vortex	(m)
H_2	Distance from the base of the bluff body or the ventilated cavity to the end of the re-circulation region	(m)
$\vec{I}_1$	Unit vector describing the incoming light in Eq. (C.3)	(m s^{-1})
$\vec{I}_2$	Unit vector describing the scattered light in Eq. (C.3)	(m s^{-1})
j	Superficial velocity $\left(\frac{4Q}{\pi D^2}\right)$	(m s^{-1})
$j_{L,T}$	Superficial liquid velocity that marks the onset of wall slugs	(m s^{-1})
K	Proportionality constant in Eq. (4.2)	(Dimensionless)
$k_L a$	Volumetric mass transfer coefficient based on the dispersion volume	(s^{-1})
$k_L a'$	Volumetric mass transfer coefficient based on the dispersion volume adjusted for power consumption	(s^{-1})
k_L	liquid side mass transfer coefficient	(m s^{-1})
ll_{ith}	Lower limit containing the i^{th} percentile	(m)
L	Length	(m)
L_P	Vertical distance from the sparger to the probe	(m)
$L_{\Delta P}$	Liquid head corresponding to the pressure difference between downcomer outlet and inlet	(m)
L_D	Distance from the transmitting lens to the perspex box surface	(m)
l_x	Traversing positioning uncertainty in the x-axis	(m)
l_y	Traversing positioning uncertainty in the y-axis	(m)
ℓ_1	Predicted energy losses per unit mass due to the sparger	(m^2 s^{-2})
ℓ_2	Predicted energy losses per unit mass due to the bubbly flow in the downcomer	(m^2 s^{-2})
ℓ_3	Predicted energy losses per unit mass due to wall friction	(m^2 s^{-2})
ℓ_4	Predicted energy losses per unit mass due to the total loss of the kinetic head at the downcomer exit	(m^2 s^{-2})

Symbol	Description	Units
ℓ_s	Predicted energy losses per unit mass due to wall shear around the ventilated cavity	($m^2 s^{-2}$)
ℓ_w	Predicted energy losses per unit mass due to the turbulent cavity wake	($m^2 s^{-2}$)
N	Number of bubbles or particles	(Dimensionless)
N_f	Inverse viscosity number $\left(\frac{\sqrt{gD}\rho_L}{\mu_L}\right)$	(Dimensionless)
N_μ	Viscosity number $\left(\frac{\mu}{\rho_L\sqrt{gD^5}}\right)$	(Dimensionless)
N_{fr}	Number of fringes in the measuring volume	(Dimensionless)
n	Exponent – Chapter 2	(Dimensionless)
n	Exponent – Chapter 5	(Dimensionless)
n	Number of holes on the horizontal sparger – Appendix A)	(Dimensionless)
n_{ci}	Number of cycles for validation of an LDV signal	(Dimensionless)
n_a	Refractive index of air	(Dimensionless)
n_w	Refractive index of water	(Dimensionless)
n_p	Refractive index of perspex	(Dimensionless)
Oh	Ohnesorge number $\left(\frac{\mu_L}{\sqrt{\rho_L\sigma D_N}}\right)$	(Dimensionless)
P	Power	(W)
P_1	Pressure under calibration conditions	($N m^{-2}$)
P_2	Pressure (conditions at rotameter)	($N m^{-2}$)
P_3	Pressure (conditions at downcomer sparger)	($N m^{-2}$)
P_{wz}	Wall pressure	($kg m^{-1} s^{-2}$)
Q	Volumetric flow rate	($m^3 s^{-1}$)
Q_F	Film-wise entrainment rate (gas carried along adjacent to the jet free surface)	($m^3 s^{-1}$)
$Q_{G,\max}$	Maximum entrainment rate, at local pressure	($m^3 s^{-1}$)
$Q_{G,1}$	Volumetric gas flow rate under calibration conditions	($m^3 s^{-1}$)

Symbol	Description	Units
$Q_{G,2}$	Volumetric gas flow rate (conditions at rotameter)	(m^3 s^{-1})
$Q_{G,3}$	Volumetric gas flow rate (conditions at downcomer sparger)	(m^3 s^{-1})
Q_j	Jet volumetric flow rate $\left(V_j \frac{\pi D_{j(z)}^2}{4}\right)$	(m^3 s^{-1})
Q_{ENT}	Gas entrainment rate as defined by Eq. (2.22)	(m^3 s^{-1})
Q_{REC}	Recoalescence flow rate of gas at the base of ventilated cavity or a slug bubble	(m^3 s^{-1})
Q_T	Trapped gas entrainment rate (gas contained within the effective diameter of the jet)	(m^3 s^{-1})
q_G	Gas entrainment rate per unit width of planar jet	(m^2 s^{-1})
R	Pipe radius	(m)
$\Re$	Radius of curvature – Chapter 2, Appendix F	(m)
Re	Reynolds number in pipe $\left(\frac{\rho_L j_L D}{\mu_L}\right)$	(Dimensionless)
Re_F	Film Reynolds number $\left(\frac{\Gamma}{\nu_L}\right)$	(Dimensionless)
Re_N	Reynolds number $\left(\frac{\rho_L j_L D_N}{\mu_L}\right)$	(Dimensionless)
Re_{H_N}	Nozzle Reynolds number $\left(\frac{\rho_L V_N H_N}{\mu_L}\right)$	(Dimensionless)
Re_j	Reynolds number of jet $\left(\frac{\rho_L V_j D_N}{\mu_L}\right)$	(Dimensionless)
Re_p	Particle Reynolds number $\left(\frac{\rho_L u_t d_p}{\mu_L}\right)$	(Dimensionless)
r	Radial distance from axis of symmetry	(m)
r_0	Radial distance to center of Hill's vortex $\left(r_0 = a\sqrt{2}\right)$	(m)
s	R.m.s. velocity fluctuation	(m s^{-1})
t_8	Elapsed time for a particle to cross 8 fringes in the measuring volume	(s)

Symbol	Description	Units
t_5	Elapsed time for a particle to cross 5 fringes in the measuring volume	
T_1	Temperature calibration conditions	(K)
T_2	Temperature (conditions at rotameter)	(K)
T_3	Temperature (conditions at downcomer sparger)	(K)
T_u	Turbulence Intensity $\left(\frac{s}{V_j}\times 100\%\right)$	(Dimensionless)
$\langle u'^2 \rangle$	Average value of the fluctuating velocity acting over a length scale equivalent to the maximum stable bubble diameter, $d_{\max}$	$(m\ s^{-1})^2$
u_t	Free settling velocity of particles	$(m\ s^{-1})$
u^*	Friction velocity $\left(\frac{\sqrt{\tau_o}}{\rho_L}\right)$	$(m\ s^{-1})$
u_w	Friction velocity (as defined by Riiser et al., 1992) $\left(U_F\sqrt{\frac{C_f}{2}}\right)$	$(m\ s^{-1})$
u_i	Velocity of particle i during the LDV measurement	$(m\ s^{-1})$
$u_{G,HS}$	Gas velocity in the pipe of the horizontal sparger	$(m\ s^{-1})$
$\vec{\bar{U}}$	Total average velocity of an LDV measurement at a single point	$(m\ s^{-1})$
$\vec{U}$	Vector representing the seeding particle velocity	$(m\ s^{-1})$
$v_{G,HS}$	Gas velocity in the vena contracta of an air hole of the horizontal sparger	$(m\ s^{-1})$
V_B	Slug bubble velocity relative to the liquid ahead of its tip	$(m\ s^{-1})$
V_s	Translational velocity of a Taylor bubble	$(m\ s^{-1})$
V_d	Taylor bubble rise velocity in a quiescent liquid	$(m\ s^{-1})$
V_e	Minimum liquid entrainment velocity	$(m\ s^{-1})$
V_{cl}	Centreline liquid velocity	$(m\ s^{-1})$
V_N	Jet velocity at nozzle exit	$(m\ s^{-1})$

Symbol	Description	Units
V_F	Film velocity at the base of the ventilated cavity	(m s^{-1})
V_G	Gas velocity of the entrained air boundary layer (calculated from the measured entrained gas volumetric flow rate)	(m s^{-1})
V_j	Jet velocity at the plunging point	(m s^{-1})
V_L	Interstitial liquid velocity	(m s^{-1})
V_j'	R.m.s. value of the jet velocity component.	(m s^{-1})
V_x	Velocity component in the x direction	(m s^{-1})
$V_{z(x)}$	Axial velocity component measured when traversing in the x axis	(m s^{-1})
$V_{z(y)}$	Axial velocity component measured when traversing in the y axis	(m s^{-1})
$V_{z(\max)}$	Maximum axial velocity inside the Hill's vortex	(m s^{-1})
V_y	Velocity component in the y direction	(m s^{-1})
V_z'	R.m.s. value of the axial velocity component	(m s^{-1})
V_x'	R.m.s. value of the velocity component V_x	(m s^{-1})
V	Total liquid volume	(m^3)
V_a	Total aerated volume	(m^3)
V_P	Aerated volume contained between the sparger and probe	(m^3)
V_∞	Rise velocity of single small bubbles	(m s^{-1})
We_N	Nozzle Weber number $\left(\frac{\rho_L V_N^{\,2} D_N}{\sigma}\right)$	(Dimensionless)
We_G	Air boundary layer Weber number $\left(\frac{\rho_G V_j^{\,2} D_N}{\sigma}\right)$	(Dimensionless)
We_j	Weber jet number $\left(\frac{\rho_L V_j^{\,2} D_N}{\sigma}\right)$	(Dimensionless)
We_{ct}	Critical Weber number $\left(\frac{\rho_L \langle u'^2 \rangle d_{\max}}{\sigma}\right)$	(Dimensionless)
We_C	Critical Weber number in Eq. (5.10) $\left(\frac{\rho_L \Delta u^2 d_{\max}}{\sigma}\right)$	(Dimensionless)

Symbol	Description	Units
We_n	Weber number of gas entrainment $\left(\frac{\rho_G V_G{}^2 D_N}{\sigma}\right)$	(Dimensionless)
We_{onset}	Weber number of the onset of entrainment $\left(\frac{\rho_L u_w^2 \delta_{onset}}{\sigma}\right)$	(Dimensionless)
We_T	Transition Weber number $\left(\frac{\rho_L j_{L,T}^2 D}{\sigma}\right)$	(Dimensionless)
w	Width of the bubble class	(m)
x	Cartesian coordinate	(m)
y	Cartesian coordinate	(m)
y	Distance of the bubble nose from the wall – Appendix F	(m)
y^+	Non dimensional normal distance from the pipe wall $\left(\frac{yu^*\mu_L}{\rho_L}\right)$	(Dimensionless)
y^*	Friction distance from the pipe wall $\left(\frac{\mu_L}{\sqrt{\rho_L \tau_0}}\right)$	(m)
z	Axial coordinate	(m)

Greek Letters

α_2	Falling film flow area at the base of the ventilated cavity attached to a HS or a CS	(m^2)
α_1	Falling film flow area at the top of the ventilated cavity attached to a HS or a CS (i.e. difference in cross-sectional area between the downcomer and the sparger)	(m^2)
Γ	Liquid volumetric flow rate per wetted perimeter $\left(\frac{Q_L}{\pi D}\right)$	($m^2\ s^{-1}$)
γ	Richardson and Zaki index	(Dimensionless)
$\Delta P_{orifice}$	Pressure drop across the holes on the horizontal sparger	($N\ m^{-2}$)
$\Delta P_{sparger}$	Average pressure drop along the horizontal pipe, in the horizontal sparger	($N\ m^{-2}$)

Symbol	Description	Units
Δu^2	Square of the velocity difference over a distance equal to the diameter of a bubble	(m s^{-1})
Δl	Probe traversing distance	(m)
Δy	Movement of measuring volume	(m)
δ	Film thickness at the base of a ventilated cavity	(m)
δ_{onset}	Film thickness at the onset of entrainment	(m)
δ_w	Wave height in Eq. (2.21)	(m)
δ_{fa}	Fringe separation distance (spacing) in air	(m)
δ_{fw}	Fringe separation distance (spacing) in water	(m)
δ_{za}	Length of the measuring volume in air	(m)
δ_{zw}	Length of the measuring volume in water	(m)
δ_{ya}	Width of the measuring volume in air	(m)
δ_{yw}	Width of the measuring volume in water	(m)
δ_{xa}	Height of the measuring volume in air	(m)
δ_{xw}	Height of the measuring volume in water	(m)
ε	Volumetric fraction of discontinuous phase	(Dimensionless)
θ_W	Angle of inclination of the plunging liquid jet sparger	(degree)
ξ	Surface disturbance of the free surface of the jet	(m)
ξ_D	Dynamical roughness as defined by equation 2.10	(m)
Ξ	Validation criterion in Eq. (3.6)	(Dimensionless)
κ_a	Half angle of the crossing beams in air	(degree)
κ_w	Half angle of the crossing beams in water	(degree)
κ_p	Half angle of the crossing beams in perspex	(degree)
λ_a	Wavelength in air	(m)
λ_w	Wavelength in water	(m)
λ_p	Wavelength is perspex	(m)
Λ	Wavelength of travelling acoustic wave in the Bragg cell	(m)
μ	Dynamic viscosity	(kg m^{-1} s^{-1})

Symbol	Description	Units
ν	Kinematic viscosity	($m^2 s^{-1}$)
ρ	Density	($kg m^{-3}$)
σ	Surface tension	($N m^{-1}$)
σ_p	Geometric standard deviation of seeding particles	(Dimensionless)
σ_{V_s}	Uncertainty in the slug velocity (68% confidence limit)	($m s^{-1}$)
σ_{C_0}	Uncertainty in the C_0 parameter (68% confidence limit)	(Dimensionless)
σ_{C_1}	Uncertainty in the C_1 parameter (68% confidence limit)	(Dimensionless)
ς	Maximum centerline combined beam light intensity in the measuring volume	($W m^{-2}$)
τ_o	Wall shear stress	($N m^{-2)}$
τ	Residence time	(s)
τ_i	Transit time for particle i to cross the measuring volume during the LDV measurement	(s)
ϕ_{st}	Standard error in time-averaged velocity	($m s^{-1}$)
ϕ	Total random error in the velocity measurements	($m s^{-1}$)
ψ	Stoke's stream function	($m^3 s^{-1}$)
$\lvert\omega\rvert$	Magnitude of the vorticity vector	(s^{-1})

Subscripts & Superscripts

B	Ventilated cavity
b	Bubble
c	Bubble cloud dispersion
D	Downcomer
G	Gas
j	Jet
L	Liquid
N	Nozzle
p	Particles
w	Wake or recirculation
$*$	Equilibrium state

Abbreviations

CFD	Computational fluid dynamics
CS	Central sparger
CPLJ	Confined plunging liquid jet
DELR	Downflow ejector loop reactor
DO	Dissolved oxygen
HS	Horizontal sparger
IPA	Isopropanol solution
PJS	Plunging jet sparger
PMT	Photomultiplier tube
PS	Peripheral sparger
UVP	Universal velocity profile
VC	Ventilated cavity
VOF	Volume of fluid

CHAPTER 1

INTRODUCTION

1.1 BAGROUND TO THE PROJECT

Vertical gas-liquid two-phase flow in pipes occurs in many industrial situations. The pressing need for reliable design methods has driven a very large research activity in this type of flow over the past several decades. Vertical gas-liquid two-phase flow often exhibits a flow pattern known as slug flow. Slug flow is frequently observed in a wide range of two-phase flows. It is characterised by a sequence of large coherent bubbles (Taylor bubbles), which are much longer than wide, nearly fill the cross section of the pipe and alternate with liquid slugs containing dispersed bubbles. At the bottom of the Taylor bubble, a liquid film at the wall of the pipe plunges into the liquid beneath and entrains a certain amount of gas in the form of small bubbles. The rate of gas entrainment at the base of a Taylor bubble can have a significant effect on the small bubble volume fraction in the slugs, which can reduce the pressure gradient in the slug flow. In oil production flows, for example, the pressure gradient can determine the rate of production. Unfortunately the understanding of slug flow is not perfect because of the complexity of the transient nature and multi-dimensional fluid dynamic process as the Taylor bubble moves along the pipe. The two main areas in which slug flow can cause difficulties in field operations are in the operability of the gas and liquid processing plant, and in the mechanical integrity of the pipework upstream of the plant (Hill and Wood, 1994).

Gas entrainment is also an important factor in the performance of circulating bubble columns and external-loop airlift fermenters/reactors. This type of fermenter/reactor is widely used because of its simplicity in operation. The gas itself is the driving force that generates the liquid circulation. Circulation is induced in the system initially by injecting gas in the riser, thus creating a net density difference between the riser and the downcomer. The driving force is the hydrostatic pressure difference between the two sections while the resisting force is the frictional pressure drop around the flow circuit (Joshi et al., 1990). The control over liquid circulation in the reactor enables good liquid phase mixing and good temperature control resulting in high mass transfer rates.

In some applications, e.g., fermentations, oxygen is required in all parts of the reactor to prevent anoxia of the organisms or anaerobic growth that can result in undesired by-products. Gas is therefore injected into the downcomer pipe where there are no bubbles and where anoxic conditions are more likely to be developed. As the liquid rushes past the gas injection device, the sparger, is diverted to the walls and a ventilated cavity is formed underneath the sparger. Small bubbles are entrained at the base of this cavity by the falling liquid film at the wall of the pipe. The cavity resembles the Taylor bubbles in slug flow.

The ventilated cavity is undesirable in fermentation plants because it can reduce the driving force for liquid circulation and in some cases can even cause stalling and result in flow reversal. The presence of the ventilated cavity is also detrimental because it reduces the available area for mass transfer, which can result in a reduced yield from the fermenter. The cavity consequently affects the system dynamics and a full understanding of the entrainment process at the base of such a cavity would allow prediction of reactor behaviour and the prevention of stalling (Bacon et al., 1995b). This research is a fundamental study of such large ventilated cavities and slug bubbles in two-phase flow.

1.2 STATEMENT OF AIMS

The work presented in this dissertation is a continuation of the work carried out by Bacon (1995a) and Lee (1998). The objectives of the current work are to:

(i) Investigate the fluid mechanics (analysis of the velocity field) behind a cylindrical bluff body shaped like a Taylor bubble and beneath two ventilated cavities attached to a central sparger. The data will provide a better understanding of the air entrainment process and will validate the model proposed by Thorpe et al. (2001).

(ii) Examine the effects of sparger design on the volumetric mass transfer coefficient $(k_L a)$ so as to establish whether various designs of sparger, that have been shown to produce an advantageous shortening of the ventilated cavity do in fact also increase the overall rate of mass transfer.

(iii) Examine the effects of sparger design on the resulting bubble size and its distribution.

(iv) Investigate experimentally and theoretically the dynamics of downward slug flow with respect to the slug bubble velocities using a variety of liquids.

1.3 THESIS ORGANISATION

The text of this thesis is divided into seven Chapters and six Appendices. The current Chapter (Chapter 1) serves as an introduction to the thesis addressing the scope and background of the present work.

Chapter 2 gives a description of the available literature that is related to the study of ventilated cavities attached to spargers in downward two-phase flow. Because of the limited work on this subject emphasis is also given on the published literature on plunging liquid jets, confined jet systems and vertical slug flow.

Chapter 3 describes the experimental apparatus used to study ventilated cavities and slug bubbles in downward two-phase flow. It outlines the experimental methods used to generate the various set of data and to determine the physical properties of the different fluids used.

Chapter 4 presents the experimental results obtained using Laser Doppler Velocimetry (LDV) of the fluid mechanics (analysis of the velocity field) of the recirculation region at the base of both a cylindrical bluff body shaped like a Taylor bubble and two ventilated cavities attached to a central sparger. The experiments have been conducted using water.

Chapter 5 presents the experimental measurements regarding the effects of sparger design on (a) the resulting dispersed bubble size and its distribution and (b) the volumetric mass transfer coefficient $(k_L a)$. The experiments have been conducting with air-water for four different spargers, namely a horizontal, a central, a peripheral and a plunging jet sparger.

Chapter 6 describes a study on the dynamics of slugs in downwards flow. The experiments have been have been carried out using tap water, 2% and 8% w/w aqueous solution of isopropanol and 3.5% w/w aqueous solution of sodium chloride.

Finally chapter 7 addresses the conclusions of this study and provides some recommendations for future research.

CHAPTER 2

LITERATURE REVIEW

The objective of this chapter is to give a description of the available literature that is related to the study of ventilated cavities attached to spargers in downward two-phase flow. The interest in this subject emerges from two different approaches. The first one is related to the performance and design of circulating bubble columns and external loop airlift fermenters/reactors. This subject has received little attention in the literature with only handful publications that are based solely on the work of Bacon (1995a) and later Lee (1998), upon which both the current work is based. The second approach is associated with the study of gas entrainment from Taylor bubbles in two-phase upward slug flow. The literature on this subject is slightly more extensive but no solid conclusions or predictions exist to date.

Thus, the investigation of other areas of research, which seem to be indirectly related to geometry where a ventilated cavity is attached to a sparger, might prove useful and aid to the understanding of the complicated process of gas entrainment. There is a wealth of information in the literature regarding plunging liquid jets and confined jet systems. It was previously thought (Bacon, 1995a; Lee, 1998) that the mechanisms involved and the trends observed in these systems could be comparable to a ventilated cavity attached to a sparger despite the geometry differences. Therefore this review also emphasises any similarities that might exist between such systems and the system where a cavity is attached to a sparger in downflowing liquids.

2.1 PLUNGING LIQUID JETS

2.1.1 Introduction

Plunging liquid jets have been studied for many years as discussed below. One use of the plunging jet in the chemical industry is in the plunging jet reactor. The plunging liquid jet reactor is defined as the flow geometry formed by a coherent liquid jet passing through reactive atmosphere into a bath of the same liquid (Burgess et al., 1972). A sketch of the plunging jet reactor is shown in Fig. 2.1. A liquid jet plunges from a nozzle to a pool. The gas around the free jet is entrained with the jet under the free surface. The entrained gas is dispersed as fine bubbles,

which are carried downwards in the pool. The reactant gas dissolves into the liquid from these bubbles. The potential of the system as a reactor was recognised by Mertes (1938) who patented it as a technique for mixing and reacting liquids and gases. Mertes (1938) described the entrainment process as being a film of gas, which was formed in the region adjacent to the liquid jet. The gas film then travelled at the same speed as the jet and when was brought below the liquid surface, was sheared by the jet momentum and distributed as bubbles throughout the liquid. There is extensive information about plunging liquid jets and comprehensive summaries dealing with certain aspects can be found at Bin and Smith (1982) and Bin (1993).

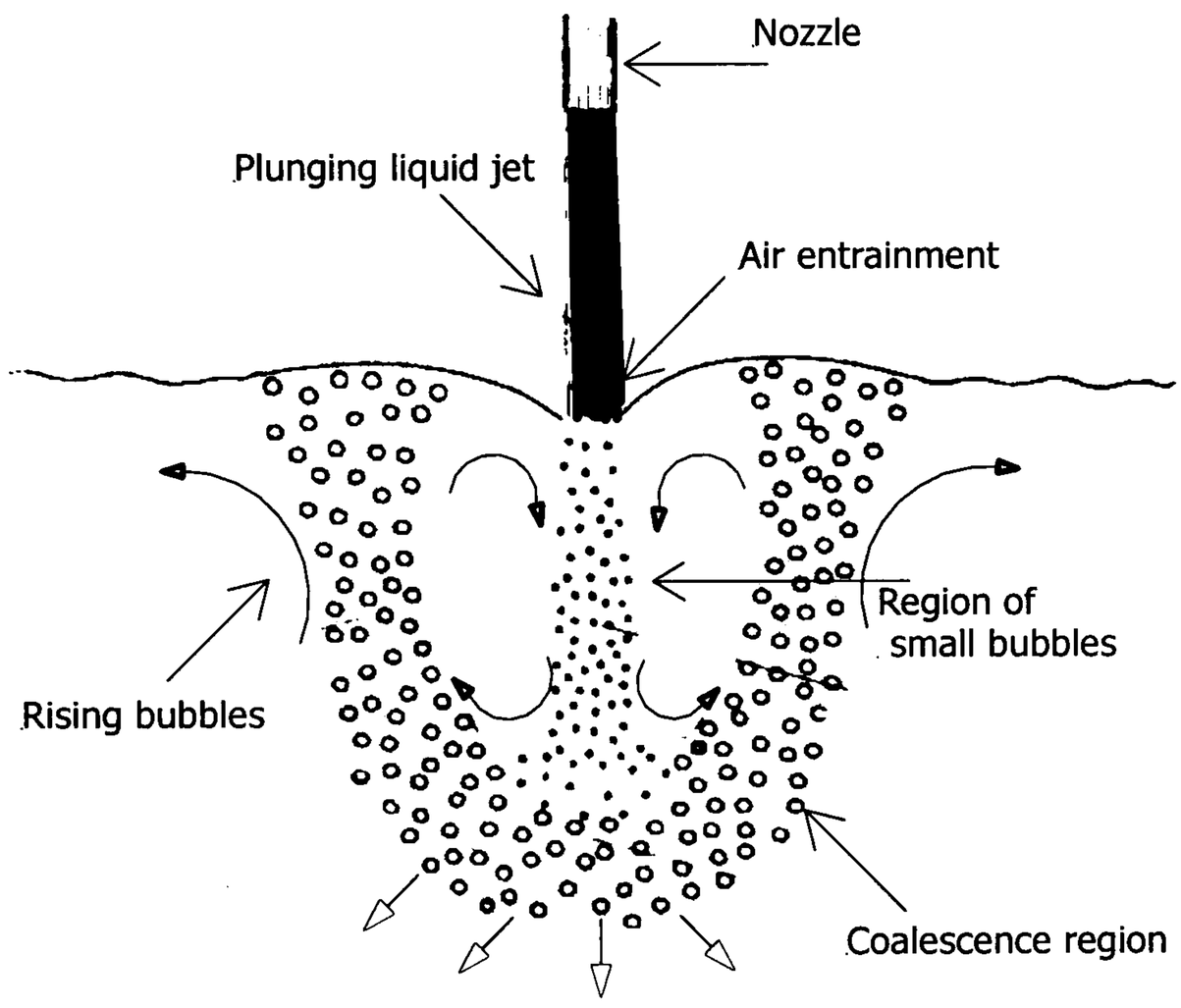

The plunging liquid jet reactor

Figure 2.1

An insight to the gas entrainment mechanisms by a plunging liquid jet is of high relevance to the investigation of gas entrainment from ventilated cavities attached to spargers. During this research it is proposed to use a type of sparger that directs the liquid to the centre of the downcomer where it *plunges*, jet-like, into the receiving liquid underneath the large bubble entraining gas as small bubbles (Thorpe et al., 1997 & Lee, 1998). Bonetto and Lahey Jr (1993), Cummings and Chanson (1994), Polonsky et al. (1999a), Taha and Cui (2002) and Thorpe et al. (2001), when discussing slug flow phenomena including ventilated cavities, suggested that the liquid film surrounding the Taylor bubble (or by analogy, the ventilated cavity beneath a sparger in this case) formed a type of annular plunging jet that produced a ring like surface depression in

the rear part of the bubble (Fig. 2.2). Gas is entrained when the annular wall liquid jet exceeds a critical velocity.

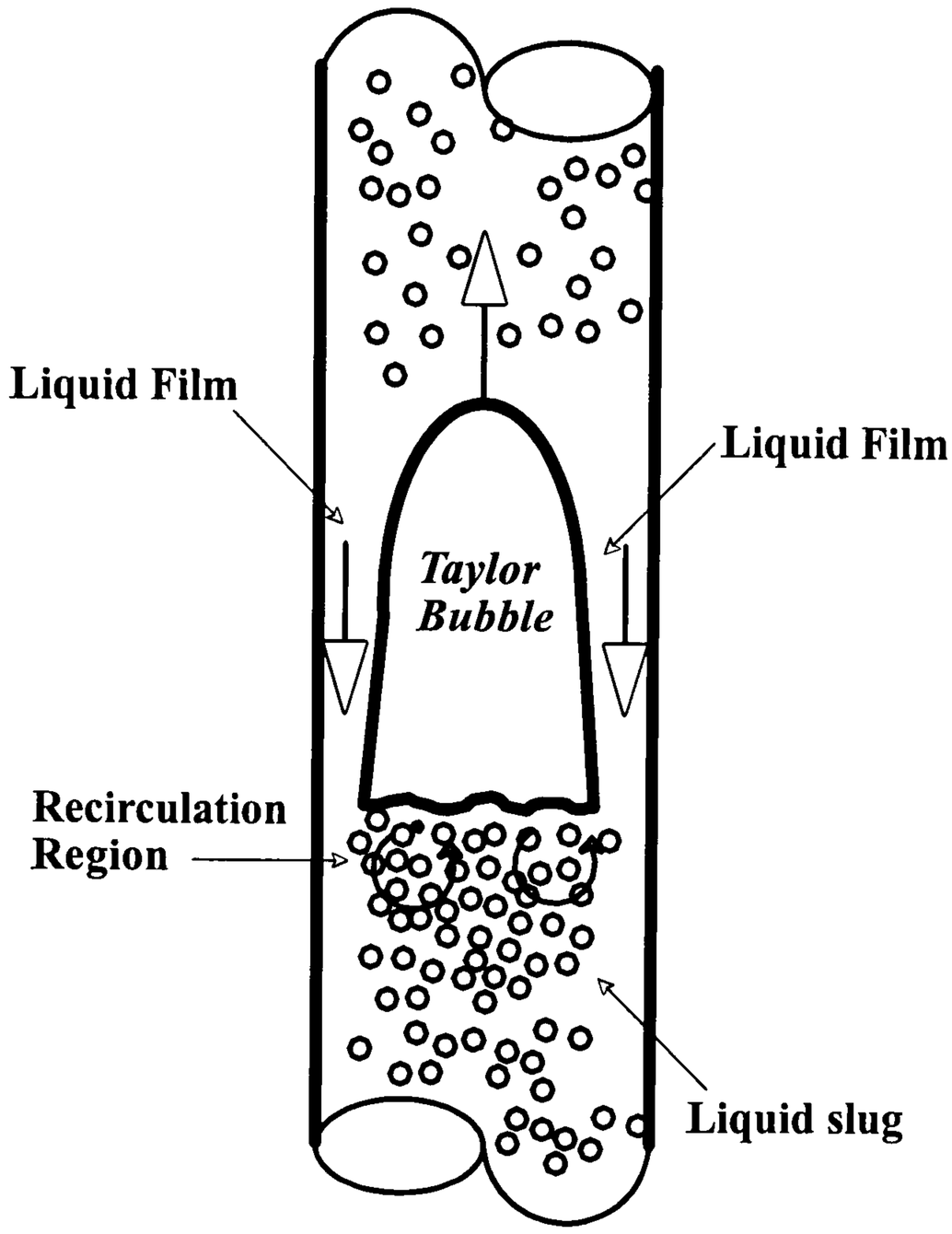

Gas entrainment at the rear of a rising Taylor bubble in a pipe.

Figure 2.2

Finally, Delfos et al. (1996) and Su (1995) who investigated gas entrainment rate from stationary slug bubbles and Bacon (1995a) and Lee (1998) who studied gas entrainment rate from ventilated cavities, supported that the gas entrainment process around a large cavity had many similarities to the gas entrainment of plunging liquid jets, a description of which will be given in the next paragraph.

2.1.2 Mechanisms of air entrainment

McKeogh and Ervine (1981) summarised the different entrainment behaviours described in the literature on plunging jets and proposed four separate mechanisms for entrainment.

i. Annular oscillation mechanism (Fig. 2.3). This type of mechanism occurs in smooth laminar (no surface disturbances) jets. The air boundary layer, surrounding the jet striking the

pool surface, causes a depression in the meniscus between the pool and the jet periphery forming an induction trumpet. Van de Sande and Smith (1976) suggested that this phenomenon arises from the flow of the liquid jet, creating an under-pressure circulation in the pool. Bin (1993) supported this statement and proposed as a primary cause for the creation of the induction trumpet the impact pressure of the associated air boundary layer. The trumpet is stabilised by surface tension and can exist without there being any entrainment. With an increase in the jet velocity a gas film (annulus) extends into the liquid pool. Its upper portion generally remains cylindrical in shape while its lower part makes an oscillating movement. The length of the vertical gas film formed at the plunging point depends on the liquid viscosity and jet velocity. Viscous jets at low velocity favour the formation of long gas films. The gas film becomes unstable because of the induced oscillations and breaks up into small bubbles, closure occurring as a result of somewhat random contacts between the jet and the converging free surface. (Lin and Donnelly, 1966; Bonetto and Lahey Jr, 1993; De Frate and Rush, 1969).

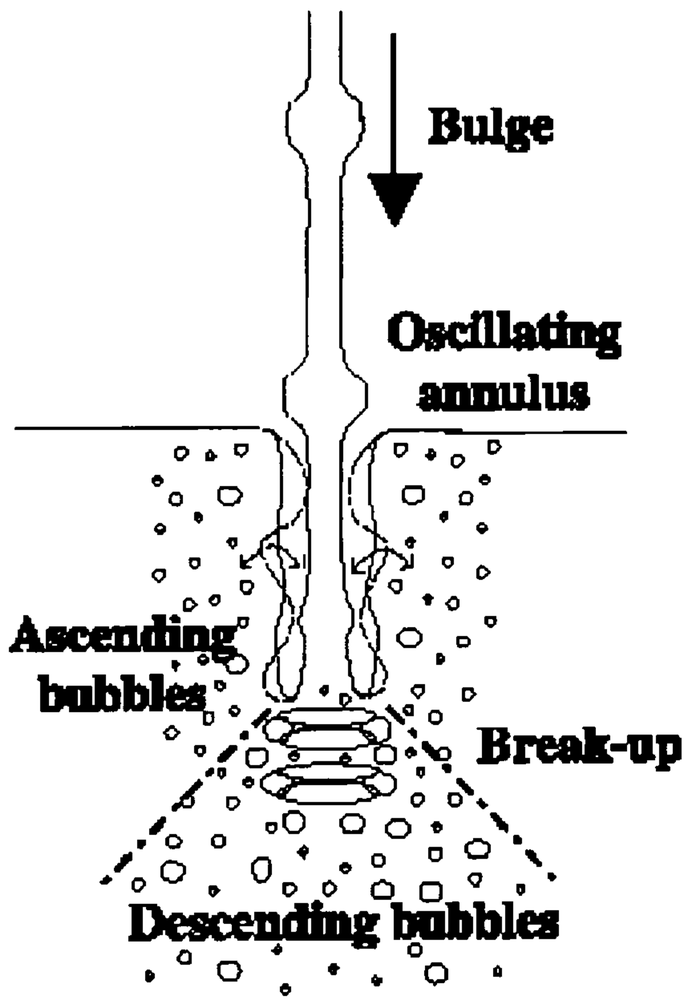

The annular oscillation mechanism as defined by McKeogh and Ervine, 1981. (Davoust et al., 2002).

Figure 2.3

ii. Intermittent mechanism (Fig. 2.4). It occurs when the jet surface is in transition between laminar and a roughened state caused by turbulence induced by the nozzle. A jet turbulence level at the point of impact of 1-1.5% is required. As the velocity of a laminar jet (i.e. with no surface disturbances) is increased, disturbances appear on the jet surface and the

entrainment becomes intermittent and irregular, taking place only when the disturbances hit the pool liquid surface (Lin and Donelly, 1966). A free surface vortex is formed at the plunge point that causes an inward radial flow. Bin (1993) stated that the formation of this surface vortex was the result of the impact pressure of the associated air boundary layer and from the flow field induced in the pool itself. The oscillating gas annulus disappears and the entrainment mechanism is governed by the interaction of the jet's disturbances with the surface vortex of the receiving pool. De Frate and Rush (1969) reported a similar transition mechanism based on qualitatively results. On the other hand, Van de Sande and Smith (1973) characterised the transition to turbulent occlusion, by the Weber number of the associate air boundary layer.

$$We_G = \frac{\rho_G V_j^2 D_N}{\sigma} = 10 \tag{2.1}$$

where V_j was the plunging jet velocity, D_N was the nozzle diameter and ρ_G was the air density. Bin (1993), checked this value against experimental data of other authors and found deviations of only ±20%.

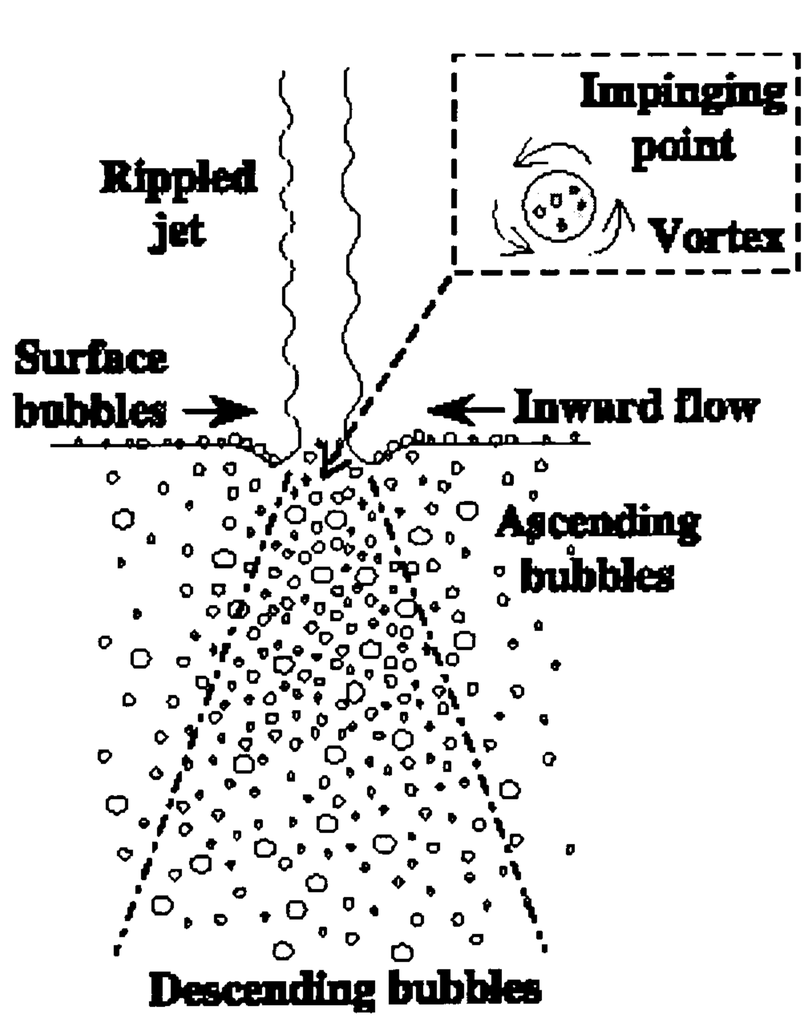

The intermittent mechanism as defined by McKeogh and Ervine, 1981. (Davoust et al., 2002).

Figure 2.4

iii. Turbulent occlusion mechanism (Fig.2.5a). Gas is carried along the jet, both within the jet envelope and also in the associated boundary layer. The jet expands as gas is continuously occluded into the jet core (Fig. 2.5b) (Evans et al., 1996; Moppett et al., 1995; Van de Sande and Smith, 1973). The surface instabilities as they propagate increase in magnitude (McKeogh and Ervine (1981). At higher jet velocities $\left(\mathrm{Re}_j \geq 18000\right)$ the jet surface is not at all smooth but ill defined and the surface instabilities are dragged into the pool surface resulting in the entrainment being increasingly vigorous (Lin and Donelly, 1966).

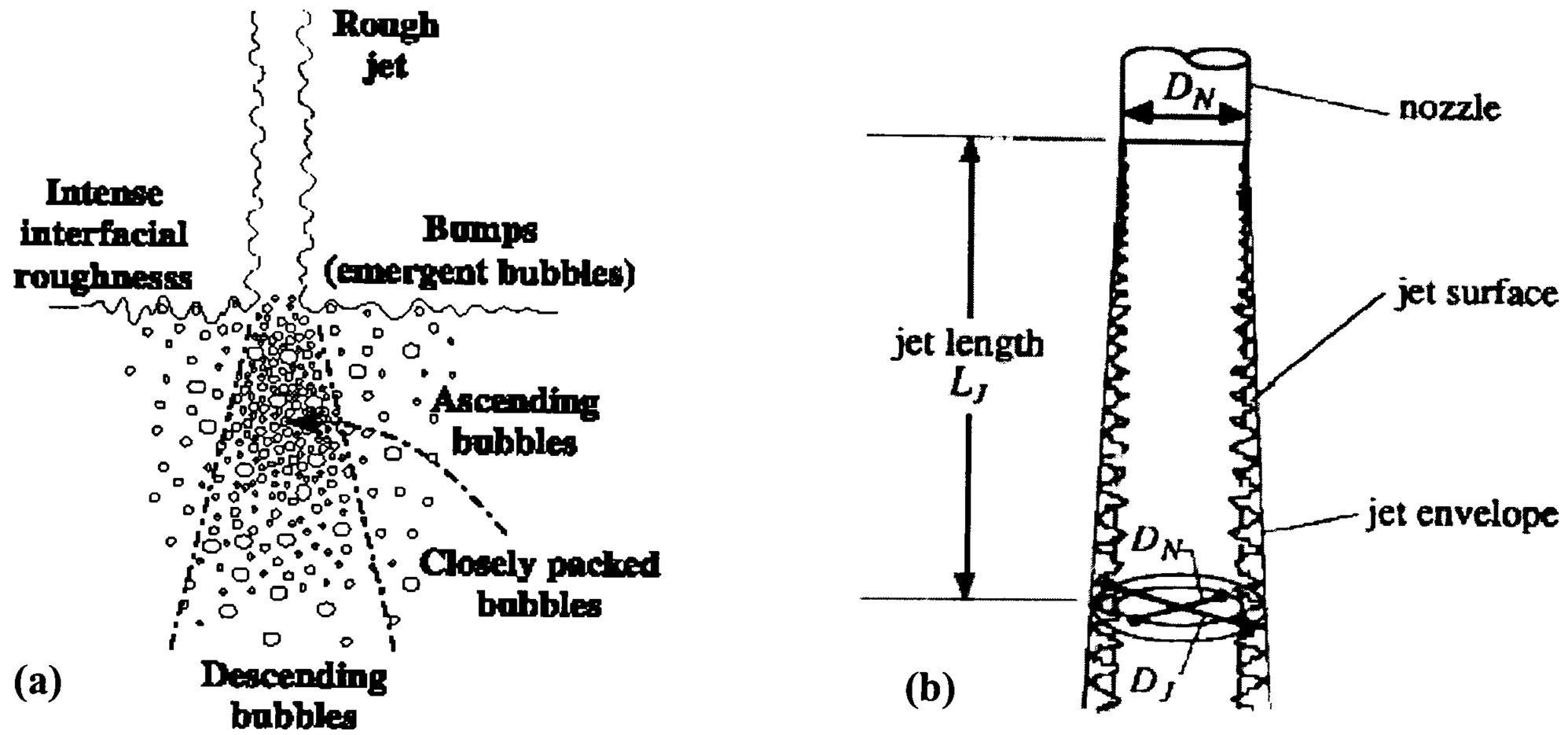

(a) The turbulent occlusion mechanism as defined by McKeogh and Ervine, 1981 (Davoust et al., 2002) and (b) the Plunging liquid jet envelope.

Figure 2.5

iv. Droplet entrainment. This mechanism occurs when the jet reaches its disintegration length before reaching the pool, twining into a stream of droplets, which entrain air upon impact with the pool. Lee (1998) did not observe the droplet mechanism during his experimental programme and so it will not be analysed further. However a good description can be found in Elmore et al. (2001), who studied extensively the air entrainment of single drops.

2.1.3 Onset of gas entrainment

Lin and Donelly (1966) were the first authors to make a detailed study of the air entrainment process. With the aid of high-speed photography they studied mainly laminar viscous

jets$\left(\mathrm{Re}_j \leq 1500\right)$ of 2 to 12 mm in diameter, although a limited number of experiments were made in the transition and turbulent flows. They used water-mineral oil and water-glycerol systems with viscosities ranging from 10 to 400 mPa s. To study the effect of a surface active agent, Tween 20 was added to some solutions. They characterised laminar jets as jets with no surface disturbances. Entrainment was observed after the jet velocity exceeded a critical value, known as the minimum entrainment velocity, V_e. This velocity was found to be a function of liquid viscosity and surface tension; the minimum entrainment velocity was monotonically reduced with increasing viscosity and decreasing surface tension. They derived an empirical correlation based on dimensionless analysis.

$$We_j = 10\,\mathrm{Re}_j^{0.74} \tag{2.2}$$

where We_j and Re_j were related to the liquid physical properties, to the jet diameter and jet velocity at the plunging point. Eq. (2.2) is valid for $8 \leq \mathrm{Re}_j \leq 1500$ and was set up from experiments with liquids of viscosity from 25 to 400 mPa s, density 876 to 1246 kg m^{-3} and surface tension from 0.03 - 0.63 N m^{-1}. However deviations were observed from the proposed correlation for jets with surfactants added to reduce surface tension. These deviations can be explained in terms of the Marangoni force. The addition of surfactants in a solution can give rise to a Marangoni force that may be able to damp the capillary waves and decrease the level of the interfacial roughness, with a direct effect on gas entrainment rate (see discussion further below on the jet's interfacial roughness). The Re_j in Bacon (1995a), Lee (1997) and this work was above 1500 and so Eq.(2.2) can not be tested. Perry (1967) confirmed the validity of Eq. (2.2) for his experimental measurements with aqueous glycerol solutions.

Ciroboski and Bin (1972), suggested for turbulent jets produced from short cylindrical nozzles $L_N/D_N \leq 8$ a very simple statement:

$$We_j = 400 \tag{2.3}$$

where L_N was the length of the nozzle. Eq. (2.3) was obtained for water and for different aqueous glycerol solutions with viscosity of 2 and 3 mPa s respectively. Bin (1988) calculated an average deviation of only 21% for the minimum entrainment velocity when he tested equation (2.3) with experimental data from other authors. Eq. (2.3) was tested with results regarding the onset of gas entrainment reported by Lee (1998) for the horizontal sparger and this work for the

central sparger (see sections 3.5.1 and 3.5.2 for a description of both spargers) and found to agree within 23%. The Weber jet number was related to the film velocity and film thickness at the base of the cavities and on the liquid physical properties $\left(We_j = \frac{\delta V_F^2 \rho_L}{\sigma}\right)$.

Sheridan (1966) suggested that entrainment was initiated by the presence of an instability formed on the surface of the meniscus at the plunging point. This instability was caused by the downward force exerted by the motion of the gaseous boundary layer being dragged along by the free surface of the jet. He actually estimated the resultant meniscus profile as a function of the jet velocity. He used a jet velocity of 2.35 m sec^{-1} when the meniscus contained a maximum, as the onset of entrainment. His experimental results supported the predicted value of 2.35 m sec^{-1} as the jet diameter tended to zero and showed that the entrainment velocity was a function of the jet diameter.

Lara (1979) studied the onset of entrainment for low viscosity jets (water-air) jets near the point where they disintegrate into droplets by capillary breakup. Lara (1979) was the first to establish two regions of the onset of air entrainment for low velocity $\left(\mathrm{Re}_j \leq 2000\right)$ liquid jets. The first region was where the jet broke into droplets, before reaching the pool surface and the second where the jet was coherent (continuous). Entrainment ceased when the jet velocity was increased to a point where the break-up length (disintegration length) was equal to the distance from the nozzle tip to the surface pool, creating a coherent jet. De Frate and Rush (1969) examined turbulent jets $\left(\mathrm{Re}_j \geq 20000\right)$ and concluded that entrainment was caused due to deformations on the surface of the jet and that the entrainment ratio[2.1] was given by:

$$\frac{Q_G}{Q_L} = 10^{-6} We \tag{2.4}$$

The Weber number in Eq. (2.4) was calculated using the liquid physical properties, the jet velocity and the jet free length.

The concept of inception velocity has been studied by many workers and has been extended to cover turbulent ($\mathrm{Re}_j \geq 2000$ where Re_j is the Reynolds number based on jet diameter and

---

[2.1] Entrainment ratio is defined as the ratio of the volumetric flow rates of gas and liquid and is a measure of the performance of the plunging jets (Bin, 1993).

velocity) jets, both planar (wall or 2 dimensional jets) (Sene, 1988; Cummings and Chanson, 1999; Bratberg and Chanson, 1998a; among others) and circular (free jets) (Bin, 1988; Van de Sande and Smith, 1973; Van de Sande and Smith, 1976; McKeogh and Ervine, 1981; among others). Lee (1998), concluded that quantitative comparisons of the minimum entrainment velocity between plunging liquid jets and the ventilated cavities observed in the current work would prove unhelpful because direct comparisons had to be based on geometrically similar nozzles. However, it would be helpful to investigate the minimum entrainment velocity of plunging jets because it would give an order of magnitude estimate for the minimum film velocity needed to initiate gas entrainment at the base a ventilated cavity attached to a sparger.

McKeogh and Ervine (1981) varied the turbulence intensity of a circular jet from 0.3% (very smooth turbulent) to 8% (rough turbulent) and found minimum entrainment velocities of 3.6 m sec^{-1} and 0.8 m sec^{-1} respectively. Other researchers determined visually similar minimum entrainment velocities, i.e. 1 m sec^{-1} for rough jets (Sene, 1988) and 2 m sec^{-1} for smooth jets (Sene, 1988; Kumagai and Endoh, 1982). Cummings and Chanson (1997) conducted experiments in a 2-dimensional wall jet and observed entrainment for $V_e \geq 1.1$ m sec^{-1} when the jet turbulent intensity at impact was 1.3% and $V_e \geq 2$ m sec^{-1} for 0.3%. Van de Sande and Smith (1976) commented that jets would entrain air when exceeded about 2 m sec^{-1} but that the exact velocity depended on local effects such as jet surface roughness and jet kinetic energy. McKeogh and Ervine (1981) and Ervine et al. (1980), Zhu et al. (2000) recorded the jet turbulence at the nozzle and Bratberg and Chanson (1998a), Bratberg and Chanson (1998b), Cummings and Chanson (1999) measured the turbulent intensity at the impact point. They all agreed that the inception of gas entrainment is a function of the magnitude of disturbances on the surface of the jet. As the turbulent intensity was increased the inception velocity decreased.

2.1.4 Rate of gas entrainment

According to Bin (1993) the nozzle geometry, jet length and diameter, turbulence intensity in the jet and liquid physical properties affect the gas entrainment of a plunging liquid jet. The parameters of direct interest to this work are the jet velocity and liquid physical properties (Bacon, 1995a; Lee, 1998).

2.1.4.1 Jet velocity

The first theoretical prediction for the gas entrainment rate was given by Szekely (1969) who assumed that the entrainment rate was equivalent to the quantity of gas contained in the gaseous film adjacent to the free surface of the jet. He derived the following equation:

$$\frac{Q_G}{Q_L} = \frac{4\rho_G^2}{\rho_L^2 D_N{}^2}\left(\frac{3\mu_L H_N}{\rho_L \rho_G V_j} + 1.73\left(\frac{V_N H_N}{V_j}\right)^{0.5}\right) \tag{2.5}$$

where Q_G and Q_L were the volumetric flow rates of the gas and liquid phases respectively and H_N was the distance from the nozzle exit to the pool surface. However, the analysis of Szekerly was very simple since he did not differentiate between laminar and turbulent jets, or consider the effects of the interfacial disturbances on the free surface of the jet.

Sene (1988) studied the entrainment rate for circular and planar jets for both low and high jet velocities. He identified two main regions with respect to the plunging velocity V_j. He controlled the roughness of the jet by conducting measurements with a nozzle (rough jets) and a weir (much smoother jets).

i. For $V_j \leq 4$ m sec^{-1}, he suggested that the surface disturbances of the jet played a significant role in the gas entrainment. He related the pressure drop across the curved liquid surface to that in the receiving flows to demonstrate that the entrainment rate was likely to increase with a reduction in the radius of curvature of the disturbances. The size of these disturbances depended on the turbulent intensity of the jet. Bubbles formed because surface tension forces prevented the receiving flows from following the disturbances on the jet, resulting in air entrainment. Bratberg and Chanson (1998a) gave an identical explanation for a planar jet but for $V_j \leq 2$ m sec^{-1}.

ii. For and $V_j > 4$ m sec^{-1} he suggested that there existed a thin air layer set in motion by shear forces at the surface of the jet entered the flow at the impact point. This layer was then broken up further downstream into a succession of bubbles due to the instability of the waves on the jet's surface. It was likely that the air layer became established at localised regions along the interface between the jet and the receiving flows. When the jet velocity was increased it was observed that these regions joined up to form a continuous layer along the interface. Bratberg and Chanson (1998a) observed the same for 3 m sec^{-1} $\leq V_j \leq$ 5 m sec^{-1}.

Sene (1988) tested the experimental results of Van de Sande and Smith (1973) on his model (they were the only relevant data at that time) and the agreement was very good for the largest diameter jet tested (10 mm), but as the diameter decreased the fit was quite bad. According to Sene, the discrepancies were possibly due to the scale effects on the smaller jets, i.e. the surface tension forces opposed the entrainment rate of these jets by reducing the thickness of the air layer at the already mentioned localised regions. However Su (1995) who investigated gas entrainment rate from stationary slug bubbles, did not observe such a gas layer because of the high turbulent intensity in the vicinity of the slug bubble.

Based on his results and the mechanisms proposed, Sene (1988) proposed) that $q_G \propto V_j^n$ for planar jets and that $Q_G/\pi D_j \propto V_j^n$ for circular jets (q_G is the gas entrainment rate per unit width of planar jet, Q_G is the total gas entrainment rate, D_j is the circular jet diameter at the plunging point and n is an exponent). He quoted values of $n = 3$ and $n = 1.5$ for low and high jet velocities respectively, for both circular and planar jets.

Bacon (1995a) and Lee et al. (1997a) tested the concept of Sene's work. They both scaled the measured maximum gas entrainment rate (see section 2.5.2.3) by the jet width and plotted it against the impact velocity in order to remove any scale dependencies. They showed that the analysis by Sene (1988) was not a satisfactory method of eliminating the size factor because the experimental results when using the same type of sparger on experimental setups of different sizes (Bacon used a 50 mm id pipe while Lee a 105 mm id pipe) did not lie on top of one another.

Van de Sande and Smith, (1976, 1973), produced a theoretical model and empirical correlations to fit their experimental data for low velocity ($2 \le V_j \le 5$ m sec^{-1}) and high velocity jets ($V_j \ge 10$ m sec^{-1}) respectively. For both cases they found a linear increase of the entrainment ratio with jet velocity. They commented that the action of moving surface deformities and the liquid physical properties were mainly responsible for the entrainment mechanism at lower jet velocities. However for higher jet velocities the contribution of the surface irregularities was reduced. For high jet velocities Van de Sande and Smith (1973) modelled the total volumetric gas entrainment rate (Eq. 2.6) as the sum of the gas contained inside the boundary layer, Q_F, which was dragged along by the free surface of the jet and the gas trapped inside the boundary of the effective jet diameter (i.e. within the geometrical undulation of the interface), Q_T.

$$Q_G = Q_F + Q_T \tag{2.6}$$

In Eq. (2.6) the component Q_T was calculated from Eq. (2.7) proposed by McCarthy (1972), who quantified the entrainment phenomenon using the jet volumetric flow rate, Q_j, and the effective jet diameter $D_{j(z)}$ (see also Fig. 2.5b) for a vertical distance z below the nozzle:

$$\frac{Q_T}{Q_j} = \left(\frac{D_{j(z)}}{D_N} \right)^2 - 1 \tag{2.7}$$

where the effective jet diameter, $D_{j(z)}$ in Eq. (2.7) was given by Van de Sande and Smith (1973) as:

$$\frac{D_{j(z)}}{D_N} = 0.125 \left(\mathrm{Re}_{H_N} We_G \right)^{1/6} \tag{2.8}$$

The We_G in Eq. (2.8) was based on the gas physical properties, the jet velocity and the nozzle diameter, whereas the Re_{H_N} was based on the liquid physical properties, the jet velocity and the free jet length. Van de Sande (1974) and Van de Sande and Smith (1973), calculated Q_F by assuming a laminar velocity profile and integrating across its thickness. Q_F was a result of a graphical solution of a log-log diagram.

Van de Donk (1981), on the other hand, found that the entrainment ratio remained more or less constant (around 0.8) with increasing nozzle velocity ($V_N = 2-10$ m sec^{-1}), when he used a simple nozzle with a conical entry ($D_N = 30$ mm). He attributed that to the fact that the turbulence in the jet was not completely developed at the point of discharge, delaying the formation of surface instabilities that would give greater entrainment.

McKeogh and Ervine (1981) were the first to develop empirical correlations between air entrainment rates and jet surface roughness for jets issuing with nozzle velocities of $V_N \leq 10$ m sec^{-1}. Their data corresponded to both the continuous and the droplet region of entrainment. They noted that the gas entrainment rate increased with jet length until the point where the jet began to breakup. After that point the opposite was observed. Highly turbulent jets $(T_u \geq 6\%)$ were found to entrain more air at short jet lengths than less turbulent jets $(T_u \geq 1\%)$, but to break up at shorter lengths. This is in agreement with the results of Van de Sande and Smith (1973), Cummings and Chanson (1994) and Moppett et al. (1995). As a result, a maximum entrainment rate existed which corresponded to the maximum length of each jet before disintegration. This agrees with Moppett et al. (1997) who observed maximum entrainment rates for a circular jet,

when the jet velocity exceeded 14 m sec^{-1} leading to the jet's disintegration into a spray. McKeogh and Ervine (1981) used high-speed photography to relate the operational parameters (nozzle velocity and diameter, turbulent intensity of the jet and jet length) to the surface disturbances. However they did not provide information of the way they measured the surface disturbances and so comments about the accuracy and validity of their derived correlation are not possible. The effect of each parameter on the jet's surface roughness was found to follow similar trends to the effects they had on the entrainment rate. For air – water systems they provided the following empirical correlation:

$$\frac{Q_G}{Q_L} = 1.4\left[\left(\frac{\xi}{D_N}\right)^2 + 2\frac{\xi}{D_N} - 0.1\right]^{0.6} \tag{2.9}$$

The term ξ represented the surface disturbance on the free surface of the jet and is shown in Fig. 2.6. The gas entrainment rate in Eq. (2.9) corresponded to the total gas entrainment rate including both Q_T and Q_F.

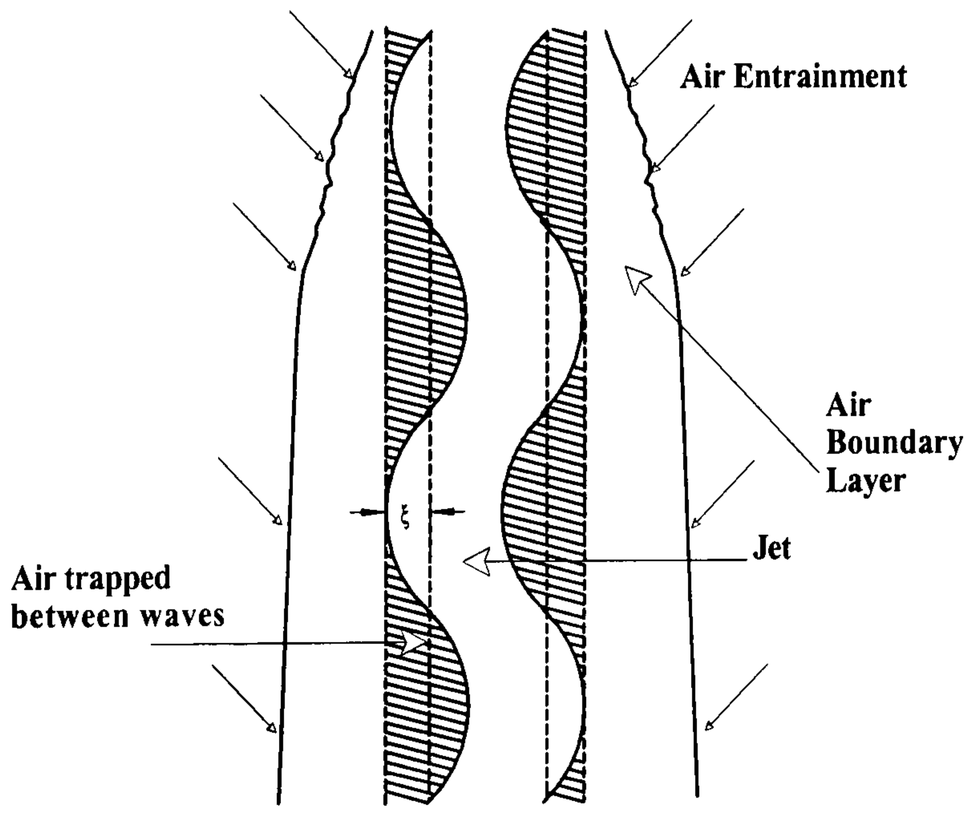

Sinuous waveform of jet as defined by McKeogh and Irvine (1981).

Figure 2.6

Davoust et al. (2002) commented that the empirical way by which the model of McKeogh and Ervine (1981) took into account the air boundary layer was questionable. They argued that the geometrical model introduced by McKeogh and Ervine (1981) suffered from a lack of generality, because the concept of the interfacial roughness was a term that characterised the jet only before its impact and was defined McKeogh and Ervine (1981) as the ratio of the typical magnitude of

the disturbances to the mean radius of the jet. Such a definition did not take into account the dependence of the amount of air carryunder on the wavelengths (or integral scales) that characterised the interfacial disturbances on the jet. On this account, they focused on the relevance of the initial interfacial roughness on gas entrainment rate. They used a rather sophisticated optical technique, based on light absorption, to measure interfacial roughness. Davoust et al. introduced a new term, the dynamical roughness, ξ_D, defined as:

$$\xi_D = \frac{V_j'}{V_j} \tag{2.10}$$

where V_j and V_j' were the jet velocity and the r.m.s. fluctuating velocity respectively. This roughness, turned out to be proportional to the magnitude of the interfacial deformation and inversely proportional to its wavelength. Davoust et al., (2002), used Lobelia oil (highly viscous jets - $Oh = \frac{\mu_L}{\left(\rho_L \sigma D_N\right)^{0.5}} = 0.04375$) and water jets $\left(Oh = 0.01251\right)$ in order to distinguish between the laminar and turbulent case respectively. They plotted their experimental data versus the Weber number of gas entrainment $\left(We_n = \frac{\rho_G V_G^2 D_N}{\sigma}\right)$, where V_G (mean velocity of the air carryunder) was estimated from the experimental measured gas entrainment rate Q_G. When the plunging jet was laminar, the dependence of We_n on ξ_D was found to be monotonic and close to a linear progression, even though there was scatter among the data. In the case of turbulent jet small variations of ξ_D led to high increases in the amount of air entrained.

However there are some issues that need to be addressed first, before any general conclusions regarding the work by Davoust et al., (2002) can be drawn. The technique they used had a limited spatial resolution and therefore was unable to detect the interfacial instabilities related to the inertial or Kolmogorov sub-regimes when the turbulence was fully established (i.e. when the liquid jet was strongly turbulent all along its falling height). That means that the dimensionless correlations they provided based on We_n were not universal since they did not apply to high turbulent jets ($V_j \geq 10$ m sec^{-1} in line with other researchers). Also a rather bad reproducibility was observed on the measurement of We_n for both the turbulent and laminar cases examined suggesting probably that there was also another mechanism apart from the initial interfacial roughness that governed the entrainment rate that was not taken into account in the dimensionless correlations they provided. The model of Davoust et al., (2002), is expected to be a reliable indicator of the entrainment efficiency, but only for a certain range of jets velocities

with $V_j \leq 10$ m sec^{-1}, if the turbulence at the receiving pool plays a negligible role to the air entrainment. This concept is important to the present study because the interfacial roughness of the falling liquid film is among the key parameters that govern the gas entrainment rate. However, in the case with the cavity attached to a sparger, the receiving flows are also thought to play a significant part on the entrainment process, by means of the recirculating vortex present underneath the ventilated cavity (see section 2.4.5).

In conclusion, for low viscosity jets it seems that the interaction between the disturbances on the jet (surface roughness) and the receiving liquid surface is the dominant factor of the entrainment rate in the low velocity region. In this region the jet disturbances are generated by the inertial forces, largely turbulence of the jet itself. The entrainment rate is affected by the size and rate of disturbances entering the receiving flows, thus linking jet velocity, turbulent intensity and magnitude of the disturbances. In the high velocity region the jet velocity contributes more that the surface roughness to the entrainment rate. Disturbances of the jet surface are again important because of the interaction of the jet with the ambient air. Entrainment rate is not only a result of the liquid interaction process, but also by the air movement itself. For viscous laminar jets gas is entrained in the form of a thin gaseous film, which breaks into bubbles (Bin, 1993).

2.1.4.2 Liquid physical properties

The effect of liquid physical properties on the entrainment rate from a plunging liquid jet has been examined by only a few researchers and has shown to be of vital importance. Kusabiraki et al. (1990a) studied the effects of liquid physical properties on the gas entrainment rate of vertical plunging liquid jets. They used tap water, potassium chloride solutions of 0.002 kmol m^{-3}, methanol, ethanol, glucose and corn syrup solutions as well Tween-60 (surface active agents). Kusabiraki et al. (1990a) combined the liquid physical properties into the dimensional number $\frac{\mu_L}{(\rho_L \sigma)^{0.5}}$, where μ_L, ρ_L and σ were the liquid viscosity, liquid density and surface tension. This dimensional group was related to the dimensionless jet Ohnesorge, Oh $\left(\frac{\mu_L}{\sqrt{\rho_L \sigma D_N}}\right)$ or stability number. Their results indicated that entrainment ratio Q_G/Q_L decreased, remained constant and then increased with increasing $\frac{\mu_L}{(\rho_L \sigma)^{0.5}}$, regardless of nozzle geometry, jet length and velocity. These regions were:

- Q_G/Q_L decreased for values of $\frac{\mu_L}{(\rho_L\sigma)^{0.5}}$ between $1.04\text{x}10^{-4}$-$1.20\text{x}10^{-4}$.
- Q_G/Q_L remained constant for values of $\frac{\mu_L}{(\rho_L\sigma)^{0.5}}$ between $1.20\text{x}10^{-4}$-$1.90\text{x}10^{-4}$.
- Q_G/Q_L increased for values of $\frac{\mu_L}{(\rho_L\sigma)^{0.5}}$ between $1.90\text{x}10^{-4}$- $4.80\text{x}10^{-4}$.

Kusabiraki et al. (1990a) proposed a correlation for the entrainment ratio Q_G/Q_L using the Oh number to account for the liquid physical properties. They quoted that $Q_G/Q_L \propto Oh^f$, where the value of the empirical exponent f was found once the regions I-III were determined. They gave values of $f=-0.5$ in region I; $f=0$ in region II and $f=0.31$ in region III for low velocity jets ($V_N = 2.5-5$ m sec^{-1}) with $5 \le L_N/D_N \le 15$. Yamagiwa et al. (1993) noted identical regions while studying inclined plunging liquid jets. They obtained an exponent f *of* –0.19, 0 and 0,14 in regions I, II and III respectively and found the exponent to be independent of the operating conditions applied. However no explanation was given for the differences in the exponents. On the other hand, in a subsequent paper, Kusabiraki et al. (1990b) did not observe the three regions when studying the gas entrainment rate in a circular plunging liquid jet from inclined nozzles using the same liquids as Kusabiraki et al. (1990a). They found that the entrainment ratio Q_G/Q_L decreased gradually with increasing Oh and the value of the empirical exponent was $f=-0.19$.

Bacon (1995a) stated that the effects of the Oh number were not thoroughly investigated in the literature because different liquids were used for different values of Oh; e.g. corn syrup was used to give high Oh (due to high viscosity) whilst ethanol gave low values of Oh (due to low viscosity). A similar comment can then be made for Yamagiwa et al., (1993) because their three regions consisted of experimental data measured with different liquids. Region I consisted of data measured with alcohol, potassium chloride and Tween-60 solutions, whereas data in regions II and III recorded from measurements with corn-syrup solutions of varying concentrations.

Kusabiraki et al. (1992), Yamagiwa et al. (1993) and Yamagiwa et al. (2001) measured the length of the undulating interface between the discharging liquid jet and the surrounding gas phase. The surface disturbance or the sinuous undulation of the liquid jet was quantified using photography from an enlarged image of the jet's surface. The results were related to the changes in liquid physical properties via the Oh. It was shown that the changes in the entrainment ratio Q_G/Q_L with respect to Oh followed very similar trends to the changes in the average jet length

(along the undulating jet surface) with respect to Oh (the three regions described above). Also the effect of Oh on the normalised jet diameter, D_j/D_N, was found to be negligible. The first observation led Kusabiraki et al. (1992) and Yamagiwa et al. (2001) to conclude that the differences of the entrainment rates between different liquids were also related to the change of the jet shape before plunging. Their second observation indicated that, in analysing the differences of entrainment rates in terms of the changes in jet shape rather than the jet diameter is more important factor.

2.1.4.3 Surface tension

Kusabiraki et al. (1990a,b), used a variety of different liquids to examine the effect of surface tension on gas entrainment rate. Some of the liquids used had similar viscosities and densities to water but different surface tension, e.g. potassium chloride 0.002 kmol m^{-3} (higher surface tension) and surface active agents (lower surface tension). They found that the gas entrainment rate increased in both cases, which led first Bacon (1995a) and then Lee (1998) to state that the effect of surface tension on entrainment rate was not conclusively determined by the work of Kusabiraki et al, (1990a,b). To determine a genuine dependence on Oh, investigation of entrainment rates using intermediate to high viscosity solutions with a variety of surface tensions would be required.

Kumagai and Endoh (1982) reduced the surface tension of tap water by adding the surface-active agent Tween 80, to examine the entrainment behaviour using plunging liquid jets inclined at 30° and 60° to the horizontal. Their results showed no dependence of gas entrainment to surface tension. However for $V_j \leq 2$ m sec^{-1}, gas entrainment rate increased slightly with surface tension, indicating some kind of dependence to surface tension. Kumagai and Endoh (1982) commented that existing gas entrainment correlations in the literature comprised the dimensionless groups of We and Oh, that are associated with the surface tension of the liquid. They concluded that their experimental result was different from those of other authors, but without providing any further explanation. Kusabiraki et al. (1990b), doubted strongly the experimental entrainment rates reported by Kumagai and Endoh (1982). Especially at high entrainment rates, the gas velocity might have disturbed the natural surface or shape of the liquid jet issuing from the nozzle affecting the measured entrainment rates. Bin (1993), tested the correlations proposed by Kusabiraki et al. (1990b) using the experimental data of Kumagai and Endoh, (1982) and found that they offered some reasonable accuracy, although deviations as high as ±70% could occur. Bin (1993) concluded that to some extent, these deviations might result from the particular method used for the determination of Q_G.

Sene (1988) considered air entrainment by planar and circular plunging jets at both high and low velocities. He proposed an expression to determine the gas entrainment rate of a low velocity jet ($V_j \leq 4\,\text{m sec}^{-1}$) stating that bubbles are formed only if surface tension forces prevent the receiving flows from following the disturbances on the jet. His criterion for one bubble to be entrained was that $\frac{2\sigma}{\Re}$ (where $\Re$ was the radius of curvature of the surface disturbance) must exceed the pressure of the liquid in the receiving flows. Sene (1988) assumed that $\Re$ (i.e. the disturbances) arose from turbulent fluctuations within the jet. He derived an expression for the entrainment rate, which predicted a decrease in the entrainment ability of low laminar jets with a reduction in surface tension. However the theoretical analysis of Sene (1988) was not tested experimentally as only water was used in his experiments involving planar jets inclined at a moderate angle of 45° to the horizontal, which may not applicable in the current work.

Oguz and Prosperetti (1994) concentrated on the effects that the disturbances of a planar jet had, as the primary cause for air entrainment. They modelled the disturbances of the falling liquid surface as overpressures of finite duration acting on the receiving liquid surface. They used large *Re* and so neglected any viscous effects modelling the flow as irrotational. They carried out simulations (boundary integral method), which showed that surface tension did not play a dominant role in the entrainment dynamics above a certain Weber number of about 10. Earlier empirical correlations confirm this finding (Van de Sande and Smith, 1973).

An interesting point set by Bin (1993) and afterwards highlighted by Lee (1998) was the effect of surfactant diffusion on the entrainment rates. Bin (1993) discussed that the surface tension measured when surfactants are present in a static liquid and that occurring at a free liquid surface in a plunging jet may differ significantly due to the finite time required for the surfactants to diffuse from the bulk liquid to the free surface. Hence, for shorter jets the equilibrium concentration of a surfactant may not necessarily be reached before plunging to the pool liquid. Some papers in the literature support this. Nicol and Davidson (1988) used Bovine serum albumen (BSA), which is a globular protein, in a circulating bubble column as a surfactant and reported that the equilibrium surface tension was attained after 800 minutes. Additionally, West and Hull (1933) reported changes in surface tension up to 30 minutes after the formation of a solution containing surfactants.

2.1.4.4 Viscosity

Kusabiraki et al. (1990b), observed a linear increase in entrainment with increasing viscosity for plunging jets with $V_N = 3.2-11$ m sec^{-1}. The results of Cumming (1975) who used circular jets of aqueous glycerol solutions of viscosities 2.2 to 12 mPa s, also indicated an increase of entrainment rate with increasing viscosity. Kusabiraki et al. (1992) observed parallel increases in jet surface roughness and entrainment rate when viscosity was increased.

On the other hand, Sene (1988) assumed that viscosity had no effect on the gas entrainment rate and neglected it from his theoretical approach. However, the model proposed by Sene (1998) was based on planar jets, inclined at a moderate angle and may not fully describe vertical plunging jets. Kumagai and Endoh (1982) examining inclined plunging jets, summarised their results into four different regions. They reported a reduction in gas entrainment rate with increasing viscosities at $V_j = 1-6$ m sec^{-1}. At higher jet velocities ($V_j = 6-20$ m sec^{-1}) an increase in viscosity produced an increase in entrainment rate. At still higher velocities the effects of kinematic viscosity were insignificant. Kumagai and Endoh (1982) produced experimental correlations based on least squares fitting for the gas entrainment rate for all the regions and tested them against the observations of Van de Sande and Smith (1973). The agreement was very good.

The differences between the results of Kumagai and Endoh (1982) and Kusabiraki et al. (1990b) may be due to the fact that when examining the effects of viscosity on gas entrainment rate, Kumagai and Endoh (1982) used inclined jets that was very likely to have affected the entrainment mechanism. Moreover, the measuring techniques of gas entrainment rate used between the researchers were different.

The effect of the liquid physical properties on gas entrainment rate from plunging liquid jets is not well understood in the literature. Most researchers dealing with plunging liquid jets used only water-air so surface tension and viscosity effects could not be taken into account. Kumagai and Endoh (1982) commented that the effect of liquid viscosity should be studied further. Bin (1993) commented that more experimental data together with a theoretical background to explain these effects would be highly desirable.

2.2 CONFINED JET SYSTEMS

A number of authors examined the influence of downflow confined jet systems on gas entrainment and mass transfer rate. For two examples of confined jet systems see Fig. 2.7. The downflow operation is achieved when both gas and liquid move cocurrently downwards in the column. Gas bubbles are then forced to move in a direction opposite to their buoyancy having a higher slip velocity compared to upflow systems. Thus the bubbles experience higher residence times. The investigation of such systems is relevant to the current work where the physical presence of the 0.105 mm diameter downcomer might play an important role in the entrainment rate, gas-liquid contacting and the spreading of the wall jet at the base of the ventilated cavity. Lee (1998) commented that an understanding of how the presence and size of such downcomers affect entrainment rates might give useful insights into the scale up aspects.

Confined jet systems of interest to the present work include confined plunging liquid jets (CPLJ) (Fig. 2.7a) and downflow ejector loop reactors (DELR) (Fig. 2.7b). In the CPLJ a vertical liquid jet ejected from the nozzle plunges into the free surface of the two-phase mixture and entrains gas from the headspace (Evans and Machniewski, 1999) (free jet zone). The submerged jet expands until it finally attaches to the pipe wall (mixing zone) allowing a fraction of the entrained bubbles to recirculate back to the headspace. A bubbly flow exists below the mixing zone. The principle of the CPLJ is similar to that of DELR. The DELR uses the high speed liquid jet ejected from the nozzle to drag air and mix it in a throat (mixing tube) so at to obtain a bubbly flow at the outlet. A diffuser is connected upstream of the mixing tube which allows for pressure recovery to take place. The bubbles are then able to flow within a duct or a pipe located upstream. A good description of the hydrodynamics and the design principles for both the CPLJ and the DELR are beyond the aims of this review and can be found elsewhere (Evans, 1990; Havelka et al., 2000; Cramers et al., 1992; amongst others).

2.2.1 Gas entrainment rate

Ohkawa et al. (1986) compared the flow characteristics of a CPLJ to a circular one (unconfined) under identical conditions ($D_N = 0.007 - 0.013$ m, $H_N = 0.025 - 0.750$ m and $V_N = 2 - 14.3$ m sec^{-1} for both systems). They conducted measurements for the gas entrainment rate in the downcomer system examining the effects of the downcomer length (L_D), downcomer diameter (D) and nozzle diameter (D_N) on gas entrainment rate. Their experimental data showed that in all cases the volumetric gas entrainment rate increased linearly with increasing jet velocity at the plunging point (V_j). The application of the downcomer enhanced both the gas

entrainment rate and the bubble penetration depth and also provided a much longer gas-liquid contacting section by confining the resulting bubble swarm. The authors derived the following empirical correlation with a ± 30% error. Ohkawa et al. (1987a) found that equation (2.11) is also applicable for longer downcomers, up to 5 m. However, the constant of 0.698 in Eq. (2.11) is dimensional with units in $s^{1.4}\ m^{-1}$.

$$Q_G = 0.698(V_j^3 D_N^2)^{0.8}(\frac{D_N}{D})^{1.3}(\frac{L_D}{D})^{-1.6} \tag{2.11}$$

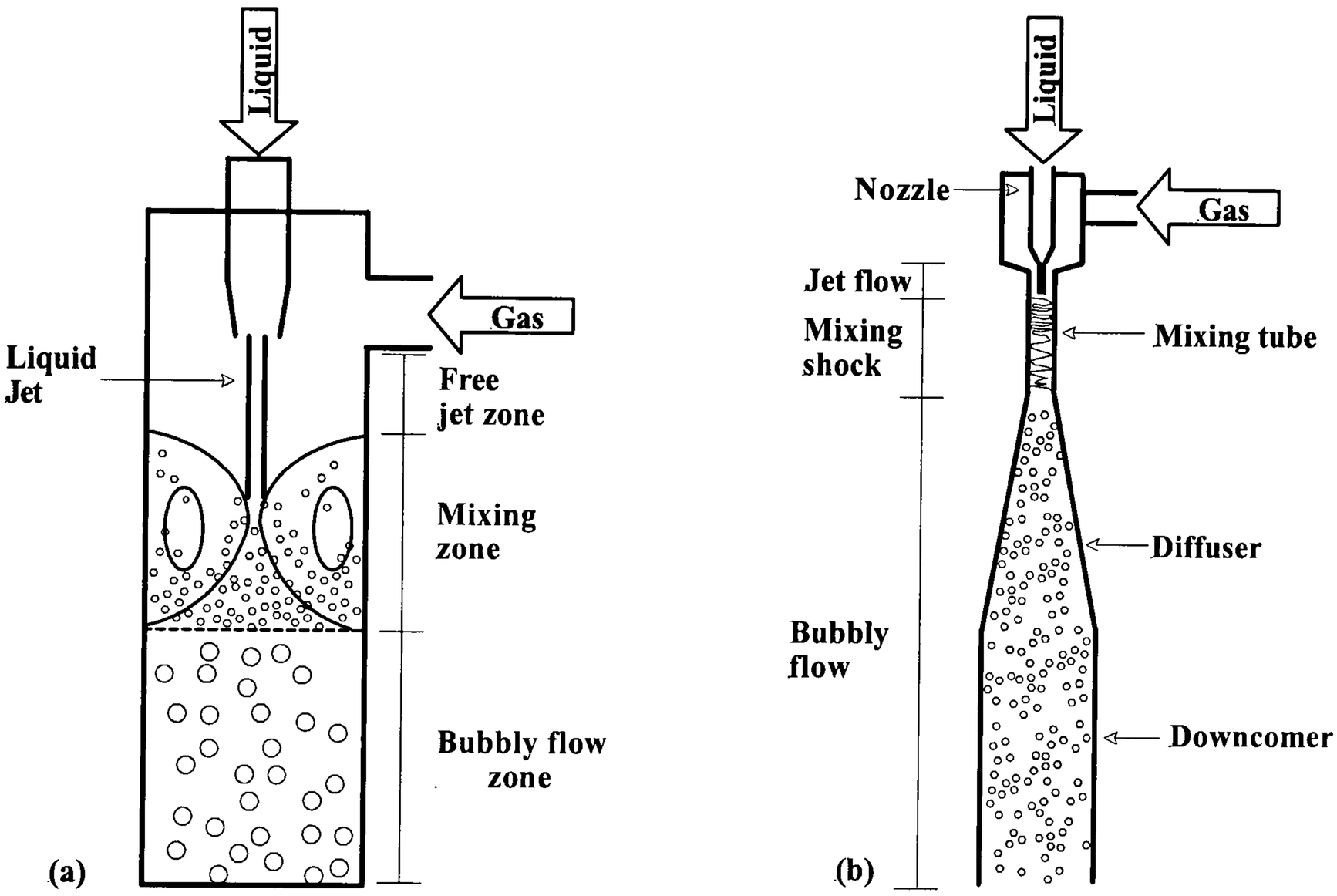

The schematic of (a) Confined plunging liquid jet (CPLJ) (Evans and Machniewski, 1999) & (b) Downflow ejector loop reactor (DELR).

Figure 2.7

Okhawa et al. (1985a), Okhawa et al. (1985b) and Yamagiwa et al. (1990) used narrow columns $(D/D_N = 2.6-8.75)$ into which gas was fed due to entrainment by a CPLJ. Okhawa et al. (1985b) found that Q_G tended to increase with increasing V_N, H_N, D_N. They proposed a dimensionless empirical correlation for the gas entrainment rate within ± 30% error based on experiments carried out in columns with $D = 0.05, 0.06 \& 0.07$ m, using nozzles with $D_N = 13-25$ mm, jet velocities at nozzle exit $V_N = 1.2-2.6$ m sec^{-1} and $H_N = 0.03-0.09$ m. No physical justification was given though for the values of the exponents.

$$\frac{Q_G}{Q_L} = 1.56\times10^{-10} Fr_L^{\,0.84}\,\mathrm{Re}^{1.65}\left(\frac{D_N}{D}\right)^{-2.1}\left(\frac{H_N}{D_N}\right)^{0.95} \tag{2.12}$$

Kundu et al. (1994), studied the hydrodynamics of a DELR $\left(D/D_N = 5.4-13.03\right)$. The downcomer was provided below the ejector assembly where gas-liquid mixing took place and had an id of 0.0516 m . Water, kerosene and paraffin were tested as working fluids. Their experimental gas entrainment measurements were fitted by multiple regression analysis within only ± 12% to the following correlation:

$$\frac{Q_G}{Q_L} = 3.15\times10^{-6}\,\frac{\rho_L}{\rho_G}\,\mathrm{Re}^{2.87}\left(\frac{D}{D_N}\right)^{2.04}\frac{L_D}{D}^{-1.27}\left(\frac{\rho_L\sigma D}{\mu_L^2}\right)^{-0.12}\left(\frac{g\mu_L^4}{\rho_L\sigma^3}\right)^{0.78} \tag{2.13}$$

Bando et al. (1989), (1988) also studied gas entrainment rate in a DELR $\left(D/D_N = 3.5-8.2\right)$ with various downcomers ($D = 0.012-0.03$ m) using mainly air-water as operating system. They observed that the gas entrainment rate increased with increasing liquid flow rate and decreasing downcomer diameter. At higher liquid rates however entrained gas decreased and beyond a certain liquid flow gas was no longer entrained. The use of aqueous sodium sulfite solution 500 mol m^{-3} (a coalescence inhibiting system) did not have any effect on gas entrainment rate and Bando et al., (1989) stated that the inertial force on liquid flow governs the gas entrainment. Their experimental results suggested that Q_G increased with decreasing pipe diameter.

Equations (2.11), (2.12) and (2.13) suggest that for low to moderate input liquid velocities, the gas entrainment rate depends to the pipe diameter. This is important for scale up purposes and is an indication that gas entrainment rate increases with increasing pipe diameter. However all the equations imply a very different dependency of pipe diameter, D, on Q_G as it can be seen by the difference in the exponents of D. On the other hand the results of Bando et al. (1989), (1988) suggest the completely opposite trend i.e. that Q_G increases with decreasing pipe diameter. No explanation can be given for this discrepancy.

At high liquid throughputs, Yamagiwa et al. (1990) observed that the gas entrainment rate, Q_G, was almost independent of the column diameter, D, i.e. the entrainment rates achieved in downflow bubble columns of various sizes were practically the same under identical operating conditions. The interaction of the plunging jet and the pool surface seemed no longer to play an important role in the determination of the gas entrainment rate. This indicated that the gas

entrainment rate for lower to moderate jet velocities ($V_j \leq 15$ m sec^{-1}), was determined on conditions taking place at the plunging point such as the kinetic energy of the jet, surface roughness of the jet and the instabilities on the surface of the receiving pool (contacting perimeter between the jet and the receiving liquid surface), which are generated by the increased liquid recirculation. They proposed the following empirical correlation for the gas entrainment rate, valid for columns with $D = 0.034 - 0.07$ m, $D_N = 8 - 13$ mm and $H_N = 0.03 - 0.15$ m. They offered no explanation for the differences in the values of the exponents comparing to Eq. (2.12).

$$\frac{Q_G}{Q_L} = 2.24 \times 10^{-3} Fr_L^{0.4} \mathrm{Re}^{0.26} \left(\frac{H_N}{D_N} \right)^{0.48} \tag{2.14}$$

Eqs. (2.11) to (2.14) have never been tested against the experimental data from other researchers. Therefore, is unclear which of the above correlations would best predict the gas entrainment rate in different confined systems. In conclusion, no solid conclusions can be drawn or a universal correlation be proposed that would predict the gas entrainment rates in confined jet systems.

Evans et al. (1996) were the only ones to attempt to develop a theoretical model to calculate gas entrainment rate in a CPLJ. The proposed model was based on the approach of Van de Sande and Smith, (1976, 1973) (see 2.1.4.1) who assumed that the overall gas entrainment rate was the sum of two components. The first one corresponded to the gas entrainment due to the annular film of gas which was carried along adjacent to the jet free surface (film-wise entrainment, Q_F) while the second was due to the quantity of gas that was trapped within the effective diameter of the jet (trapped gas component, Q_T – see Fig. 2.5b). The outer boundary of the film was defined as a streamline separating the entrained and unentrained components of the moving gas boundary layer. On the basis of the above assumptions they identified three distinct regions of entrainment in relation to the jet length. For jets of around $3 - 5D_N$, film-wise entrainment took place only. For longer jets than $3 - 5D_N$, waves on the jet surface resulted in gas being entrained within the jet envelope (Q_T) as well as in the film adjacent to the jet free surface (Q_F). At the point where the gas film thickness was reduced to zero (and so the effective jet diameter reached a maximum value) the gas entrainment was entirely attributed to the trapped gas component. Evans et al. (1996) took the gas entrainment rate, Q_{ENT}, to be the difference between the total amount entrained, Q_G (i.e. entrainment rates measured in the plunging jet literature) and that of the re-circulated gas, Q_{REC}, which disengaged from the re-circulating liquid at the top of the column and reentrained by the jet (Eq. 2.15).

$$Q_{ENT} = Q_G + Q_{REC} \tag{2.15}$$

The model gave good agreement with the experimental data with a deviation of only 20%. The main drawback was that a number of parameters needed to be determined from regression analysis applied to their experimental results. Nevertheless, the novelty of the model was that it also accounted for reentrainment of the recirculated gas in the confined system. However, Lee (1998) commented that the model by Evans et al. (1996) could not be applied in a geometry where a cavity is attached to a sparger (including those from spargers which produced a plunging jet) because the model was developed for freely expanded jets, which was not observed in his work (he showed with photographs that the jets produced accelerated under gravity and thinned).

In all the cases in the confined jet systems investigated in this review, the downcomer diameter is generally much larger than the nozzle diameter e.g. Okhawa et al. (1985a), Okhawa et al. (1985b) and Yamagiwa et al., 1990), used $D/D_N = 2.6-8.75$, Bando et al. (1989), (1988) used $D/D_N = 3.5-8.2$ whereas Kundu et al. (1994) used $D/D_N = 5.4-13.03$. However this is not the case in the current work where the plunging jet sparger has a much smaller ratio of $D/D_N = 2.1$. This is an indication that probably the correlations proposed in the literature might not apply in the current work. Yet, the effects on the confined geometry on the ability of plunging jets to entrain gas rate are essential and cannot be ignored.

2.2.2 Submerged jet expansion in a CPLJ

The hydrodynamic characteristics of the two different zones that can be identified beneath the impingement point in a CPLJ (Fig. 2.7a) govern the distribution and flow of the two phases, the mixing intensity and the rate of mass transfer. Especially the velocity profile generated within the recirculation zone of CPLJ is important to the present study because it determines both the velocity at the boundary of the free surface which forms the induction trumpet that controls the rate of filmwise entrainment (Q_F) and the expansion of the submerged jet. However no such information is available in the literature yet. Nevertheless any information on the resulting flow field in these two zones might provide some insight to the flow field beneath a ventilated cavity attached to a sparger (see Chapter 4). Therefore an understanding of the hydrodynamics below the plunging point in a CPLJ is essential to the present study.

According to Evans (1990), the jet upon striking the middle of the pool expanded downwards creating a high recirculation and energy dissipation region, defined as the mixing

zone, where the entrained gas was broken into fine bubbles. The boundaries of this region were marked by the attachment of the submerged jet to the pipe wall. Some of the bubbles recirculated back into the headspace as they could escape from the mixing zone through the free surface. Below the mixing zone the downward liquid transported steadily the remaining entrained bubbles and a homogeneous bubbly flow was established. Visual observations showed that the average gas void fraction in the mixing zone was higher than the homogeneous bubbly flow due to the bubble accumulation in the recirculating vortex. The hydrodynamic differences of the two zones are accurately depicted in the experimental measurements of Evans and Machniewski, (1999) who showed that the volumetric mass transfer coefficient per unit volume in the mixing zone was an order of magnitude higher that in the bubbly flow below and determined the overall performance of the reactor.

Evans (1990) determined the length of the mixing zone, L_w, experimentally from the wall pressure profile, P_w, inside the column and defined it as the distance from the free surface until the point where the normalised pressure $\left(P_w/P_{atm}\right)$ became a linear function of the axial distance, z. The linear region corresponded to the uniform two-phase bubbly flow zone where any pressure variations were negligible due to the constant gas void fraction and to small fluctuations within the liquid. The length of the mixing zone varied significantly (with differences up to 85%) depending on the operating parameters. It was found to increase with increasing Q_G/Q_L, decrease with increasing downcomer pipe diameter and be independent of surface tension.

The variations in the mixing zone length can be explained by the high energy consumption Q_G/Q_L (up to 1) used by Evans (1990) to achieve high entrainment rates. With increasing entrainment rates, the void fraction would also increase both in the mixing zone and in the liquid column below it. This would increase the drag in the bubbles that could eventually distort the vortex. On the other hand, in the case of a ventilated cavity attached to a sparger such high Q_G/Q_L would cause the cavity to grow unboundedly leading to system instabilities (see section 2.4.3). Thus most of the results reported by Evans (1990) are not directly applicable to the present work apart from two measurements for $Q_G/Q_L = 0$ and $Q_G/Q_L = 0.01$ using water in a downcomer with internal diameter of $D = 0.074\,\text{m}$ where the measured mixing length was approximately $L_w = 2D$.

The vortex in the wake of a CPLJ is created by a central jet and drives most of the two-phase mixture towards the wall (fish like wake) whereas in the case where a wall jet plunges at the base of a ventilated cavity it would be directed towards the centre of the pipe (drag wake). Although

the major differences in geometry and vortex rotation, the phenomena encountered in such systems will help explain some of the observations in the present work. To sum up, it seems that a recirculation region of intense mixing followed by dissipation further downstream is to be expected in the wake of a ventilated cavity attached to a sparger. Based on the results of Evans the length of this recirculation region is expected to be close to $L_w = 2D$.

2.3 VERTICAL SLUG FLOW

2.3.1 Introduction

The base of a ventilated cavity attached to an air sparger (horizontal or central – see section 3.6) when it is long enough (several pipe diameters) is bell shaped and therefore is similar to a Taylor bubble in two-phase slug flow (Fig.2.2). An understanding of the Taylor bubble behaviour will therefore help support any conclusions drawn from this work on ventilated cavities and vice versa. Slug flow is frequently observed in oil production wells, flow lines and risers, steam boilers, process vaporisers, circulating fermenters, nuclear reactors during transient situations, gas-liquid chemical reactors, coffee-maker and deep shaft wastewater treatment. The slug flow pattern exists over a range of gas and liquid flow rates and is characterised by a sequence of large coherent bubbles which are much longer than wide (Taylor bubbles) and that nearly fill the cross section of the pipe. Slugs of aerated liquid separate these large bubbles. At the base of the Taylor bubbles, a liquid film at the wall of the pipe plunges into the liquid beneath and entrains a certain amount of gas in the form of small bubbles. A fraction of these entrained bubbles recoalesces back into the Taylor bubble at its base while the remaining bubbles will eventually be carried downward with the bulk two phase flow.

There are two main differences between a ventilated cavity attached to an air sparger studied in this work and a Taylor bubble in vertical slug flow:

- A slug bubble is able to move freely inside the pipe or vessel within which it is contained whereas a ventilated cavity assumes a fixed position attached to a sparger or other fixed object in the flow.
- The falling liquid film at the base of a ventilated cavity plunges concurrently into a downflowing liquid, whereas in two-phase slug flow, the falling film plunges counter-currently into an upflow of slugs of aerated liquid. This suggests that some differences

might exist in the turbulence intensity in the wake of the two flows, which may influence the hydrodynamic behaviour and the entrainment rate.

2.3.2 Gas entrainment from Taylor bubbles

Riiser et al. (1992) conducted experiments to study the entrainment mechanism at the rear of a Taylor bubble. The Taylor bubble was formed at the centre of a 0.051 m id pipe using a cylindrical solid body that was drilled in its axis to allow the air passage. Air was introduced at the central axis of the body forming a standing bubble with bell shaped base. The air entrainment rate was found to increase with increasing bubble length, air flow rate and water flow rate. Riiser et al. (1992) used high-speed video to observe the entrainment rate. The motion pictures showed that waves developed, which travelled downward on the interface of the falling film. The waves were responsible for the oscillation of the bubble base at the point where air was entrained in the form of small bubbles with a typical size of a few millimetres.

Delfos et al. (1993) and Delfos (2001a) investigated the flow phenomena around a fixed Taylor bubble in a 0.1 m id pipe. The Taylor bubble was formed by injecting air at the pipe's centreline through a 5 mm id tubelet. They suggested that the entrainment rate was initiated only when the turbulent fluctuations in the liquid film were sufficiently strong to provoke it. However they did not test their assumption by measuring the film turbulent fluctuations. Both Delfos et al. (1993) and Delfos (2001a) found that the air entrainment increased with increasing bubble length, air flow rate and water flow rate in agreement with the results of Riiser et al. (1992). Delfos (2001a) observed large oscillations at the level of the bubble base, which apparently were strongly dependent on the bubble length. Polonsky et al. (1999a) made similar observations for cocurrent upward slug flow. They stated that the amplitude of the oscillations increased with increasing bubble length and therefore with increasing air entrainment rate.

Based on their experimental results for air and water, Riiser et al. (1992) suggested that the onset of air entrainment occurred at a critical Weber number defined as:

$$We_{onset} = \frac{\rho_L u_w^2 \delta_{onset}}{\sigma} = 0.4 \tag{2.16}$$

where δ_{onset} was the falling film thickness at the onset of entrainment and u_w was the friction velocity defined by Riiser et al. (1992) as:

$$u_w = V_F \sqrt{\frac{C_f}{2}} \tag{2.17}$$

where V_F was the falling film velocity at the base of the fixed bubble, C_f the wall friction factor $\left(0.079\,\mathrm{Re}^{-0.25}\right)$ and the Re was based on the pipe diameter $\left(D\right)$ and superficial liquid velocity $\left(j_L\right)$. Eq. (2.16) suggests that the turbulent motion destabilised the gas-liquid interface resulting in gas entrainment while surface tension acted to restore the symmetry.

Lee (1998) found that $We_{onset} = 0.92$ for the onset of air entrainment at the base of ventilated cavity attached to a horizontal sparger (see section 3.5.1) when $Q_L = 0.003$ m^3 s^{-1} with a corresponding film velocity of 2.5 m s^{-1}. In the present $We_{onset} = 0.86$ for the onset of air entrainment at the base of ventilated cavity attached to a central sparger (see section 3.5.2) when $Q_L = 0.003$ m^3 s^{-1} with a corresponding film velocity of 2.35 m s^{-1}. Delfos et al. (1993) found that the air entrainment was initiated at a $We_{onset} = 0.87$ with a corresponding film velocity of 2.5 m s^{-1}. This is in good agreement with the results by Lee (1998) and the present work, but again almost twice of the value suggested by Riiser et al. (1992).

On the other hand, Su (1995), who performed extensive measurements at the bottom of a fixed Taylor bubble in a 0.05 m id pipe, i.e. similar to Riiser et al. (1992), found that the air entrainment was initiated at 0.54 (Table 2.1). It is clear from Table 2.1 that the pipe diameter has an effect on the We_{onset} [2.2]. It seems that the onset of air entrainment takes place at $We_{onset} = 0.47$ for a pipe diameter of around 51 mm id whereas $We_{onset} = 0.88$ for a pipe diameter of around 105 mm id.

An attempt was made to resolve the pipe diameter dependence for the onset of air entrainment. Two alternative dimensionless correlations for the onset of air entrainment at the base of a ventilated cavity attached to a sparger are proposed in this study. These correlations are shown in Eqs. (2.18) and (2.19) while the overall results are presented in Table 2.2. The uncertainties in Eqs. (2.18) and (2.22) are based on a 95% confidence interval. Eq. (2.18) is essentially a Weber number $\left(\frac{\rho_L V_F^2 \delta_{onset}}{\sigma}\right)$ multiplied by a geometric factor $\left(\frac{\delta_{onset}}{D}\right)$ to take account of the pipe

---

[2.2] A similar dependency of the pipe diameter on a Weber number was found in Chapter 6 (Table 6.2) for the formation of slug bubbles in downcomer pipes that had slightly distorted noses and rose close to the pipe's centreline.

diameter. On the other hand, Eq. (2.19) is a more useful correlation since only the knowledge of easily measured parameters such as the liquid flow rate, the pipe diameter and the liquid physical properties are required to make a prediction. It can be seen (Table 2.2) that both correlations predict the onset of entrainment at a unique number irrespective of pipe diameter. Interestingly Eq. (2.19) does not include the film thickness at the base of the cavity, an important parameter for air entrainment as already discussed, and still gives good results.

$$\frac{\rho_L V_F^2 \delta_{onset}^2}{\sigma D} \simeq 11.4 \pm 0.76 \tag{2.18}$$

$$\frac{\rho_L Q_L^2}{\sigma D^3} \simeq 103.8 \pm 1.91 \tag{2.19}$$

Air and water	D (mm)	j_L (ms^{-1})	We_{onset} *(Eq. 2.16)*
Riiser et al. (1992)	51	0.49	0.4
Su (1995)	50.8	0.49	0.54
Lee (1998)	105	0.35	0.92
Delfos et al. (1993)	100	0.35	0.87
This work	105	0.35	0.86

Onset of air entrainment at the base of ventilated cavities based on the model of Riiser et al. (1992).

Table 2.1

Su (1995) as already mentioned, performed extensive measurements at the bottom of a fixed Taylor bubble in a 0.05 m id pipe. The Taylor bubble was formed by injecting air through a central sparger with 14 mm id. Su (1995) measured the resulting bubble size and the air entrainment rate for three different liquids; tap water, aqueous solution of 0.1 % w/w HDTMA ($\mu_L = 0.00101$ kg m^{-1} s^{-1} $\sigma = 0.034$ N m^{-1}) to investigate the influence of surface tension on air

entrainment rate and aqueous solution of 50% w/w glycerine ($\mu_L = 0.00606\,\text{kg m}^{-1}\,\text{s}^{-1}$ and $\sigma = 0.063\,\text{N m}^{-1}$) to investigate the influence of the liquid viscosity on air entrainment rate. Su (1995) found that decreasing the surface tension led to a slight increase of gas entrainment rate and a significant decrease of bubble size. On the other hand, the effects of liquid viscosity were more important in the air entrainment process. Increasing viscosity led to a significant decrease of both air entrainment rate and resulting bubble size. The following data were derived from Su's graph to give an indication of the changes in bubble size due to the difference in liquid physical properties. For $Q_L = 0.001\ \text{m}^3\ \text{s}^{-1}$ and $L_B = 0.6\ \text{m}$, the maximum bubble size was equal to 5.6 mm for water, 3.5 mm for water/HDTMA and 2.99 mm for water/glycerine.

Air and water	D (mm)	$\frac{\rho_L V_F^2 \delta_{onset}^2}{\sigma D}$ *(Eq. 2.18)*	$\frac{\rho_L Q_L^2}{\sigma D^3}$ *(Eq. 2.19)*
Riiser et al. (1992)	51	12.8	102.2
Su (1995)	50.8	10.7	103.5
Lee (1998)	105	11.7	107.6
Delfos et al. (1993)	100	11.0	102.5
This work	105	11.3	103.2

Onset of air entrainment at the base of ventilated cavities based on the dimensionless numbers of Eqs. (2.18) and (2.19).

Table 2.2

Su (1995) provided an empirical model for the air entrainment rate regarding the results in water. Using least squares method, his data were fitted to two linear equations:

$$Q_G = -2.2\times10^{-5} + 3.7\times10^{-3} E_k, E_k < 42\times10^{-3} m^4 s^{-3} \tag{2.20}$$

$$Q_G = 7\times10^{-5} + 1.5\times10^{-3} E_k, E_k \geq 42\times10^{-3} m^4 s^{-3} \tag{2.21}$$

where Q_G was the measured air entrainment rate and E_k the relative kinetic energy flux defined by Su (1995) as:

$$E_k = \delta V_F^3 \tag{2.22}$$

where δ was the falling film thickness at the base of the fixed Taylor bubble and was given as a function of the pipe Re number.

$$\delta = 0.143\,\mathrm{Re}^{0.58} \tag{2.23}$$

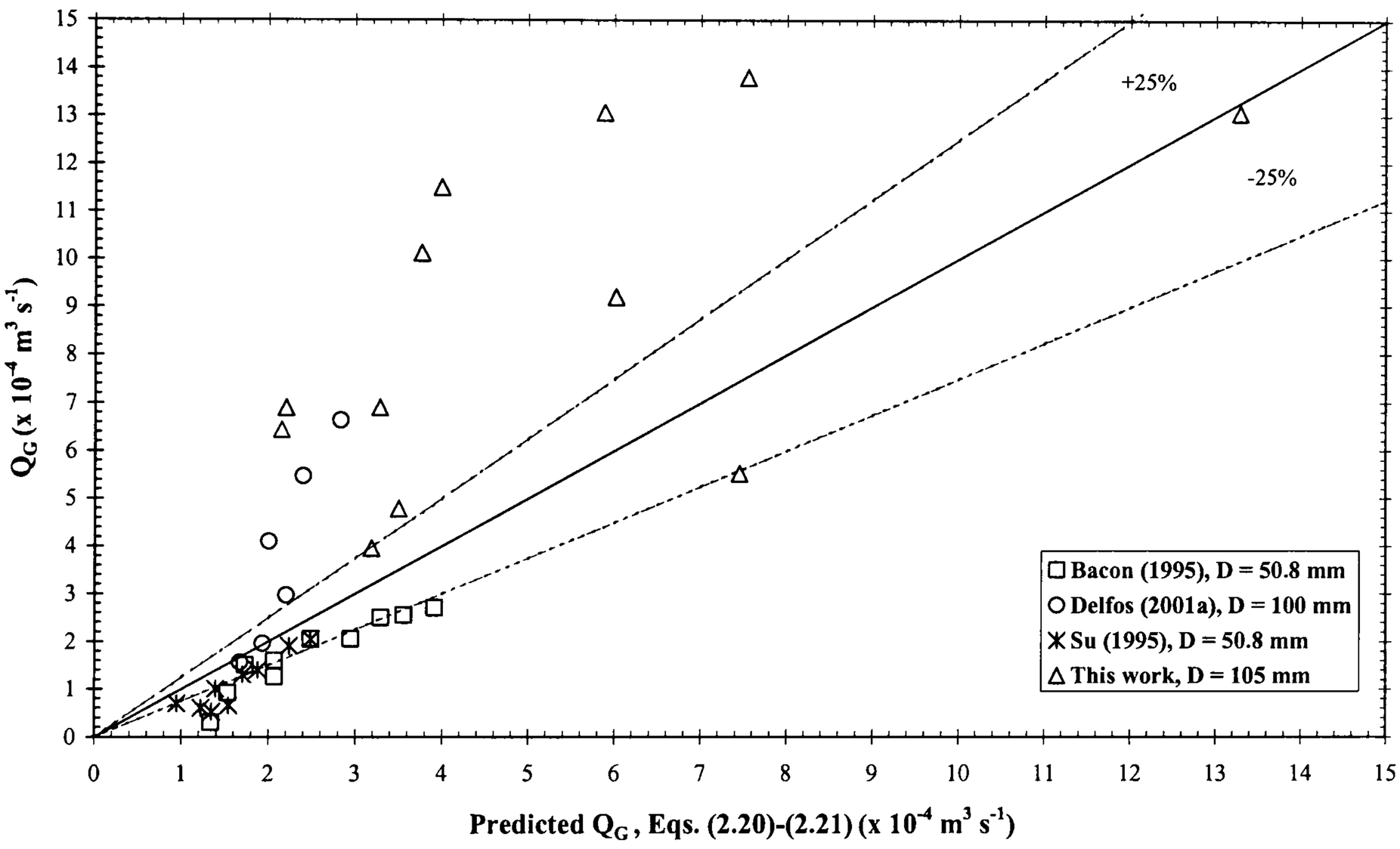

Comparison of Eqs. (2.20) and (2.21) with the experimental results of Su (1995), Bacon (1995a), Delfos (2001a) and this work.

Figure 2.8

Eqs. (2.20) & (2.21) are tested in Fig. (2.8) against the experimental results of Su (1995), Delfos et al. (2001a), Bacon (1995a) and this work. It is worth mentioning that all the data in Fig. (2.8) correspond to measured air entrainment rates from fixed Taylor bubbles and ventilated cavities that are attached to central spargers (CS), i.e. the air is introduced by a tube at the centre of the pipe (see section 3.5.2). The model fits the data that correspond to the 50.8 mm id pipes within approximately ±25%. On the other hand the model under predicts significantly

(deviations as high as ±90%) the data that correspond to the larger pipe diameters (increase by about a factor of two in pipe size).

Certain questions arise about the physical concept behind Su's model. First of all, Eqs. (2.20) & (2.21) are both dimensional correlations and are therefore system dependent and not universal correlations. In addition to this, parameters such as the geometry of the flow field (e.g. the rotating vortex), bubble length or the fluid properties that were identified by Su (19995) as important in determining the air entrainment rate were ignored in Eqs. (2.20) & (2.21).

In a very recent paper, Kockx et al. (2005) suggested a very interesting geometric entrainment model at the base of a fixed Taylor bubble. They assumed that the perturbations on the falling film (wavy film) were responsible for the air entrainment, similar to the case of turbulent rough plunging liquid jets (see section 2.1.4.1). The authors observed that the air entrainment increased rapidly with an increase in the film surface roughness. They concluded that: "*entrainment is supposed to be caused by the fact the free surface of the pool is not capable of responding to the transverse oscillations of the incoming film*". This process is shown schematically in Fig. 2.9 (see also discussion in section 2.4.5).

When a travelling wave on the film surface approached the receiving pool it created a gravity wave in the wake (caused the pool surface to be splashed away and therefore left a gap on the pool surface), which propagated on the receiving pool surface (Fig. 2.9a). When the slope of the induced gravity wave (provoked steepness) became higher than the slope of the incoming fast film waves (inverse steepness), then the crest of the gravity wave contacted the next wave on the film surface and a portion of air was enclosed (Fig. 2.9b).

The concept behind the Kockx et al. (2005) model is certainly not new. McKeogh and Ervine (1981) showed that for a circular turbulent water jet the entrainment rate was about equal to the volume enclosed in between the crests of the disturbances present on the film surface. According to the above entrainment mechanism (Fig. 2.9) at least two subsequent waves are needed to be present in the film so that air could be trapped in between them. When only one wave is present then air entrainment does not take place. Therefore the entrainment mechanism suggested by Kockx et al. (2005) is more likely to apply in the case of rough turbulent falling films but not in the case for smooth liquid films (see also discussion in section 2.4.5).

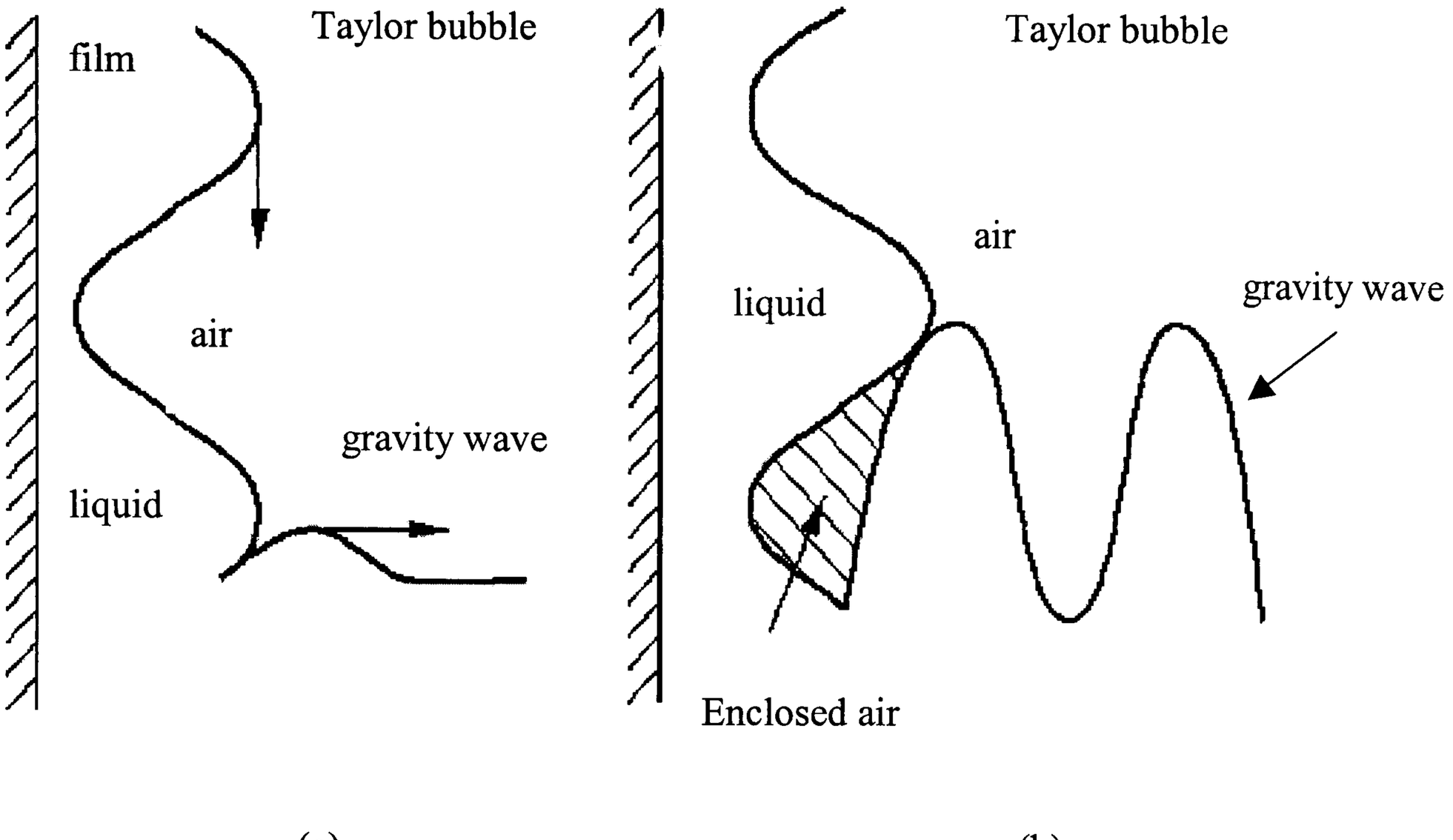

Entrainment mechanism at the bottom of a Taylor bubble due to distortions on the falling liquid film (Kockx et al., 2005).

Figure 2.9

Kockx et al. (2005) proposed a model for the air entrainment based on the liquid film characteristics. According to their model, the air entrainment was proportional to the waviness of the film (its intermittency) and the wave height and inversely proportional to the film thickness, as is also shown in Eq. (2.24).

$$Q_G = 1.2 Q_L I \frac{\delta_w}{\delta} \tag{2.24}$$

where I was the intermittency and δ_w the wave height. To determine the entrainment rate using Eq. (2.24) Kockx et al. (2005) used the LIF (Laser Induced Fluorescence) technique to measure the intermittency, wave height and film thickness in their experimental facility. The film thickness was derived from the measured emitted fluorescence intensity of the excited dye. The intermittency was defined as the percentage of time that waves occurred on the film surface and the method used to measure it, was essentially the same as the variable-interval time-averaging

(VITA) technique suggested previously by Alferdsson and Johansson (1983) (however they are not referenced by Kockx et al., 2005). According to the VITA technique, the local standard deviation is calculated over a small time interval (2 ms was chosen by Kockx et al., 2005). If this local standard deviation is higher than a threshold value (corresponding to a film with no surface waves – 0.04 V was chosen by Kockx et al., 2005) waves are present on the film surface (Kockx et al. supported that these waves were responsible for the entrainment rate at a base of a Taylor bubble). The intermittency factor is then the ratio between the time period of the signal that corresponds to the presence of waves over the total time period of the time series. The wave height was calculated from the standard deviation of the filtered signal and the assumption of sinusoidal waves.

Kockx et al. (2005) argued that the recoalescence rate at the base of the fixed Taylor bubble i.e. the fraction of the entrained bubbles that coalescence back to the main body of a Taylor bubble, was not negligible at high gas entrainment rates (i.e. at high gas input flow rates, Q_G). They commented that the correct way to model the entrainment rate, Q_{ENT}, should be based on the gas material balance shown in Eq. (2.25) and not only on the supply of gas in the system under steady state $\left(Q_{ENT} = Q_G\right)$ i.e. when the bubble reached a constant length.

$$Q_{ENT} = Q_G + Q_{REC} \tag{2.25}$$

They used the data for the recoalescence rate, Q_{REC}, measured by Delfos et al. (2001b) (see next section) to estimate the entrainment rate from Eq. (2.25). They showed that the recoalescence rate was an important parameter in the air entrainment measurements at long bubble lengths ($L_B \geq 750$ mm). For shorter bubbles the recoalescence rate was negligible compared to the inlet gas flow rate, Q_G and therefore the entrainment rate could be very well approximated by Q_G. Kockx et al. (2005) found good agreement between Eqs. (2.24) and (2.25). They concluded that thorough measurements in the wake are mandatory to give an insight in the physics of the recoalescence rate. However, the model by Kockx et al. (2005) does not constitute a practical predictive method for the entrainment rate.

2.3.3 Wake flow field beneath a Taylor bubble

Delfos et al. (1993) analysed video motion pictures taken at the flow field below their fixed Taylor bubble and suggested that probably a toroidal vortex was formed as the liquid film plunged at the base of the fixed Taylor bubble. The vortex seemed to influence the dispersion of

the entrained bubbles. According to Delfos et al. (1993) most of the entrained bubbles were recirculated back to the main Taylor bubble body. They concluded that the suggested toroidal vortex was axisymmetric only if the entrainment rate was low. At higher entrainment rates the vortices sloshed to all sides of the tube. However no quantitative results were presented to support any of the above observations. The length of the recirculating wake below the fixed Taylor bubble was determined from photographs later by Delfos et al. (2001a) (qualitatively). They found that the vortex extended 1-1.5D below the fixed Taylor bubble independent of the liquid flow rate.

Su (1995) also observed that a toroidal vortex was probably formed in the wake of a fixed Taylor bubble attached to a central air sparger. He stated that when the fixed Taylor bubble length reached a critical value, the air entrainment was initiated because the vortex became asymmetric occasionally and engulfed a small amount of air from the fixed bubble. According to Su (1995) at higher bubble lengths the vortex became highly turbulent and was continuously entraining bubbles along the entire perimeter of the slug base. Su (1995) commented that the vortex was the only source of entrainment, which is in direct contrast with the entrainment mechanisms in the plunging liquid jet literature outlined in section 2.1.2 or the mechanism suggested by Kockx et al. (2005) in the previous section.

Su (1995) measured the recoalescence rate of the entrained bubbles back to the main body of the fixed slug at high gas entrainment rates and found that it was independent of the bubble length and negligible compared to the inlet gas flow rate. This is in contrast with other observations in the literature (Delfos et al. 1993; Delfos et al. 2001b) that supported that the recoalescence rate increased with entrainment rate and hence inlet gas flow rate. However, there are two major issues of concern about Su's measurements. The first is that he actually did not include the experimental data of the recoalescence rate in his thesis. The second has to do with the way he quantified the recoalescence rate. Su (1995) introduced an acrylic cap at the bottom of his fixed bubble that prevented the entrained small bubbles coalescing back to the fixed bubble. He then calculated the recoalescence rate as the difference between the gas flow rates with and without the structure when all other experimental conditions were the same. However the acrylic cap disturbed the flow by allowing the gas to be entrained only at the edges of the fixed bubble and prohibiting the oscillation of the top surface, which is contrast with the entrainment mechanism that Su suggested and described in the previous paragraph, which requires oscillation of the top surface.

Fernades et al. (1983) presented a complete semi-theoretical model to predict the characteristics of slug flow in a vertical tube. In their model they predicted the void fraction in the liquid slug by taking mass balances for the air going into and out of the slug bubble. They derived the following equation to calculate the recoalescence flow rate at the base of the slug bubble.

$$Q_{REC} = \frac{\pi}{4}\left[\frac{3}{4}(D-2\delta)\right]^2 \frac{V_F}{4}\frac{Q_G}{Q_G+Q_L} \tag{2.26}$$

where Q_{REC} was the recoalscence flow rate at the base of the slug bubble. The success of the Fernades model has been queried by a number or researchers including Thorpe et al. (2001), Mao and Duckler (1991) and Delfos et al. (2001b). Fernades et al. (1983) did not take account of the entrained bubble velocity or the vortex velocity in their model. Also they assumed that the bubbles were transported towards the slug base at a velocity equal to the turbulent fluctuations in the flow (i.e. the r.m.s velocity fluctuations were modelled as 0.25 times the velocity of the liquid film at the base of the Taylor bubble). However, these turbulent fluctuations would need to last long enough to carry the bubbles the require distance in the upward direction (turbulence is not directional as Fernades et al. assumed). Still Eq. (2.26) might give a feeling about the significance of the recoalscence flow rate. If typical values obtained in this work for a ventilated cavity attached to a central sparger (see Table 4.1 – Case VC1) are substituted in Eq. (2.26), is found that $Q_{REC} = 0.58Q_G$. This suggests that even for low air flow rates (Table 4.1 – Case VC1) a large portion (almost 60%) of the entrained bubbles recirculate back to the main body of the cavity, which is in direct contrast to Su's (1995) conclusions. It has to be noted, that Eq. (2.26) is only a minor part of the Fernades et al. (1983) model much of which has proved useful.

Delfos et al. (2001b) were the first to demonstrate experimentally that the existence of the recoalescence flux at the base of a fixed Taylor bubble was not negligible. They conducted measurements injecting helium (He) at points throughout the wake of a fixed Taylor bubble (to increase the measurement resolution) and used a katharometer to measure the concentration of the helium that coalesced to the fixed Taylor bubble due to the rotating vortex. In this way they managed to quantify (though mass balances) the recoalscence probability i.e. the probability that a small gas bubble after being entrained, coalesced back into the fixed Taylor bubble. They showed that almost 50% of the entrained bubbles were recycled back to the fixed Taylor bubble at high gas entrainment rates. The authors showed that the coalescence probability was dependent on both the radial and axial position of He injection below the Taylor bubble; it

increased towards the pipe centre, decreased with axial distance from the bottom of the fixed Taylor bubble and near the wall was close to zero. These results strongly suggest the existence of a recirculating structure in the wake of the fixed Taylor bubble.

Van Hout et al. (2002) is the only study in the literature that has provided data of the flow field around a slug bubble rising in a vertical pipe filled with stagnant water using PIV. They used a 0.025 m id pipe and their falling film at the base of the Taylor bubble was in laminar flow $\left(\mathrm{Re}_F = 813\right)$ whereas the slug body between the slug bubbles was in turbulent flow. Their average velocity results showed the formation of a toroidal vortex stretching up to $2D$ in the vicinity of the Taylor bubble, which was dominated by vigorous mixing due to expansion of the falling film jet as it plunged at the base of the rising Taylor bubble (Van Hout et al. measured the flow field in the wake of rising Taylor bubbles). Van Hout's et al. results agree with the findings of Evans (1990) for a CPLJ (see section 2.2.3).

However a number of researchers have queried Van Hout's et al. (2002) experimental methods and results (Nogueira et al., 2004; Nogueira et al., 2003; Pinto and Campos, 2004; amongst others). They all stated that the technique used by Van Hout et al. (2002) had a problem in determining accurately the liquid velocity field both in the liquid film and in the near wake field. Van Hout et al. (2002) determined separately the shape of the Taylor bubble using the method suggested by Polosky et al. (1999b). Polosky et al. (1999b) used an inter-lanced image technique to perform PIV measurements around the nose of the gas slug. Due to the high liquid velocities in the film region (much higher than the Taylor bubble velocity) they had to use a streak length method (the seeding particles produced long streaks whose length was proportional to the local liquid velocity) to determine the liquid velocities. However none of the above researchers quantified the error in Van Hout's measurements. This was also not possible in this work.

In addition to this, Van Hout et al. (2002) concluded that "*memory limitation dictated the choice of the maximum ensemble size. However the mean distributions of both velocities and turbulent quantities did not differ notably for ensemble sizes ranging 70-100*". Van Hout et al. (2002) did not clarify what the "*ensemble sizes*" correspond to. They did not mention how many images they processed to calculate the liquid velocity field. For example a number of 70-100 processed pair of images is not enough to measure accurately the turbulence intensity in the wake of a Taylor bubble. However, it is acceptable to evaluate the mean velocity.

In conclusion, there is still no satisfactory way of predicting the gas entrainment rate at the base of a Taylor bubble. The gas entrainment at the base of a fixed Taylor bubble occurs only if the slug length exceeds a certain minimum length. The gas entrainment increases with increasing bubble length, air flow rate and liquid flow rate. The recoalscence flow rate at the base of a fixed Taylor bubble is an important parameter in determining the gas entrainment rate at long bubble lengths ($L_B \geq 750$ mm). If it is not taken into account, the results will be biased towards high values of the entrainment rate. A toroidal vortex is formed below a fixed Taylor bubble extending around $1-2D$ in the axial direction. This vortex determines the physics of the recoalescence rate and the resulting entrained bubble size. The height and intermittency of the waves that develop on the falling film around the Taylor bubble determine the amount of gas that is entrained at its base.

2.4 VENTILATED CAVITIES ATTACHED TO SPARGERS

2.4.1 Introduction

The ideal sparger system for the downcomer pipe of a circulating bubble column and external-loop airlift fermenters/reactor should be characterised by no significant pressure loss in the liquid phase i.e. no ventilated cavity formation and the creation of equal sized bubbles. However a ventilated cavity attached to a sparger is formed in a downflowing liquid (Bacon, 1995a; Bacon et al., 1995b, Bacon et al., 1995c; Lee et al, 2000; Lee et al., 1999; Lee, 1998; Lee et al., 1997a; Lee et al. 1997b). The presence of the cavity has been shown to increase the energy losses (causes lower circulation velocities) in a circulating bubble column and hence a tendency to instability (Lee et al., 2000) (see also section 5.3).

Bacon (1995a) studied extensively such ventilated cavities attached to spargers. He conducted experiments in a 0.057 m id pipe using three different spargers, namely a horizontal, a central and a peripheral sparger. Lee (1998) continued Bacon's work and examined mainly the effects of scale on gas entrainment rate. He carried out experiments in a 0.105 m id pipe using the horizontal and peripheral spargers used by Bacon (1995a), their geometric scale-up designs (made for his 0.105 m id downcomer) and the scale-up design of a plunging jet sparger suggested by Thorpe et al. (1997). The scale up designs of the horizontal, peripheral and plunging jet spargers were also used in this work can be found in section 3.5. Therefore only the main general results derived from Bacon's and Lee's work will be considered in this section.

2.4.2 Effects of sparger design

Under the vast majority of the operating (gas, liquid flow rates) conditions investigated by both Bacon (1995) and Lee (1998) the length of ventilated cavities that were attached to any of the four different spargers used, increased with increasing gas flow rate and decreasing liquid flow rate, similar to the results for fixed Taylor bubbles[2.3] analysed in the previous section. The horizontal and central spargers gave similar cavity lengths for any combination of liquid and gas flow rates i.e. they exhibited identical entrainment behaviour. As already mentioned there was a minimum stable ventilated cavity length attached to these spargers before any gas entrainment took place (see section 2.3.2).

At any given gas and liquid flow rates, the peripheral sparger produced cavities that were consistently shorter than those produced by the horizontal and central spargers. Also air was instantly entrained upon commencement of injection, i.e. a minimum stable cavity length was not first established. Lee (1998) stated that this occurred probably because there was physical protection at the point of air injection of the peripheral sparger. However, the peripheral sparger suffered from flow instabilities at increasing air flow rates which resulted in sudden changes in the ventilated cavity length and therefore in the entrainment rate. A close examination of the data by Bacon (1995) and Lee (1998), which are for different pipe diameters, indicates that this phenomenon was initiated in the region $0.15 \leq \frac{Q_G}{Q_L} \leq 0.33$ for their results regarding air and water. Finally the peripheral sparger suffered from hysteresis i.e. the cavities produced behaved differently when the air flow rate was reduced to the required level, rather than increased. The reason for this instability was the way the six initial individual cavities (see section 5.2) coalesced to form a single ventilated cavity as the air flow rate was increased and the way that the same cavity broke down into individual cavities as the air flow was decreased.

In general, the plunging jet sparger had a superior performance over the other three spargers as it produced the shortest cavities over a wide range of gas and liquid flow rates. However, at low liquid flow rates ($Q_L \leq 0.004$ m^3 s^{-1}) the reverse was true. At these low flow rates a minimum stable cavity length was established before any air was entrained similar to the results of the horizontal and central spargers respectively.

[2.3] There is essentially no difference between the fixed Taylor bubble and the ventilated cavity formed by the central sparger.

2.4.3 Maximum entrainment rate

The maximum entrainment rate, $Q_{G,\max}$, is the highest air flow rate that can be supplied into the downcomer via a sparger before unbounded cavity growth occurs i.e. the point at which the ventilated cavity continues to expand without reaching a constant length. Knowledge of $Q_{G,\max}$ is important because it represents the upper bound to the air flow rate that can be supplied to the sparger downcomer in a circulating bubble column and external-loop airlift fermenters/reactor without the reactor being guaranteed to stall due to driving force reversals (Lee, 1998).

Bacon (1995a) and Lee (1998) measured maximum entrainment rates for all the different spargers they used. The horizontal and central spargers produced similar cavity lengths at the maximum entrainment rate conditions. On the other hand, the maximum entrainment rates for the peripheral sparger were significantly larger than those for the horizontal and central spargers. The superiority of the peripheral sparger was also exhibited in the cavity length data mentioned in the previous section.

Bacon et al. (1995b) explained the better performance of the peripheral sparger by considering the nature of the top of the cavity for each sparger. For the horizontal and central spargers the water flowed smoothly to the downcomer walls and formed a stable film. However, the liquid flow in the region of the peripheral sparger was forced away from the tube walls and therefore the amount of energy lost due to wall friction was reduced (i.e. more energy was available for air entrainment). Also the specific design of the peripheral sparger (see section 3.5.3) allowed the development of vertical "ridges" on the falling film of significantly larger thickness than the film itself. These "ridges" corresponded to the regions between the air holes in the sparger where the falling water was not pushed away from the wall by an air jet. Since the ridges were thicker than the falling film fall faster. Bacon et al. (1995b) concluded that the ridges behaved in a similar manner to the surface disturbances of plunging liquid jets and entrained large amounts of air.

On the other hand, the ventilated cavity length data for the plunging jet sparger did not show an approach to a maximum entrainment rate, i.e. the cavity reached a constant length for all the combinations of gas and liquid flow rates and different liquids used (Lee, 1998). This fact demonstrates the superiority of the plunging jet sparger over the other three spargers in cases where high gas entrainment rates are required (high gas throughput in the system).

2.4.4 Effect of liquid physical properties

Bacon (1995a) and afterwards Lee (1998) used a variety of liquids to examine the effects of the liquid physical properties on air entrainment rate. Under all the different liquids investigated the ventilated cavities showed a similar behaviour to the results of water analysed above irrespective of sparger design.

2.4.4.1 Surface tension

Bacon (1995a) used 6 M aqueous propanol solution ($\mu_L = 0.002$ kg m^{-1} s^{-1} and $\sigma = 0.036$ N m^{-1}) to examine the effects of surface tension on air entrainment rate. He found that a reduction of surface tension increased significantly the air entrainment rate. On the other hand, Su (1995) found that a reduction in surface tension led only to a slight increase of gas entrainment rate (see section 2.3.2). Bacon (1995a) commented that the reduction in surface tension reduced the surface energy of the small entrained bubbles at the base of the cavity. Therefore, assuming that the same proportion of the falling film's kinetic energy was lost to fragmentation of the cavity and formation of small bubbles and that the bubble size distribution remained constant, the liquid with the lower surface tension would have been expected to produce more bubbles and hence entrain more air. Also the reduction in surface tension might have allowed the development of larger waves on the falling film. It has already been mentioned that a rough film would enhance the entrainment rate (see 2.1.4.1 and 2.3.2).

Lee (1998) used an aqueous solution of Rheovis RC2 ($\mu_L = 0.0028$ kg m^{-1} s^{-1} and $\sigma = 0.055$ N m^{-1}), an associative polymeric colloidal thickener with Newtonian rheology at low concentrations, to study the effects of surface tension on air entrainment rate in a 0.105 m id downcomer pipe. The thickening action of the Rheovis RC2 was activated by the addition of ammonia to increase the pH of the mixture to 8. Lee's results for both the horizontal and peripheral spargers were contradictory to those of Bacon (1995a) and Su (1995) at low liquid flow rates ($Q_L = 0.003$ m^3 s^{-1} for the horizontal sparger and $Q_L = 0.005$ m^3 s^{-1} for the peripheral sparger) where the air entrainment rate decreased with a reduction in surface tension. However, at higher liquid flow rates ($Q_L = 0.009$ m^3 s^{-1} for both spargers) the air entrainment rate increased slightly with a reduction in surface tension in agreement with Su (1995). Lee (1998) attributed the above variation of the ventilated cavity behaviour with changes in surface tension to the additional effect of the high liquid viscosity of Rheovis RC2 and to the change of entrainment mechanism between low and high liquid flow rates previously suggested by Sene (1988) (see

section 2.1.4.1). Lee (1998) did not present any experimental results regarding the use of Rheovis RC2 with the plunging jet sparger.

2.4.4.2 Viscosity

Bacon (1995a) used glycerol solution ($\mu_L = 0.009$ kg m^{-1} s^{-1} and $\sigma = 0.072$ N m^{-1}) to examine the effects of viscosity on air entrainment rate. His results for all spargers used showed that the increase in the liquid viscosity acted to slow down the flow and slightly decreased the entrainment rate. This in contrast with the results reported by Su (1995) (see section 2.3.2) but in line with the results of Kumagai and Endoh (1982) and Kusabiraki et al. (1990b) (see section 2.1.4.4).

Lee (1998) also used a glycerol solution (60% w/w) ($\mu_L = 0.0065$ kg m^{-1} s^{-1} and $\sigma = 0.072$ N m^{-1}) to investigate the influence of viscosity on the air entrainment rate. However, his results were contradictory to those of Bacon (1995a) but in agreement to those of Su (1995), suggesting that the entrainment rate increased with increasing liquid viscosity regardless of sparger design. Lee (1998) stated that the enhanced entrainment ability was a result from the development of surface disturbances of greater amplitude. He commented that the falling film at the base of the ventilated cavity in glycerol was thicker that the one in water. It is well accepted in the falling liquid film literature that thicker films allow the development of greater amplitude and therefore in the case of Lee (1998) higher entrainment rates. Lee (1998) concluded that the effects of viscosity were not so important compared to the ones of surface tension. This in contrast with the results reported by Su (1995) (see section 2.3.2).

It is concluded that effects of viscosity and surface tension on air entrainment rate at the base of a ventilated cavity are not clear. The contradictory results of Bacon (1995a), Su (1995) and Lee (1998) just add up to the already existing conflicting studies in the literature of air entrainment by a plunging liquid jet (see section 2.1.4).

2.4.4.3 Dimensionless correlations for the maximum entrainment rate

Lee (1998) correlated successfully the maximum measured entrainment rates of both the horizontal and peripheral spargers to within ±20%, taking into account the effects of liquid physical properties (surface tension and viscosity) and scale (i.e. the data in a 0.057 m id pipe by Bacon, 1995a). The correlations he produced are shown in Eqs. (2.27) and (2.28).

$$Fr_{G,\max} N_{\mu}^{-0.06} Eo_D^{-0.5} = 0.0085 Fr_L + 0.002 \quad \text{[Horizontal sparger]} \tag{2.27}$$

$$Fr_{G,\max} N_{\mu}^{0.07} Eo_D^{-0.5} = 0.0039 Fr_L + 0.0002 \quad \text{[Peripheral sparger]} \tag{2.28}$$

where $Fr_{G,\max}$ was the Froude number at the maximum entrainment rate $\left(\frac{Q_{G,\max}}{\sqrt{(gD)^5}}\right)$, Fr_L was the liquid flow Froude number $\left(\frac{Q_L}{\sqrt{(gD)^5}}\right)$, N_{μ} was the Viscosity number $\left(\frac{\mu_L}{\rho_L\sqrt{gD^5}}\right)$ and Eo_D was the Eotvos number $\left(\frac{gD^2(\rho_L-\rho_G)}{\sigma}\right)$. Eqs. (2.27) and (2.28) indicate that the Viscosity number does not play an important role in determining the maximum entrainment rate for both the horizontal and peripheral spargers. On the other hand surface tension is predicted to have a relatively strong effect on the maximum entrainment rate.

2.4.5 Proposed mechanisms for air entrainment at the base of a ventilated cavity

After the careful investigation of the literature the following three mechanisms are proposed in this study for gas entrainment at the base of a ventilated cavity. In all three mechanisms the presence of the vortex, i.e. the speed of rotation in the receiving flow below the plunge point is not ignored.

i.) Gas entrainment due to film waviness (Fig. 2.10a): This type of mechanism occurs for rough turbulent falling films $\left(\mathrm{Re}_F \geq 2000\right)$ where waves of significant amplitude are present on the surface of the film around the ventilated cavity. These waves have peak heights greater than the mean film thickness, δ and carry the majority of the liquid. The waves accelerate under gravity and overtake the liquid in front of them growing in height as they travel on the falling film. When these waves reach the oscillating bottom of the ventilated cavity, they come in contact with the receiving flow i.e. the recirculating vortex. The waves then stop their descend and plunge on the vortex. The interaction of the waves and the vortex results in the entrainment of gas. The surface roughness of the film is increasing with Re_F. Therefore the gas entrainment increases with increasing Re_F. This mechanism is essentially the same as the turbulent occlusion mechanism suggested by McKeogh and Ervine (1981) for turbulent plunging jets (see section 2.1.2) and the entrainment mechanism due to the interaction of a travelling wave and a gravity wave suggested by Kockx et al. (2005) (see section 2.3.2).

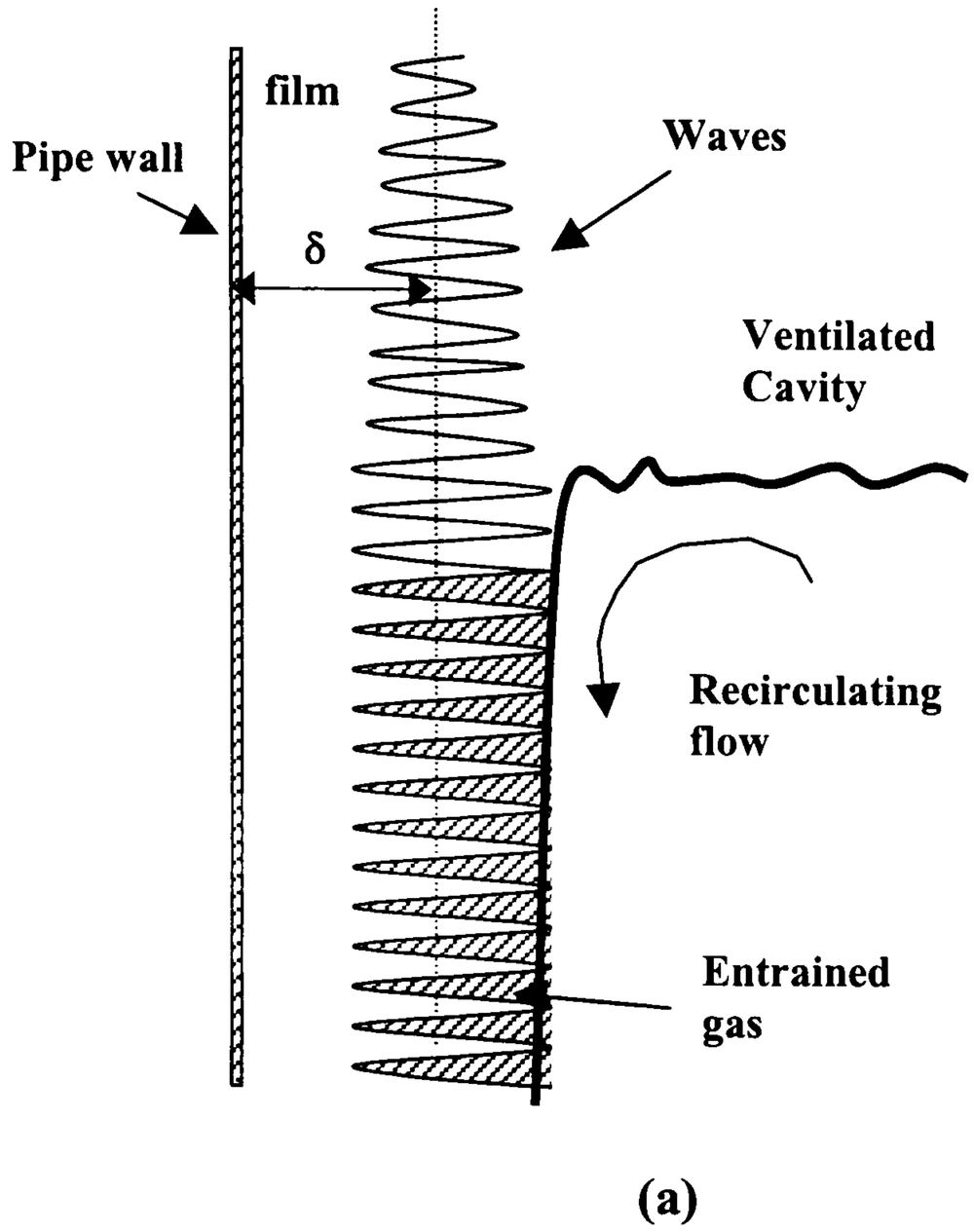

(a)

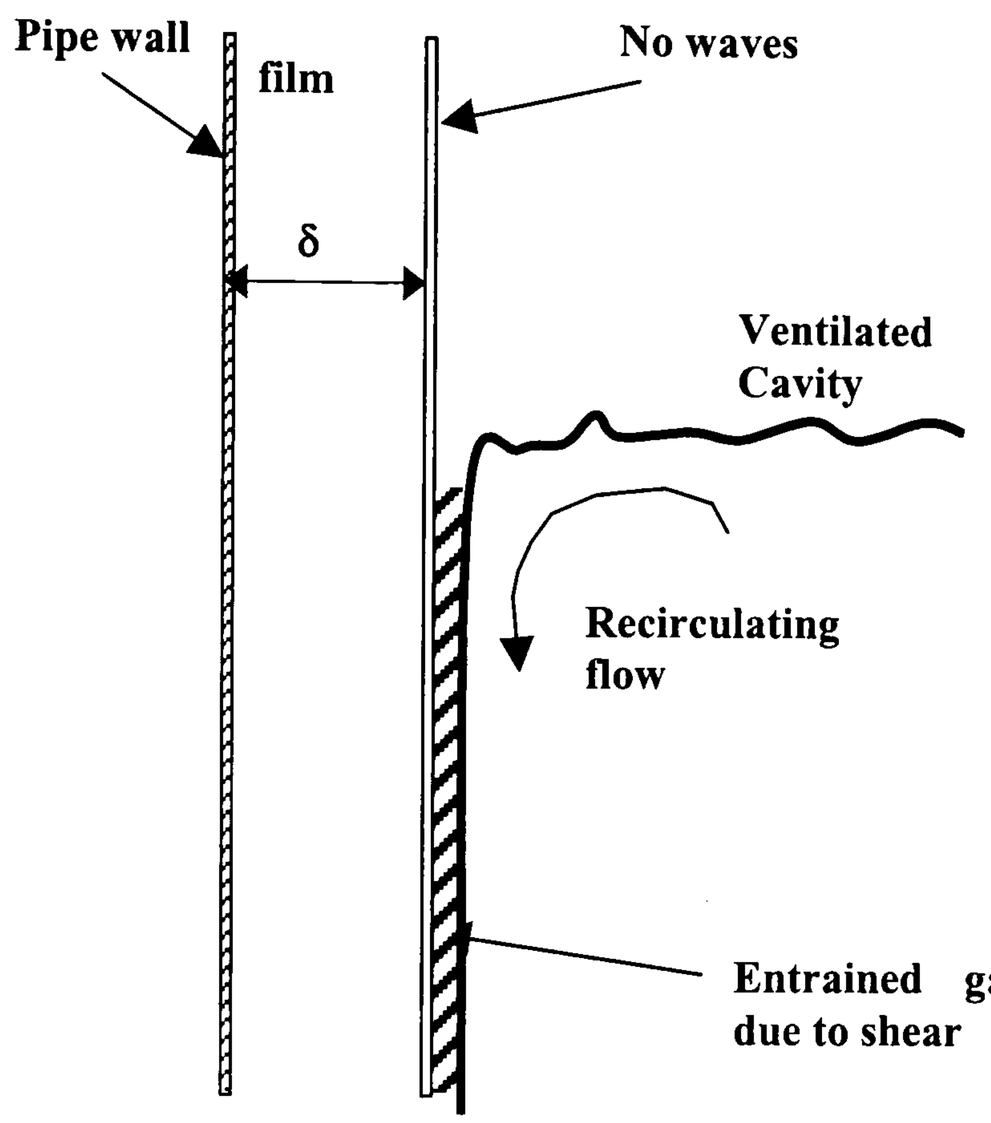

(b)

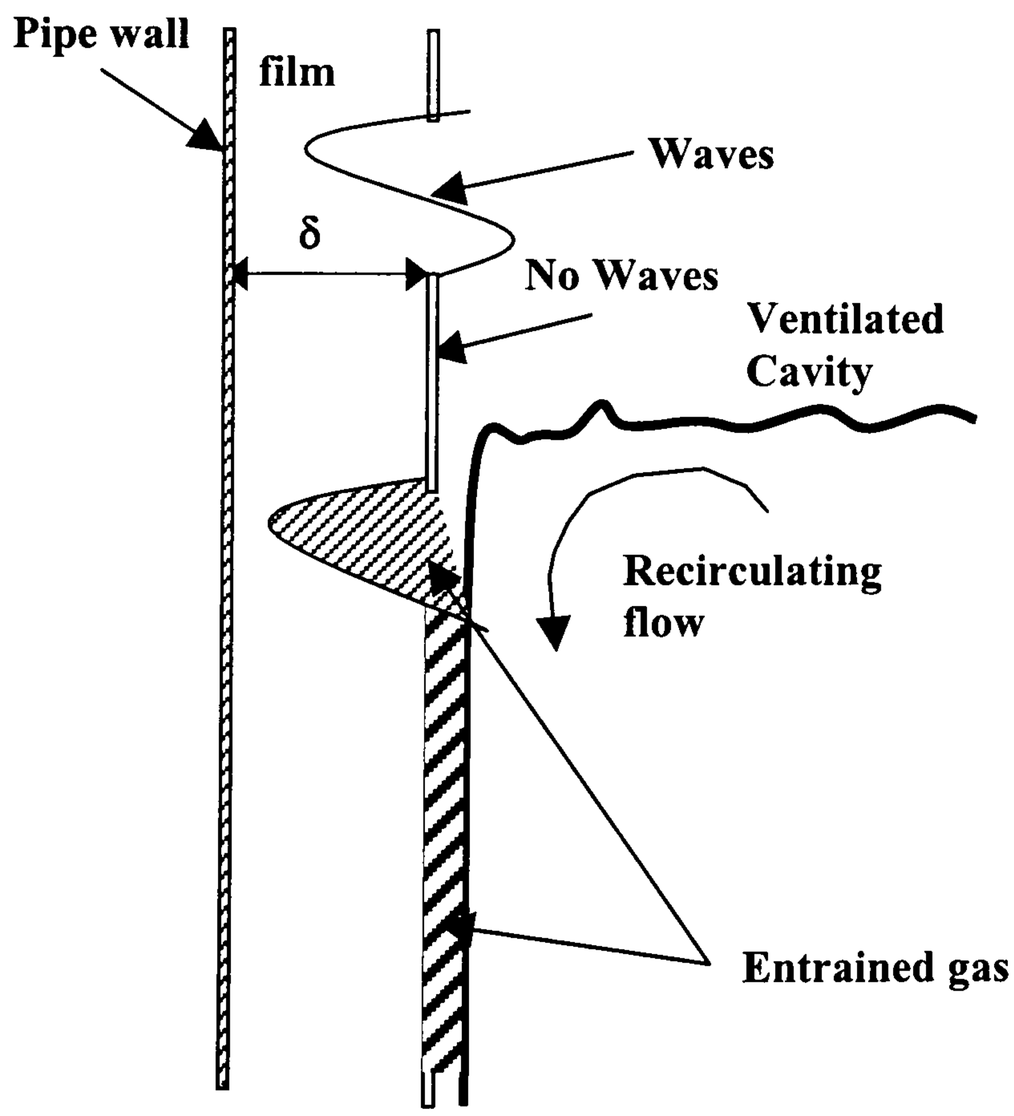

(c)

Proposed entrainment mechanisms at the base of a ventilated cavity: (a) entrainment due to the waviness of the film, (b) entrainment due to shear and (c) intermittent entrainment.

Figure 2.10

ii.) Gas entrainment due to shear (Fig. 2.10b): This type of mechanism occurs for smooth laminar $\left(\mathrm{Re}_F \leq 1000\right)$ falling films with no waves present on their surface. Gas entrainment occurs due the velocity difference between the fast falling film and the slow receiving flow. This velocity difference creates a shear layer between the two adjacent liquid surfaces that is responsible for the fragmentation of the ventilated cavity at the plunge point and the subsequent entrainment of gas. The amount of gas entrained in this case is much less compared the mechanism due to the waviness of the film.

iii.) Intermittent entrainment (Fig. 2.10c): This type of entrainment occurs for fallings films that are in transition between laminar and turbulent flow $\left(1000 \leq \mathrm{Re}_F \leq 2000\right)$. The film is mainly smooth along its length, but some large isolated waves develop randomly. The entrainment of gas is a combination of the above two other mechanisms. More gas is entrained when a large wave come in contact with the receiving flow, whilst less gas is entrained due to shear. This results in entrainment being highly intermittent. Such a mechanism has been observed by both Bacon (1995a) and Lee (1998) for the horizontal and central spargers at low liquid and gas flow rates (low entrainment rates).

CHAPTER 3

EXPERIMENTAL SET UP & PROCEDURES

This chapter contains a description of the experimental apparatus used to study ventilated cavities and slug bubbles in downward two-phase flows. The downcomer pipe in the apparatus has an internal diameter of 0.105 m and was inherited from a previous project (Lee, 1998). Therefore the design of the experimental apparatus will not be considered in great detail. The designs of the four air spargers (horizontal, peripheral, central and plunging jet) used in the current work are also discussed in this chapter but will be described briefly because they are similar to those used by Bacon (1995a) and Lee (1998). On the other hand, the design of the cylindrical bluff body used in the LDV experiments is novel and will be discussed in more depth.

The LDV experimental setup used to measure liquid velocities beneath both the bluff body and the ventilated cavities is discussed in detail. The experimental methods used to generate the various set of data are discussed, as are the methods to determine the physical properties of the fluids used.

3.1 EXPERIMENTAL APPARATUS

The experiments in the current work were performed in the re-circulation apparatus shown in Fig. 3.1. The liquid was drawn from a tank of volume 1.3 m^3 by a three-phase centrifugal pump and discharged into a small pipe of internal diameter 0.035 m. This pipe fitted concentrically into a larger pipe of internal diameter 0.098 m, forming an ejector pump that drew further liquid from the tank; a conical entry was used to reduce energy losses. Detailed calculations about the ejector pump system can be found elsewhere (Bacon, 1995a). The liquid flow rate was controlled using a ball valve situated at the riser section. A non-intrusive, fast response and supplier calibrated magnetic flowmeter (ABB Kent-Taylor Ltd) was used to measure and record the liquid flow rates. The manufacturer suggested a distance of ten pipe diameters of straight pipe before the magnetic flowmeter. The test circuit ended with a vertical downcomer section made of perspex of internal diameter 0.105 m (5 mm wall thickness) in which the spargers were positioned.

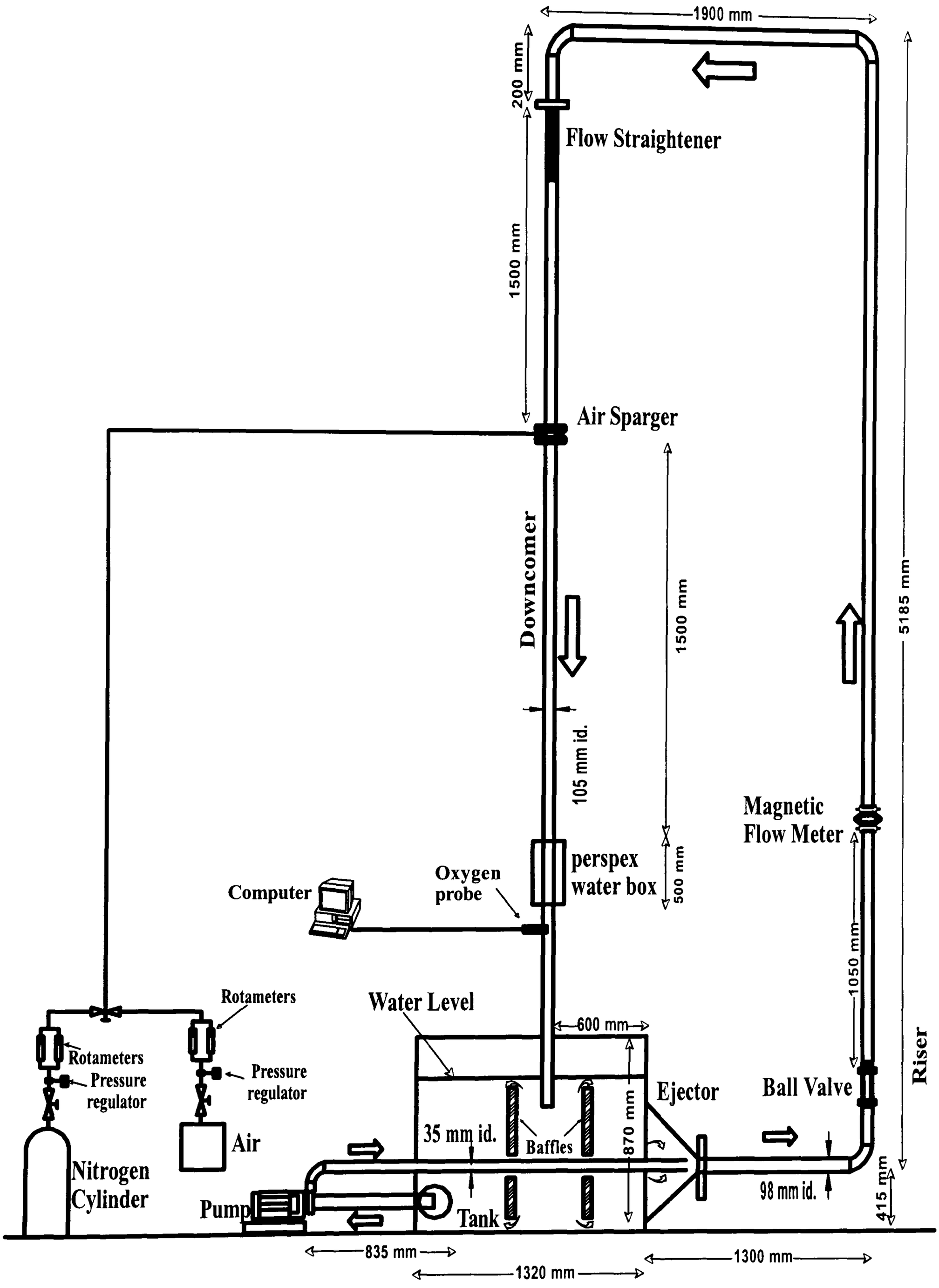

Schematic diagram of the experimental apparatus.

Figure 3.1

An adaptor was placed, at the top of the perspex downcomer in order to gradually increase the internal pipe diameter from 0.098 m to 0.105 m. An Etoile flow straightener of length 0.15 m with four vanes was included to reduce secondary flow effects as the liquid was pumped around the last 90° bend at the top of the downcomer. This type of flow straightener has been shown to be most effective in suppressing the swirl in the flow induced by upstream bends (Wendt et al., 1996). Beneath these items was a section of perspex pipe of length $16D$ before the spargers, which enabled the liquid velocity profile to develop fully. The shape of the ventilated cavity was observed through the perspex pipe and its length was measured using a tape measure. The liquid volume in the tank was 1 m^3 for most of the measurements. The temperature of the water and other liquids was held constant, using a cooler at 21±1.5 °C.

At the point of disengagement inside the tank (section numbered 2 – Fig. 3.2) two vertical baffles were installed that ran down almost the entire length of the tank. The baffles controlled the disengagement of the bubbles and prohibited them to be entrained in the pump or the ejector and subsequently the riser. These two baffles were open at the top and bottom side so that the liquid enriched with oxygen of section 2 flowed steadily to sections 1 and 3. The presence of baffles was essential to achieve a well-mixed behaviour inside the tank for the mass transfer experiments. This was confirmed with an RTD experiment as is discussed in Chapter 5.

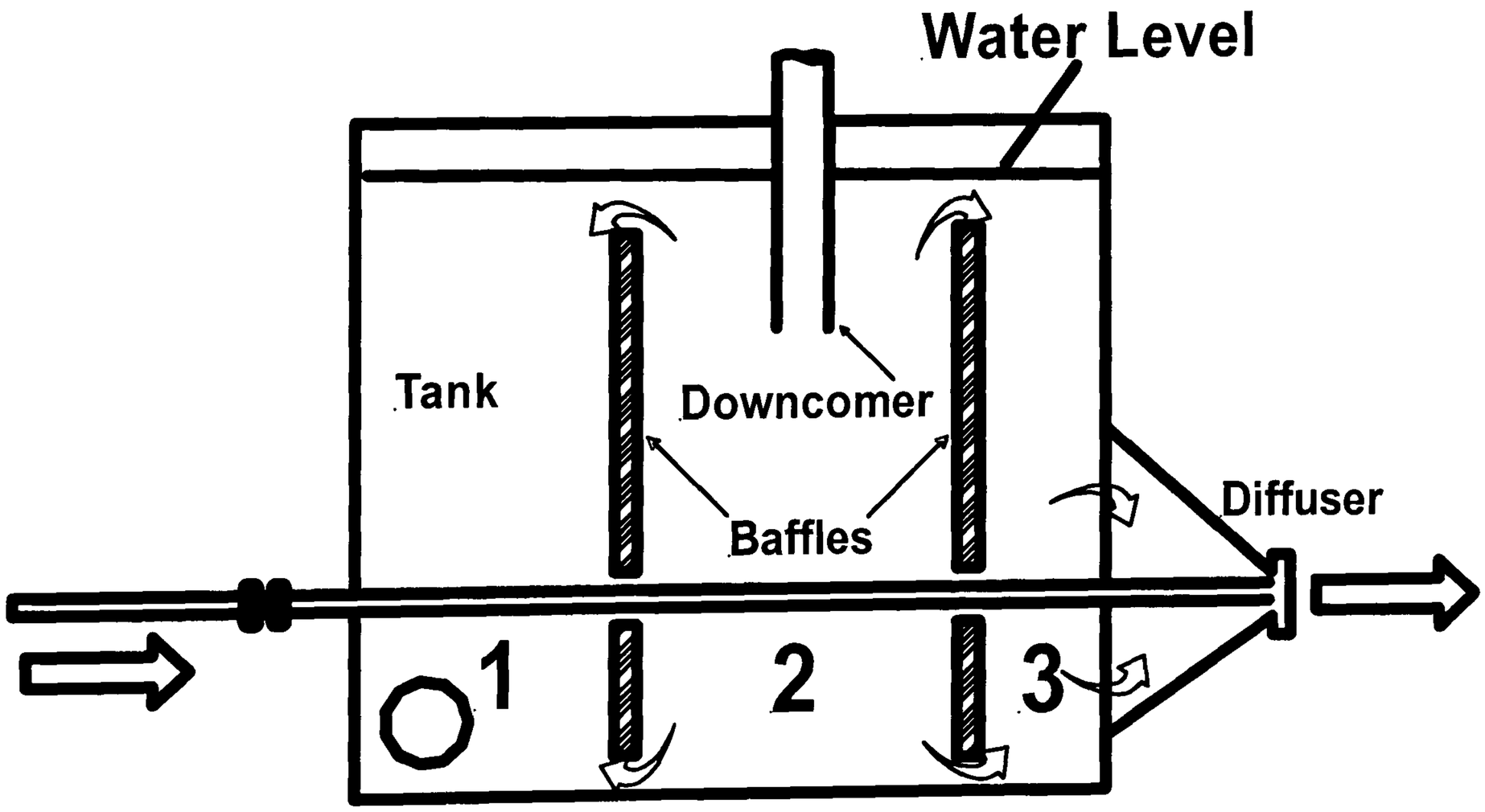

Cross-section of the tank, showing the baffles.

Figure 3.2

3.2 FLOW RATES

3.2.1 Liquid flow rates

The magnetic flow meter (ABB Kent-Taylor Ltd) did not produce any pressure loss and could accurately record the flow rate. The liquid flow rates were displayed on a digital screen as either a liquid velocity or a volumetric flow rate. The magnetic flow meter was supplier calibrated and had an accuracy of ± 0.5% of the actual liquid volumetric flow rate. Liquid flow rates between 0 to 0.0136 m^3 s^{-1} corresponding to a superficial liquid velocity in the downcomer pipe of $j_L = 1.57\,m\ s^{-1}$, were used in the current work. The principle of operation of the magnetic flow meter is based on the electromagnetic field theory. For vertical symmetric flows, non-appearance of the gas phase on the wall allows one to measure the liquid velocity based on the magnetic flow measurement technique. The fluid moving through a magnetic field experiences an electromotive force, which is perpendicular to both the imposed magnetic field and the direction of motion of the fluid.

3.2.2. Gas flow rates

Air was supplied from the high-pressure departmental mains at 6.9 barg. A pressure regulator maintained the air supply pressure at 1 barg and the readings were displayed on the bourdon gauge. The air-flow rate was measured using two pre-calibrated rotameters (CT Platon Ltd.) with different ranges and was controlled by means of needle valves directly downstream of the rotameters. The nitrogen was supplied from a pressurized cylinder at 1 barg (Fig. 3.1) by means of a pressure regulator and was also controlled by a rotameter. Gas flow rates of up to 0.00088 m^3 s^{-1} corresponding to a superficial gas velocity in the downcomer pipe of $j_G = 0.102\,m\ s^{-1}$ were used.

The rotameters were already calibrated at 1 bar absolute and 20°C, and a correction factor was used to take into account the temperature and pressure differences between the calibration and experimental conditions in the rotameter. Ower (1949) recommended the following expression for air rotameters:

$$Q_{G,2} = Q_{G,1}\sqrt{\frac{P_1 T_2}{T_1 P_2}} \tag{3.1}$$

where Q_G, P and T are the volumetric air flow rate, pressure and temperature, respectively. Now if the subscripts "1" and "2" refer to the conditions and flow rate during the calibration and

experiment respectively, then Eq. (3.1) can be used to calculate the gas volumetric flow rate through the rotameter. An average air supply temperature of 288 K was assumed for all calculations (fluctuations in air temperature were not likely to exceed ± 10°C resulting in an error of under 2%). Bacon (1995) compared Eq. (3.1) with measurements using a soap film meter and found that values predicted differed from values measured by under 5%.

However, $Q_{G,2}$ is the gas flow rate through the rotameter only. In order to obtain the air flow rate through the sparger in the downcomer, $Q_{G,2}$ needs to be corrected for the location of the sparger, i.e. the pressure at the point where gas is injected. The correction for ideal gas behaviour is shown below (Lee, 1998):

$$Q_{G,3} = Q_{G,2} \frac{P_2 T_3}{T_2 P_3} \tag{3.2}$$

where the subscripts '2' and '3' represent the conditions in the rotameter and downcomer sparger respectively. Based on the Eq. (3.2) the actual gas volumetric flow rate through the sparger could be calculated once the distance of the bubble base above the liquid surface in the tank was taken into account. Hence all gas flow rates quoted from henceforth will be at a pressure approximately of 0.7 bar absolute (the spargers are located about 3 m above the water level in the tank).

3.3 LIQUID PHYSICAL PROPERTIES

In the current work, the test liquids used were water, salt solution, 2% w/w isopropanol solution (IPA) and 8% w/w IPA. The Thermo Haake sensor system NV with the C25P control vessel connected to a host computer were used to determine the viscosity and rheology of the liquids used in the present work. The sensor system NV consisted of cup and a bell shaped rotor. It is classified as a coaxial cylinder sensor system with two gaps for shearing the samples on the inside and on the outside of the rotor. According to the Thermo Haake help guide the NV sensor should be used when low viscosity liquids are to be measured such as water or aqueous solutions. Measurements were taken by controlling the shear stress (CL mode) at the constant temperature of 20°. A range for the shear stress was inserted in the software by defining a start and an end value. The software automatically calculated the related torque and the results were plotted on a shear stress versus shear rate curve (there was also the option to plot viscosity versus shear rate curve). The software at the end of each experiment calculated the viscosity. All liquids

used exhibited Newtonian rheology, i.e. the graph of shear stress against shear rate was a straight line.

Surface tension was measured using a digital micro-tensiometer (Kibron Ltd.) suitable for fast accurate and easy measurements of a large variety of liquids. The key component in the instrument was a microbalance adapted for measuring small forces. The resolution of the balance was 0.0001 N m^{-1}. While the surface tension measurement was based on the Du Nouy method[3.1], the micro-tensiometer utilized a small needle (probe) instead of a Du Nouy ring. The probe had a diameter of 0.5 mm and the measurement solutions were assumed to wet completely the surface of the probe, which is reasonable. The maximum force exerted by the surface tension was recorded as the probe was withdraw from the measurement solutions. One measurement, i.e. the recording of one surface tension value took around 25 sec. Every measurement was repeated five times and the surface tension was calculated based on the average value of these five runs. The same measurement probe was used in all measurements, but was cleaned by flaming between different liquids.

The density of the liquids used was required to calculate the Re during the experiments. The density was found by taking a 0.5 litre sample in a beaker of known weight and weighting on an electronic balance. This was repeated three times and the average value was taken. The density was then calculated based on the average value of these three runs. As is shown in Table 3.1 the density of all the liquids used varied slightly from that of water.

The measured liquid physical properties used in the current work are shown in Table 3.1, where μ_L is the viscosity of the liquid, ρ_L the density of the liquid and σ the surface tension. The uncertainty represents the standard error of the measurements.

3.4 VENTILATED CAVITY LENGTH MEASUREMENTS

The ventilated cavity length was measured using the same method as in Bacon (1995) and Lee (1998). The ventilated length was measured from its point of formation at the sparger to the

---

[3.1] This method utilizes the interaction of a platinum ring with the surface being tested. The ring is submerged below the interface and is raised upwards. The calculation of surface tension is based on the measurement of the maximum force to lift the ring through the surface.

base using a tape measure, for a range of water and air flow rates. The bubble base was identified as the lower limit of annular flow or the top of the high void fraction recirculating region immediately underneath the cavity. The exact location of the bubble tended to fluctuate up and down within 0.01 m, depending on the operating conditions (water and air liquid flow rates) as well as sparger design. This made it necessary to allow for a short time interval of 1 min before any cavity length measurements were taken so as to establish a stable cavity.

Every time the air flow rate was increased the ventilated cavity grew as well which lead to greater losses in the circuit (Lee et al., 2000). If the pump were to operate at the same operating point on the pump characteristics curve the liquid flow rate would then decrease because of the additional losses (Lee, 1998). Therefore it was necessary to adjust the liquid flow rate after each adjustment of air flow rate to ensure that the liquid flow rate was constant for a given set of experiments.

Liquid 20°C	μ_L $\left(kgm^{-1}s^{-1}\right)$	ρ_L $\left(kgm^{-3}\right)$	σ $\left(Nm^{-1}\right)$
Tap Water	0.00101 ± 0.00003	995 ± 2.0	0.0725 ± 0.00005
Salt Water	0.00107 ± 0.00003	1026 ± 2.1	0.0741 ± 0.00005
2% w/w IPA	0.00111 ± 0.00004	992 ± 2.3	0.0575 ± 0.00006
8% w/w IPA	0.00120 ± 0.00004	983 ± 1.6	0.0417 ± 0.00006

Measured liquid physical properties.

Table 3.1

3.5 SPARGER DESIGNS

3.5.1 Horizontal sparger

The horizontal sparger, HS, was modelled on a sparger suspected of producing a ventilated cavity in an industrial fermenter (Bacon, 1995a). It consisted of a horizontal brass pipe, with

twelve air holes, arranged in a straight line. A schematic diagram of the horizontal sparger used in the current work is shown in Fig. 3.3.

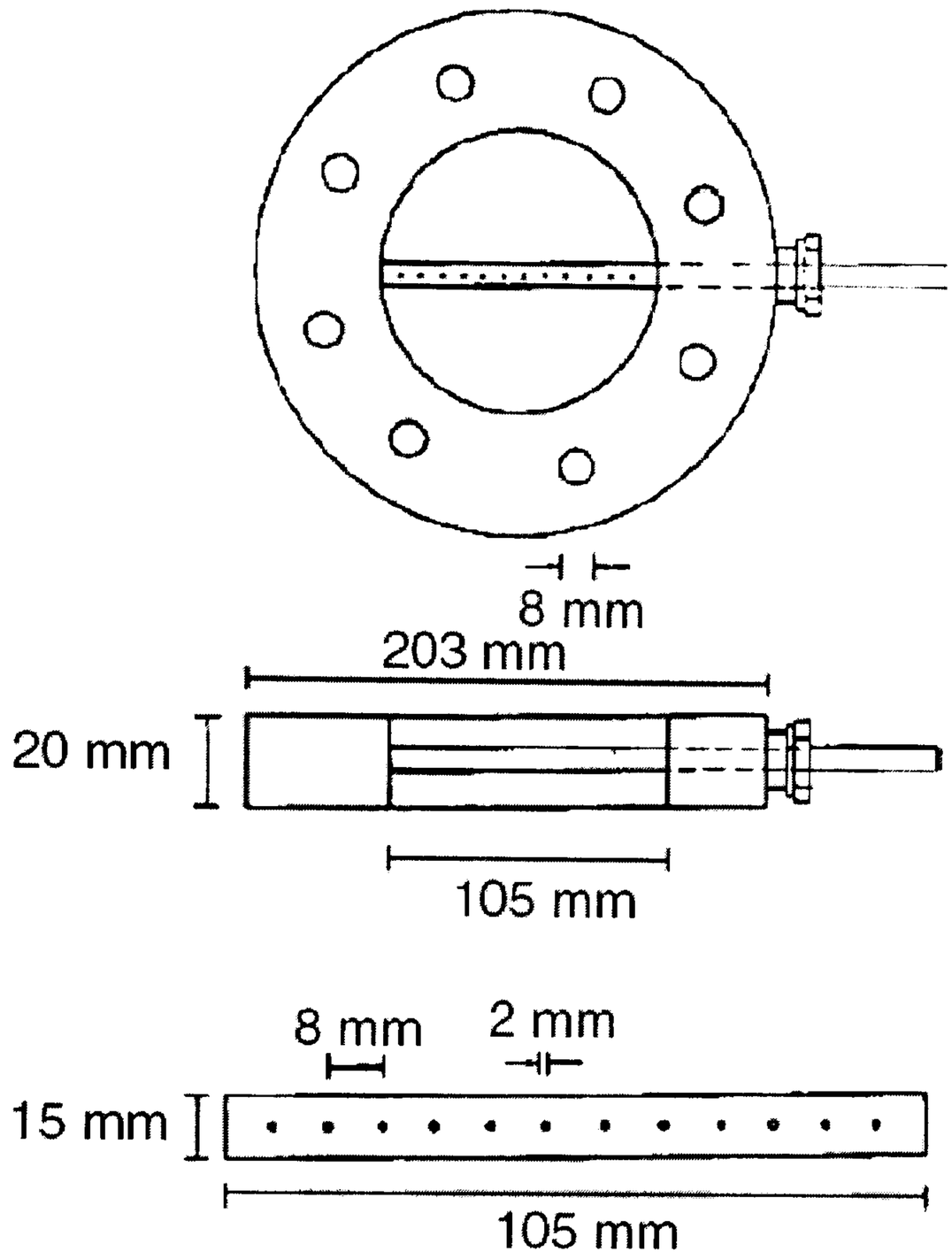

Schematic diagram of the Horizontal Sparger (HS) (Lee, 1998).

Figure 3.3

The holes faced vertically downwards, with air injection in the direction of the liquid flow. Bacon (1995a) found that the layout of the air holes in the brass pipe did not affect the cavity attached to the sparger. The sparger was designed to generate even flow of air through each of the air holes. Details about the horizontal sparger design are given in Appendix A.

The horizontal sparger produced a distorted bell-shaped ventilated cavity extending from the horizontal pipe. For low air to water volumetric flow rates ratios (Q_G/Q_L), the ventilated cavity was short and had a rectangular shape. As the cavity grew, its base approached the downcomer walls. Eventually the base of the cavity became cylindrical with the liquid flowing as an annular falling film about the cavity. A full description of the ventilated cavity growth dynamics can be found elsewhere (Bacon, 1995a; Bacon et al., 1995b; Lee, 1998).

3.5.2 Central sparger

The central sparger, CS, was a scale-up design of the one used by Bacon (1995a). A schematic diagram of the central sparger is shown in Fig. 3.4. It consisted of a single brass pipe 0.3675 m long with a 0.013 m internal diameter. The pipe was mounted on a perspex flange and the point where the sparger passed through the flange was air-sealed with silicon rubber sealant. The pipe was sited vertically on the central axis of the downcomer when the flange was positioned into the test section. A 45° cone, made of brass, was carefully soldered at the end of the pipe to stabilise the cavity. For a wide range of gas to liquid volumetric flow rates, (Q_G/Q_L), a stable bell-shaped ventilated cavity with a circular cross-section at all levels was formed underneath the CS.

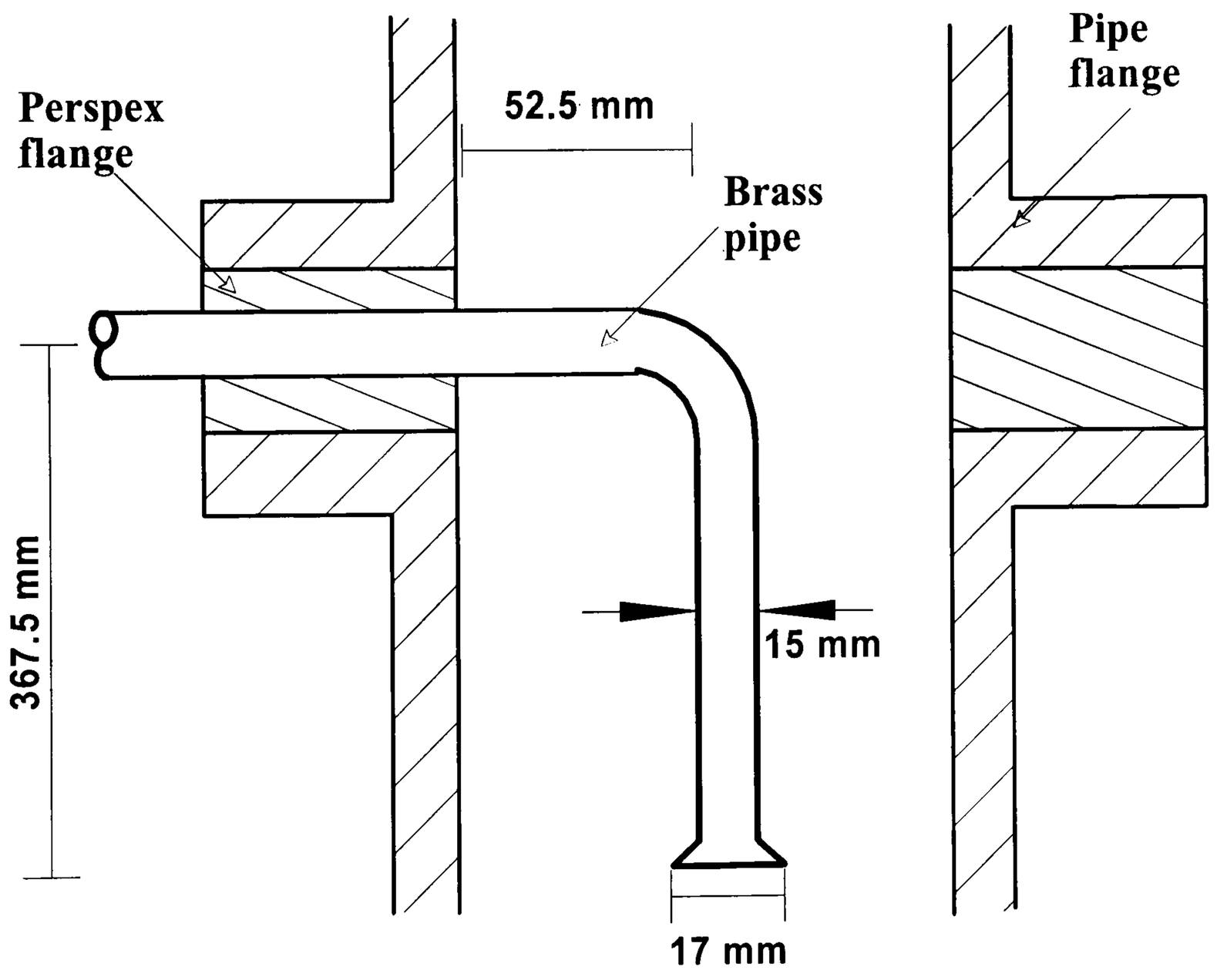

Schematic diagram of the Central Sparger (CS).

Figure 3.4

3.5.3 Peripheral sparger

The peripheral sparger, PS, consisted of a section of full bore pipe flange, i.e. with extra thick walls and with a number of air holes spaced uniformly around the downcomer periphery. It is shown in Fig. 3.5.

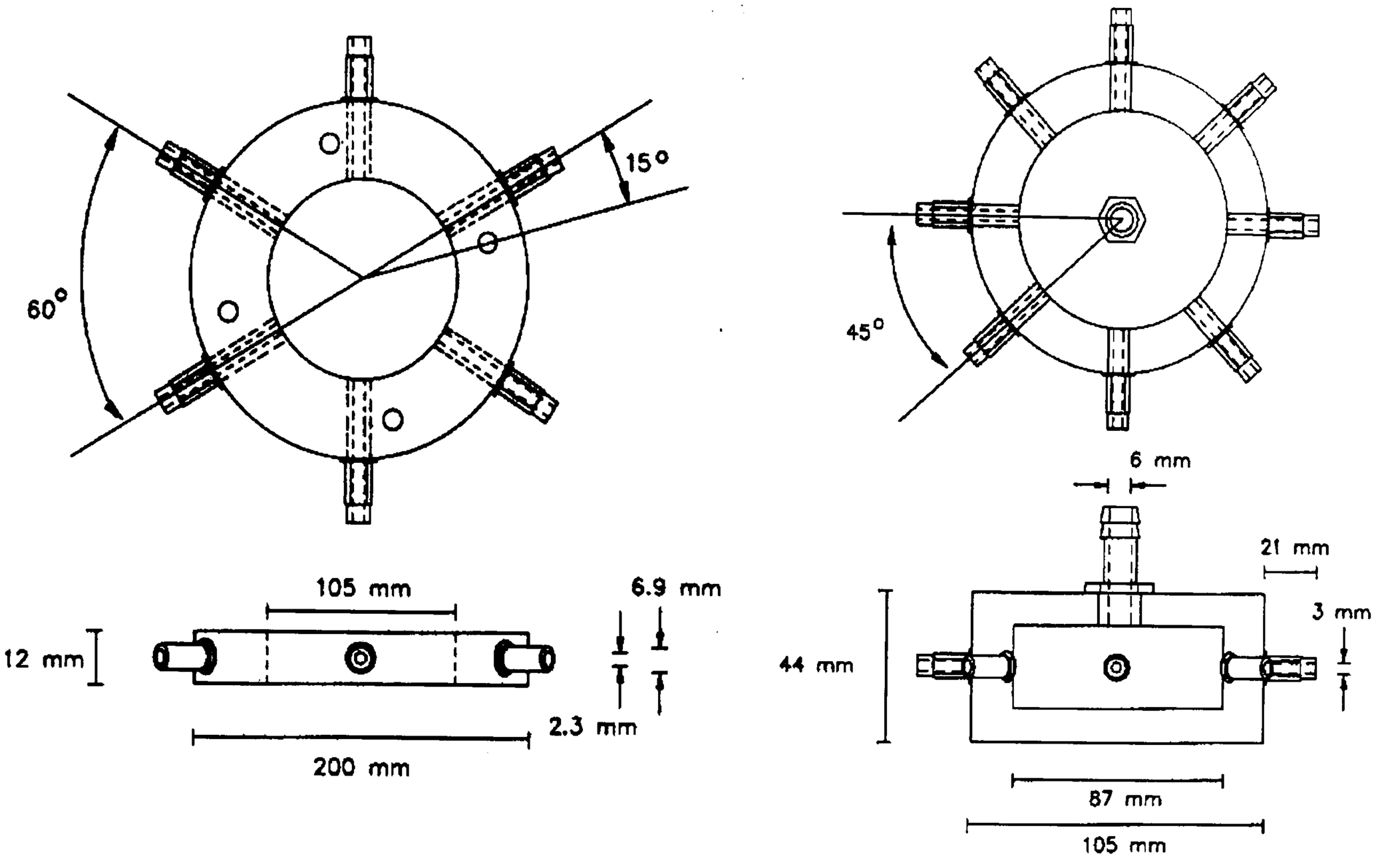

Schematic diagrams of (a) The Peripheral Sparger (PS) (After Lee, 1998) and (b) the air distributor (Lee, 1998).

Figure 3.5

It was designed such that it can be fitted between two flanges in the downcomer. The peripheral sparger injected air directly though the wall of the downcomer and so would not present any physical obstruction to the flowing liquid. Air was injected perpendicular to the liquid flow direction by six holes. Equal air flow through each hole was ensured by use of an air distributor, the design of which is also shown in Fig. 3.5. The distributor was an air sealed tight perspex box, with the air supplied through at the cylinder centreline and leaving via the six holes in the curved wall, all of which were perpendicular to the feed direction. In this way none of the exit directions was favoured over any other and even flow rates were assured. Each exit air hole on the distributor was connected to the peripheral sparger by flexible tubing of the same length.

In the case of the PS the resulting flow pattern was more chaotic compared to that beneath the HS. For low Q_G/Q_L , six individual ventilated cavities were formed and were clinging from each hole of the sparger. The cavities were also attached to the downcomer wall. As the air flow rate

was increased these cavities began to join up forming eventually a ring (or a large ventilated cavity) of air next to the downcomer wall which forced the flowing liquid into the centre of the downcomer. Any further increase in the air flow rate caused the base of this ring to grow as a cylinder of air within an annular liquid film flowing down the walls and some liquid falling freely inside the air ring. A detailed account of the air ring growth dynamics can be found in Lee (1998).

3.5.4 Plunging jet sparger

The plunging jet sparger, PJS, was introduced by Thorpe et al. (1997) and the version used in the experiments reported here is shown in Fig. 3.6. It consisted of a carefully tapered perspex section with the inlet having the same diameter as the downcomer and exit in the form of a protruding lip section. The PJS deliberately channelled the liquid to the centre of the pipe and injected the air at the wall. The air was uniformly injected perpendicular to the liquid flow direction and was deflected downwards by the lip of the sparger. A detailed design procedure for the PJS suggested by Thorpe et al. (1997) is given in Appendix A. The PJS was found to have superior performance to the above spargers as it produced shorter cavities and had greater resistance to stall at high gas flow rates (Lee, 1998).

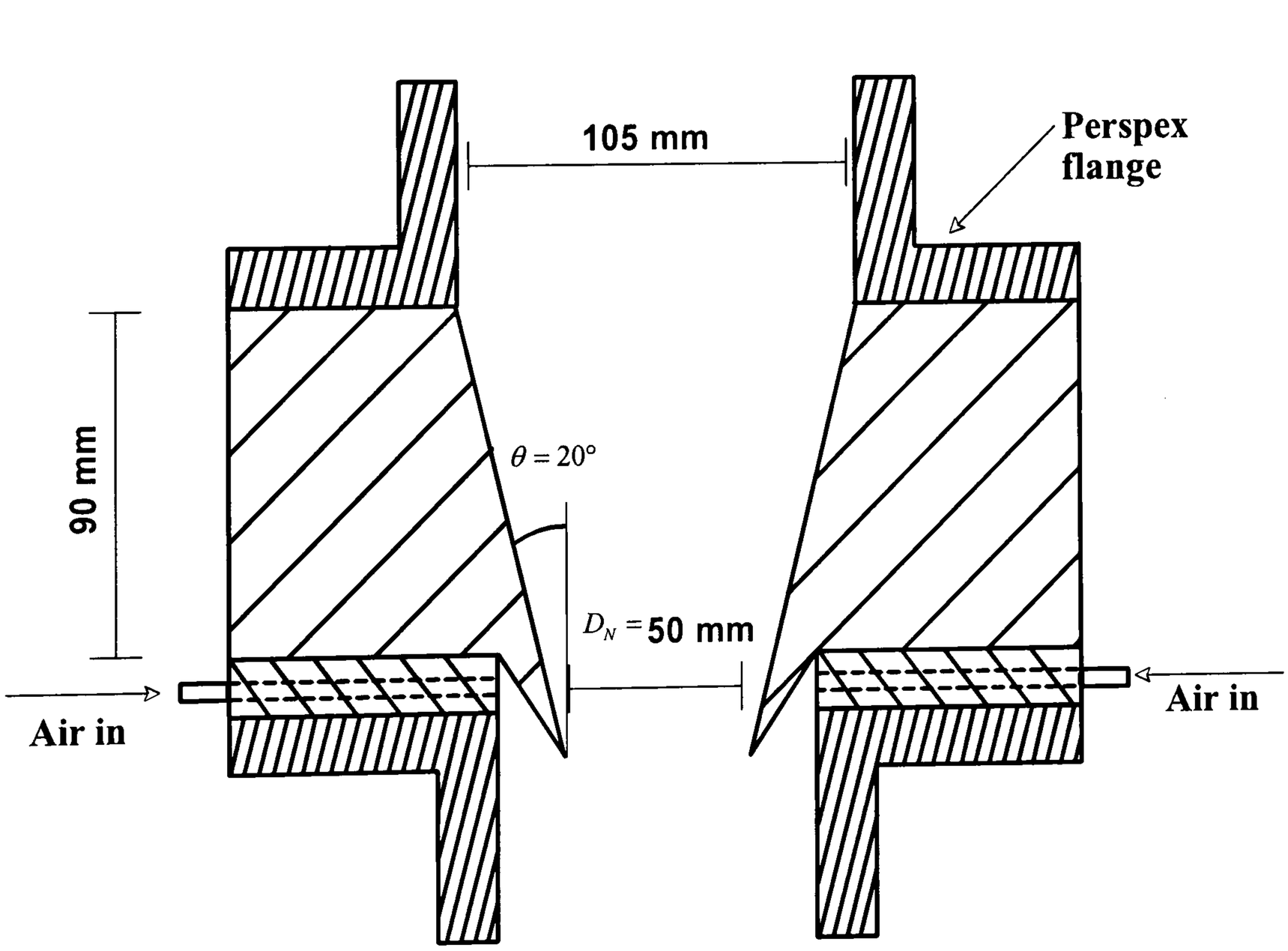

Schematic diagram of the Plunging Jet Sparger (PJS).

Figure 3.6

The sparger used in the experiments reported here was a slightly different design from that of Thorpe et al. (1997) since the experiments in the present study were conducted for a pipe diameter twice as large and the sparger was adapted from an existing piece of perspex equipment. The ratio of the pipe diameter to the sparger's rim diameter (D/D_N) was 2.1 (Fig. 3.6), compared with the 1.25 of the original design and 1.33 of the PJS used by Lee (1998). This higher ratio caused a greater energy loss than the original design but also produced smaller cavities. The extent of the way this increase influenced the bubble size and the volumetric mass transfer coefficient, $k_L a$ are discussed in Chapter 5. On reflection, a ratio of 2.1 is not an ideal design choice.

3.6 BLUFF BODY

The LDV was used in the current work in order to obtain the full liquid velocity field beneath a cylindrical bluff body in turbulent single-phase flow. The motivation for these measurements was that the flow field formed behind the bluff body had been suggested to have many similarities to the flow field beneath large ventilated cavities and slug bubbles in two-phase flow (Thorpe et al., 2001).

The bluff body was made of perspex and had a cylindrical shape. It had a diameter of 0.095 m, a length of 0.1 m and an area blockage ratio of 82% (ratio of bluff's body area to pipe's cross sectional area). The bluff body was screwed on a brass cover and was mounted coaxially on the pipe flange by four lugs (Fig. 3.7). There was a uniform 5 mm gap between the bluff body and the pipe wall, leaving a length of 20 gap diameters between the top and bottom parts of the bluff body. This distance ensured that at the base of the bluff body the flow in the annulus was fully developed.

3.7 DISSOLVED OXYGEN PROBES

The dissolved oxygen (DO) transfer rate in the aerated part of the column below the downcomer sparger, was determined for tap water and air. The overall gas-liquid volumetric mass transfer coefficient $k_L a$ was determined by the well-known dynamic method, by using unsteady state absorption of oxygen (Chisti, 1989). To get dynamic values of $k_L a$ the gas being sparged was switched from air to nitrogen (down step) and back to air again (up step) (Muller and Davidson, 1992). A polarographic (Clark cell), temperature compensated oxygen electrode

(Data-Harvest Ltd., Model 3131) was used to monitor the variation of the DO concentration in the system with respect to time. Details about the measurement principles of the electrode are given in Appendix B. The electrode was placed $23D$ below the point of injection in a location where the turbulent two-phase bubbly flow was fully developed. The measured DO profiles were recorded and stored for future analysis in a computer via a data logger.

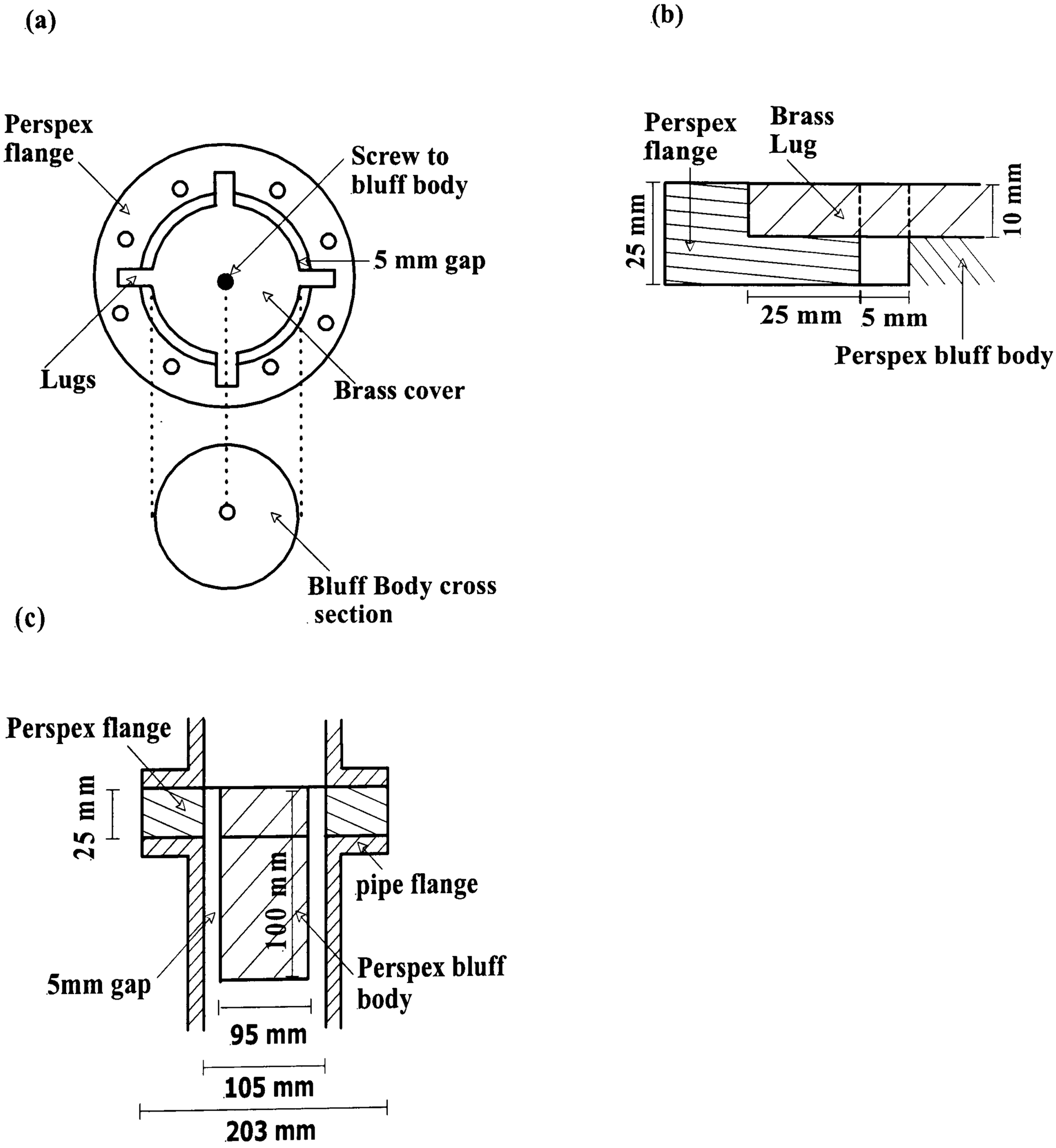

Diagram of the bluff body assembly: (a) Expanded top view, (b) Cross-section of a lug and (c) cross-sectional view of the pipe with the bluff body in place, not showing the brass cover for clarity.

Figure 3.7

3.8 BUBBLE SIZE MEASUREMENTS

A wide number of techniques developed to measure bubble sizes in two-phase flows have been used by several workers. Schugerl (1991) summarised these techniques into three main groups:

1. Optical techniques (Photography): the sensor does not contact the bubble phase (non-intrusive).
2. Measurement of bubble penetration length in the direction[3.2] in which most movement takes place (bubble probes): the sensor contacts the bubble phase (intrusive).
3. Measurement of bubble volume (isokinetic sampling probes/ultrasound)[3.3]: the sensor contacts the bubble phase (intrusive).

Photography was used in this work to characterise the resulting bubble size as a function of the operating conditions (gas and liquid flow rates) using the four different air spargers described in the previous sections of this Chapter namely, the HS, CS, PS and the PJS. Photography was chosen due to its extensive use in the literature regarding bubble size measurements. The photographs were taken at a position of approximately 18*D* below the location of the sparger. This location was chosen as being representative of a fully developed turbulent bubbly flow. The procedure for taking a bubble photograph involved adjusting the gas and liquid flow rates so that a stable ventilated cavity of length of 0.1 m was attached to the sparger. Also, at each new gas and liquid flow rates, a short time interval (about 2 min) was allowed before a photograph was taken, allowing time for a stable cavity to be formed. The photographs were taken with a digital camera (Model Olympus C-2500L) that was provided by the departmental experimental officer. The camera was placed 600 mm from the column with a field view of 600 x 140 mm. The technical specifications of the camera are summarised in Table 3.2.

There are some limitations for the use of photography to measure bubble sizes inside pipes. The cylindrical surface of the pipe distorts the view of the bubbles. The camera's focal length

---

[3.2] Usually upwards.

[3.3] Isokinetic probes involve sucking a small portion of dispersion from the vessel into a capillary where the bubbles form elongated slugs. Ultrasound methods are inverse methods, relying on the fact that bubbles have a strong effect on the propagation of acoustic waves.

decreases with magnification and the lens can not be positioned close enough to the pipe to allow sufficient image enhancement. Hepworth et al. (2004) have discussed these issues.

To overcome the distortion due to the curvature of the pipe a rectangular box was used to surround the pipe with a flat bottom to fit on the perspex pipe (Fig. 3.8). The dimensions of the box were 500 x 150 x 150 mm. The box was filled with water and a white ruler with black marks along its length was inserted and stabilised in the middle of the box to provide a measure of the scale.

The high magnification and fast shutter speed used in some measurements were combined with high levels of lighting focused on a small area that allowed the capture of quality images. Lighting was providing by three Draper (The Tool Company, UK) Halogen HL500/T 500 W light sources. Each light source was mounted on a telescopic stand to allow better direction of the lighting at the measurement location. Care was taken to ensure that there were no shadows produced by the lighting and to avoid specular reflections off the lens.

The images acquired by the camera were processed digitally using Image Pro Plus software and manually using a ruler. Both methods showed good agreement, within 5%. However the manual method offered a better bubble tracing at higher void fractions and therefore the results presented in this thesis have been analysed manually. Nevertheless for the shake of completeness both methods are described in the next paragraphs.

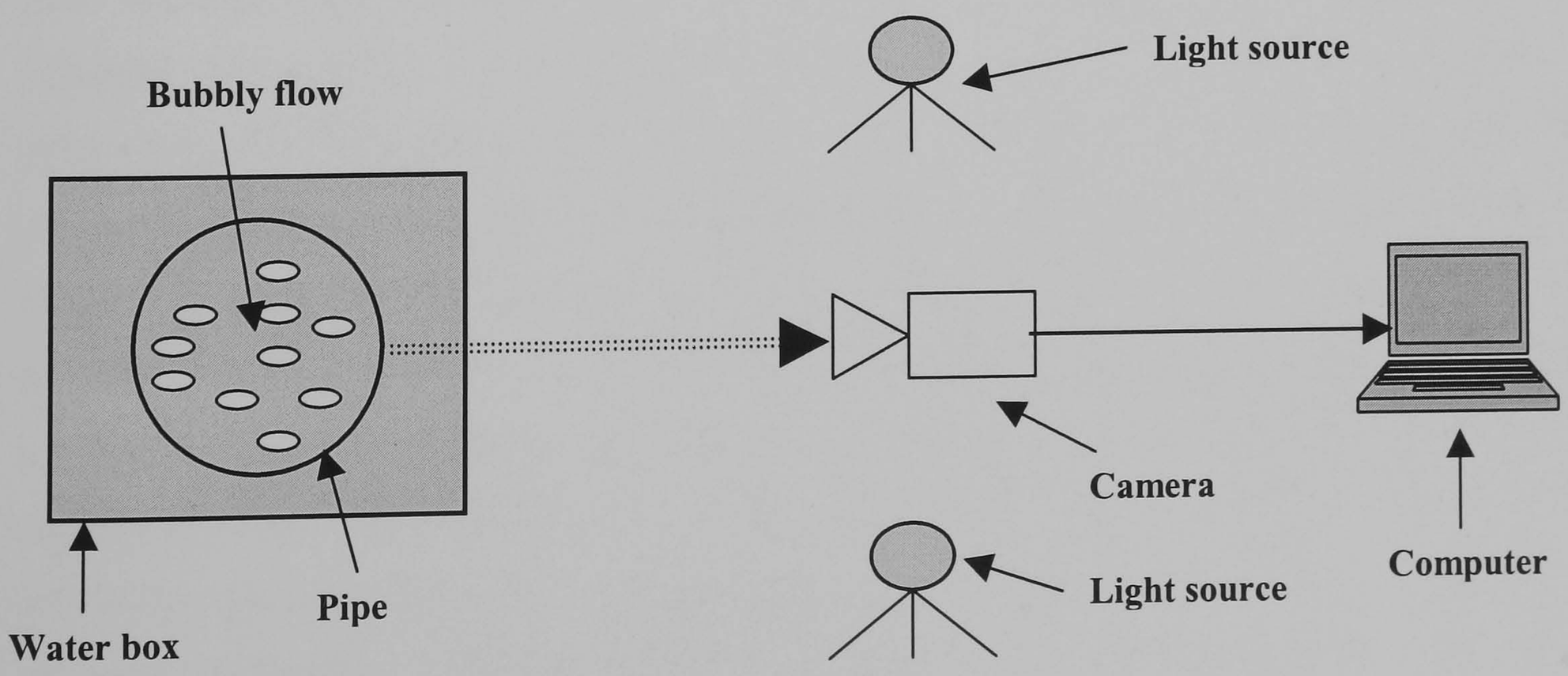

Schematic diagram of the setup used to measure bubble size.

Figure 3.8

Pixels	Sensor Pixels	5.5 million pixel
	Image Pixels	1712 x 1368 max, 1024 x 768, 640 x 480
Camera	Optical Zoom	Optical 3 x
	Focal Length	36 – 110 mm f: 2-11
	ISO equivalent	100/200/400
	Shutter Speed	1/2 to 1/10000 s
Storage	File Format	JPEG x 3, Tiff
	Number of images stored	4-49 pictures (8 MB)

Technical specifications of camera Olympus C-2500 L.

Table 3.2

3.8.1 Image analysis using Image Pro Plus software

The image was saved in the computer and was divided using the Image Pro Plus software into three equal parts. Each part corresponded to a field view of 190 x 110 mm of the original picture (this was called AOI –area of interest). Each image was saved as 256-grey scale bitmap image so that each pixel was identified by its position on an array. The image was then segmented. Segmentation was the process by which the grey levels in the image were visually identified and then isolated from the image as a whole. During this process the image was divided into "classes" representing the bubbles and "background noise" representing the water. This was done using the "Histogram-based model". A threshold value was chosen such that all the pixels with grey value larger than the threshold value were coloured white and taken as classes (bubbles), while the rest with the grey value less than the threshold value were coloured black and taken as background noise. The threshold application increased the noise and was necessary to apply a filter to eliminate apparent or false edges and distinguish the bubble boundaries clearly. A Sobel filter with a 3 x 3 mask was used to enhance and detect the edges (Soler et al., 2003) (see also Fig. 3.9). This filter extracted and enhanced the edges of the image by expressing intensity differences between neighbouring pixels as an intensity value. This was done by combining the difference between the top and bottom rows in a neighbourhood, with the difference between the left and right columns, using the following formulas.

$$\sqrt{\left(X^2+Y^2\right)} \tag{3.3}$$

where,

$$\begin{aligned} X &= \left(C+2F+I\right)-\left(A+2D+G\right) \\ Y &= \left(A+2B+C\right)-\left(G+2H+I\right) \end{aligned} \tag{3.4}$$

A	B	C
D	E	F
G	H	I

Neighbouring pixels in an image.

Figure 3.9

The image was then processed through the "measure menu", where it was spatially calibrated and the various properties (diameter, area etc) of the white objects (bubbles) were automatically measured. This technique provided very fast and accurate results (within 2% of the manual method) for low void fractions. However with growing bubble density there was significant bubble overlapping in the image and the software interpreted overlapping bubbles as one big bubble. For this reason the tracing of the bubbles had to be done manually and the agreement was within 5% of the manual method described next. To the best of the author's knowledge there are no reports in the literature of automatic tracking bubble size measurements when significant bubble overlapping occurs.

3.8.2 Manual image analysis

The image was digitised in a computer and was divided using the Image Pro Plus software into three equal parts. Each part corresponded to a field view of 190 x 110 mm of the original picture. Each image was then saved and printed into A3 size paper. A ruler was used to measure the minor and major axis for each bubble. All overlapping bubbles were eliminated consistently from the measurements in order to avoid their interpretation as one big bubble. Only well-focused bubbles were measured. The elimination of badly focused bubbles meant that the sample of bubbles taken was biased somewhat towards those found near the center of the pipe. A careful

examination of the photographs showed that there were more bubbles in the center of the pipe than close to the wall and the focus was better in the center of the pipe. In most of the flow conditions the radial distributions of the bubble sizes were quite uniform. Thus, the potential bias in the bubble size distribution due to the bubble sampling near the center was small and was not expected to influence the results.

3.9 LASER[3.4] DOPPLER VELOCIMETRY (LDV)

3.9.1 Introduction

Laser Doppler Velocimetry is a point-wise optical measuring technique that measures fluid velocity accurately and non-invasively with no need for instrument calibration. Laser light illuminates the flow and two crossing beams form an interference pattern in a well defined measuring volume. Small particles added in the flow (seeding particles), are moving through the measuring volume and scatter light of varying intensity, some of which is collected by a photodetector, where the fluctuations in light intensity are converted into fluctuations in a voltage signal (i.e. the light is converted to electrical energy). An electronic device known as a signal processor is then used to determine the dominant frequency of the signal, f_D (this is the Doppler frequency – see Appendix C). The resulting frequency, of the photodetector output is related directly to the particle velocities.

This technique has been introduced by Yeh and Cummings (1964) and since then has been well established as an optical technique. Its ability to make accurate velocity measurements with high spatial and temporal resolution, even in high turbulent flows, have led to the widespread use of LDV in numerous fluid flows. There are no reports in the literature in which the LDV has been applied to measure fluid velocities in a geometry where a ventilated cavity is attached to a sparger in a downflowing liquid. A comprehensive discussion on the subject of LDV can be found elsewhere (Watrasiewicz and Ruud, 1976; Durst et al., 1981). Some basic principles will only be considered in this thesis (Chapter 3 and Appendix C), in order to give sufficient background information of the general ideas and the measurement methods.

[3.4] *LASER* is the acronym for Light Amplification by Stimulated Emission Radiation and hence describes the way it is produced.

3.9.2 The TSI 2-D LDV system

The EPSRC Engineering Instrument Pool provided the LDV system employed in the present work for a period of six months. It was a two-channel, four-beam, fiber-optic system operating in the dual-beam and back-scatter mode, manufactured by TSI Inc. It comprised of an optical and a signal processing system. Through the optical system the measuring volume was formed and the light scattered by particles in the flow was collected and sent to the signal processing system where the Doppler frequency, f_D, of the scattered light was obtained. Additional main components of the LDV system used in this work included a multicolour beam separator (Model 9201 ColourBurst), a digital burst correlator (Model IFA 650-3), a fiberoptic probe (Model 9253-350), a multicolour receiver (Model 9230-3 ColorLink), a computer with the control software (FIND 1.4 for Windows) and a traversing mechanism. A short description of the fiber optic system, the signal processing system and the traverse is given in the following paragraphs.

3.9.2.1 Fiber optic system

A schematic diagram of the two component fiber-optic system is shown in Fig. 3.10. The laser source used was a Spectra-physics (Model 2017-04S), 5 W argon-ion laser, mounted on an optical rail. It generated a laser beam that emitted coherent and monochromatic[3.5] light. A beam collimator was used (Model 9108) to minimise the generated beam divergence. Water was used to cool the laser.

The argon-ion laser generated an emission, which was concentrated into several spectral lines, with a particular concentration of the energy in the blue (wavelength of 499 nm) and green lines (wavelength of 514.5 nm). The multicolor beam separator (Model 9201 ColourBurst) was used in the transmitting side of the optical system to generate two laser beams of different colour. It generated green and blue colour beams, which were used to measure the radial and axial components of the velocity vector respectively. Each of these beams was separated into two parallel beams of equal intensity by beam splitters (Model 9115), which then were polarised orthogonally (Models 9102-11 and 9102-12) to prevent interference in the measuring volume with each other.

[3.5] The fact that the laser beam was coherent meant that all emitted radiation had the same phase, both in space and in time, whereas monochromatic meant that its energy was concentrated in an extremely narrow bandwith (i.e. of one frequency and wavelength).

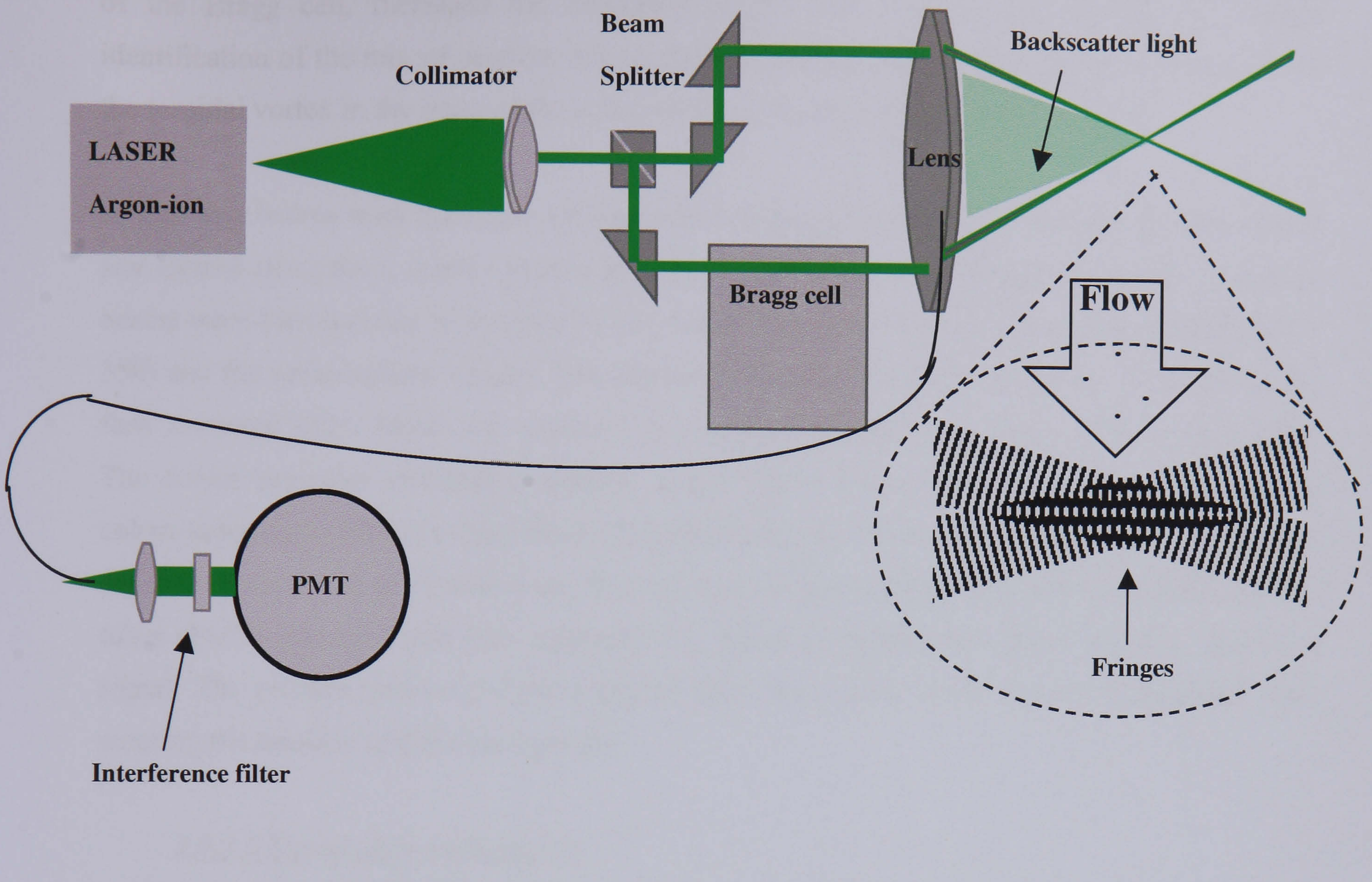

Basic schematic diagram for the 514.5 nm fiber-optic assembly in this work.

Figure 3.10

An acoustic optical cell (Model 9832X), commonly called as Bragg cell (Appendix C) was used to shift the frequency of these beams by 40 MHz (Appendix C). The Bragg cell contained a transparent medium through which the laser beam passed. Continuous passing of ultrasonic sound waves excited the medium. These sound waves (which were also density waves and therefore waves of refractive index) diffracted the laser beam. Since they were moving they also shifted the beam frequency, by an amount equal to the frequency of the sound wave. The frequency shift caused the fringes (see Appendix C for an explanation of the "fringe" model used by the LDV system) in the measurement volume to move at a constant speed depending on the direction of the frequency shift. Stationary particles exposed to these moving fringes produced signals of constant frequency (frequency shift). Particles moving with the fringes produced signals of lower frequency than this and particles moving against the fringes produced signals of higher frequency. The effective shift of the Doppler frequency was selected in the range of 100 KHz to 5 MHz, as required by the velocity range of each channel. The frequency shift, by means

of the Bragg cell, increased the flexibility of the LDV system, by enabling the correct identification of the mix of positive and negative velocities in the expected flow reversal, i.e. in the toroidal vortex in the wake of the cylindrical bluff body and the ventilated cavity.

The four beams were then coupled into a double input coupler. The focus of each laser beam was shifted along the x, y and z axes to achieve optimum coupling into the optical fibre. The four beams were then focused in the flow by the transmitting lens located in the probe (Model 9253-350) and the measurement volume was formed at the intersection of the beams. Particles in the flow scattered light, which was received by a multicolour receiver (Model 9230-3 ColorLink). The colour separator included a dichroic mirror whose angle of reflection provided efficient colour separation and two colour filters (Models 9158 and 9159) one for each of the wavelengths detected. Finally, the two beams were focused onto the pinhole apertures of two photomultipliers tubes (PMT) (Model 9160) (see Appendix C), which converted the optical signal to electrical signal. The pinhole prevented light scattered from other parts of the beams or apparatus from entering the detector and producing noise.

3.9.2.2 Signal processing system

The electrical Doppler signals from each of the two PMTs were received and processed by two digital counter type signal processors (IFA 650) (burst[3.6]correlators). The processors measured the residence time (corresponded to the duration of the scattered signal), t_i (±2 ns), which elapsed for a particle to cross a fixed number of fringes (or as more commonly known a fixed number of cycles) n_{ci} using a high resolution digital clock. The reciprocal value of this time gave the estimated Doppler frequency and thus the particle velocity:

$$f_D = \frac{n_{ci}}{t_i} \tag{3.5}$$

Noise contributions were eliminated or minimised by checking the repeatability of the time for each cycle within the burst. To ensure that only appropriate estimates were made on the sample and that the background noise was reduced, the counter measured the elapsed times for the particle to cross first five and then eight fringes. The two times were then compared. If the

---

[3.6] The term Doppler *burst* essentially describes the current pulse generated by the PMT when, ideally, a single seeding particle crosses the measuring volume.

number of cycles in the measurement, was 8 and the number of cycles used for comparison, was 5, the measurement was validated (accepted) by the processor only when:

$$\Xi \geq 1 - \frac{t_8 \times 5/8}{t_5} \tag{3.6}$$

where Ξ was an accuracy criterion taken as 1%. A thorough description of the operation of the counter type signal processor used in this work is given in Appendix C.

3.9.2.3 LDV traverse system

The LDV provided measurements at a single point in the flow, yet the flow field in the wake of the cylindrical bluff body or the ventilated cavity required multipoint measurements. This was accomplished using a TSI traverse system. The traverse provided accurate, stable positioning for the fibre-optic probe and precise motion in the three orthogonal directions. The mechanical slides on the traverse were constructed of aluminium alloy with a low friction polymer bonded to the sliding surface. A stepper motor and high quality machine screw drove each axis. The computer via an RS232 serial port controlled all three axes of travel. The software control of the traverse positioning allowed absolute and incremental motion for each axis, while a front panel LED display of position provided the relative movement for each axis. The traverse provided up to 600 mm by 600 mm by 600 mm of travel with 0.01 mm resolution.

3.9.3 Experimental considerations

The experimental apparatus of Fig. 3.1 was slightly modified to accommodate the LDV system. The traverse system used to mount the fiber-optic probe was extremely heavy. For this reason it was very difficult to lift it 3 m above the ground and install it underneath the air sparger (see Fig. 3.1). Therefore the cylindrical bluff body and the central sparger were positioned $15D$ further downstream of the location where the spargers were initially positioned during the mass transfer and bubble size measurements.

The operation of the pump induced vibrations in the traverse, which in turn caused the continuous movement of the measuring volume inside the flow reducing the overall spatial resolution of the instrument. To alleviate this problem the traverse was positioned on top of four special rubber-made anti-vibration pads (Mason UK L.t.d.). The special pads absorbed the incoming pump vibrations.

For safety reasons the space around the traverse and the downcomer pipe at the measuring point was sealed with thick (2.5 mm) black curtains to ensure that the laser light did not escape. The maximum laser power used during the LDV measurements was 2 W. This value was chosen, following the advice of the TSI Inc. technical support team, because it provided a good signal to noise ratio (SNR) for the experimental conditions under investigation. A higher laser operating power was not used for safety reasons.

3.9.3.1 The dimensions of the measuring volume in air

The size of the measuring volume was an important parameter than needed to be determined for the application of the LDV. The measuring volume needed to be small enough so that good spatial resolution of the flow in the wake of the cylindrical bluff body or the ventilated cavity would be achieved. For this reason the two laser beams were aligned to cross at the position of their waists, i.e. the location along the beam where the cross-section was the smallest. This configuration produced the best scattering intensity for the PMT (TSI, 1993). The probe used in this work (Model 9252-350) was factory-manufactured to provide beam crossing at the location of the beam waist.

The TSI laser setup produced a Gaussian intensity distribution across the laser beam at all cross-sections (TSI, 1993). The measurement volume of the LDV system was an ellipsoid and its edges were defined as the points where the amplitude of the Doppler signal was $\frac{1}{\varsigma^2}$[3.7] of its centreline value where ς was the maximum combined beam light intensity in the measuring volume. The dimensions of the measuring volume depended on the laser wavelength and the optic parameters. The physical dimensions of the measuring volume are given by the following equations and shown in (Fig. 3.11) (TSI, 1993):

$$\delta_{ya} = \frac{4F_a\lambda_a}{\pi d_{\varsigma^{-2}}} \qquad \text{[Width of the measuring volume]} \qquad (3.7)$$

$$\delta_{xa} = \frac{\delta_{ya}}{\cos\kappa_a} \qquad \text{[Height of the measuring volume]} \qquad (3.8)$$

[3.7] For example if the beams had an approximate combined power of 100 mW but focused to form a measuring volume of 1mm in diameter, then the light intensity in the measuring volume would have been approximately $0.1/0.001^2 = 100{,}000$ W/m^2.

$$\delta_{za} = \frac{\delta_{ya}}{\sin \kappa_a} \qquad \text{[Length of the measuring volume]} \qquad (3.9)$$

where δ_{xa}, δ_{ya}, δ_{za} were the height, length and width of the measuring volume respectively, κ_a was the half angle of the beam pair in air, $d_{\varsigma^{-2}}$ was the diameter of the focused laser beams at their waist, F_a was the focal distance in air and λ_a was the wavelength in air. The half angle of the beam pair was related to the fringe spacing in air, δ_{fa}, by:

$$\delta_{fa} = \frac{\lambda_a}{2 \sin \kappa_a} \qquad (3.10)$$

The manufacturer provided the factory values for the δ_{fa}, F_a λ_a and $d_{\varsigma^{-2}}$. The rest of the optical parameters were then calculated from Eqs. (3.7) – (3.9) and the results are given in Table 3.3.

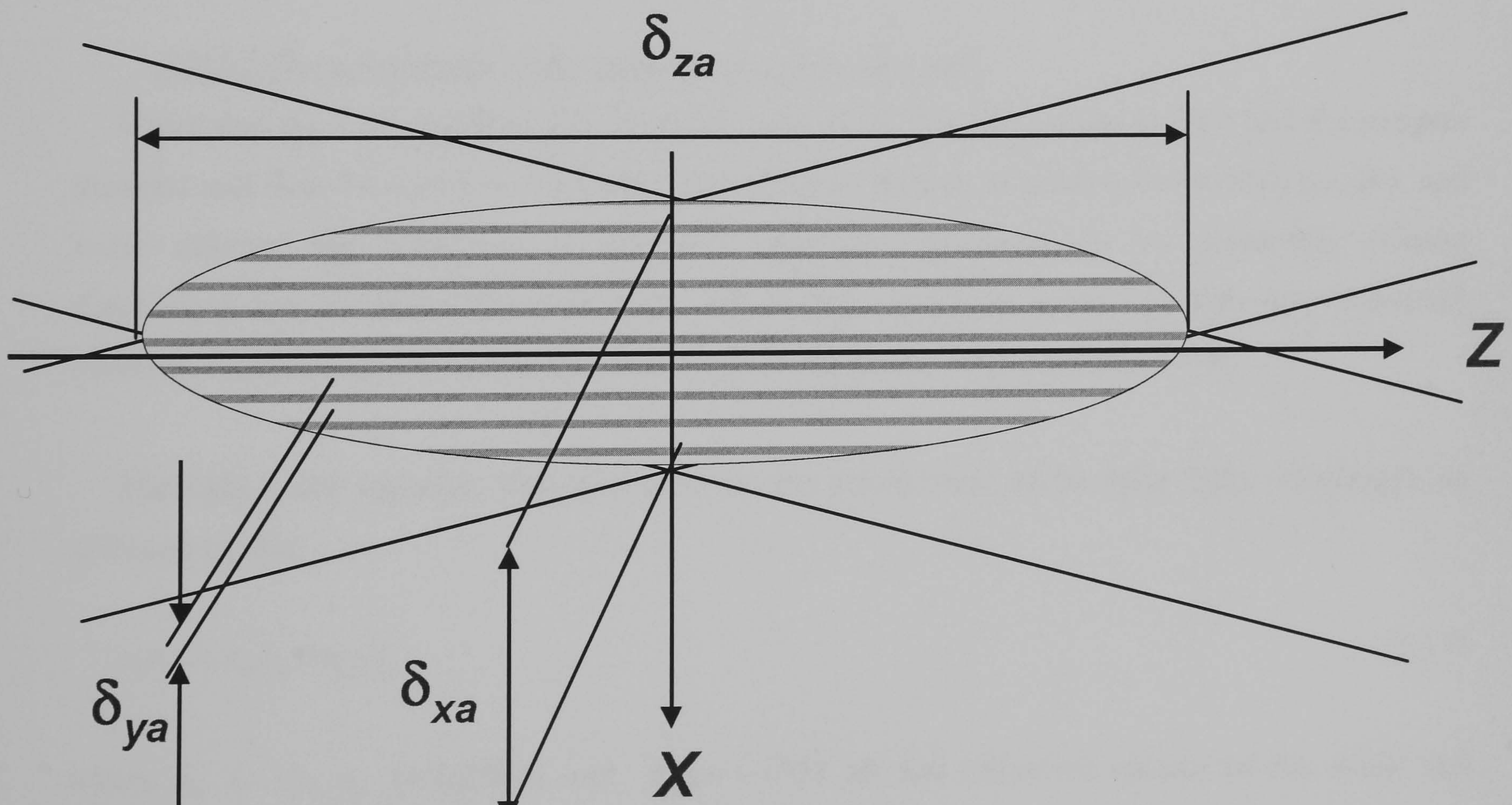

Schematic diagram of the measuring volume dimensions in air.

Figure 3.11

Medium: Air	Green colour	Blue colour
Wavelength, λ_a (nm)	514.5	488
Probe beam diameter at the beam waist, $d_{\varsigma^{-2}}$ (mm)	2.82	2.82
Fringe spacing, δ_{fa} (μm)	3.704	3.513
Focal length in air, F_a (mm)	350	350
Beam half angle in air, κ_a (°)	3.983	3.983
Height, δ_{xa} (mm)	0.081	0.077
Width, δ_{ya} (mm)	0.081	0.077
Length, δ_{za} (mm)	1.171	1.110

LDV measuring volume dimensions in air.

Table 3.3

3.9.3.2 The dimensions of the measuring volume in water

Water was the working fluid used in the present work. The laser beam passed first the perspex material and then focused into the water. The different indices of refraction between perspex and water affected the behaviour of the laser beam and consequently the measuring volume dimensions and the actual focal distance. The fringe spacing in water was also very important because it determined the recording parameters in the control software FIND 1.4.

The light speed equation was used to relate the dependence of the laser light wavelength on different media:

$$n_a \lambda_a = n_w \lambda_w = n_p \lambda_p \tag{3.11}$$

where $n_a \ (=1)$, $n_w \ (=1.3384)$ and $n_p \ (=1.495)$ are the refractive indices of air, water and perspex. The fundamental equation of Snell's law (Eq. 3.12) was used to relate the change of the half angle of a beam pair during its passage through different media.

$$n_a \sin \kappa_a = n_w \sin \kappa_w = n_p \sin \kappa_p \tag{3.12}$$

where κ_w and κ_p were the half angle of the beams in water and perspex respectively. By substituting the indices of water and perspex the half angle between a laser beam pair in water and perspex were found. The fringe spacing in water remained constant and independent of the type of medium. From Eq. (3.10) the fringe spacing was given by:

$$\delta_{fw} = \frac{\lambda_w}{2\sin\kappa_w} \tag{3.13}$$

Combination of Eqs (3.11), (3.12) and (3.13) yielded the following:

$$\delta_{fw} = \frac{\lambda_w}{2\sin\kappa_w} = \frac{\lambda_a}{2\sin\kappa_w}\frac{n_a}{n_w} = \frac{\lambda_a}{2\sin\kappa_w}\frac{\sin\kappa_w}{\sin\kappa_a} = \delta_{fa} \tag{3.14}$$

To find the actual focal distance in water, F_w the following equation was used (TSI, 1993).

$$F_w = F_a\frac{\tan\kappa_a}{\tan\kappa_p} + b_p\left[1-\frac{\tan\kappa_p}{\tan\kappa_w}\right] + L_D\left[1-\frac{\tan\kappa_a}{\tan\kappa_w}\right] \tag{3.15}$$

where b_p is the thickness of the perspex water box and L_D is the distance from the transmitting lens to the perspex surface. The optical parameters in water are shown in Table 3.4.

Medium: Water	Green colour	Blue colour
Beam half angle in water, κ_w (°)	2.974	2.974
Beam half angle in perspex, κ_p (°)	2.663	2.663
Actual focal length in water, F_w (mm)	382	382
Height, δ_{xw} (mm)	0.066	0.063
Width, δ_{yw} (mm)	0.066	0.063
Length, δ_{zw} (mm)	1.280	1.213

LDV measuring volume dimensions in water.

Table 3.4

3.9.3.4 Pipe curvature

Making measurements through a pipe using an LDV poses more problems than measuring through a flat window. There are changes in the refractive index and the pipe acts as a cylindrical lens. A cylindrical lens focuses light in the cross-sectional plane, (the plane perpendicular to the cylindrical axis) but does not focus along the parallel plane (the plane parallel to the cylindrical axis). As a result the location of the measurement volume moves and the amount of scattered light that can be collected by the receiving optics is generally reduced. In a two-component system, if one beam pair is aligned with the cylindrical axis, each beam in the beam-pair crosses, but the two beam pairs do not cross at the same location. Each pair of beams is refracted differently and problems arise when the intersection volume of each beam pair is at different locations in the pipe. The two different measurement volumes, one for each velocity component, are then separated and the LDV velocity measurements do not correspond to the same point in the flow.

To minimise these problems the sealed perspex box with a flat window that was built for the bubble size measurements was fitted on the perspex pipe. This kind of box has been used for many years to reduce optical distortion. Recently, Vial et al. (2005) used such boxes when measured the liquid velocities in an external-loop air-lift reactor with LDV. The box was filled with water substantially reducing the refractive index mismatch at the pipe outer wall (TSI, 1993) (Fig. 3.12).

3.9.3.5 Measurement procedure

It was possible to obtain a 3-D velocity distribution across the pipe's diameter for each axial position below the bluff body or the ventilated cavities, by traversing the measuring volume across the x and y axis (Fig. 3.13). The axial $V_{z(x)}$ and the V_x (velocity component in the x direction) velocity components were measured by traversing across the x axis; traversing across the y axis, enabled the measurements of the axial $V_{z(y)}$ and the V_y (velocity component in the y direction) velocity components. Since the measuring volume was traversed across the pipe's diameter, then the measured velocity components of V_x and V_y could be related in cylindrical polar coordinates to the radial, V_r and azimuthal, V_θ velocity components respectively.

Direct measurements could be made when traversing along the x axis (Fig. 3.13). On the other hand, when traversing along the y axis the actual movement of the measuring volume, Δy, in water $(n_w = 1.3384)$ was different from the probe traversing distance in air $(n_a = 1)$ Δl. This is the effect commonly known as the real and apparent depth problem. When two light beams

originate in an optically thinner medium and crossed inside an optically denser one, then displacement of the crossing point occurs and the following relationships can be established (Durst et al., 1981).

$$\frac{\Delta l}{\Delta y} = \frac{\tan \kappa_a}{\tan \kappa_w} = \frac{\sin \kappa_a}{\sin \kappa_w} \times \sqrt{\frac{1-\sin^2 \kappa_w}{1-\sin^2 \kappa_a}} \tag{3.16}$$

where κ_a and κ_w are the half angle between the two intersecting beams in the media of air and water, Δy is the movement of the measurement volume in water and Δl is the probe traversing distance in air. In this work the two half angles were very small and differed only one degree between them (Tables 3.3-3.4). Thus, one then can accurately approximate Eq. (3.16) as:

$$\Delta l = \frac{\tan \kappa_a}{\tan \kappa_w} \Delta y \tag{3.17}$$

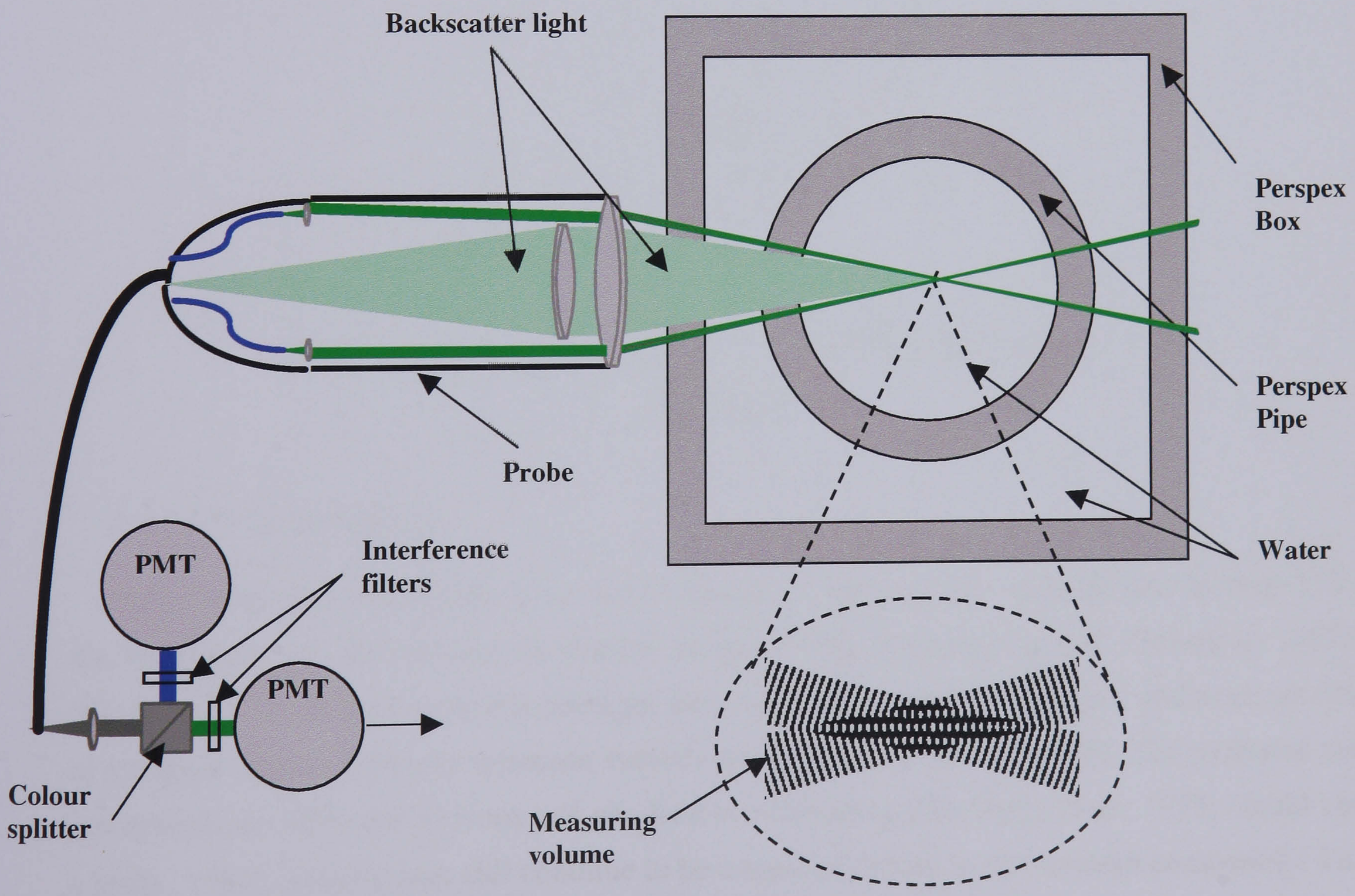

Schematic diagram of the water box assembly and the backscatter LDV mode.

Figure 3.12

These half angles between the intersecting beams can also be related through Snell's law (Eq. 3.12). Following Sun et al. (2002) who combined Eqs. (3.12) and (3.17) to eliminate κ_a and κ_w and using the values of the refractive index given above, the following coordinate correction was obtained and applied in the present experiment:

$$\Delta l = 1.332 \Delta y \tag{3.18}$$

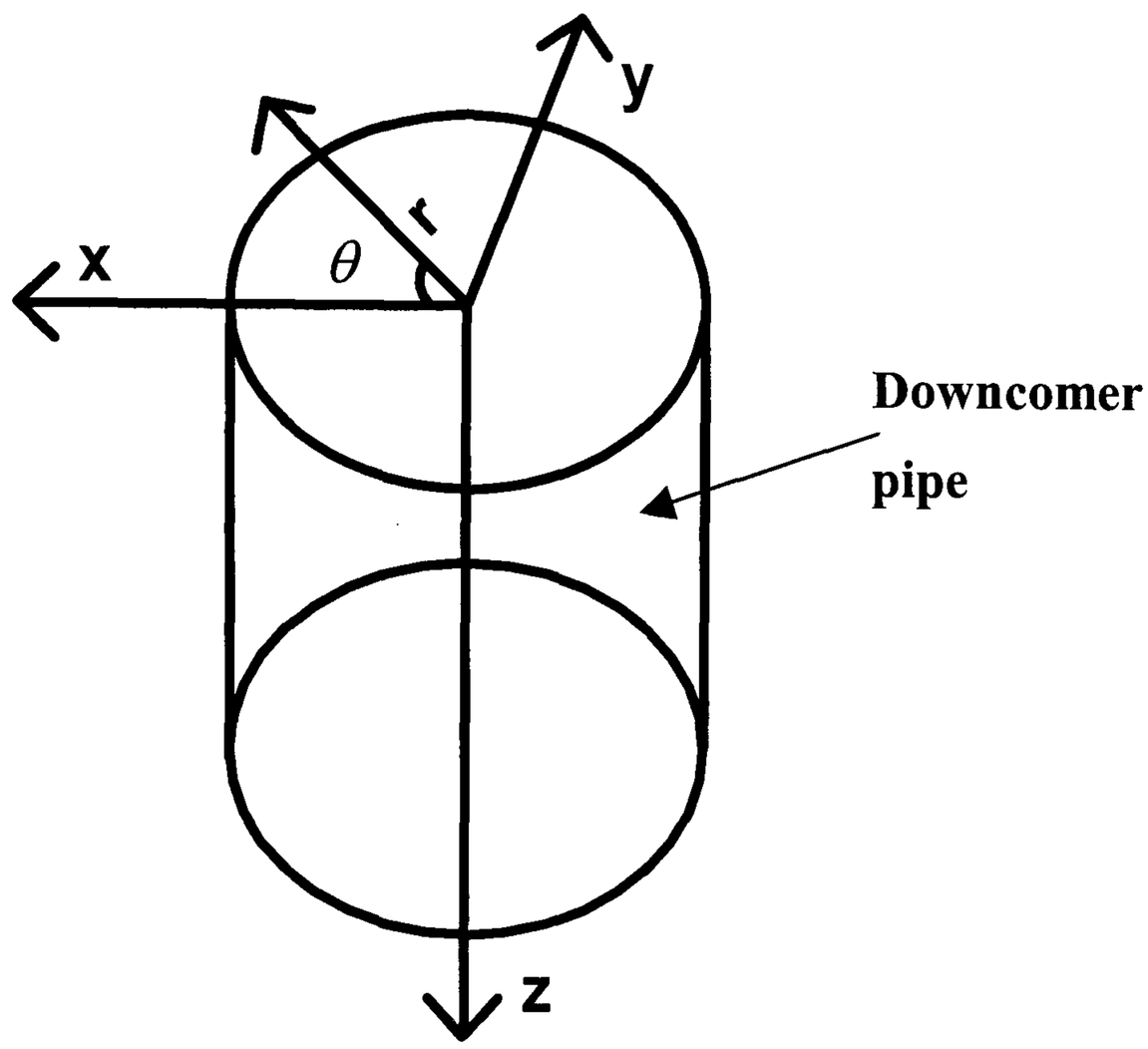

Coordinate systems: cartesian (*x, y, z*) & cylindrical polar (*r, θ, z*).

Figure 3.13

3.9.4 LDV uncertainties

Many studies in the literature do not comment on the possible uncertainties in their LDV measurements (as for instance in Becker et al., 1999). McLaughlin and Tiederman (1973) studied the formation of ensemble averages from LDV bursts signal processors and were the first to recognise issues of bias in the mean velocity and turbulence measurements. The problems and corrections are often not obvious and can lead to misleading (Buchhave et al., 1979; Gould and Loseke, 1993). These issues still continue to be a topic of debate in the research community. The following sections discuss the relevant biasing problems for the present study.

3.9.4.1 Velocity bias

The LDV measurements in this work were carried out in burst mode, which operated on signals generated by single particles passing through the measuring volume and measured the velocity of the particle while it was in the measuring volume. Averaging the measurements to get for example the mean velocity would give the wrong answer. This arose from the fact that the number of particles going through the measuring volume per unit time was higher at high velocities than at low velocities. Hence simply averaging all of the data points taken during the measurement would bias the derived statistical properties towards the high velocity end. This is a problem commonly known in LDV practitioners as "velocity bias".

The velocity bias problem was expected to increase by the level of turbulence and had to be taken into account during the LDV measurements in the turbulent wake of the cylindrical bluff body or the ventilated cavity. The solution to the velocity bias was to weight the individual measurements with a factor inversely proportional to the probability of making the measurement. The transit time weighted average was used (McLaughlin and Tiederman, 1973; Asalor and Whitelaw, 1976). In the literature this term is often called residence time. This correction was built as a tool in the control software Find 1.4 supplied by TSI Inc., in the form of Eq. (3.19). All first moment statistical quantities (mean velocity, variance, root means square) in this work were calculated as transit time weighted results to eliminate the effects of the velocity bias.

$$\vec{\bar{U}} = \frac{\sum u_i \tau_i}{\sum \tau_i} \tag{3.19}$$

3.9.4.2 Fringe bias

Fringe bias (also called angular bias) stems from the fact that several fringe crossings (i.e. a minimum number of fringes) are needed in order to validate a measurement, so a particle passing through the measuring volume at a large angle may not be registered. In flows with considerable changes in the direction of the velocity vector (such as the flows in the wake of a ventilated cavity or cylindrical bluff body - see chapter 4), particles approaching a direction parallel to the fringes will lead to insufficient fringes being present in the burst. Therefore it was important in the present work that the validation circuit rejected these particles. Bragg shifting the beams, so the fringes were moving relative to the flow obviated this problem. In addition there was no variation in the measuring volume projected cross-sectional area (e.g. beam steering) for the flow conditions examined in this study. Thus negligible fringe bias was expected during the measurements.

3.9.4.3 Velocity gradient bias

Due to the finite size of the measuring volume, LDV data are not quite point measurements but measurements integrated in space over the measuring volume. The velocity gradient broadening occurs when a scattering volume of finite size covers a region of the flow, where there is a mean velocity gradient (Durst et al. 1995). As a result, particles traversing the scattering volume have a range of velocities. Durst et al. (1998) developed correction formulae to correct for velocity gradient bias. However, they mentioned that the effect of streamwise turbulence intensity was negligible for $y^+ \geq 15$, where y^+ was the non-dimensional normal distance from the pipe wall. In the present work, measurements were taken for $y^+ \geq 30$.

Another important consideration was that the flow in the wake of both the cylindrical bluff body and the ventilated cavity has been suggested to be that of a toiroidal vortex (Thorpe et al., 2001). This type of flow is generally characterised by steep velocity gradients. Therefore to make accurate measurements with the LDV the spatial resolution of the technique must had been able to resolve any bias due to velocity gradients. Considerable error may be introduced when the probe volume length is of the order of the vortex radius (AIAA, 1995).

However, the simulations of Thorpe et al. (2001) showed that the vortex in the present work was expected to be very large (almost the size of the pipe) and much greater than any turbulence length inside the pipe. It is then safe to speculate that the steep and huge velocity gradients found in small coherent vortex rings (i.e. as in exit of small orifices in aerodynamics) might not be present in the vortex beneath the cylindrical bluff body and the ventilated cavity.

Nevertheless, the above possible problem was checked with a quick literature review. Martin et al. (2000) investigated the vortex in the wake of a sub-scale helicopter rotor operating in hover and they found that a probe volume length of $0.1r_0$ was required to reduce the error due to velocity gradients to less than 0.1% over the entire velocity profile. In their CFD simulations Thorpe et al., (2001) found that the radius of their vortex was 16.3 mm. The length of the LDV measurement volume in water during the experiments in the direction of the high velocity, i.e. the axial was 1.213 mm (Table 3.4). That means that the probe volume length was expected to be $0.074r_0$ i.e. less than $0.1r_0$. Therefore the spread in the velocities was considered insignificant, resulting in a negligible spread in the Doppler frequency. Hence, the correction formulae suggested by Durst et al. (1998) for this phenomenon were not applied in this work.

3.9.4.4 Others: frequency bias and errors due to noise

The measured frequency of the LDV bursts, which depended mainly on laser wavelength and the cross-angle of the beams, could introduce some errors. Allthough the error associated with wavelength for the Argon laser was negligible, the beam crossing angle (which was determined by the beam spacing and the lens focal length) can introduce an uncertainty of 1% in the real velocity (Degraaf, 1999). This error was a systematic error one in this work since the optical configuration was unvaried and affected all measurements equally.

Electronic noise resulting from signal processing equipment as well as light scattered from small impurities on the perspex pipe wall or the perspex box could give an erroneous contribution to LDV measurements. Durst et al. (1998) have treated such errors and showed that the effect of electronic noise is negligible for $y^+ \geq 2$. In the present work, measurements were taken for $y^+ \geq 30$ and therefore no corrections were made to account for errors due to electronic noise.

3.9.5 Seeding particles

Seeding was an important consideration during the LDV measurements in this work since the seeding particles were the flow velocity probes. Physical and geometrical properties of the seeding particles can generally influence the quality of signals supplied to the PMT. Ideally, the seeding particles should be neutrally buoyant in the fluid, provide adequate scattered light intensity for detection, have large enough number concentration and have uniform properties from particle to particle.

TSI metallic coated particles (Model 10087) were used as seeding particles. They were spherical in shape with a mean diameter of $d_p = 12$ μm and a geometric standard deviation of $\sigma_p = 1.6$. It was also important that these particles to have no significant effect upon the flow. Since the LDV was actually measuring the velocity of the seeding particles, the terminal settling velocity of the particles was initially estimated to determine the importance of any slip effects due to the physical presence of the particles in the flow. For spherical particles of diameter d_p, the terminal or free settling velocity u_t, at low Re is given by (Perry and Green, 1999):

$$u_t = \frac{g d_p^2 \left(\rho_p - \rho_L\right)}{18 \mu_L} \tag{3.20}$$

where ρ_L was the water density; g is the gravitational acceleration and μ_L was the viscosity of water. The terminal velocity of the particles was $u_t = 1.25\times10^{-4}$ m s^{-1}, the particle Reynolds number $\left(\mathrm{Re}_p = \frac{d_p \rho_L u_t}{\mu_L}\right)$ was 1.5×10^{-4} and therefore the particles were in the Stokes regime. Since the velocities of the experiments were of the order of 1 m s^{-1}, the seeding particles used in the present study were used successfully to follow the liquid-phase motion without significant error.

3.9.6 LDV in the bubbly flow below the ventilated cavity

The application of the LDV in the bubbly flow beneath the ventilated cavities was not as straightforward as in the single phase measurements beneath the cylindrical bluff body for two reasons: (i) the bubbles also scattered, reflected and refracted light that could be interpreted as liquid phase velocity information by the LDV system and (ii) the bubbles blocked the optical path of the beams reducing the data rate in the signal processor leading to insufficient data for the r.m.s. calculation. These two problems were taken into account before any measurements were conducted in the wake of the ventilated cavities.

Guet et al. (2004) stated that the LDV technique could provide meaningful liquid velocity results in bubbly flow, as long as the gas void fraction was low and the bubble size was large compared to the measuring volume. Velidandla et al. (1996) applied a backscattering LDV system in bubbly flow and found that the bursts of the seeding particles could be well separated from those of bubbles by using different frequency shift and PMT voltage values. Mudde et al. (1998) have shown that for low gas void fractions the LDV when operated in the backscatter mode predominantly measured the velocity of the liquid and that phase discrimination based on burst amplitude offered no significant improvement.

Sun et al. (2004a), Sun et al. (2004b) and Sun et al. (2003) managed to get accurate measurements of the liquid velocity in a downward two-phase bubbly flow. They found that for an average gas void fraction of less than 8.5%, the bursts of the seeding particles could be well separated from those of the bubbles without any further signal discrimination requirements by using enough seeding particles (the ratio of the seeding particle number concentration to the bubble number density was of the order of 100), high laser power to increase the beam intensity scattered by the seeding particles and a high Photomultiplier tube (PMT) voltage (around 1150 V) so they could detect the light scattered by the seeding particles. In this way the fraction of

bursts by number from bubbles in the original signals was negligible compared to that from small seeding particles.

A similar approach was adopted for the measurements beneath the ventilated cavities in this work. The LDV setup was operated in backscatter mode so predominantly the liquid velocity was measured (Mudde et al., 1998). The measurements were conducted for 1% and 2% average gas void fractions (see section 4.4.3). The ratio of the seeding particle number concentration to the bubble number density was of the order of 100 (the number of bubbles was estimated from photographs). The PMT voltage was set at 1200 V so the light from the seeding particles was also detected. A laser power of 2 W was used during the measurements to increase the beam intensity scattered by the seeding particles. The LDV system was set to collect a huge number of particles (200,000) in a 500 sec window, so that contributions from the bubble interfaces were always swamped in the data analysis. Finally, the signal scattered by large bubbles (at least three times the size of the measuring volume length), which may not follow the flow correctly were automatically rejected by the signal processor by the use of a high-pass filter that was used to remove the pedestal[3.8], setting an upper limit to the pedestal amplitude accepted (Lee and Durst, 1982) (Appendix C). The average bubble size in this work was measured around 3 mm work, i.e. almost three times the measuring volume length (see Chapter 5). The signal processor automatically rejected the relative contributions from these larger bubbles.

3.10 SLUG VELOCITY IN DOWNWARDS FLOW

The aim of the experiments was to determine the slug bubble velocity in downwards two phase slug flow, for various liquid superficial velocities, j_L. This was done by measuring the time needed for a single slug bubble to rise (or descend) between two planes at known distance apart (1 m) (time of flight) (Fig. 3.14). The slugs were created by natural entrainment. Other researchers have also used this method (Martin, 1976; Thorpe et al., 1989). The experimental procedure was as follows. Using the ball valve, the flow was slowed down, until a point was reached that a single air slug managed to slip into the downcomer. When the slug had clearly entered the pipe the liquid flow rate was altered (increased or decreased) allowing the investigation of slug speeds at different values of j_L. A length of $20D$ from the bottom up and a

---

[3.8] The pedestal wave results from the intensity increase and decrease of the scattered light when a particle crosses the measuring volume (see also Appendix C).

length of 16*D* from the flow straightener down was allowed before any measurements were taken to compensate for any secondary effects due to entry effects. Two different perspex downcomer sections were used with internal diameters of 0.105 m and 0.050 m respectively. Two different adaptors were placed, at the top of the perspex downcomer in order to gradually increase the internal pipe diameter from 0.098 m to 0.105 m or to decrease it from 0.098 m to 0.050 m (Fig. 3.1). The two downcomer sections stopped one pipe diameter above the liquid level in the tank.

In order to minimise the experimental error, two mirrors were installed adjacent to the downcomer at the measuring points, as shown in Fig. 3.14. The mirrors allowed simultaneous alignment of the eyes and lines on the pipe in two planes reducing the possibility of parallax error.

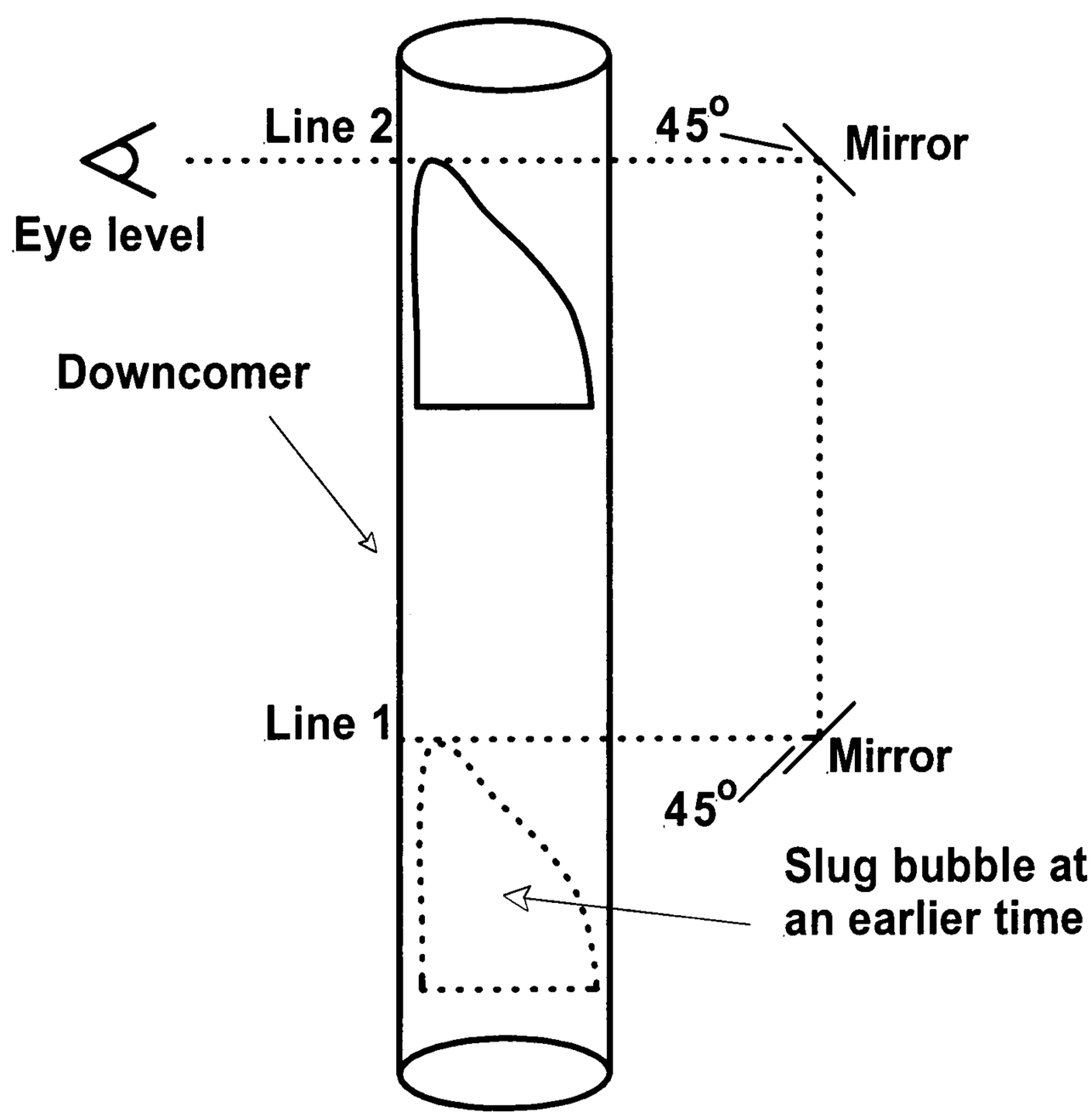

Method of slug velocity measurement, where line 1 is the start point of measurement and line 2 is the finish point of measurement.

Figure 3.14

The positioning of the slug at each plane had an uncertainty of ± 0.015 m. The slug velocity was measured using a stopwatch. The timing had an uncertainty of ± 0.1 s. These errors were

quantified and are shown as errors bars in the experimental figures of Chapter 6. The times taken with the stopwatch were compared (to double-check their validity) with the results obtained using an analog-digital card (Amplicon, Model PC27E, 16 channel 12 bit board) that was bought after the first set of experiments was carried out. The data were processed using the software HP Vee Pro 6. The return signal from the magnetic flowmeter was sampled from the A/D converter at a sampling frequency of 25 kHz and stored in a data file. Specific values of the superficial liquid velocity were stored with a single mouse click. The time elapsed between two clicks was calculated from the software. Good agreement between the two methods of timing was found (within ± 3 %).

*CHAPTER 4

WAKE VELOCITY FIELD

4.1 INTRODUCTION

In terms of the operational performance of gas-liquid contacting devices where a ventilated cavity is present, it is important to be able to predict the gas dispersion characteristics of the cavity. However our understanding of the hydrodynamics at the base of such cavities is still very limited. In particular the mechanism by which small bubbles are torn off the cavity, i.e. the entrainment process is still unclear. Therefore, to try and improve our understanding of this process a thorough investigation is presented in this chapter through the application of laser based optical techniques to measure the liquid velocities in the wake. These measurements can then be used to investigate if available mathematical models are consistent with what is observed. It is hoped that the results presented in this chapter will contribute to an indepth view of the multiphase dynamics of ventilated cavities attached to spargers in downwards flow.

4.2 WAKE VELOCITY FIELD SIGNIFICANCE

The velocity field has never been measured. Therefore information on the velocity field in the wake of a ventilated cavity is essential to provide a more detailed analysis of the rate of entrainment. The turbulence within the wake flow enhances the breakup and coalescence of the entrained gas resulting in a concentrated dispersion of bubbles immediately below the cavity. The extent (length) of the wake and the nature of flow within it, will determine the occurrence of breakup and coalescence events, producing a resulting bubble size and gas void fraction (Evans

---

* Some of the the results of this chapter have been published in:

Sotiriadis, A. A., Thorpe, R. B., Kirkby, N. F. and Rockliff, N., (2004), Liquid recirculation beneath a ventilated cavity in a vertical pipe, *3rd International Symposium on Two-Phase Modelling and Experimentation*, Pisa, Italy, September, ISBN 88-467-1075-4, Paper BJA09.

Sotiriadis, A. A. and Thorpe, R. B., (2005), Liquid recirculation in turbulent vertical pipe behind a cylindrical bluff body and a ventilated cavity attached to a sparger, *Chemical Engineering Science*, **60**, 981-994.

et al., 2004). The downstream length of the wake is of interest as it defines the volume of fluid where there are higher rates of energy dissipation, relative to that of pipe flow without the cavity present.

Delfos et al. (2001b) showed that almost 50% of the entrained bubbles were recycled back to their fixed Taylor bubble depending on the operating conditions (gas and liquid flow rates). Hence, analysis of the velocity field in the wake of the cavity is important to be able to model the recoalescence flux of the gas. If this flux is known then the average gas void fraction can be predicted as in models like Fernandes (1983).

In many aspects the flow phenomena of a ventilated cavity resembles that of a moving slug bubble inside a pipe (see section 2.5). Fabre and Line (1992) commented on the importance of the wake field for slug flow. Polonsky et al. (1999) commented that detailed knowledge of the flow field in the wake of a slug bubble was essential in order to model undeveloped and transient slug flow in entry regions as well as in terrain slugging observed in pipe of varying inclination. Also the flow in the wake of these large bubbles is largely responsible for determining whether subsequent bubbles will overtake and eventually coalesce with the preceding bubble (Pinto and Campos, 1996). As a result, this behaviour determines the size of the bubbles and the liquid slugs. The length in the wake of a slug bubble determines the minimum distance between gas slugs beyond which there is no interaction, i. e., the distance behind a single gas slug for which the liquid becomes motionless. Zukoski (1966) reported that when two Taylor bubbles rise with a short separation, the flow disturbances in the wake of the leading bubble can cause large scale distortions of the trailing bubble which lead to an increase in the rise velocity of the trailing bubble and coalescence of the two bubbles. The slug catcher design in the petroleum industry depends on empirical experience, mainly on the longest encountered slug. Therefore to get a better understanding of the mechanism of coalescence, the knowledge of the flow field in the wake of the leading Taylor bubble becomes essential.

Slug flow has lately found wide applicability in cross flow filtration (Taha and Cui, 2002). Cross flow filtration is a very useful downstream process in the food and biochemical industries. However, the decrease in the permeate flux caused by the internal and external fouling of the membrane limits its industrial development. High wall shear stresses and unsteadiness were found to be good hydrodynamic conditions to improve the performances of the filtration. Such hydrodynamic conditions are found in gas-liquid slug flow where both natural intermittence and high velocity are capable to erode the cake or limit its growth. However, information of the

turbulence level in the slug wake is among the parameters needed to control the intermittence and enhance the flux across the filtering membrane.

Slug flow is also the preferred flow regime in structured catalysts called monolithic reactors (Bauer et al., 2005; Kapteijn et al., 2005; Bercic and Pintar, 1997). The rate of mass transfer in these reactors is high when they are operated in the slug flow regime. According to Kapteijn et al. (2005) for multiphase operation of the reactor under slug flow conditions the mass transfer increase is an order of magnitude larger than for single-phase liquid flow, whereas the increase in friction, that is pressure drop, is much less. Kapteijn et al. (2005) comment that the intense liquid circulation in the liquid slug combines very good local mixing and is especially beneficiary for mass transfer. Therefore to model the hydrodynamic behaviour of the reactors information is needed in the flow field of the liquid slugs.

The associated vortex structure believed to exist beneath a ventilated cavity (Thorpe et al., 2001) is shown in (Fig. 4.1). Experimental data on the wake of such cavities in pipes are scarce. Direct measurements of the velocity field in the wake of such cavities are difficult because (1) there are bubbles present in the flow that would interfere and induce noise in any experimental instrument and (2) the cavity bottom oscillates. Polonsky et al. (1999) showed that for a slug bubble the amplitude of the oscillations increased with increasing bubble length. Van Hout et al. (2002) who used Particle Image Velocimetry (PIV) to describe the flow field around a single slug bubble rising in a vertical pipe filled with stagnant water, commented that it would be instructive in this context to consider measurements in turbulent wakes of solid bluff bodies in pipes.

A thorough literature survey had shown that there were no reports in the literature of velocity measurements in the turbulent wake of confined cylinders. Taylor and Whitelaw (1984) used LDV to study the effects of blockage ratio (ratio of bluff's body area to pipe's cross sectional area) and geometry on the velocity characteristics in the wakes of two confined axisymmetric disks and a cone with blockage ratios of 25%, 50% and 25% respectively. They found that the recirculation length (defined as the distance where the axial velocity component became zero) and the maximum centerline velocities increased with increasing blockage ratio. A doubling of the blockage ratio between the two disks increased the recirculation length from $0.8D$ to $1.55D$ and the location of the vortex eye from $0.45D$ to $0.6D$. According to the simple model of Thorpe et al. (2001) described next, both these lengths should scale as the diameter of the obstruction, i.e. 1 to $\sqrt{2}$.

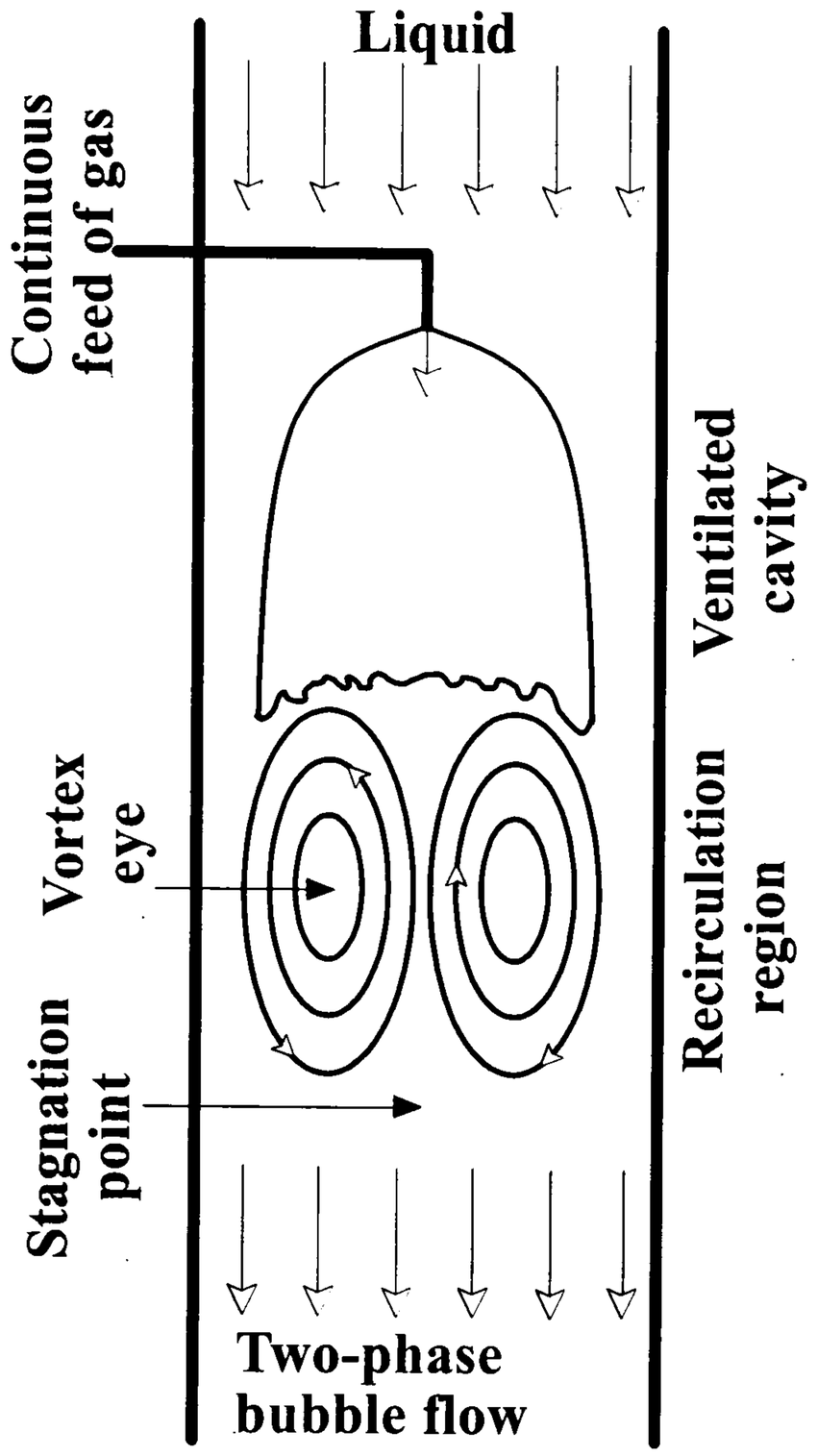

(a) Flow geometry for ventilated cavity and recirculation region; (b) Definition of various parameters associated with the vortex.

Figure 4.1

For the ventilated cavity, H_2 refers to the stagnation point and δ to Eq. (4.14).

4.3 HILL'S VORTEX APPROACH

Thorpe et al. (2001), have proposed a simple model of the recirculation region beneath a ventilated cavity. In this model, a ring vortex was held stationary beneath the cavity. Hill (1894) gives the Stoke's stream function, ψ, for this kind of vortex as:

$$\psi = \frac{Br^2}{10}\left(a^2 - z^2 - r^2\right), \tag{4.1}$$

where r is the radial co-ordinate, a is the radius (half the lateral size) of the vortex, z is the axial (vertical) coordinate measured from the lateral plane of symmetry of the vortex and B is related to the irrotational motion outside the vortex by a velocity potential which is that due to a rigid sphere moving through ideal fluid with propagation speed, $U = \frac{2Ba^2}{15}$ and it is also related to the vorticity ω of the flow since $\omega = Br$. This velocity field is an exact incompressible solution to Euler's axisymmetric inviscid fluid equations.

The velocity profile of the re-circulating vortex was derived by assuming that the maximum axial velocity inside the vortex, $V_{z(\max)}$, occurred at the outer boundary taken to be at $r = (R - \delta)$, where δ is the falling film thickness at the base of the cavity (Fig. 4.1). It was proposed that the axial component was directly proportional to the velocity of the liquid falling film, V_F, which plunged at the base of the ventilated cavity.

$$K \equiv \frac{V_{z(\max)}}{V_F} = 0.38 \tag{4.2}$$

Eq. (4.2) was established by Computational Fluid Dynamics (CFD) based on a *k*-epsilon turbulence model using CFX and was experimentally confirmed for a ventilated cavity by velocities deduced from a high-speed video camera of small bubbles entrained at the base of ventilated cavities. The value of $K = 0.38$ was obtained for all their simulations and was just consistent with other studies in the literature from which values for K ranging from 0.4-0.55 were deduced (Thorpe et al., 2001). The velocity profile within the internal vortex of the re-circulation region was obtained by differentiation of Eq. (4.1) and by reference to the size of the vortex given by Thorpe et al. (2001), which was for example:

$$V_{z(r=0)} = \frac{B}{5}\left[(R-\delta)^2 - 2r^2\right] \tag{4.3}$$

$$V_{z(r)} = -KV_F\left[1 - 2\left(\frac{r}{R-\delta}\right)^2\right] \tag{4.4}$$

An interesting result from the CFX simulations of Thorpe et al. (2001) was that the velocity field in the wake of a cylindrical bluff body, was similar when modeling its base as a free surface (corresponding to a gas cavity) or a fixed surface (corresponding to a cylindrical bluff body)

(Fig. 4.2). This implies that the base of a cylindrical bluff body resembles the base of a ventilated cavity attached to a sparging device when little or no gas is being entrained. This is an unexpected result since there are some fundamental differences in the hydrodynamics between a cylindrical bluff body and a ventilated cavity attached to a sparger. The absence of interfacial shear at the ventilated cavity interface would result in the development of a different velocity profile in the falling liquid film compared to the one in the annulus between the cylindrical bluff body and the pipe wall. Because of that the momentum flux forcing the flow at the base of the bluff body and the cavity would be slightly different. The oscillatory motion of the bottom of the ventilated cavity due to the gas shed from its base and the presence of the bubbles might also influence the vortex structure in the wake. Moreover the flow in the wake (the standing vortex) has a no-slip boundary condition at its top-side but that would not be expected to influence the velocity field for the high Re used in their simulations.

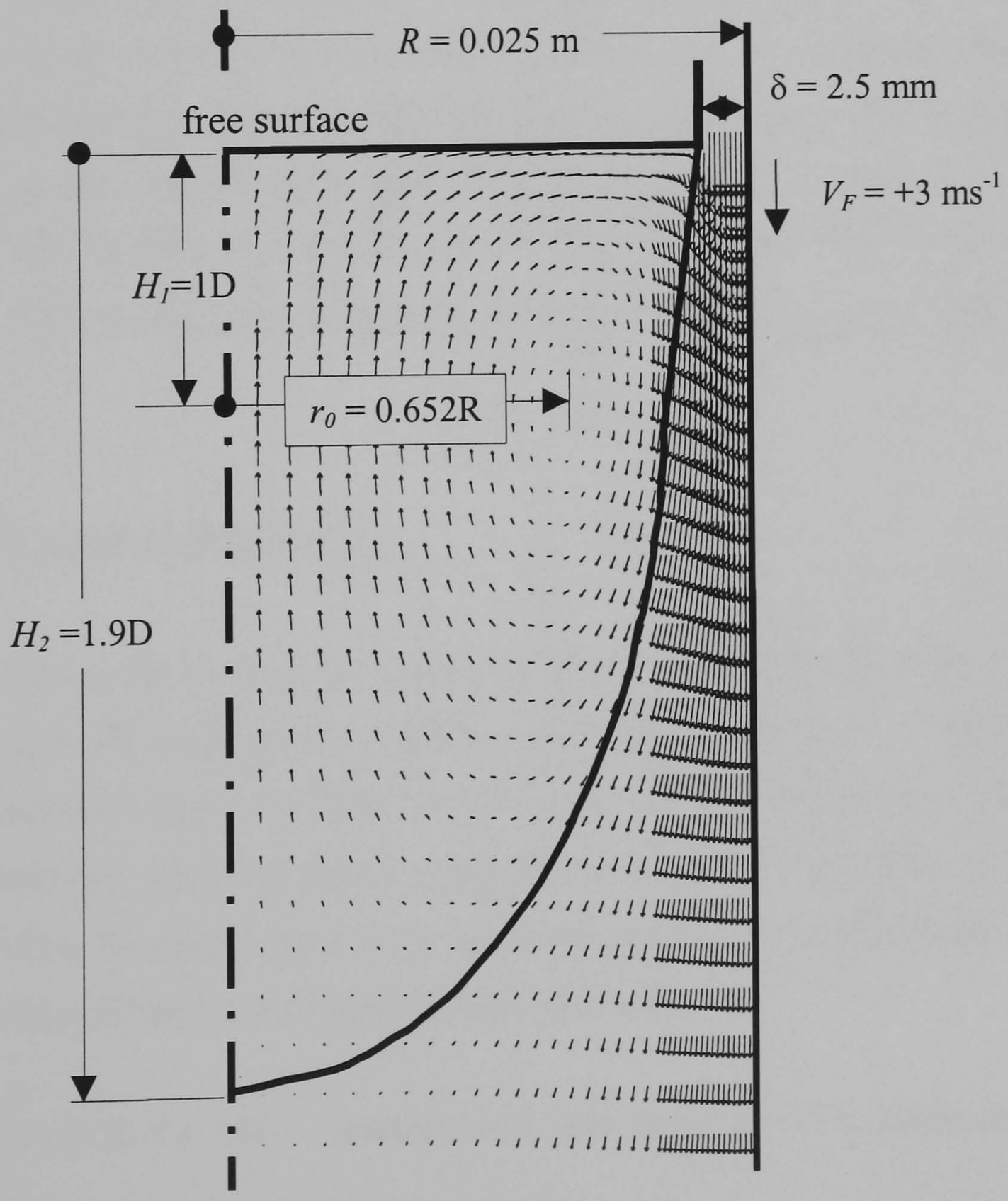

The CFX simulation of Thorpe et al. (2001).

Figure 4.2

The black line is the separatrix.

On the other hand, the results from a recent paper by Tudose and Kawaji (1999) seem to support the suggestion of Thorpe et al. (2001). Tudose and Kawaji (1999) performed total drag force measurements on a stationary, solid model of a Taylor bubble placed in a downward flowing liquid in a vertical tube in order to study the mechanisms responsible for the acceleration of a Taylor bubble in the wake region of a preceding Taylor bubble in gas-liquid slug flow. They used moderate *Re* up to 4349 in their experiments. They found that after around $2D$ below the base of their solid Taylor bubble, the total drag force remained constant. This value compared very well with other results they had obtained for gaseous Taylor bubbles. Tudose and Kawaji (1999) concluded that the differences between the boundary conditions at the gas-liquid interface and solid bubble surface for the liquid film entering the bubble wake did not appear to cause major modifications on the structure of the wake flow field.

Therefore analogous experiments were conducted in the present work to provide an insight of the velocity field in the wake of a ventilated cavity and also to test the validity of the suggestions made by Thorpe et al. (2001). This chapter considers first the detailed characteristics of the complete flow field in the wake of a cylindrical bluff body with an area blockage ratio of 82% in turbulent pipe flow $\mathrm{Re} \simeq 60000$ using LDV. Similar LDV measurements in turbulent two-phase flow $(\mathrm{Re} \simeq 46000)$ are also reported beneath actual ventilated cavities with an area blockage ratio of 80-82%. The results from both experiments were then compared with predictions based on Eq. (4.4).

4.4 RESULTS AND DISCUSSION

The velocity field in the wake of both the bluff body and the ventilated cavity was determined by LDV according to the measuring principles outlined in section 3.9. A benchmark experiment in single-phase turbulent flow was first carried out to test the performance of the LDV system. The agreement between the LDV and a widely accepted profile was very good. Then, first the bluff body and after the central sparger were positioned in the downcomer and measurements were taken at various different axial positions below them.

The standard error in the LDV measurements was based on 95% confidence interval $(\pm 2s)$ and was represented by:

$$\phi_{st} = \pm \frac{2s}{\sqrt{N-1}} \tag{4.5}$$

where N is the total number of samples and s is the root-mean-square velocity fluctuation. The LDV measurements were taken across the test section with a traversing positioning uncertainty of about $l_x = l_y = \pm$ 0.75 mm (estimated from the comparison in single phase flow with the log law). The total random uncertainty in the velocity measurements was therefore:

$$\phi_x = \sqrt{\phi_{st}^2 + \left(\frac{\partial U}{\partial x} l_x\right)^2} \quad \& \quad \phi_y = \sqrt{\phi_{st}^2 + \left(\frac{\partial U}{\partial y} l_y\right)^2} \tag{4.6}$$

where $\frac{\partial U}{\partial x}$ (traversing the x axis) and $\frac{\partial U}{\partial y}$ (traversing the y axis) were the velocity gradients at a given point in the flow. This uncertainty was calculated for all the measurements and is shown as error bars in Fig. 4.3 for one of the velocity profiles obtained, at $z/D = 0.33$ below the bluff body. For values of ϕ_x or ϕ_y lower than 0.05 m s^{-1} the error bars are omitted.

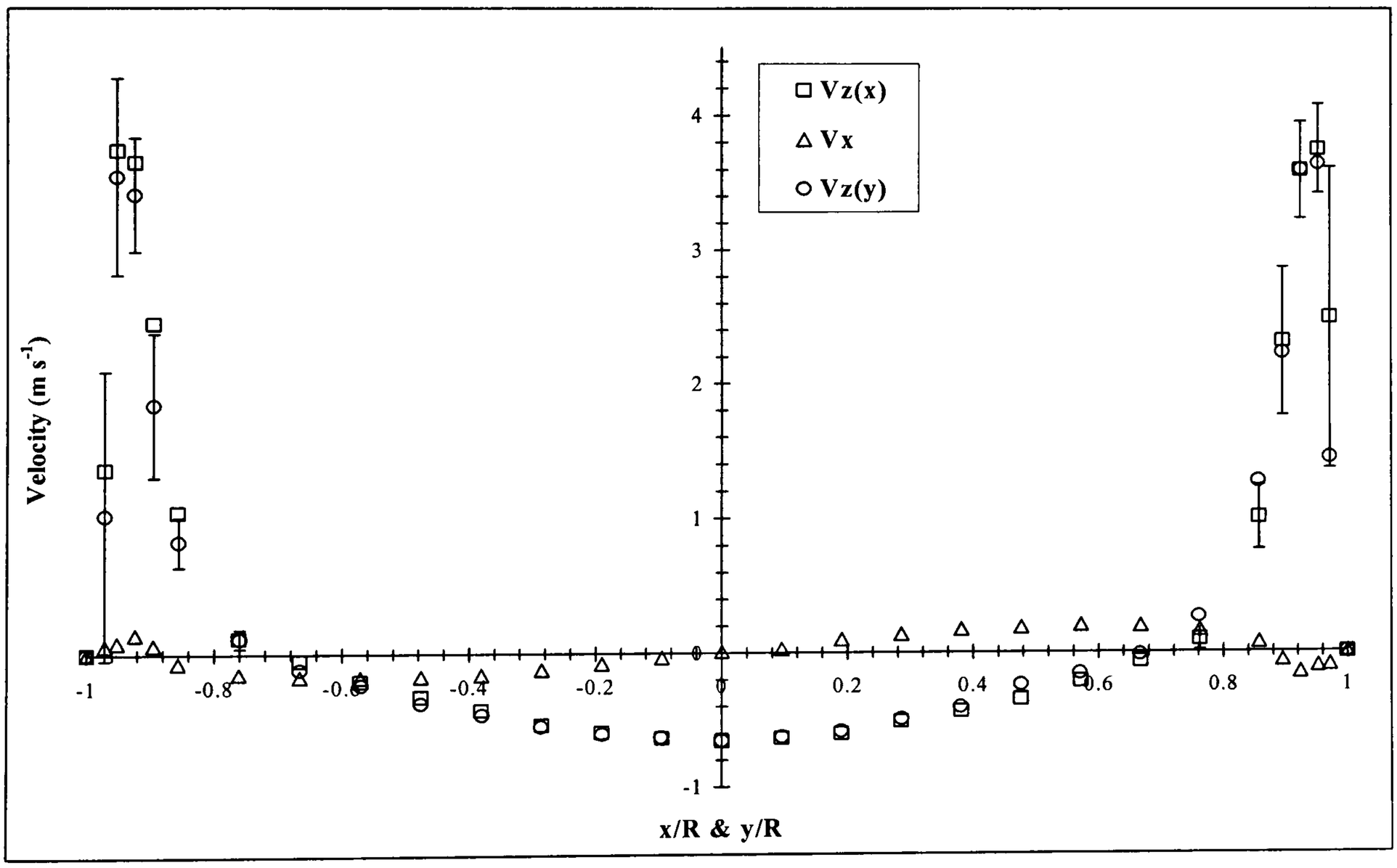

Velocity measurements at $z/D = 0.33$ below the bluff body. The error bars are based on Eq. (4.6). For clarity the error bars that correspond to $V_{z(y)}$ are plotted at the left side of the graph whereas the error bars that correspond to $V_{z(x)}$ at the right side.

Figure 4.3

The measurements of the V_x (Fig 3.13) velocity components, very close to the wall became progressively very difficult because of the increasing refraction at the interface between pipe wall and contents of the pipe. Taylor and Whitelaw (1984) encountered the same problem. For positions of $x/R \geq 0.9$ the results for the component V_x were not very reliable. Also the results for the bluff body case, for the axial component, $V_{z(y)}$ (Fig 3.13), at $y/R \geq 0.97$ were unreliable because the number of particles that passed through the measurement volume at all different axial positions was very low. These errors could not be quantified in Eq. (4.6).

The void fraction beneath the ventilated cavities was not measured but was estimated using the correlation suggested by Wallis (1969). This correlation relates the void fraction, ε_G, of small bubbles to the volumetric gas and liquid flow rates with the rise velocity of single, small bubbles, V_∞:

$$\frac{Q_G}{A\varepsilon_G} - \frac{Q_L}{A(1-\varepsilon_G)} = V_\infty (1-\varepsilon_G)^{\gamma-1} \tag{4.7}$$

where A is the pipe's cross sectional area and γ is the Richardson and Zaki (1954) index γ which takes the value of 2.39 for air bubbles above 1 mm in size. The bubbles in this work were mostly ellipsoidal and had a diameter above 1 mm. Therefore $\gamma = 2.39$ was used for the calculations reported in this chapter.

There are two equations that can be used to calculate the single-bubble rise velocity V_∞, depending on the bubble size. The Eotvos number $\left(Eo_{d_{32}} = \frac{g(\rho_L - \rho_G) {d_{32}}^2}{\sigma} \right)$ is generally used to show this dependency. If $Eo_{d_{32}} \geq 1$ then the single-bubble rise velocity V_∞, was obtained from the Eq. (4.8) suggested by Hamarthy (1960). Eq. (4.8) is independent of bubble size, which is known to be true over the size range that applies here (Kay and Nedderman, 1985). For air and water this equation gives a rise velocity of 0.25 m s^{-1}.

$$V_\infty = 1.53 \left[\frac{\sigma g (\rho_L - \rho_G)}{{\rho_L}^2} \right]^{1/4} \tag{4.8}$$

If $Eo_{d_{32}} \leq 1$ and $d_{32} \geq 1.3$ mm then for ellipsoidal air bubbles in water, the terminal bubble rise velocity V_∞, was obtained from the equation suggested by Mendelson (1967):

$$V_{\infty} = \sqrt{\frac{2.14\sigma}{\rho_L d_{32}} + 0.505 g d_{32}} \tag{4.9}$$

The liquid physical properties were measured according to the methods outlined in section 3.3. Air and water were used as operating fluids in this chapter. The water physical properties are shown in Table 3.1. Mass conservation was checked for all the measured liquid velocity profiles presented in this chapter against the experimental measurements from the magnetic flow meter and found to be closely satisfied with an average deviation of only ±5.2 %. This error could be further reduced if the velocity was measured for more radial positions across the profile so as to get the most accurate possible numerical integration of the experimental velocity profile. Nevertheless, the 5% error in the measured velocity profiles of the present work is of the same range with errors given by other authors in the literature that used PIV to examine the wake of Taylor bubbles in water and viscous solutions. Van Hout et al. (2002) and Nogueira (2000) reported average deviations of 5%, while Bugg et al. (2002) reported 3%.

4.4.1 Benchmark experiment in single phase flow

A benchmark experiment was first carried out in single-phase turbulent flow to test the performance of the LDV system. The measuring volume was traversed in 1 or 1.5 mm increments in the region near the wall and 5 mm in the regions $-0.857 \le {}^{x}/_{R} \le 0.857$ and $-0.857 \le {}^{y}/_{R} \le 0.857$. The LDV was set to collect 60,000 samples per measurement location for a superficial liquid velocity of $j_L = 0.585$ m s^{-1} $\left(\mathrm{Re} \simeq 60500\right)$. The data rate (effective measured data points obtained by the LDV per unit time) was typically around 1400 Hz in the central region of the pipe and about 600 Hz closer to the wall. The magnitude of the data rate obtained in this work agrees with other studies in the literature that measured liquid velocities in turbulent single phase pipe flow using LDV (Velidandla et al., 1996; amongst others). The results are compared in Fig. 4.4 with the Prandtl *one seventh power law* equation (Kay & Nedderman, 1985) for the velocity distribution in turbulent flow. The Prandtl law is valid for $\mathrm{Re} = 10^4 - 10^5$ (Schlichting, 1979). All the experimental *Re* quoted in this chapter are within this range. Both the V_x and V_y velocity components were zero during the single phase flow measurements and are not plotted in Fig. 4.4. for clarity.

$$\frac{V_{(z)}}{V_{cl}} = \left(\frac{x}{R}\right)^{1/7} \tag{4.10}$$

$$j_L = 0.817 V_{cl} \tag{4.11}$$

where, x and R, are the radial coordinate originating from the pipe wall and the pipe radius respectively and V_{cl} is the liquid velocity at the pipe centerline. The comparison indicates that the there is a good agreement between the experimental results and the correlation. The experimental profiles were flatter than the correlation in the center of the pipe. Eq. (4.10) implies a finite gradient profile at $x/R = 0$, whereas the actual liquid velocity profiles should be flat with a zero velocity gradient at $x/R = 0$.

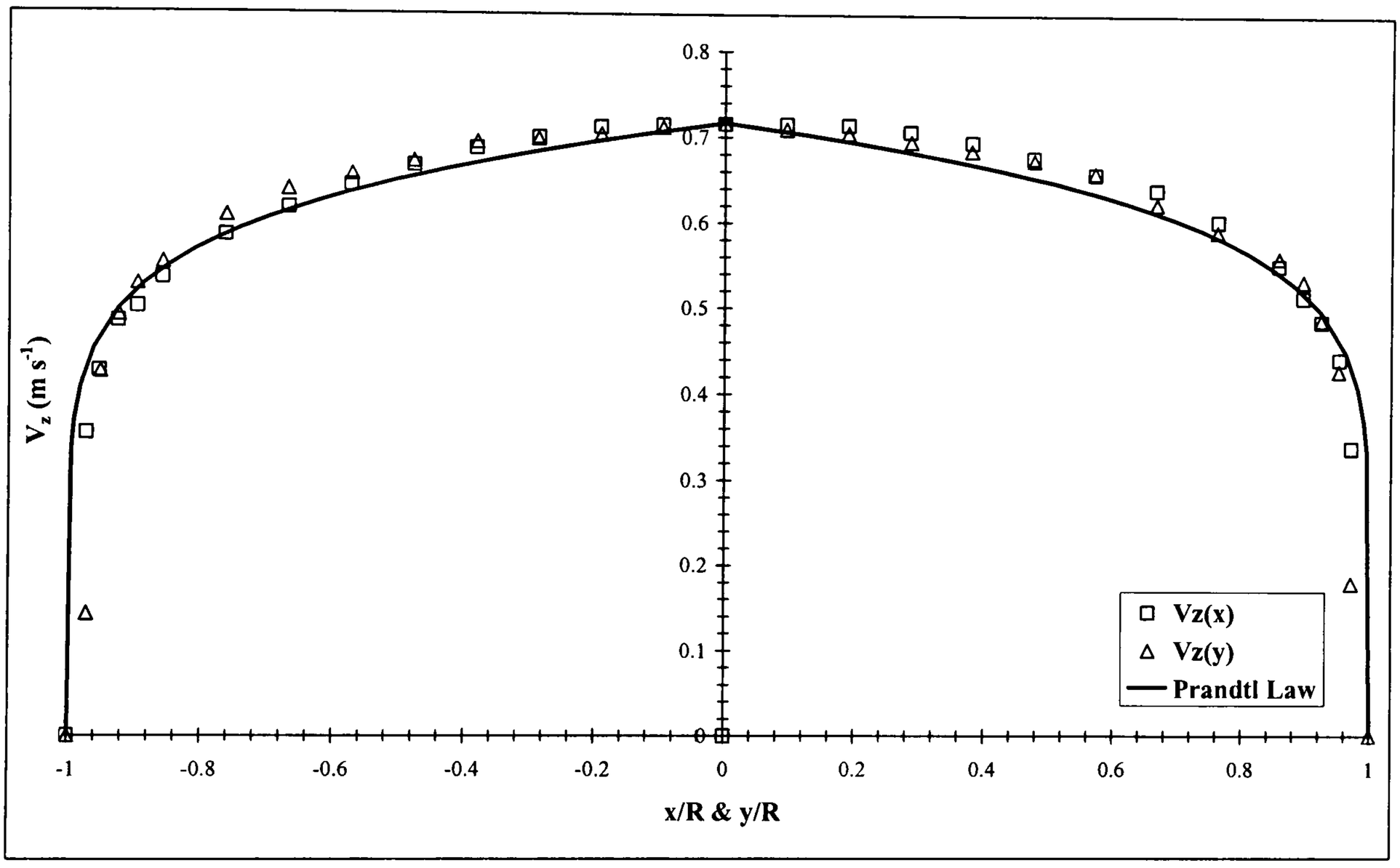

Benchmark experiment: Diametrical velocity distributions for turbulent flow of water in the downcomer and comparison with the Prandtl law.

Figure 4.4

4.4.2 Velocity field beneath the bluff body

4.4.2.1 Introduction

The velocity field in the wake of the bluff body was determined using LDV according to the method outlined in section 3.9. During the measurements below the bluff body the LDV system was set to collect 70,000 samples per measurement location or as many data as possible within a 300 sec window, depending on the condition first reached. The value of 70,000 samples was carefully selected because it gave reproducible results. For the vast majority of the cases good

data rates were present (typically around 1500 Hz) and all 70,000 samples were taken by the system. The measuring volume was traversed in 1 or 1.5 mm increments in the region near the wall and 5 mm in the regions $-0.857 \le x/R \le 0.857$ and $-0.857 \le y/R \le 0.857$. A 3-D velocity distribution across the pipe's diameter for each axial position below the bluff body was obtained by traversing the measuring volume across the x and y axis (Fig 3.13). The axial $V_{z(x)}$ and the V_x (velocity component in the x direction) velocity components were measured by traversing across the x axis; whereas traversing across the y axis, the axial $V_{z(y)}$ and the V_y (velocity component in the y direction) velocity components were respectively measured. Since the measuring volume was traversed across the pipe's diameter, then the measured velocity components of V_x and V_y can be related in cylindrical polar coordinates to the radial and azimuthal velocity components respectively. The blockage ratio in the bluff body case was 82%. The superficial liquid velocity was $j_L = 0.577$ m s^{-1} for most of the measurements. However once the full liquid velocity field below the bluff body was determined, some measurements were taken at the superficial liquid velocities of 0.346 m s^{-1} and 0.808 m s^{-1}.

4.4.2.2. Results

The results for $j_L = 0.577$ m s^{-1} $(\mathrm{Re} \simeq 60000)$ at 8 axial positions below the bluff body are presented in Fig. 4.5 to 4.7. These positions were chosen because they offer a clear view of the changes in the velocity field with axial distance. For a global view of the wake field a vector plot with all the measurements taken below the base of the bluff body is shown in Fig. 4.8. The axial coordinate represents the distance relative to the bottom of the bluff body. The downward velocities have been defined to be positive. The average liquid velocity in the annulus at the base of the bluff body was calculated based on continuity (Eq. 4.12),

. The average liquid annulus velocity calculated in this way was equal to $V_F = 3.18$ m s^{-1}.

$$V_F = \frac{4Q_L}{\pi\left[D^2 - (D-2\delta)^2\right]} \tag{4.12}$$

continued

Several authors have observed that there is a vortex behind bluff bodies (Taylor and Whitelaw, 1984) or in the wake of Taylor (slug) bubbles (Nogueira et al., 2000; Bugg et al., 2001; Van Hout et al., 2002; Nogueira et al., 2003). Only Van Hout et al. (2002) and Taylor and Whitelaw (1984) have provided detailed measurements of the velocity field itself. It is observed in Fig. 4.5 to 4.7 that when the liquid entered the space beneath the bluff body a toroidal vortex was formed in the middle of the flow field. Beneath the base of the bluff body a wall jet spread,

giving rise to a 2 dimensional velocity flow field. The time-averaged values of the velocity component V_x were considerably lower than the corresponding axial velocity component and never exceeded 0.41 m s^{-1}. The V_x velocity component became negligible at about $2D$ below the bluff body. For the whole range of measurements the velocity components, V_y were always close to zero and that is why they are not included in this thesis. This lack of swirl confirmed that the flow straightener at the top left bend of the rig (Fig. 3.1) had done its job.

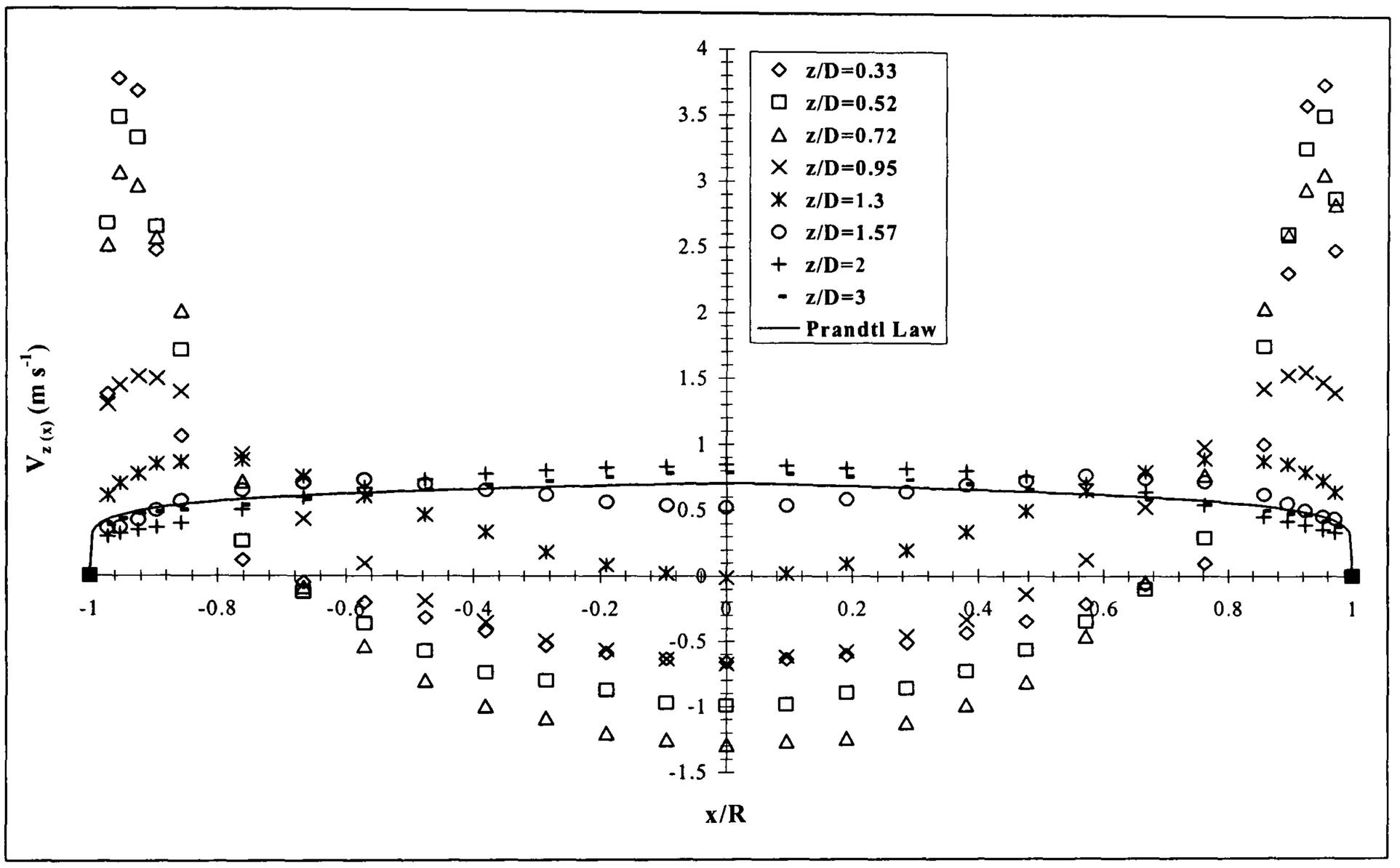

Diametrical velocity distributions for the axial velocity component, $V_{z(x)}$ at various distances z below the bluff body.

Figure 4.5

The boundaries of the vortex were marked by a channel of high downward velocities due to the developing width of the annular wall jet. There was an inward drift of flow towards the centre of the vortex. The annular jet was quickly absorbed into the wake flow field. Its width increased with increasing axial distance and eventually occupied the entire cross pipe sectional area. From this point and onwards the flow was always directed downwards. The eye of the vortex (see Fig. 4.1) when V=0 was located at $H_1 = 0.72D$ (Figs. 4.5 and 4.7) below the bluff body. The rotational center of the vortex, r_0, was located at a radial distance of $0.666R$ from the pipe's centerline. Assuming that the stagnation point (see Fig. 4.1) where the axial velocity along

the centerline of the column was zero, marked the end of the recirculation flow, the length of the recirculation region was found at, $H_2 = 1.3D$ (Figs. 4.5 and 4.7) below the bluff body.

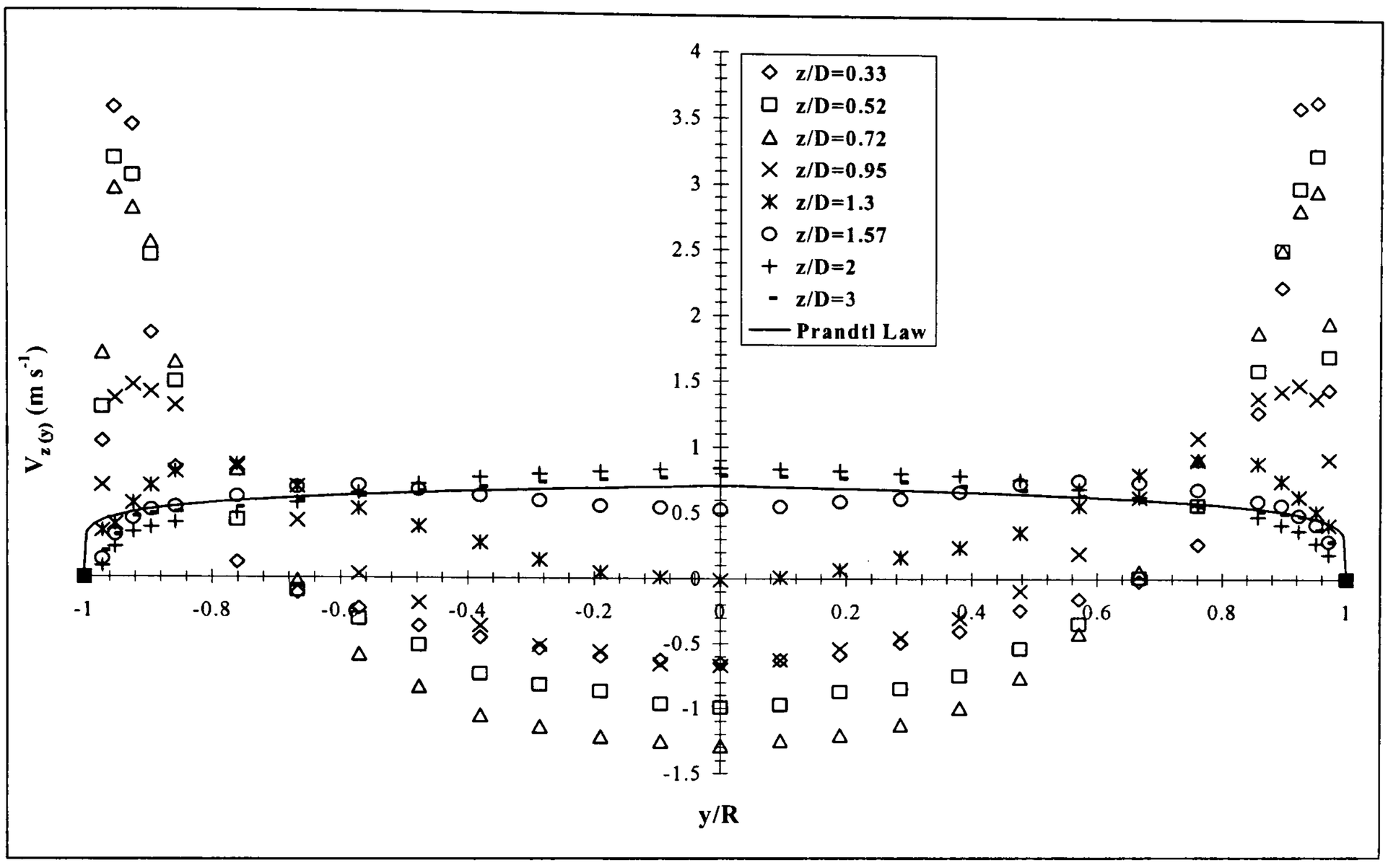

Diametrical velocity distributions for the axial velocity component, $V_{z(y)}$ at various distances z below the bluff body.

Figure 4.6

The above distance of $H_2 = 1.3D$ compares well with some previous studies. Some of these studies used different possibly inconsistent definitions for H_2, for which deduced or reported values are in the range $1-2.5D$. Delfos et al. (2001) provided photographs that showed a very aerated wake length of a ventilated cavity attached to a central sparger of about $1-1.5D$. The stagnation point deduced from photographs from the data of Campos and Guedes de Carvalho (1988a) for a 52 mm i.d. pipe (their Fig. 5, cases e and f) seemed to be around $1.25-1.6D$. Van Hout et al. (2002) reported a "wake length" of around $2D$. However their experimental stagnation point was deduced from their velocity vector plot and corrected for the geometry of this work because the cavity was stationary relative to the pipe wall; the stagnation point was then found at around $1.6D$ below the slug bubble. Nakoryakov et al. (1989) reported also a wake length of $2D$. However the length of the re-circulating wake was taken at the point where the liquid velocity profile started to level off, which as measured in this work is at a position below the stagnation point $(H_2 = 1.3D)$ (Fig. 4.9). Evans et al. (1992) defined the mixing zone length

as the distance from the free surface inside the column where the wall pressure profile became linear. They reported values of around 2-2.5 D. Lee et al. (2000) showed that the linear increase of the pressure profile in the wake of a ventilated cavity took place after the wall jet had occupied the entire downcomer. Campos and Carvalho (1988b) indirectly defined the wake length, based on tracer dispersion caused by Taylor bubbles moving in a vertical pipe. They found that the wake length was around $2.2-2.8D$. This length was determined as a parameter of the model they used to fit experimental tracer concentration profiles along the pipe. This definition is again different than the one adopted in this work and over predicted the stagnation point.

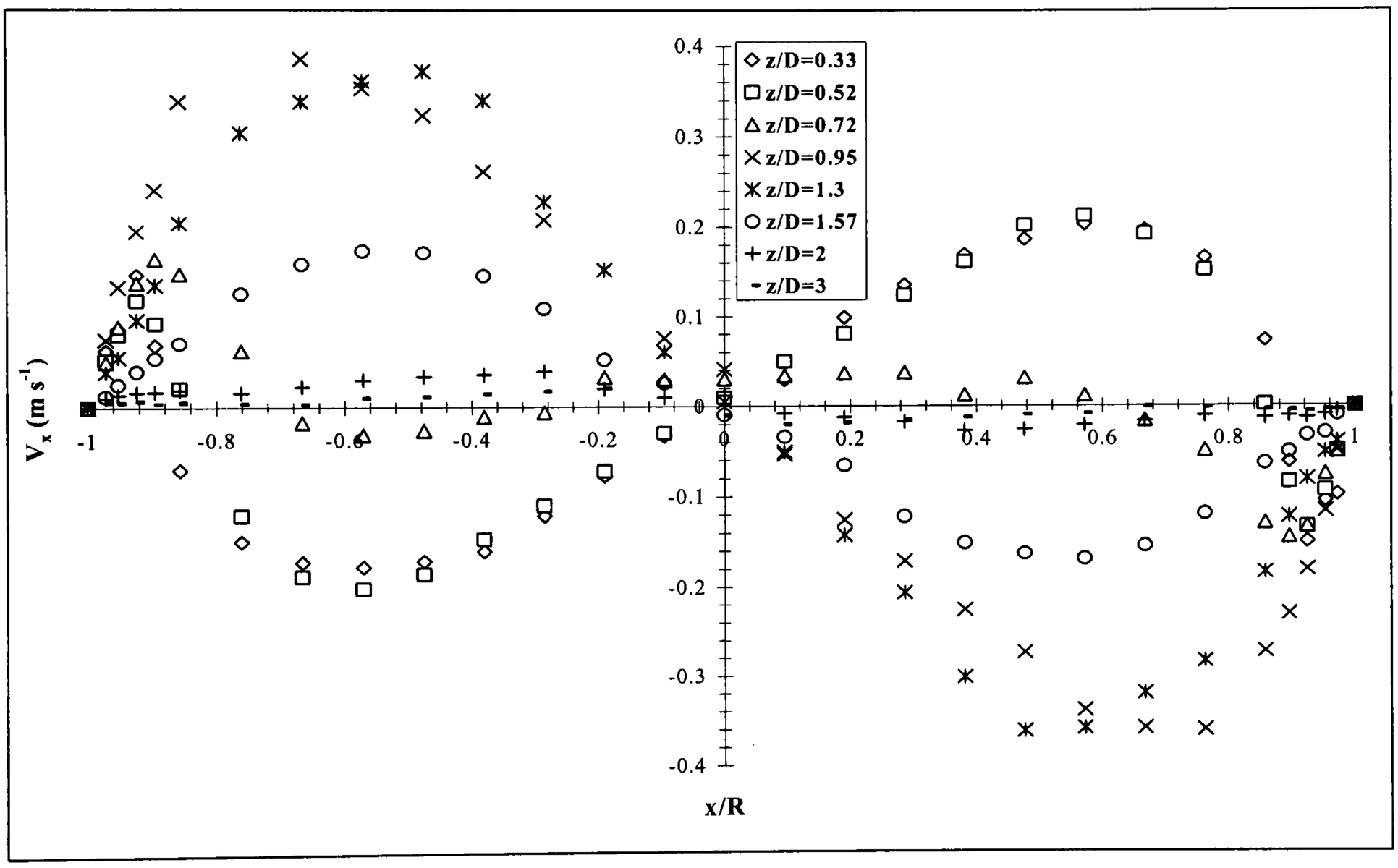

Diametrical velocity distributions for the V_x velocity component at various distances z below the bluff body.

Figure 4.7

At $z = 3D$ (Figs. 4.5 and 4.6) the flow field was still developing because the experimental liquid velocity profile was above the Pradtl law. This can be seen from the comparison with the results of Fig. 4.4, which corresponded to a fully developed flow. No attempt was made to observe the second much weaker vortex with opposite sense of rotation for $2 \le z/D \le 4$ reported by Van Hout et al. (2002) (see section 2.3).

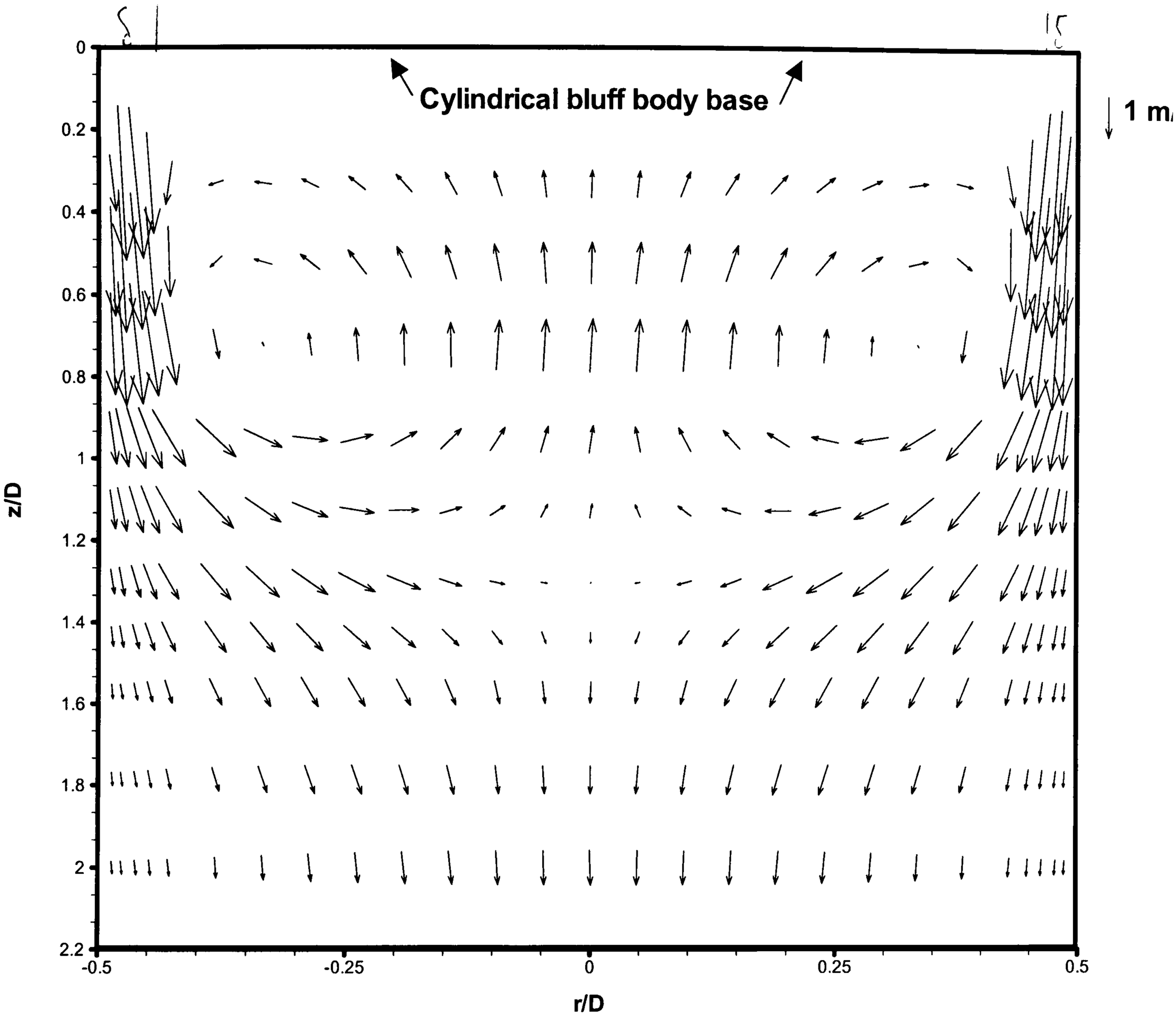

Ensemble averaged diametrical vector velocity plot in the wake of the bluff body. The superficial liquid velocity is $j_L = 0.577$ m s^{-1} and the annulus gap between the bluff body and the pipe wall is $\delta = 5$ mm.

Figure 4.8

In Figs. 4.10 and 4.11 the radial profiles of the r.m.s. values of the axial, V_z' and V_x' velocity fluctuation are shown at different axial locations from the bottom of the bluff body. The maximum of V_z' was found near the wall, in the wall jet where high liquid axial velocities were

present marked by the boundaries of the vortex and the pipe wall. The peak close to the wall is in agreement with results for turbulent intensities, obtained for slugs rising in stagnant water (Van Hout et al., 2002), continuous slug flow (Nakoryakov et al., 1989) and behind bluff bodies (Taylor and Whitelaw, 1984).

This peak gradually decreased, due to the decaying of the penetrating annular wall jet. The wall jet was the source of the turbulent kinetic energy in the wake of the bluff body. Thus, as the wall jet spread and weakened the turbulent kinetic energy dissipated. It therefore appears that the flow field in the near wake of the bluff body was a region of high turbulence dominated by vigorous mixing and circulation of fluid, similar to the results of Taylor and Whitelaw (1984) for smaller bluff bodies. At $z = 3D$ below the bluff body the shape of the axial r.m.s. profile has flattened and qualitatively resembled the one for single flow taken during the benchmark experiment corresponding to single phase flow (section 4.4.1). There wasn't a peak in V_z' at the wall and the turbulence levels (values of V_z') were still much higher than the corresponding one for single-phase flow.

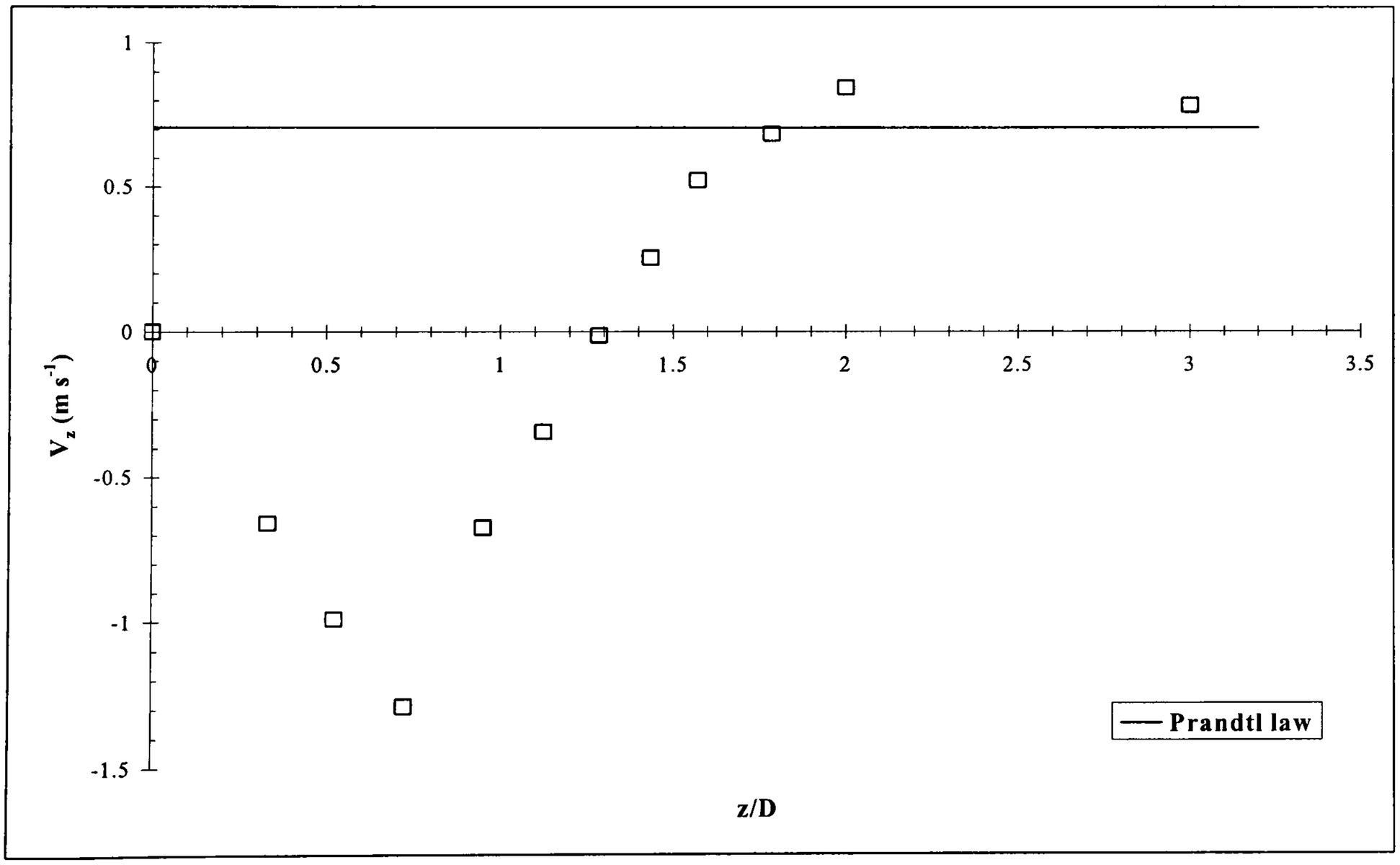

The variation of the ensemble averaged axial velocity at the centreline of the pipe as a function of the axial distance from the bluff body base.

Figure 4.9

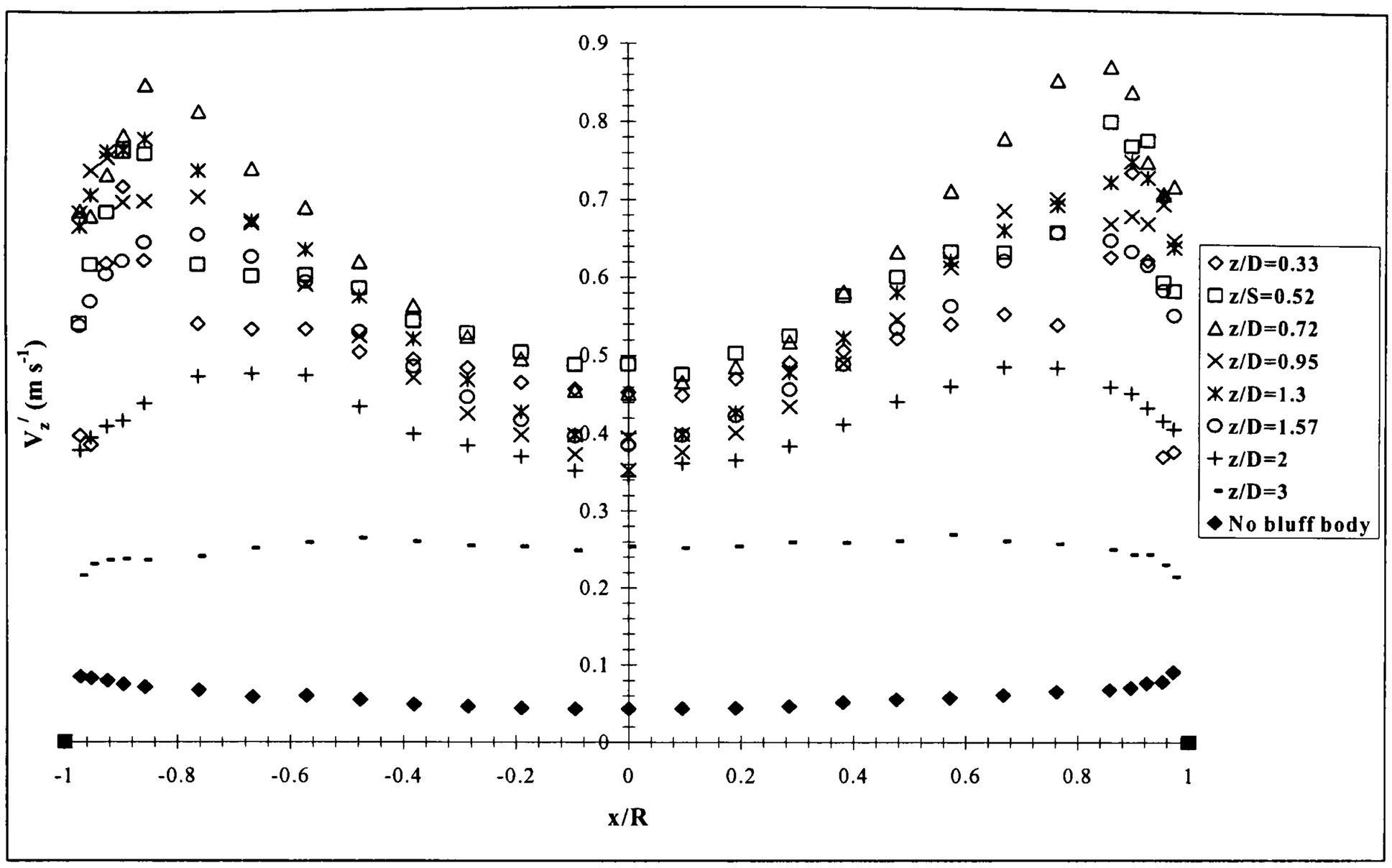

Radial distributions of the r.m.s. values of the axial velocity component, V_z' at various distances z below the bluff body.

Figure 4.10

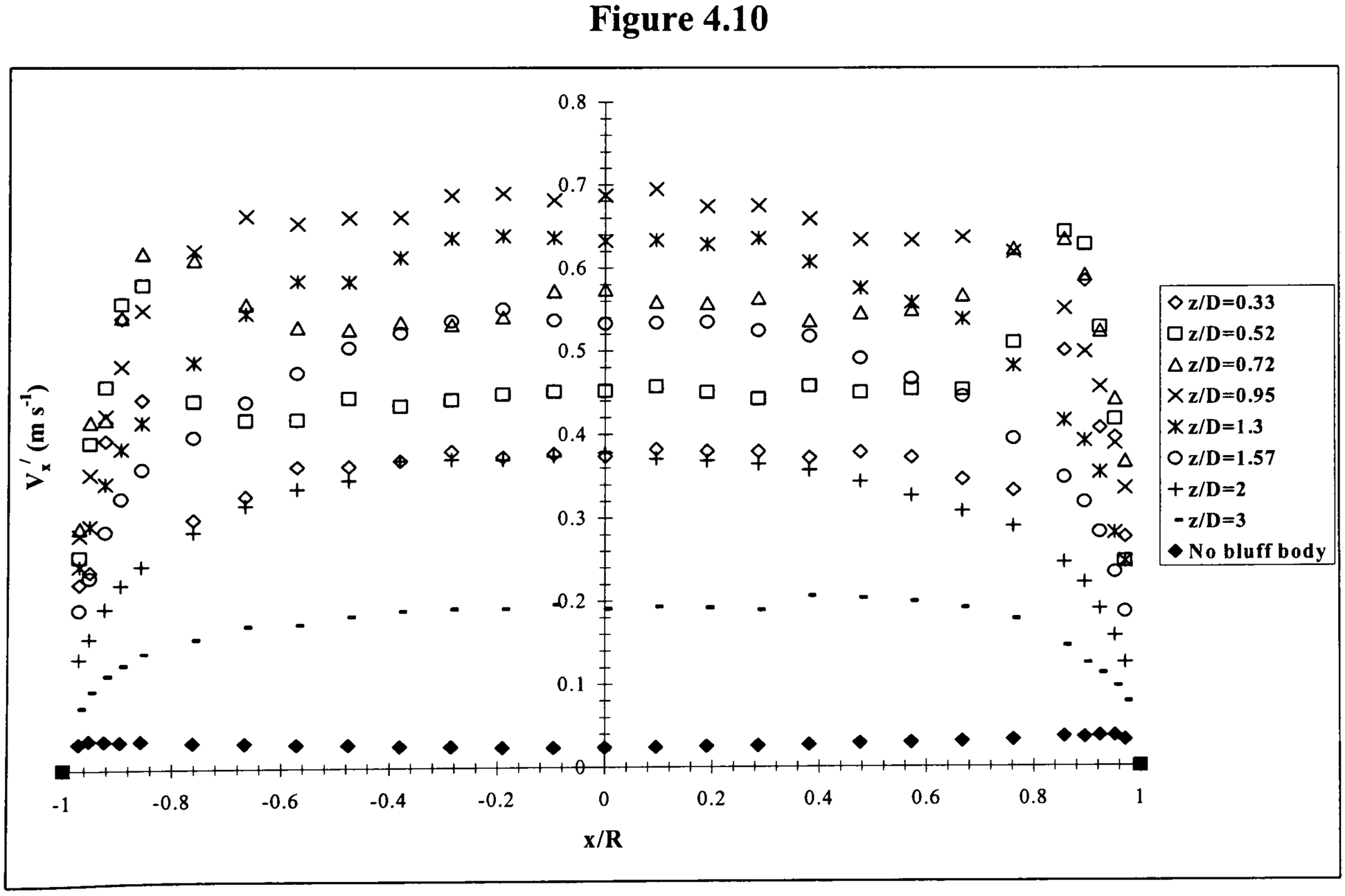

Radial distributions of the r.m.s. values of the radial velocity component, V_x' at various distances z below the bluff body.

Figure 4.11

The r.m.s. values of the V_x velocity fluctuation, V_x' at each axial location below the bluff body were of the same order of magnitude as V_z', which is in agreement with the results of Van Hout et al. (2002) and Taylor and Whitelaw (1984). Van Hout et al. (2002) attributed that to the vortical nature of the flow in the near wake of slug bubbles but no further explanations was given. Van Hout et al. (2002) studied the flow field around a slug bubble rising in a vertical pipe filled with stagnant water using PIV. They used a four times smaller pipe diameter and their falling film at the base of the bubble was laminar $\left(\mathrm{Re}_F = 813\right)$ and not turbulent $\left(\mathrm{Re}_F \simeq 60000\right)$ as in the case of the bluff body.

Measurements were also taken at the axial positions in the region of $z = 0.72D$ and around $z = 1.3D$ below the base of the bluff body for the superficial liquid velocities of 0.346 m s^{-1} and 0.808 m s^{-1} (Fig. 4.12). The aim was to check if the geometry (i.e. size) and speed of the toroidal vortex were influenced by the superficial liquid velocity (i.e. the strength of the vortex). Thorpe et al. (2001), implied that the size and position of the vortex should not change but that the speed of the rotation should be proportional to the superficial liquid velocity. The data are plotted in dimensionless coordinates to highlight that they are collapsing (Fig. 4.12).

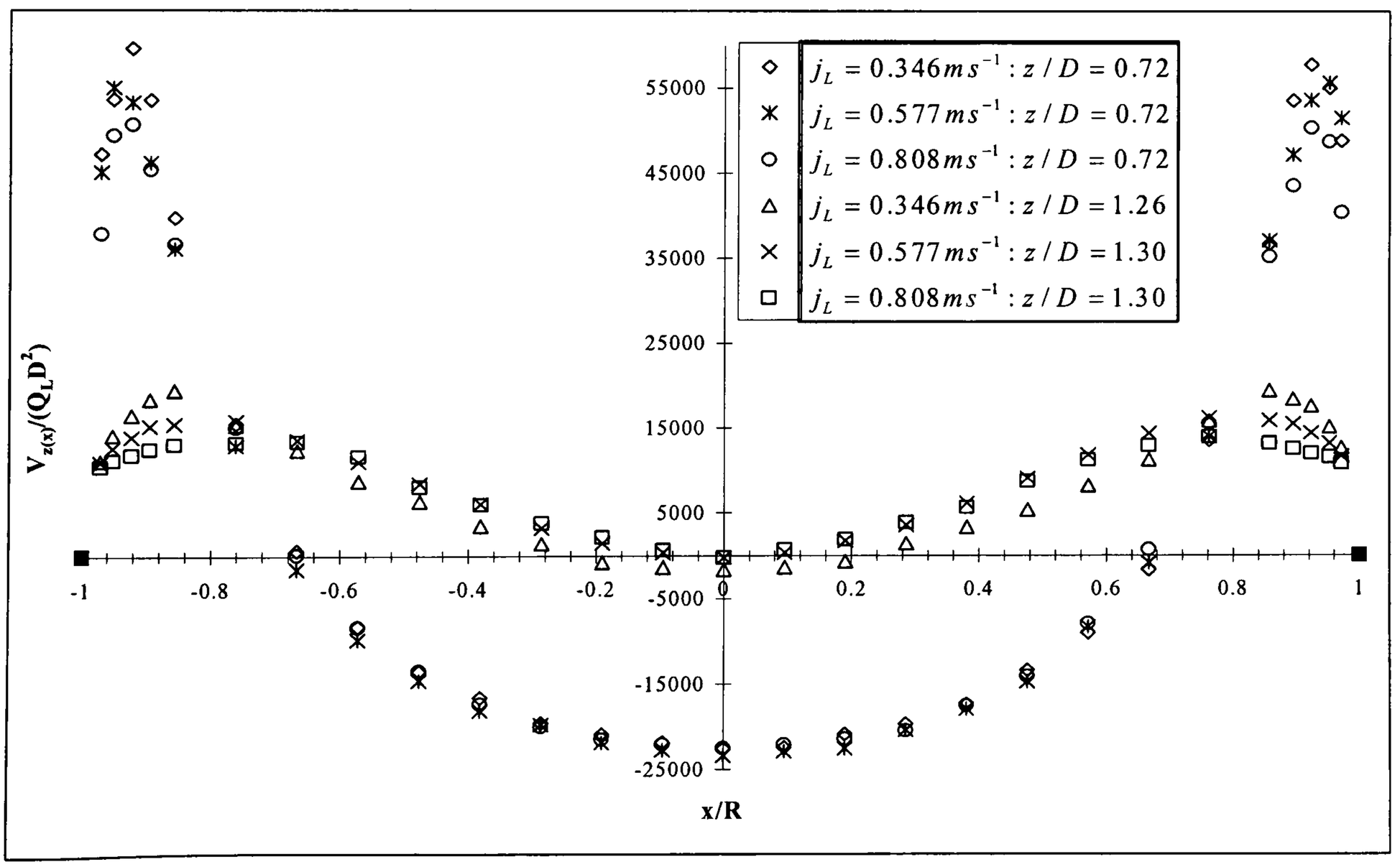

Vortex structure below the bluff body at different superficial liquid velocities.

Figure 4.12

It is shown that the axial locations of the eye of the vortex and the end of the recirculation region were similar in both cases to the results taken for the superficial liquid velocity of 0.577 m s^{-1}. These results confirm that the size of the vortex behind the bluff body was not dependent primarily on the superficial liquid velocity. Also the maximum axial recirculation velocity in the plane of the eye of the vortex for both measurements was 0.39 times the liquid velocity in the annular gap at the base of the bluff body $\left(\frac{V_{z(\max)}}{V_F} = 0.39\right)$, which is in excellent agreement with the value of 0.38 in Eq. (4.2).

4.4.3 Velocity field beneath ventilated cavities

4.4.3.1 Introduction

The wake velocity field was measured for two different ventilated cavities with similar blockage ratios to the bluff body. The aim was to obtain an insight of the velocity field in the wake of a ventilated cavity that would allow comparisons with Eq. (4.4) and also test the validity of the suggestion made by Thorpe et al. (2001) (see section 4.3). The experimental conditions of the LDV experiments are shown in Table 4.1. The film thickness, δ, at the base of each cavity was calculated using the model of Lee et al. (2000) who defined the ventilated cavity shape based on a force balance as:

$$\int_{\alpha_2}^{\alpha_1} \frac{d\alpha}{g\alpha^3 - \frac{1}{2}\pi D C_f Q_L{}^2} = \frac{z}{Q_L{}^2} \tag{4.13}$$

$$\alpha_2 = \pi\left[D^2 - (D-2\delta)^2\right] \tag{4.14}$$

where α_2 is the falling film flow area at the base of the ventilated cavity attached to the sparger, α_1 is the falling film flow area at the top of the ventilated cavity attached to sparger and C_f is the Fanning friction factor. Wallis (1969) suggested that $C_f = 0.005$ as a simple first approximation. The area at the nose of the ventilated cavity occupied by the flow of water, α_1, which would become film, was taken to be the difference in cross-sectional area between the downcomer and the CS and was thus not much less than the area of the downcomer. Integrating Eq. (4.13) numerically allowed the flow area of the liquid film to be determined at any general axial location z and then from Eq. (4.14) the film thickness was estimated. The average falling film velocity, V_F, was calculated from Eq. (4.12).

Ventilated Cavities	Q_L (m^3s^{-1})	Q_G (m^3s^{-1})	j_L (ms^{-1})	j_G (ms^{-1})	Q_G/Q_L	$\varepsilon_G{}^a$ (%)	L_B (mm)	δ^b (mm)	V_F (ms^{-1})	*Re*	*Blockage* (%)
Cases											
VC1	0.00380	0.000055	0.438	0.0064	0.015	1	284	5.3	2.29	45500	80
VC2	0.00383	0.0001	0.442	0.0115	0.026	2	357	4.9	2.49	46000	82

[a] Based on the Wallis 1-D approach, Eq. (4.7)-(4.9)

[b] Based on Eq. (4.14)

Experimental flow conditions for the LDV measurements beneath the two ventilated cavities.

Table 4.1

The LDV system was set to collect 200,000 samples per measurement location or as many data as possible within a 500 sec window, depending again on the condition first reached. For axial locations located inside the boundaries of the vortex, the measurements became progressively more difficult and time consuming towards the center of the pipe (see discussion also further below). The bubbles tended to accumulate in the rotating vortex, thus obscuring the center of the pipe all the time. The system needed all 500 sec to obtain the 200,000 particles. The measuring volume was traversed only across the x axis in 1 or 1.5 mm increments in the region near the wall and 5 mm increments in the region $x/R \leq 0.857$. The axial $V_{z(x)}$ and V_x liquid velocity components were measured.

The vortex structure beneath the VC1 was first determined and compared to the LDV results of the bluff body. Then the gas flow rate was almost doubled and measurements were taken beneath VC2 to check if the position of the stagnation point had changed. Meaningful measurements using the LDV inside the boundaries of the vortex were not possible for higher void fractions. Some initial test measurements in the core of the vortex had shown that for an average void fraction of $\varepsilon_G = 0.06$ (6%) the presence of the bubbles interfered with the LDV setup leading to ambiguous results (data rates as low as 0.1 Hz and high values of both the velocity and r.m.s. velocity fluctuation and mass conservation was not satisfied). This at first seemed surprising since the difference in the gas void fraction was only 4% to the conditions shown in Table 4.1 and the LDV setup used in the present study had shown to give acceptable results in bubbly flows for void fractions up to 8.5% (Sun et al., 2004a; Mudde et al., 1998; amongst others).

However there is a plausible explanation to the above. Visual observations showed that in the near wake region the local gas void fraction was higher than in the rest of the pipe because the entrained bubbles were trapped in the recirculating vortex. Van Hout et al. (1992) measured such a gas void fraction gradient for a Taylor bubble rising in water. They reported a very steep void fraction decrease from a high value in the near wake region to a constant value at around $z = 2 - 2.5D$. Van Hout et al. (1992) reported differences of up to an order of magnitude in the value of the void fraction between $z = 0 - 2D$. Delfos et al. (2001b) showed that the re-coalescence probability of the entrained bubbles back to the main body of their ventilated cavity increased with increasing gas void fraction in the wake. This increased probability led to accumulation of bubbles in the vortex and creation of bubble clusters.

The data rate of LDV measurements in bubbly flows is a strong function of the distance from the wall (Velidandla et al., 1996; Mudde et al., 1998; Guet et al., 2004; Sun et al., 2004a). Ohba et al. (1976) have shown that the probability for a laser beam to penetrate into a bubbly flow decreases exponentially with gas fraction and path length. Due to the particularities associated with the LDV application to bubbly flows, i.e. the restricted optical access, the data rate in this work was expected to be larger closer to the wall than when measuring towards the pipe's centreline. Therefore it was expected that the data rate obtained in this work would follow the same dependence on distance in the bubbly flow beneath the ventilated cavity as the one given by Ohba et al. (1976). This was indeed the case as is illustrated in semi log plot of Fig. 4.13.

The data in Fig. 4.13 correspond to the LDV measurement in the plane of the eye of the vortex beneath the VC1, i.e. the case investigated in the present work that is most sensitive to bubble interference due to the bubble accumulation mentioned above. The plot in Fig. 4.13 shows clearly an exponential drop in the data rate with increasing distance from the wall, in agreement with the theoretical consideration by Ohba et al. (1976). Note that the data rate in the center of the pipe was close to 100 Hz, which is much higher compared to other studies in the literature that used LDV to measure the liquid velocity in bubbly flows, where reported data rates are in the range of 0.1 – 50 Hz (Mudde et al., 1998; Guet et al., 2004; Sun et al., 2004a). The high data rate in the center of the pipe obtained in this work is sufficient for a reliable estimate of the r.m.s. velocity fluctuations. To investigate the possibility of multiple bubble scattering detection by the LDV, the data rate was recorded during measurements under the same operating conditions without bubbles . The data rate when measuring with scattering particles was always 6% higher that the corresponding data rate with no bubbles

particles. This was a good confirmation that multiple bubble scattering was negligible during the experiments.

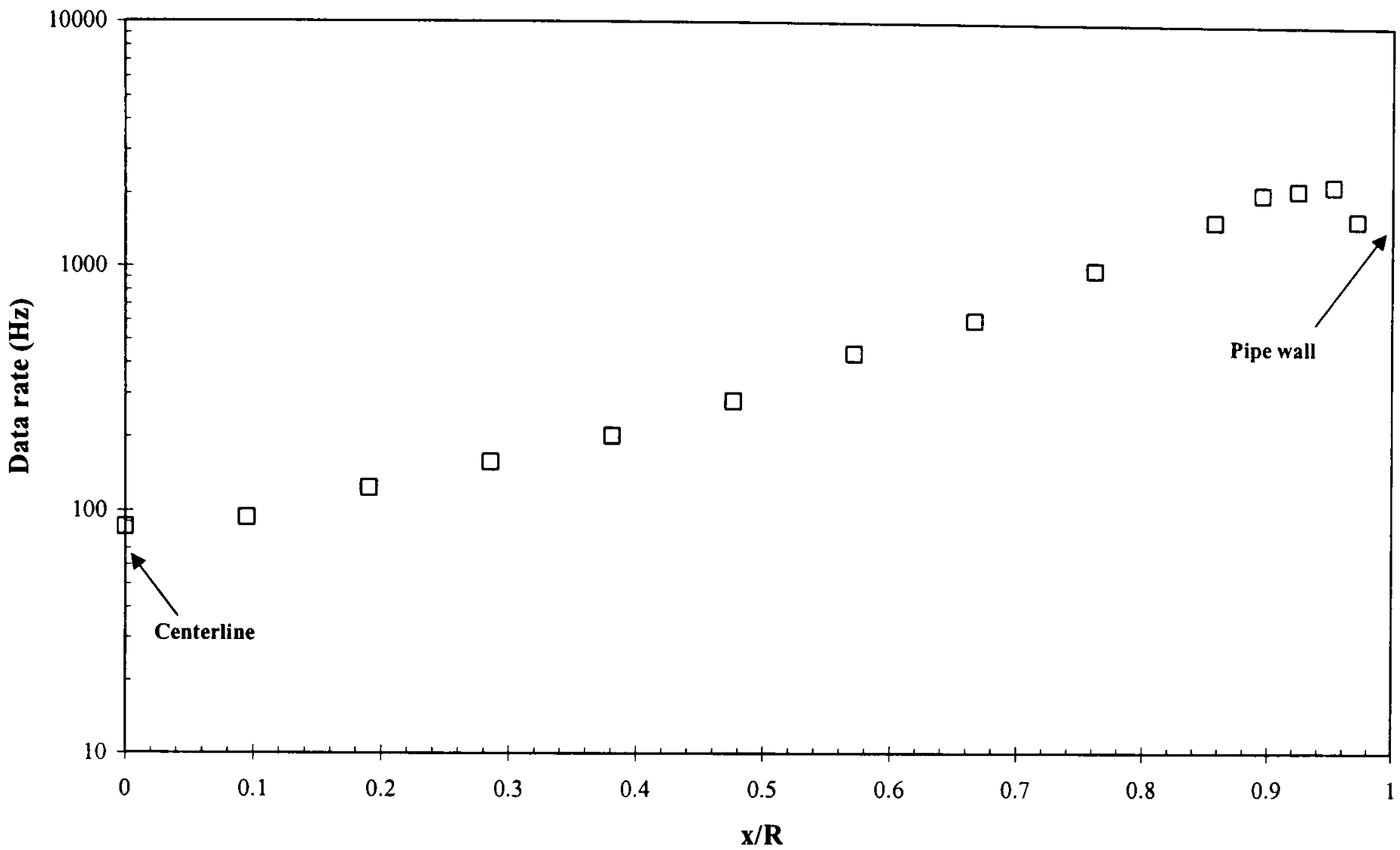

Data rate versus dimensionless distance from the wall in the plane of the eye of the vortex beneath VC1. See Table 4.1 for the operating conditions.

Figure 4.13

An increased presence of bubble clusters could interfere with the LDV by blocking the beam paths, decreasing the data rate in the signal processor of the liquid phase and adding an additional frequency to the complete Doppler signal that was connected to the rising velocity of bubbles. Therefore, to avoid any form of ambiguity in the interpretation of the LDV measurements the velocity flow field beneath a ventilated cavity was examined for the low gas void fractions conditions of Table 4.1 where mass conservation was closely satisfied.

4.4.3.2 Results

The velocity field beneath the ventilated cavities had many similarities to the toroidal vortex formed below the bluff body as shown in Figs. 4.14 - 4.16. The length of the recirculation region was taken to be at about $H_2 = 1.32D$ below both ventilated cavities (Fig. 4.14 and 4.15). The eye of the vortex, was located at approximately, $H_1 = 0.78D$ (Fig. 4.14). The rotational center of the vortex, r_0, was located at a radial distance of $0.624R$ from the pipe's centerline.

The above agreed very well with the experimental results obtained for the bluff body, where $H_1 = 0.72D$, $H_2 = 1.3D$ and $r_0 = 0.666R$ (Section 4.4.2).

At $z = 340$ mm (Fig. 4.17) which corresponded to an axial distance of approximately $z = 3.25D$ below the bottom of the ventilated cavities the experimental velocity profile agreed very well with the Prandtl 1/7 power law. This correspondence with the $1/7^{th}$ power law is misleading. It is more normal in homogeneous bubbly flow for the profile to be flatter than the $1/7^{th}$ power law as shown by Sun et al. (2002) and Kashinsky and Randin (1999), which is clearly not the case for the data in Fig. 4.15. The fact the profile showed a central maximum proves that the flow field in the wake of the cavity was still developing at $z = 3.25D$. When comparing with the bluff body results (no bubbles present) (Fig. 4.4), the velocity profile of Fig. 4.16 was much flatter, demonstrating that outside the vortex boundaries and at around $3D$ from the cavity the presence of the bubbles started to have an influence on the flow pattern.

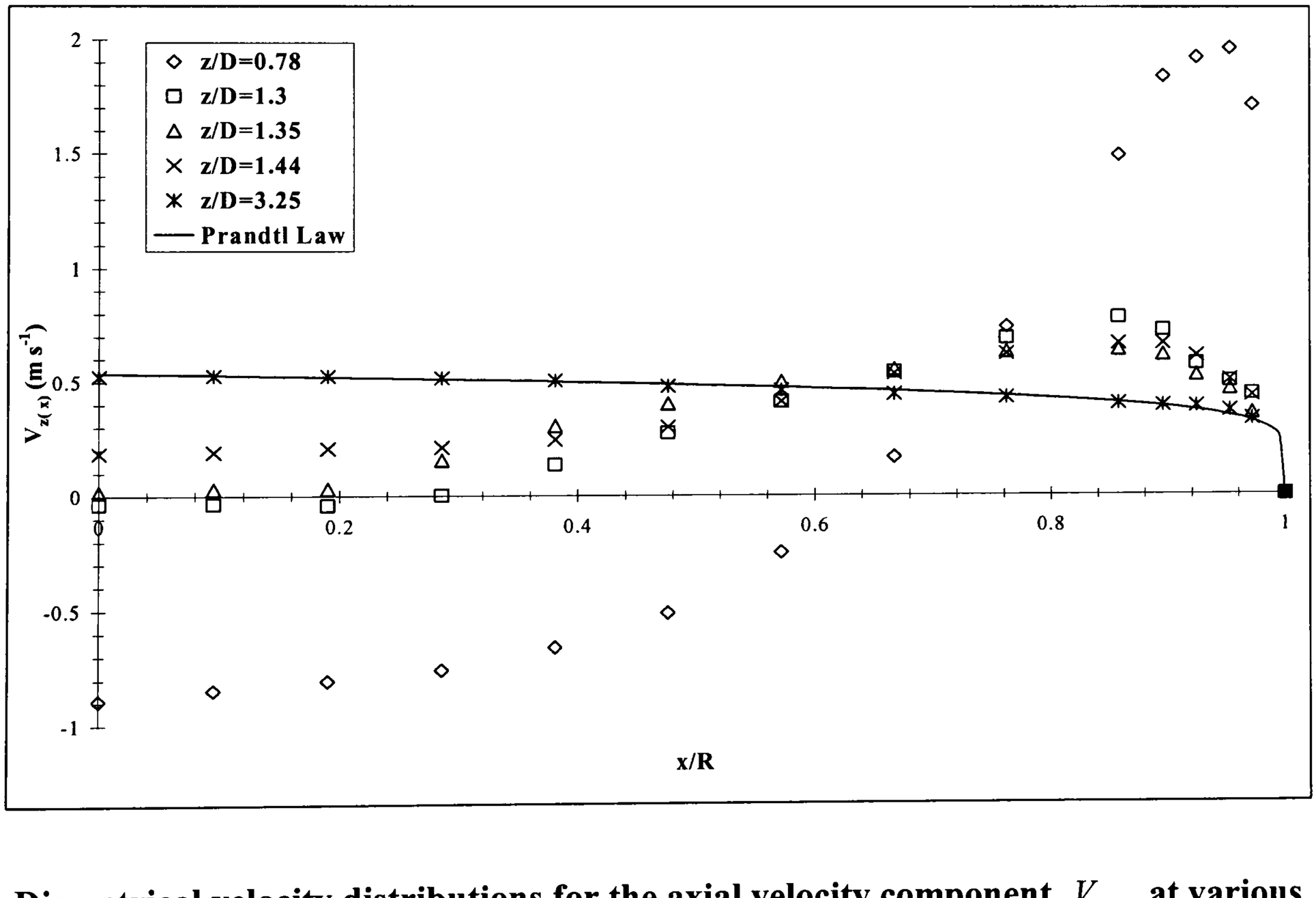

Diametrical velocity distributions for the axial velocity component, $V_{z(x)}$ at various distances z below the bottom of VC1. See Table 4.1 for the operating conditions.

Figure 4.14

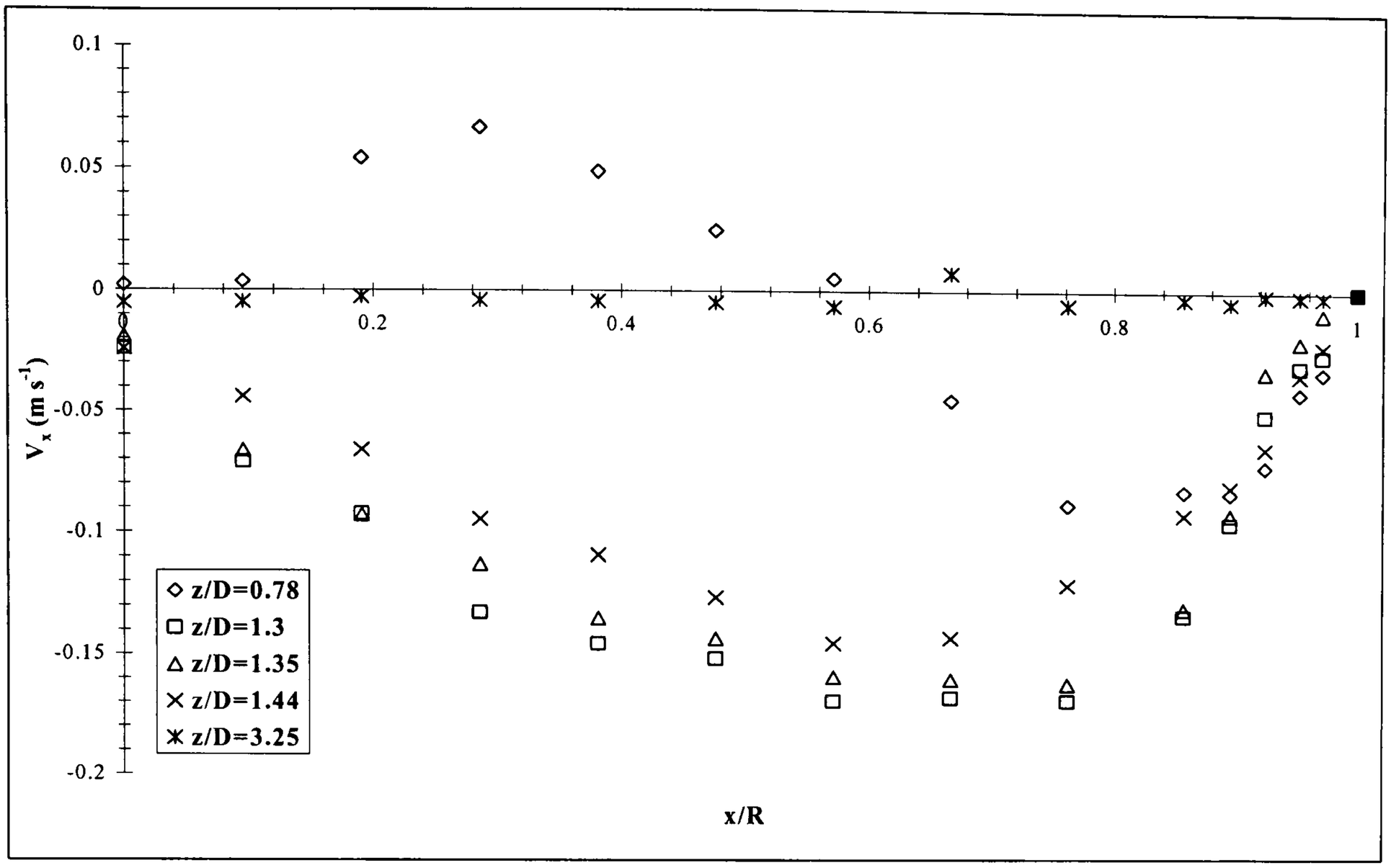

Diametrical velocity distributions for the V_x velocity component at various distances z below the bottom of VC1. See Table 4.1 for the operating conditions.

Figure 4.15

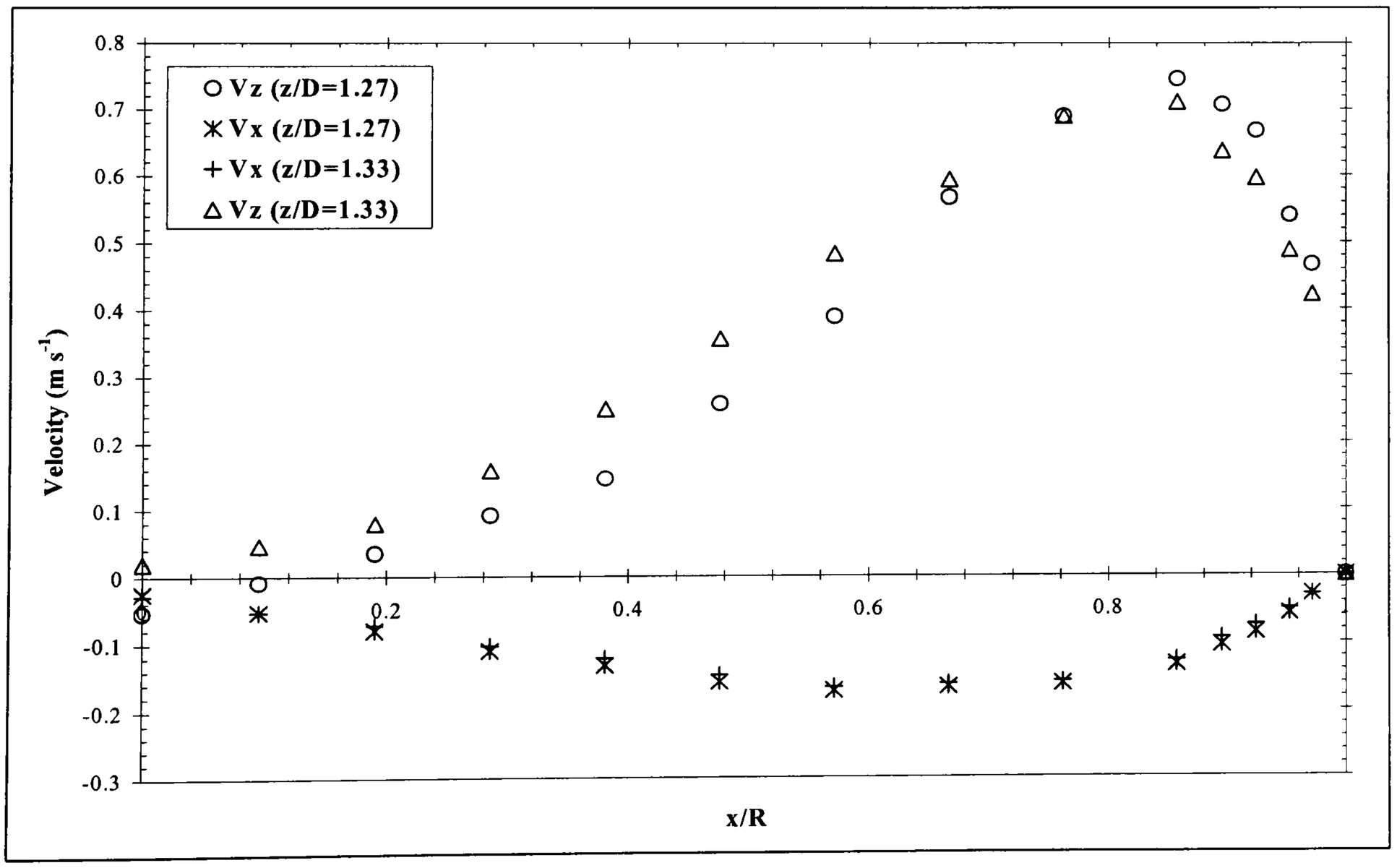

Axial and radial diametrical velocity distributions in the plane of the stagnation point below the bottom of VC2. See Table 4.1 for the operating conditions.

Figure 4.16

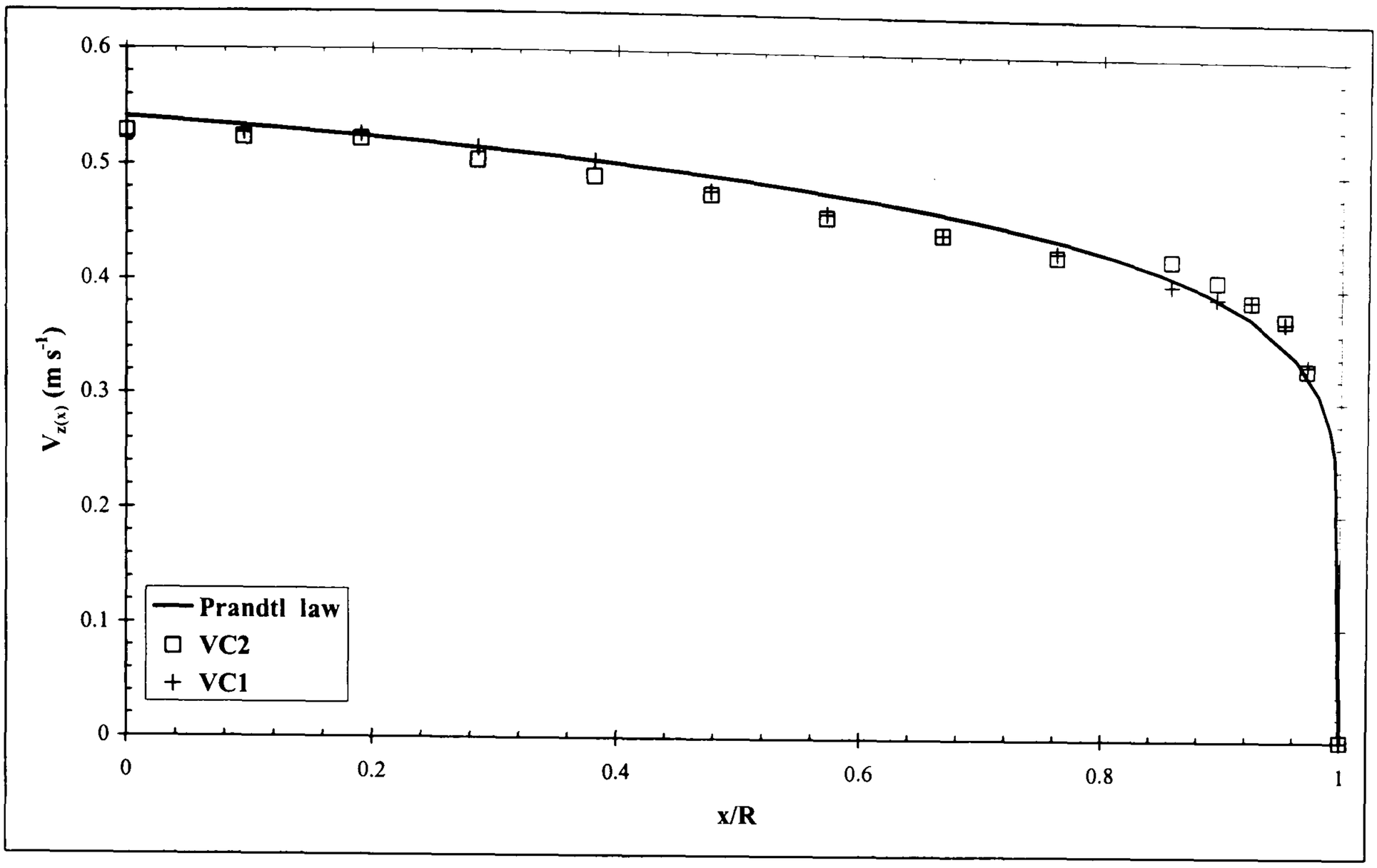

Axial and radial diametrical velocity distributions at $z = 3.25D$ below the bottoms of VC1 and VC2. See Table 4.1 for the operating conditions.

Figure 4.17

In Fig. 4.18 and 4.19 the radial profiles of the r.m.s. values of the axial, V_z' and V_x' velocity fluctuation are shown at different axial locations from the bottom of VC1. The maximum of V_z' was again found near the wall, which is in agreement with Fig. 4.10. It can be seen that the near wall peak of the distribution gradually flattened, reflecting the absorption of the wall jet in the liquid. The r.m.s. values of the V_x velocity fluctuation, V_x' at each axial location below the VC1 were of the same order of magnitude as V_z'. This is again in agreement with the bluff body results (Fig. 4.10).

The above results generally support the proposal of similarity made by Thorpe et al. (2001), reported in the introduction of this chapter. The size of the toroidal vortex formed below the ventilated cavity was almost identical to the one below the bluff body, confirming that the cylindrical bluff body provided a convenient experimental substitute for the study of the flow pattern beneath the cavity.

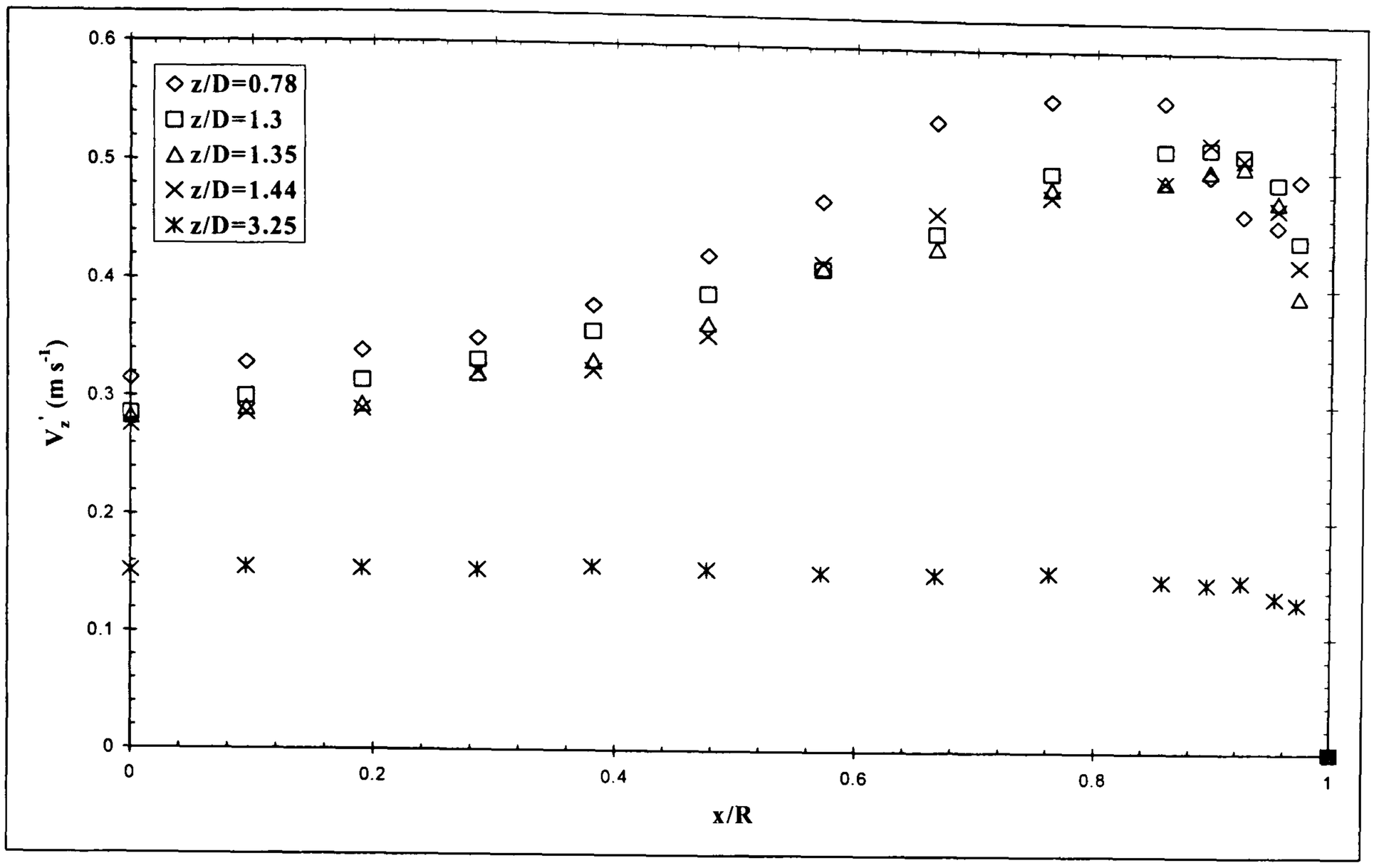

Radial distributions of the r.m.s. values of the axial velocity component, V_z' at various distances z below the bottom of VC1. See Table 4.1 for the operating conditions.

Figure 4.18

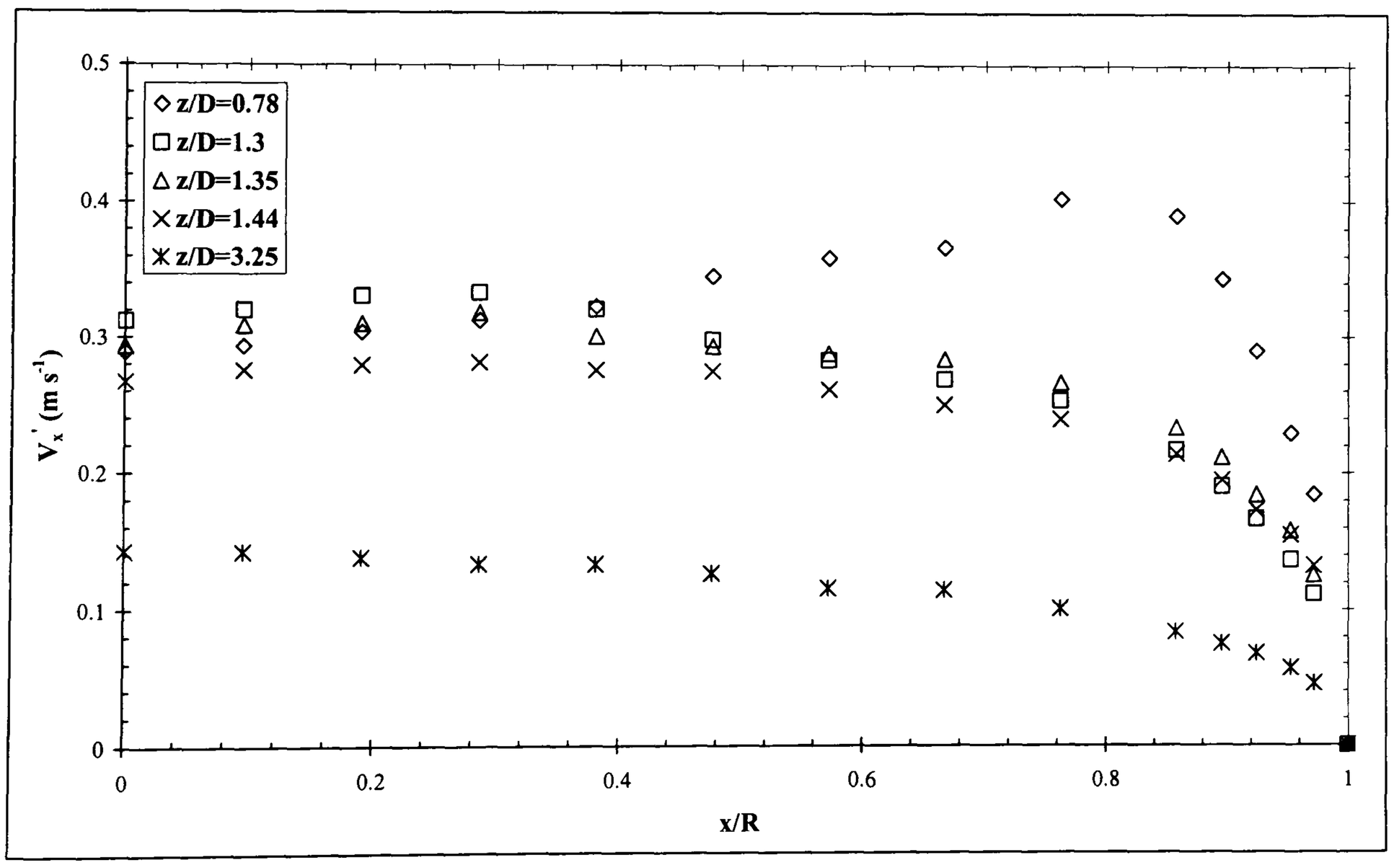

Radial distributions of the r.m.s. values of the radial velocity component, V_x' at various distances z below the bottom of VC1. See Table 4.1 for the operating conditions.

Figure 4.19

The results presented in this Chapter provide a better understanding of the bubble coalescence phenomenon in undeveloped two phase slug flow briefly mentioned in section 4.2. The short liquid film penetration depth in the wake (of around $1.3-1.4D$) of the cylindrical bluff body and the ventilated cavities and the rapid decay of turbulent eddies (Fig. 4.8), suggest that the acceleration of the trailing bubble in two phase slug flow is not directly related to the effect of film penetration and large scale eddies in the wake of the leading bubble. Hasanein et al. (1996) experiments have indicated that deformation of the slug nose and bubble acceleration starts at about 6 D below the tail of the leading bubble, which is much further below the wake length as measured in the presented work. Probably some residual eddies that remain in the liquid flow field (the flow field is still undeveloped at around $3D$ as shown in Figs. 4.9 and 4.17) following the decay of large scale eddies can initiate lateral movements and the deformation of the trailing bubble nose. These two effects then possibly can cause an increase in the rise velocity of the trailing bubble, which eventually will coalesce with the leading one.

4.5 COMPARISON BETWEEN LDV RESULTS AND HILL'S VORTEX PREDICTIONS

The average liquid axial velocity in the re-circulating vortex behind the bluff body in the plane of the eye of the vortex was measured using the methodology described in section 3.9. The results are compared in Fig. 4.20 with predictions based on Eq. (4.4) and are summarized in Table 4.2. The annulus gap used in the model was $\delta = 5$ mm. The model profiles were obtained for two different values of the proportionality constant, K, Thorpe's et al. (2001) value of 0.38 and 0.515; $K = 0.515$ was the value of K in the model which predicted an equal liquid volumetric flow rate, Q_w, inside the toroidal vortex to the experimental one derived from the LDV measurements. The value of $K = 0.515$ was within the range derived from previous studies. (Thorpe et al., 2001).

The experimental liquid volumetric flow rate was derived by numerically integrating the experimental velocity profile of Fig. 4.20. The predicted liquid volumetric flow rate, Q_w, was estimated by numerically integrating the axial velocity, $V_{z(r)}$ inside the vortex:

$$Q_w = 2\pi \int_0^{r_0} V_{z(r)} r dr \tag{4.15}$$

In the center of the vortex, the predicted profile based on the value of $K = 0.38$ agreed better with the LDV results than the fitted profile based on a value of $K = 0.515$. It was also found that

the corresponding maximum experimental axial recirculation velocity, at $r = 0$, was 0.405 times the velocity of the annular flow at the base of the bluff body, which is in excellent agreement with the value of 0.38 in Eq. (4.2). On the other hand, for $K = 0.515$ the predicted maximum axial recirculation velocity was 27% higher of the experimental result as shown in Table 4.2. However, there was a rather high deviation of 35% between the liquid volumetric flow rates with $K = 0.38$. Inside the recirculation region the shape of the three curves in Fig. 4.20 is similar, with the Hill's vortex having a flatter profile at the regions close to the outer boundary of the vortex. The model did not fit very well the experimental data away from the center of the vortex. This is highlighted by the difference in the rotational center of the vortex, $r_0 = 0.640R$ for the model as compared with the $r_0 = 0.666R$ obtained from the experiments.

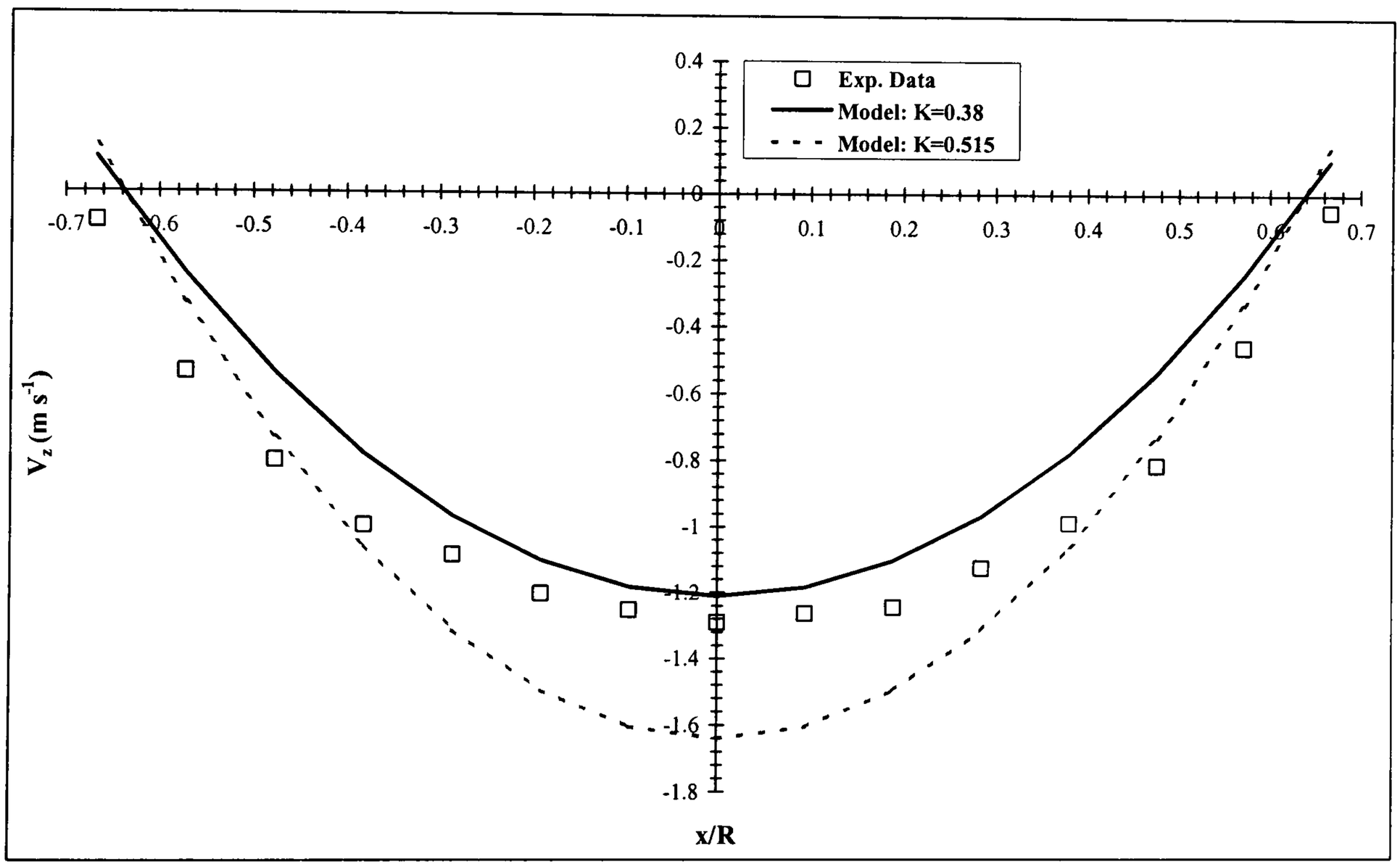

Comparison between Eq. (4.4) and the LDV experiments on the flow behind the bluff body in the plane of the eye of the vortex.

Figure 4.20

The liquid is water and the superficial liquid velocity is 0.577 m s^{-1}.

The model was very sensitive to the definition of the rotational center r_0, a parameter which was deduced assuming the vortex was not squashed by the flow. A difference of only 4% in the rotational center between experimental and predicted values $(K = 0.38)$, yielded a deviation of 35% for the liquid volumetric flow rates, while the magnitudes of the maximum axial re-circulation velocities in the center of the vortex were almost identical. The above becomes

apparent when a rotational center of $r_0 = 0.666R$ and the proportionality constant of $K = 0.38$ are considered. The model then, predicted the maximum axial recirculation velocity and the volumetric liquid flow rate inside the vortex with deviations of only 2% & 18% respectively, from the experimental results for Q_w (Table 4.2).

	Q $\left(\times 10^{-3} m^3 s^{-1}\right)$	r_0/R	$V_{z(\max)}$ $\left(ms^{-1}\right)$	$V_{z(\max)}/V_F$	*Difference*[a] (%)	*Difference*[b] (%)
Bluff Body						
Exp	2.908[c]	0.666	-1.291	0.405	-	-
Model, $K = 0.38$	2.150[c]	0.640	-1.209	0.380	35	7
Model, $K = 0.38$	2.530[c]	0.666	-1.313	0.380	18	2
Model, $K = 0.515$	2.908[c]	0.640	-1.641	0.515	0	27
VC1						
Exp	0.876[c]	0.624	-0.893	0.39	-	-
Model, $K = 0.38$	0.761[c]	0.634	-0.869	0.38	15	3
Model, $K = 0.436$	0.876[c]	0.634	-0.998	0.436	0	12

[α] Difference is defined as $\frac{Q - Q_w}{Q_w} \times 100\%$ 4.1

[b] Difference is defined as $\frac{V_{z(\max)} - V_{Kz(\max)}}{V_{Kz(\max)}} \times 100\%$ 4.2

[c] Based on $Q = 2\pi \int_0^{r_0} V_z x dx$

Comparison with the model of Thorpe et al. (2001).

Table 4.2

The velocity profile for the ventilated cavity (VC1) in the plane of the eye of the vortex and inside the boundaries of the vortex is compared in Fig. 4.21 with predictions based on Eq. (4.4) and the results are summarised in Table 4.2. The theoretical profiles were obtained for $K = 0.38$ and $K = 0.436$ and a plunging film thickness of $\delta = 5.3$ mm (Table 4.2); $K = 0.436$ was the

---

4.1 Difference between experimental and predicted liquid volumetric flow rates divided by the predicted liquid volumetric flow rate.

4.2 Difference between maximum experimental and maximum predicted axial recirculation velocity in the centre of the vortex divided by the maximum predicted axial recirculation velocity in the centre of the vortex.

value of K in the model which predicted a liquid volumetric flow rate equal to the experimental value, Q_w, inside the toroidal vortex derived from the LDV measurements. The value of $K = 0.436$ was within the range derived from previous studies (Thorpe et al., 2001).

There is a much better agreement to the bluff body results in the plane of the eye of the vortex, with only a 15% deviation between predicted and experimental liquid volumetric flow rates. This better agreement is reflected in the position of the rotational center; the experimental rotational centre of the vortex was $r_0 = 0.624R$, which is in excellent agreement with the predicted value of $r_0 = 0.634R$ (Table 4.2). Also, it is found that the corresponding maximum experimental axial recirculation velocity, at $x = 0$, was 0.39 times the velocity of the falling film at the base of the ventilated cavity, which is again in excellent agreement with the value of 0.38 in Eq. (4.2). The reason for the better agreement with the model in the ventilated cavity may be the less perfect connection between the vortex and the falling film caused by entrainment of gas at the plunge point.

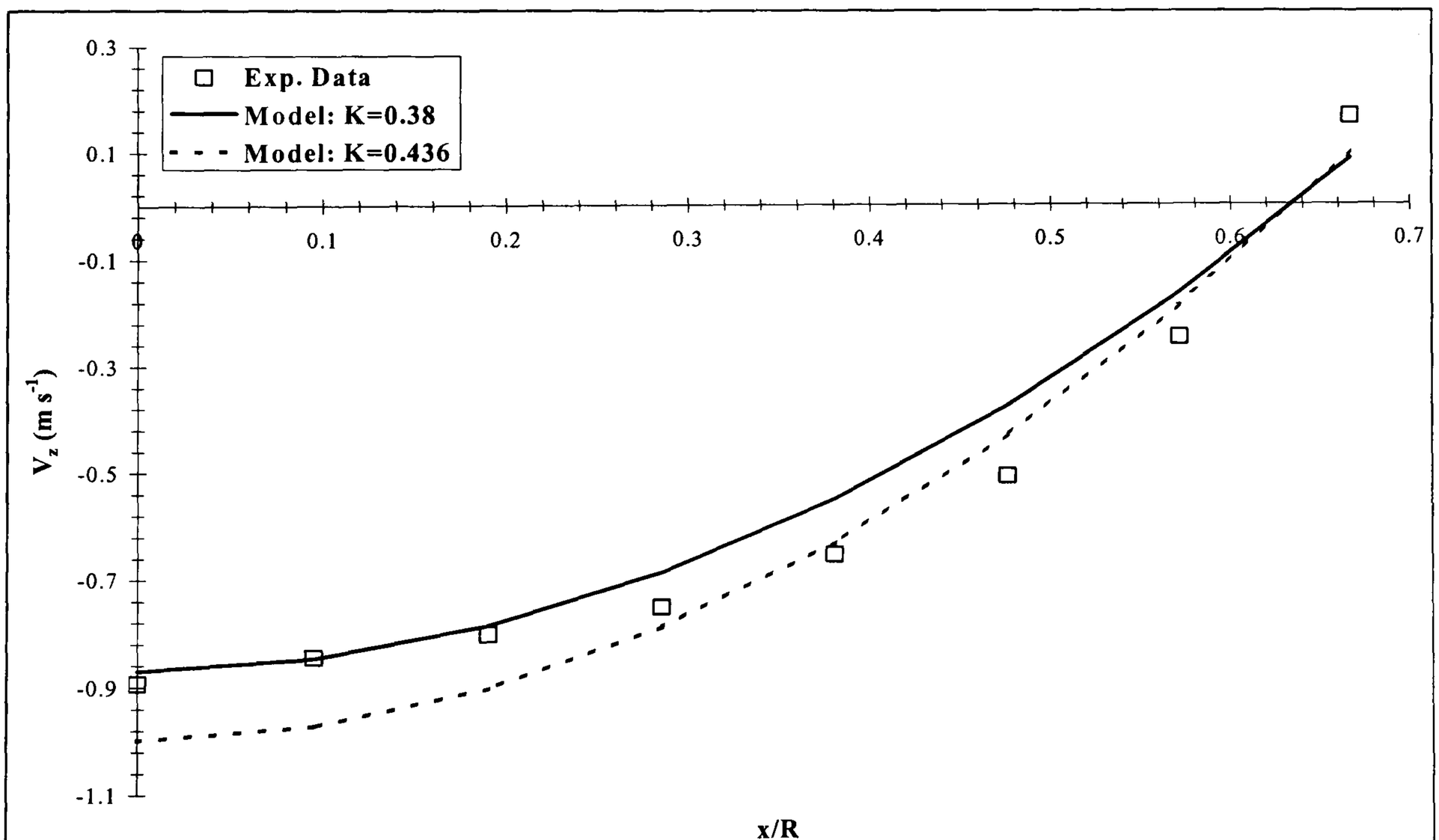

Comparison between Eq. (4.4) and the LDV experiments on the flow behind the ventilated cavity (VC1) in the plane of the eye of the vortex.

Figure 4.21

The liquid is water and the superficial liquid velocity is 0.438 m s^{-1}.

The experimental data obtained by Van Hout et al. (2002) in the plane of the eye of the vortex and inside the boundaries of the vortex behind a slug bubble rising in stagnant liquid are compared with predictions based on Eq. (4.4) in Fig. 4.22. The falling film thickness at the base of the slug bubble, as measured by van Hout et al. (2002), was $\delta = 0.75$ mm. The data were deduced from Figure 3(b) in their paper and were adjusted for the conditions in this work because the cavity was stationary relative to the pipe wall. In every deduced axial velocity, the drift velocity of a Taylor bubble rising in stagnant liquid was added, which for the 0.025 m id pipe used by Van Hout et al. (2002) was 0.174 m s^{-1}. The maximum axial recirculation velocity at the centreline after this adjustment was 0.37 times the falling film velocity at the base of the slug bubble $\left(\frac{V_{z(\max)}}{V_F} = 0.37\right)$. There is a very good agreement between the experimental data and the theoretical profile for $K = 0.38$ thus supporting that Eq. (4.4) is also applicable in the wake of rising slug bubbles. In the plane of the eye of the vortex there is an average deviation of only 21% between predicted and experimental results.

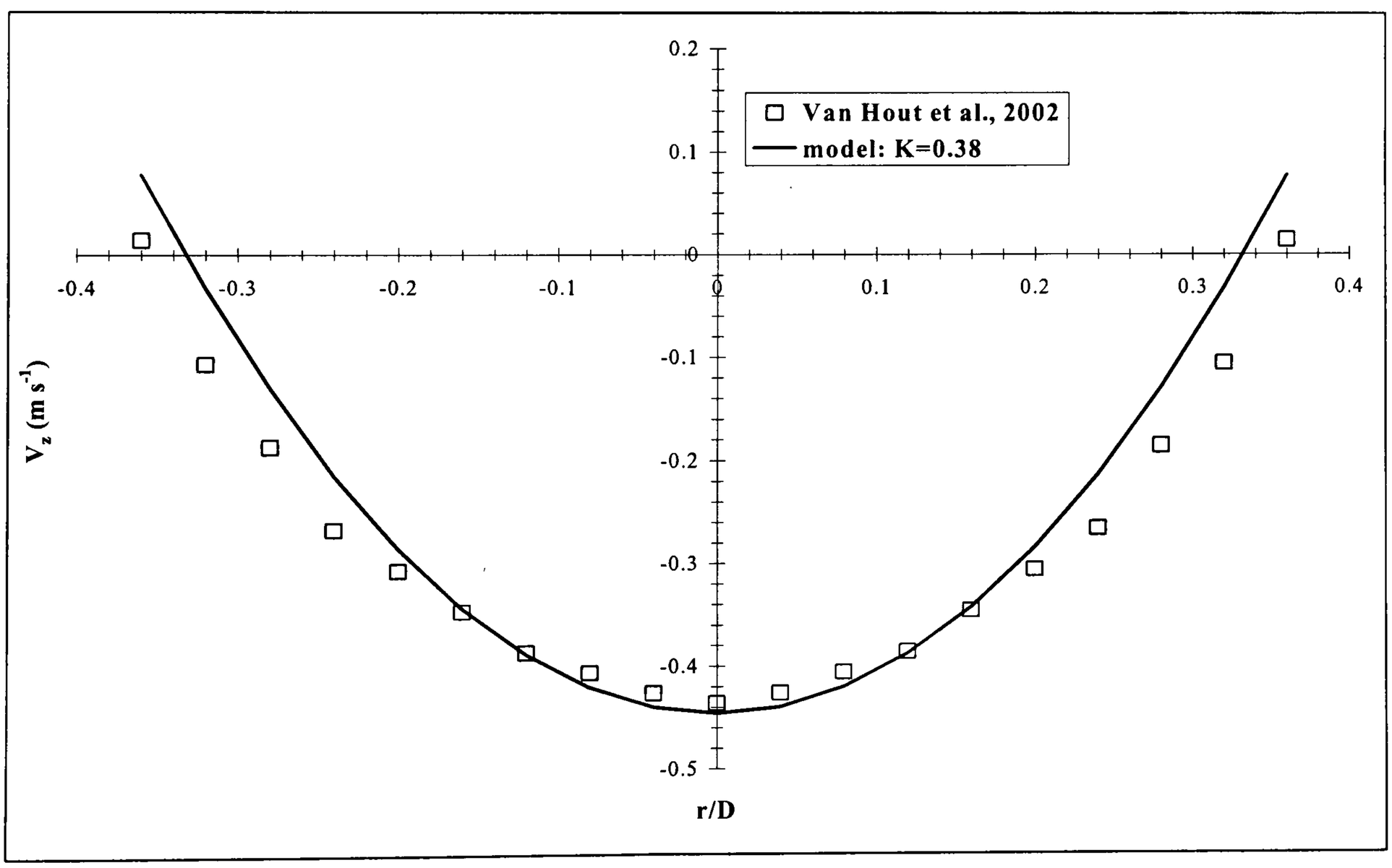

Comparison between Eq. (4.4) and the experimental data for a Taylor bubble of van Hout et al. (2002) in the plane of the eye of the vortex, when adjusted to bring the Taylor bubble at rest relative to the pipe wall.

Figure 4.22

The liquid is water and the superficial liquid velocity is 0 m s^{-1} (rising in stagnant liquid).

The above results generally support the suggestion of Thorpe et al. (2001) that the flow in the wake of the ventilated cavity or a gas slug evolved into a spherical vortex ring where the velocity distribution was close to the theoretical solution of the Hill-type vortex, but only towards the centre of the vortex. It is clear in the vector plot (Fig. 4.9) that the vortex was squashed by the flow and was slightly non axisymmetric.

The fact that a Stokes stream function (Eq. 4.1) described the wake flow field does not imply that the flow was irrotational. However, the Hill's vortex is an explicit vortex because it is an exact incompressible solution to the Euler's axysymmetric inviscid (i.e. without friction) fluid equations. Therefore the flow in the vicinity of the bluff body or the ventilated cavity was on a time-average basis a potential flow (no shearing occurring of fluid elements) and the toroidal vortex behaved as a free vortex especially towards the centre of the pipe. The speed of rotation was about 40% of that in the film, which according to Thorpe et al. (2001) is the driving force of the vortex.

A free vortex such as that described by Hill does not require a lot of energy to drive it (i.e. does not take energy out of the flow). Hence the energy dissipation was very low inside the vortex boundaries below the bluff body and the cavity. Therefore most of the processes that break up the entrained bubbles that determine the resulting bubble size and void fraction further downstream, take place at the outer boundaries of the vortex, in the channel defined by the high downward axial liquid velocities. Also the vortex beneath the bluff body or the cavity was much bigger than any of the turbulent eddies in the pipe (Fig. 4.8) and much more stable with respect to small ring vortices. According to Saffman (1992) any small instability that comes in contact with such a stable ring vortex is spat out as vorticity from its tail so the ring vortex maintains its coherence and stability.

4.6 SIMILARITY LAW

In Fig. 4.23 the CFX simulations of Thorpe et al. (2001) in the plane of the eye of the vortex are plotted against the LDV data of the cylindrical bluff body and the ventilated cavity presented in this work and the data obtained by Van Hout et al. (2002) for a Taylor bubble rising in stagnant liquid. The CFX simulations were carried out for a 0.050 m id pipe and a $\delta = 2.5$ mm film thickness, a flow exactly the same as the flow behind the bluff body in the experiments presented in this thesis. The data have been plotted as V_z / V_F, following Eq. (4.2) and the

suggestion of Thorpe et al. (2001) that the speed of the toroidal vortex was linearly related to V_F. It can be seen from Fig. 4.23 that even if the experiments were carried out in a different pipe size and with a different film thickness, the overall agreement is very good. Especially in the centreline the agreement is excellent with the value of $K = 0.38$ in Eq. (4.2), suggesting that the value of $K = 0.38$ is a value with wide applicability since it successfully describes systems with totally different physical dimensions and boundaries.

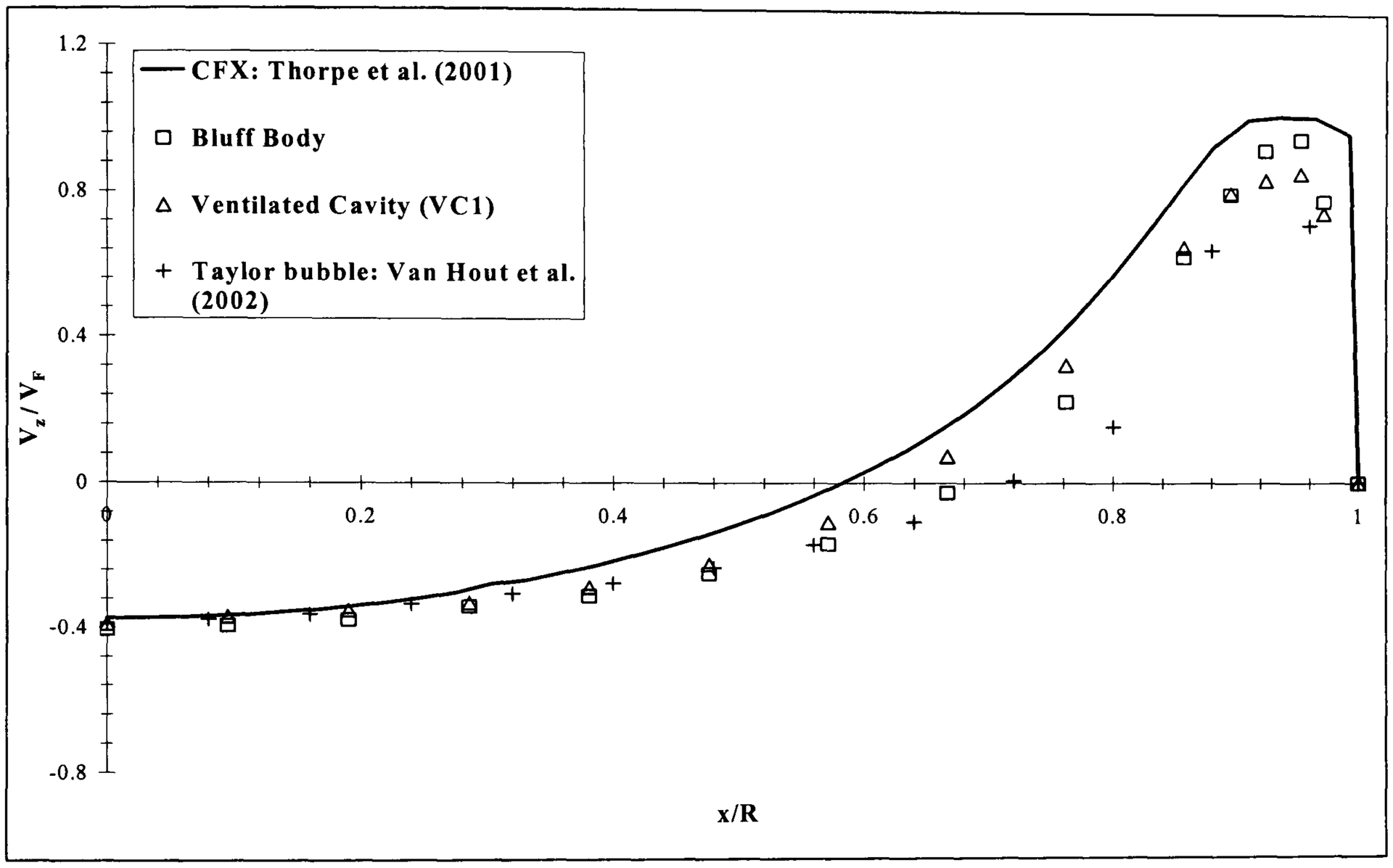

Comparison between the CFX predictions of Thorpe et al. (2001), the LDV experiments and the data for a Taylor bubble of van Hout et al. (2002) in the plane of the eye of the vortex; the comparison is made in dimensionless co-ordinates that should make the data and predictions, which are for different pipe sizes, broadly similar.

Figure 4.23

In an analogous approach, the LDV data in the plane of the stagnation point were plotted as V_z/V_F and the results are presented in Fig. 4.24. The data points are all again collapsing thus supporting the concept behind Eq. (4.2). It is clearly demonstrated in Fig 4.23 and 4.24 that the film velocity primarily determined the velocity field in the wake of the bluff body, a Taylor bubble and the ventilated cavities.

An attempt was also made to correlate the axial and radial r.m.s. velocity fluctuations data in the wake of the two ventilated cavities, the bluff body and the Taylor bubble rising in stagnant liquid by Van Hout et al. (2002). The agreement between the four sets of data was very poor when we correlated the data in the expected dimensionless forms of Eqs. (4.16) and (4.17):

$$V_z'/V_F \qquad \text{and} \qquad V_x'/V_F \tag{4.16}$$

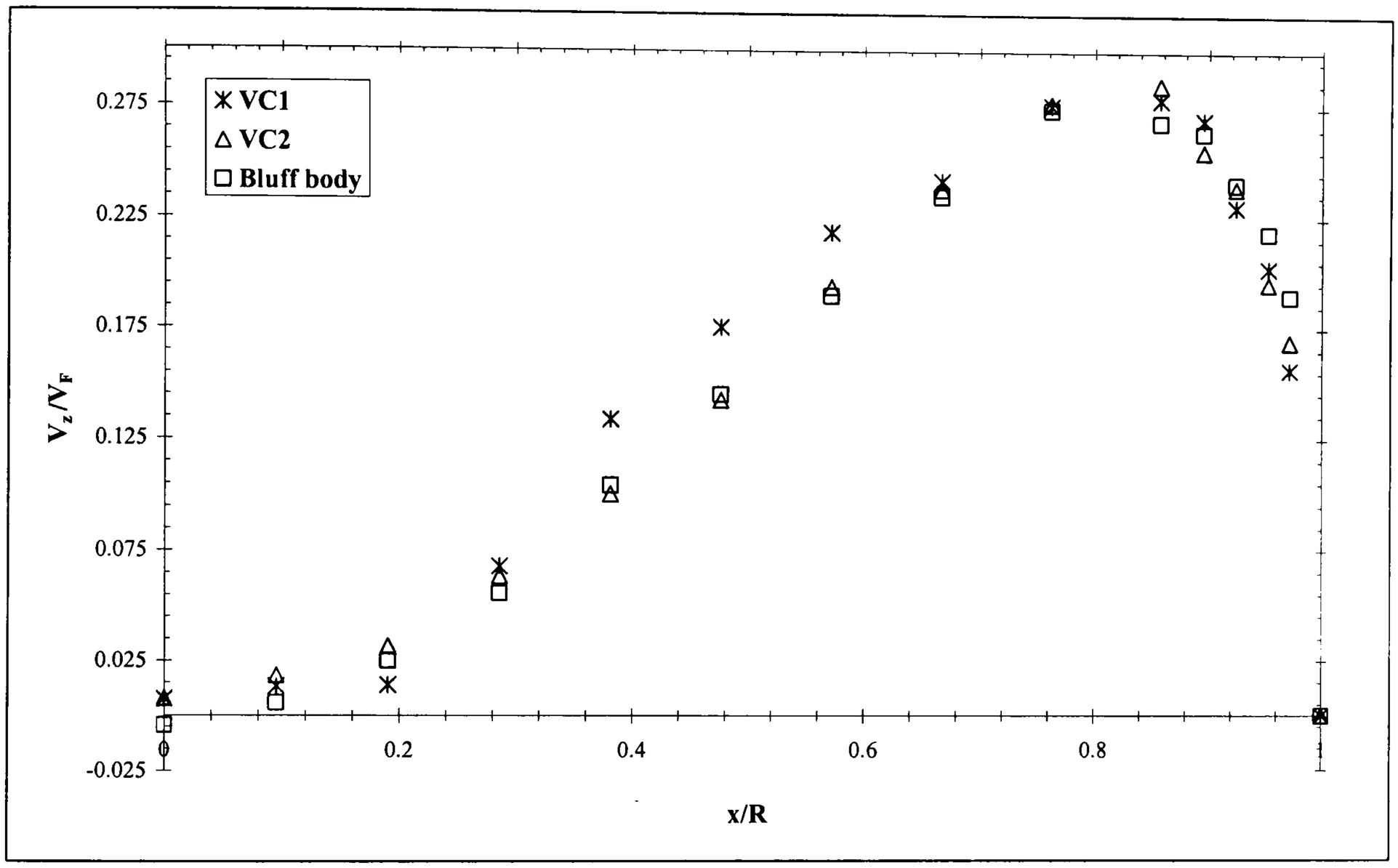

Comparison between the LDV results in the plane of the stagnation point.

Figure 4.24

$$\frac{V_z'\delta}{V_F D} \qquad \text{and} \qquad \frac{V_x'\delta}{V_F D} \tag{4.17}$$

The best way to make the data for the axial and radial r.m.s. velocity fluctuations collapse onto itself, for all four cases was to use the following scaling dimensionless form of Eq. (4.18). The results are shown in Figs. 4.25 and 4.26.

$$V_z'\sqrt[3]{\frac{D^2}{V_F^{\,2}Q_L}} \qquad \text{and} \qquad V_x'\sqrt[3]{\frac{D^2}{V_F^{\,2}Q_L}} \tag{4.18}$$

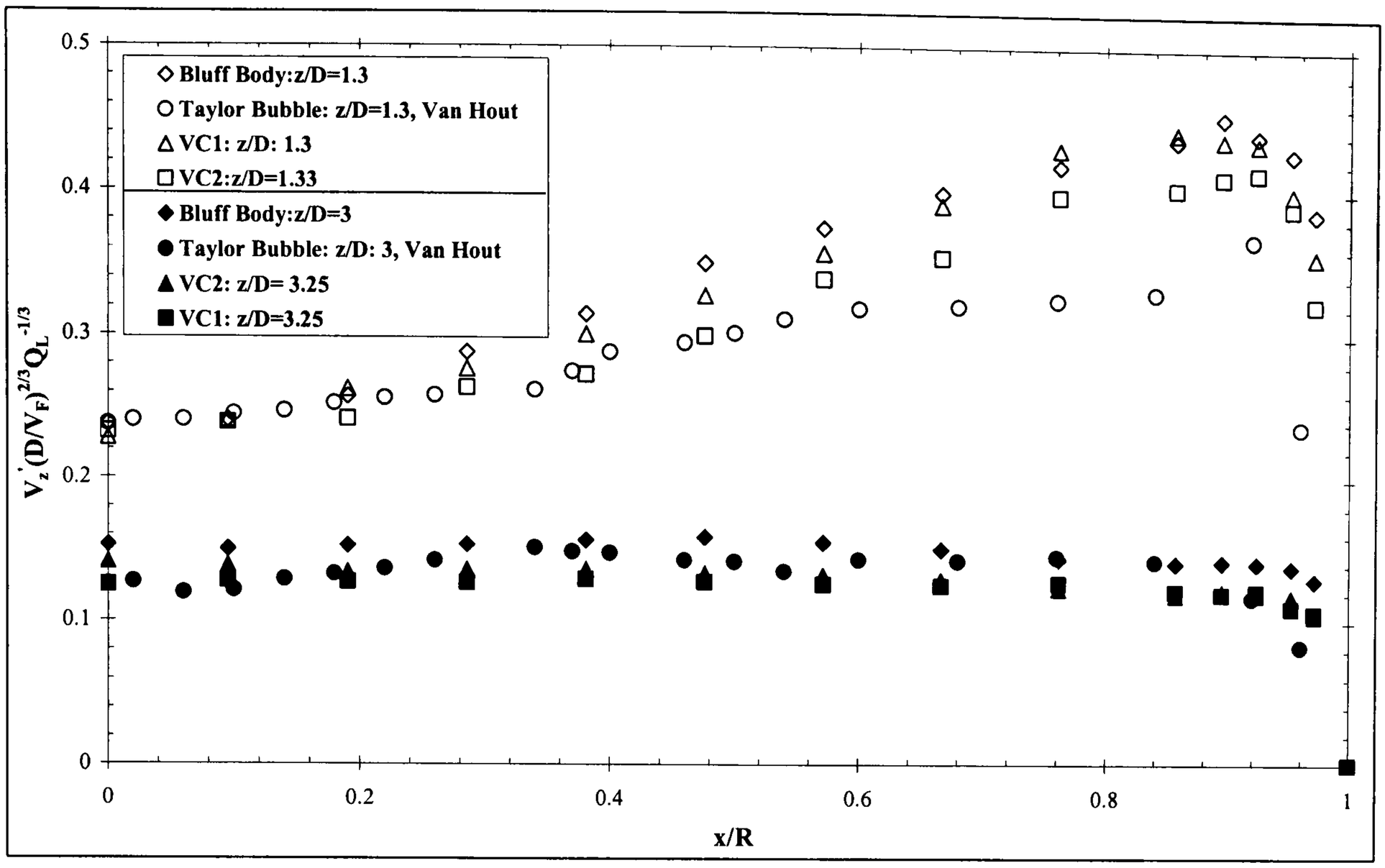

Collapsing of the axial r.m.s. velocity fluctuations data when correlating them in the form of Eq. (4.18).

Figure 4.25

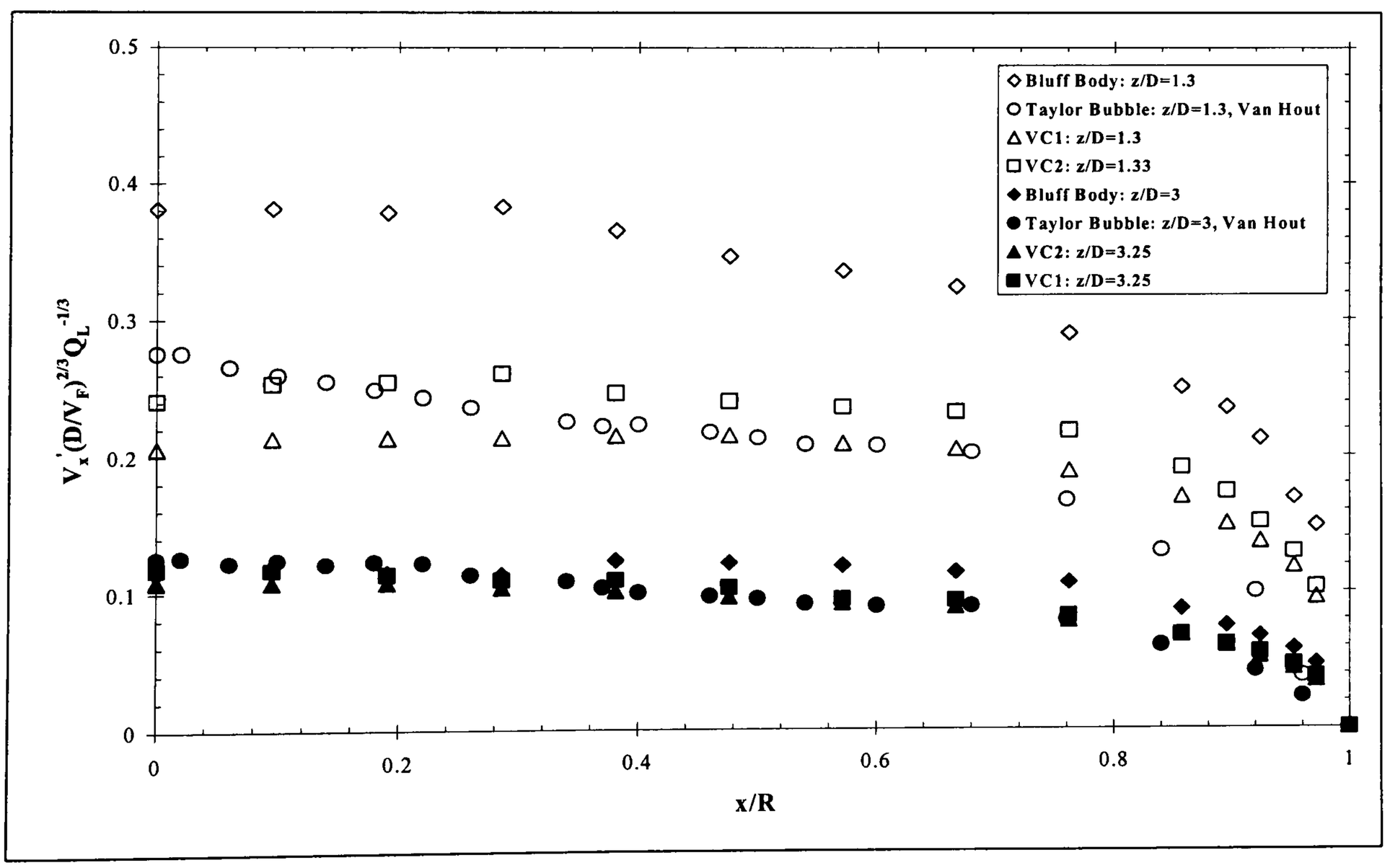

Collapsing of the radial r.m.s. velocity fluctuations data when correlating them in the form of Eq. (4.18).

Figure 4.26

The agreement of the data in Fig. 4.25 for the axial r.m.s. velocity fluctuations between the four cases is pretty good. The data correspond to two different axial locations, at approximately $z = 1.3D$ and $z = 3.2D$. All lines are partially collapsing supporting the suggestion of similarity made by Thorpe et al. (2001). The only discrepancy is in the region $x/R \geq 0.7$ where the correlated data reported by Van Hout et al. (2002) are lower than the rest. This region corresponds to the spreading of the wall jet (see sections 4.4.2 and 4.4.3). As already mentioned (see section 2.3) in the case of the bluff body and the ventilated cavities the liquid film penetrated concurrently a downflowing liquid, whereas for the Taylor bubble in Van Hout's case the liquid film plunged in a countercurrent upflow of liquid in the liquid slug. Hence the turbulence intensity at the plunge point was not the same between them. Also the falling film at the base of the Taylor bubble in the case of Van Hout (2002) was laminar $(\mathrm{Re}_F = 848)$ and not turbulent as in the case of the bluff body $(\mathrm{Re}_F \simeq 60000)$ and the ventilated cavities $(\mathrm{Re}_F \simeq 46000)$. Therefore any differences between the data of Van Hout et al. (2002) and this work are expected in the region marked by the boundaries of the vortex and the pipe wall, i.e. at $x/R \geq 0.7$. For the radial r.m.s. velocity fluctuations (Fig. 4.26) there was some scatter in the plane of the stagnation point but very good agreement further downstream.

4.7 SUMMARY

The velocity characteristics of the turbulent flow field in the wake of a cylindrical bluff body (blockage ratio 82%) and beneath two ventilated cavities attached to a central sparger (blockage ratio 80% and 82% respectively) in turbulent flow were measured using LDV. The results for the time-averaged velocity revealed in detail the formation of a toroidal vortex with very similar characteristics below both the bluff body and the ventilated cavities. The axial boundary of the vortex was defined to be the position of the stagnation point on the centreline, which was found at around $z \simeq 1.32D$ for all cases.

It was confirmed by the experiments that the geometry (i.e. size) of the toroidal vortex formed below the bluff body or the ventilated cavities did not depend on the liquid volumetric flow rate or the speed of the vortex. On the other hand, the speed of the vortex was directly proportional to the film velocity. The film velocity determined the velocity field in the near wake of the ventilated cavity. The speed of rotation was 40% of that in the film, which was the driving force the vortex. Away from the boundaries of the vortex at around $z = 3.25D$ the presence of bubbles

started to have an influence on the flow pattern. This influence was demonstrated by the tendency of the bubbles to flatten the velocity profile.

The model of Thorpe et al. (2001) gave good predictions for the velocity distribution in the centre of the vortex ring against the LDV results of the cylindrical bluff body and the ventilated cavity. The model also agreed well with the experimental data for a Taylor bubble rising in stagnant liquid obtained by van Hout et al. (2002). The ability of the model to predict the volumetric flow rate of the vortex, Q_w, was very sensitive to the definition of the rotational center r_0, which determined the boundary of the vortex. Consequently the deviations in the determination of Q_w were many due to the small inaccuracy in the prediction of r_0.

It seems that the flow in the wake of a ventilated cavity evolved into a spherical vortex ring where the velocity distribution was close to the theoretical solution of the Hill-type vortex. The Hill-type vortex is a potential vortex (inviscid vortex). That means that the vortex in the wake of a cavity did not need a lot of energy to drive and thus little or no energy was dissipated inside it.

The radial distributions of the r.m.s. values of the axial, V_z' and V_x' velocity fluctuation indicated a recirculation region of intense turbulence followed by dissipation further downstream. The above results suggest that the bluff body provided a convenient experimental substitute for the study of the flow pattern beneath the ventilated cavity.

*CHAPTER 5

BUBBLE SIZE DISTRIBUTION & MASS TRANSFER

5.1 INTRODUCTION

The interfacial area is the available area for mass transfer and is an essential parameter in the design of gas-liquid contacting systems. Interfacial area determines the productivity of bioreactors and is most often the limiting factor of the reactor performance (Chisti, 1989). To achieve high interfacial area for mass transfer in a gas-liquid system the two phases are usually come in contact in a form of a bubbly dispersion. However the success of such a dispersion in downflowing liquids can be undermined by the presence of a ventilated cavity attached to a sparger. The ventilated cavity reduces the available area per unit volume for mass transfer, which can result in a reduced yield from a fermenter (see Chapter 1).

Bacon (1995a) and Lee (1998) who studied the behavior of ventilated cavities in terms of the effects of sparger design, liquid physical properties and operating conditions (gas and liquid flow rates), showed that for all the liquids used in their experiments under the same operating conditions a ventilated cavity of any significant length, could be shortened by replacing the common industrial design of a horizontal sparger (HS) by either of two novel spargers; a peripheral sparger (PS) and a plunging jet sparger (PJS) (see section 2.4). The PJS was found to have the best performance of all the spargers investigated as it produced the shortest cavities and had the greatest resistance to stall at low liquid flow rates.

But it is essential to establish whether the shortened ventilated cavities of the PS and PJS do in fact increase the overall rate of mass transfer. If both spargers have inferior mass transfer capabilities to the HS, then their advantages with respect to the cavity length will be equivocal. Mass transfer capacity is often determined in gas-liquid systems by measuring the volumetric mass transfer coefficient $k_L a$. The $k_L a$ provides information on the ability of a system to

---

* Some of the results of this chapter have been published in:

Sotiriadis, A. A., Thorpe, R. B. and Smith J. M., (2005), Bubble size and mass transfer in sparged downwards two-phase flow, *Chemical Engineering Science*, **60**, 5917-5925.

dissolve gaseous reactant; in the case of fermentation plants the $k_L a$ value has an important influence on the growth and metabolism of the cells and hence the productivity of the plant.

There is no information available in the literature on bubble size and mass transfer for systems with gas injection in the downcomer. Therefore any experimentally determined bubble size or gas-liquid mass transfer coefficient would be of very significant value. Hence this chapter considers the effects of sparger design on (1) the resulting dispersed bubble size and its distribution and (2) the volumetric gas-liquid mass transfer coefficient, $k_L a$. Four different sparger designs – a horizontal, a central, a peripheral and a plunging jet sparger - were investigated in the current work and the findings for each sparger will be considered in detail. Then a comparison of the different sparger performances will be carried out.

5.2 BUBBLE SIZE DISTRIBUTION

The bubble size distributions were determined by non invasive image processing according to the method described in section 3.8. The captured images provided a two-dimensional representation of the bubbles in the column and the outline of the bubbles needed to be interpreted accurately to reflect the volume in three-dimensions. Depending on the shape of the bubbles there are two different approaches in the literature to measure bubble size. For small and nearly spherical bubbles an equivalent bubble diameter is estimated based on the image area. The assumption of spherical shape and the assumption of spherical shape (Camarasa et al., 1999) leads to the area average bubble diameter defined by:

$$d_{area} = \sqrt{\frac{4A_b}{\pi}} \tag{5.1}$$

where A_b is the projected area of a bubble in the plane of the two-dimensional image. The bubbles in our system were clearly not spherical. On the other hand, for ellipsoidal bubbles the major and minor axis of the image are measured. The third dimension is calculated assuming that the bubbles are symmetric around the minor axis (i.e. the shape resembles a flying saucer). The bubble diameter is then calculated by assuming a sphere of volume equal to the volume of the ellipsoid bubble (Wongsuchoto et al., 2003; Couvert et al., 1999). In the experiments in this work the majority of the bubbles were ellipsoidal (Figs. 5.1a and 5.1b). The shape was taken to resemble a flying saucer rather than a rugby ball. Bubbles shaped like a rugby ball are highly unstable, are not expected in a geometry where a ventilated cavity is attached to a sparger

(Smith, 2004) and are scarcely ever encountered in the literature for gas-liquid flows. The volume equivalent bubble diameter, d_v, was therefore calculated as:

$$d_v = \sqrt[3]{d_1^{\,2} \times d_2} \tag{5.2}$$

where d_1 and d_2 were the major and minor axis lengths of the ellipsoid respectively in a two dimensional projection (Fig. 5.1c). The number average bubble diameter, d_b and the mean volume-surface diameter or Sauter mean bubble diameter, d_{32}, were subsequently calculated from the sample of N_b bubbles for each experiment by:

$$d_b = \sum_{i=1}^{Nb} d_{vi} / N_b \tag{5.3}$$

$$d_{32} = \frac{\sum_{i=1}^{Nb} d_{vi}^{\,3}}{\sum_{i=1}^{Nb} d_{vi}^{\,2}} \tag{5.4}$$

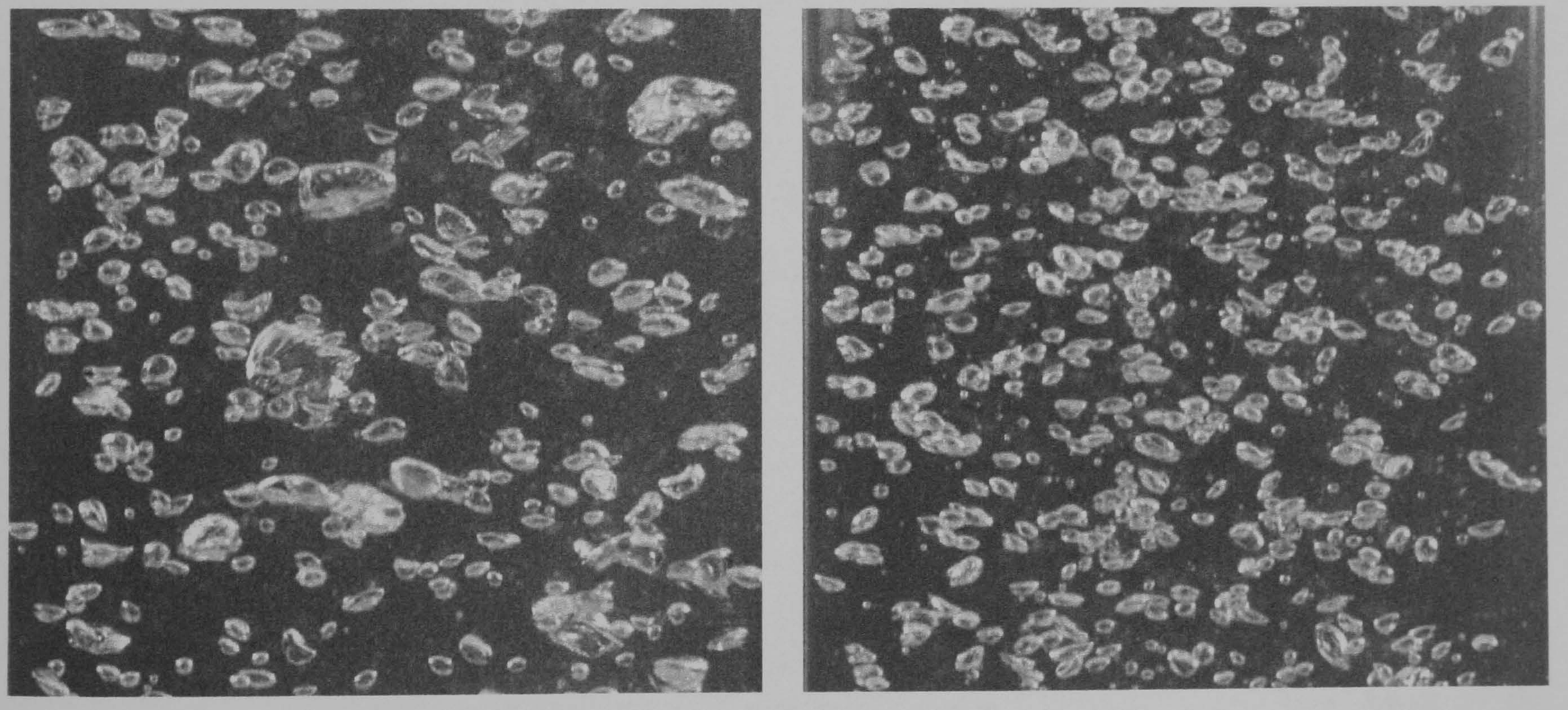

(a) (b)

(This space intentionally blank)

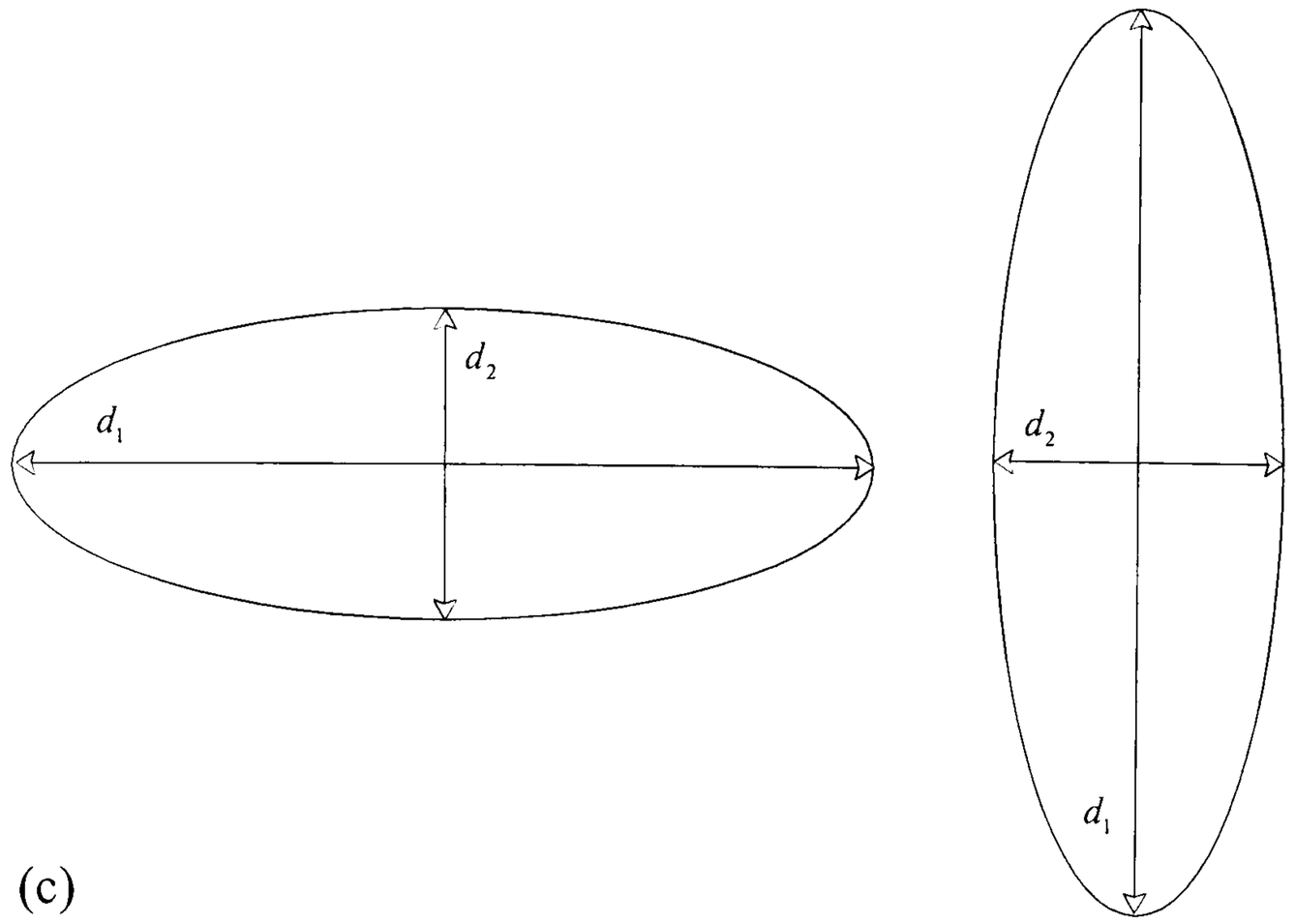

(c)

Typical images obtained in the bubbly flow beneath the spargers in this work showing that the bubbles were mostly ellipsoidal (a) HS for Case II (see Table 5.1), (b) PJS for Case II (see Table 5.1) and (c) major and minor axis lengths of an ellipsoidal bubble.

Figure 5.1

The Sauter mean diameter is useful when comparing the experimental results for different bubble size distributions. The ratio of the standard deviation of the sample to the mean diameter is commonly used to give an indication of the range of bubble sizes. For a unimodal distribution the standard deviation and the mean value are clearly defined and their ratio is easily calculated. On the other hand for bimodal distributions the interpretation of the mean value and standard deviation are not clear and the ratio of the Sauter mean to the maximum bubble diameter is then used to indicate the spread of the distribution.

For each set of measurements, the observed maximum bubble diameter, $d_{max,}$ of five different images was measured according to Eq. (5.3) and the average value was taken. Most of the studies in the literature quote the 99.9 percentile, $d_{99.9}$, instead of the maximum observed bubble size. Therefore for meaningful comparisons with these works, the 99.9 percentile, $d_{99.9}$, was estimated, which was defined as the bubble diameter that was greater than 99.9 % of all the diameters in the cumulative distribution. The 99.9 percentile was estimated by the following equation:

$$d_{99.9} = ll_{99.9} + \left(\frac{N_b P - cf}{f_i} \right) w \tag{5.5}$$

where $ll_{99.9}$ was the lower limit of the interval containing the 99.9th percentile, P was the proportion corresponding to the 99.9th percentile, cf was the cumulative frequency of scores below the 99.9th percentile, f_i was the number of scores above the 99.9th percentile and w was the width of the bubble class.

	Q_L $\left(m^3 s^{-1}\right)$	Q_G $\left(m^3 s^{-1}\right)$	j_L $\left(ms^{-1}\right)$	j_G $\left(ms^{-1}\right)$	Q_G/Q_L	ε_G $(\%)$	L_B (mm)	μ_L $\left(kgm^{-1}s^{-1}\right)$	ρ_L $\left(kgm^{-3}\right)$	σ $\left(Nm^{-1}\right)$
Case I										
	0.00825	0.000037	0.95	0.0043	0.0045			0.00101	995	0.0725
CS						0.4	35			
HS						0.4	35			
PS						0.4	45			
PJS						0.39	0			
Case II										
	0.00825	0.00016	0.95	0.0185	0.0194			0.00101	995	0.0725
CS						1.8	80			
HS						1.8	100			
PS						1.8	100			
PJS						1.8	0			
Case III										
	0.01362	0.00016	1.57	0.0185	0.0117			0.00101	995	0.0725
CS						1.2	35			
HS						1.2	20			
PS						1.2	85			
PJS						1.2	0			
Case IV										
		0.00023						0.00101	995	0.0725
HS	0.0095		1.10	0.0266	0.0242	2.0	100			
CS	0.0093		1.07	0.0266	0.0247	2.1	100			
Case V										
	0.0155	0.00046	1.79	0.0531	0.0297			0.00101	995	0.0725
HS						2.7	100			

Summary of the operating conditions for the bubble size measurements.

Table 5.1

The bubble size was determined from images for the operating conditions of Table 5.1. The liquid physical properties and the bubble length were measured according to the methods outlined in Chapter 3 and are also shown in Table 5.1. The void fraction was not measured but

was estimated using the correlation suggested by Wallis (1969). Care was taken to ensure that for the range of d_{32} obtained in this study the correct terminal bubble velocity was estimated and then applied to the Wallis correlation (see section 4.4). The bubble sizes for the PS and PJS were not measured for Cases IV and V. These two Cases corresponded to some initial measurements taken for a constant bubble length and are only presented here to increase the amount of data that will be tested further below (see section 5.4) with existing models and empirical correlations from the literature.

The results presented in Tables 5.1 and 5.2 revealed that the PJS had a superior performance over the other spargers in all of the different cases investigated. Compared to the other spargers the PJS did not allow the formation of a ventilated cavity (Table 5.1), produced significantly smaller bubbles and gave the smallest Sauter mean bubble diameter (Fig. 5.2). The likely consequence is that the PJS produces a high gas-liquid interfacial area, which is desirable for mass transfer purposes. On the other hand, the HS, CS and PS produced very similar bubble sizes (differences within 10% of the HS results in most cases) and are therefore likely to have produced similar gas –liquid interfacial areas for mass transfer.

It can be seen from Table 5.2 that the PS produced the longest cavities over the range of air and water flow rates used in this work. This is somewhat misleading since it has already been mentioned that the PS can produce shorter cavities than HS and CS (Lee, 1998). With the PS at low gas flow rates six individual bubbles appeared to be attached to the air holes of the sparger. When the air flow rate was increased these individual bubbles coalesced to produce an annulus of air around the downcomer wall, with the water flowing down the center of the tube. Most of the ventilated cavity length measurements by Lee (1998) were made at moderate to high air flow rates when this air ring had already been formed. However, in the present study, in order to be able to measure the resulting bubble size accurately, moderate liquid speeds and low void fractions were needed requiring low air flow rates that did not lead to the air annulus formation. Hence, the cavity length measurements for the PS corresponded to the average length of the six individual bubbles and not to a single cavity as was the case for the rest of the spargers.

It was found that the bubble size increased with increasing air flow and decreased with increasing water flow regardless of the sparger used (Table 5.2). The only discrepancy to this general trend was the behavior of the PS between Cases I and II. The air entrainment mechanism was very different between these two cases. In Case I there was a cyclic behaviour in which the six individual cavities grew continuously until a large portion of air was cut off their main body

and carried downwards within the bulk flow. This returned the cavity to its original size. The "large portion" was then broken up by the flow but resulted in large Sauter mean bubble diameter. This anomaly of the PS is much better depicted in the cumulative distribution in Fig. 5.2, where the results for all spargers are plotted together. The presence of larger bubbles is obvious in the case of the PS. On the other hand, for the operating parameters of Case II the six individual cavities were much more stable and smaller bubbles were entrained from their base.

	N_b	d_b [a] (mm)	d_{32} [a] (mm)	$d_{\max}$ (mm)	$d_{99.9}$ (mm)	$d_{32}/d_{99.9}$	Difference[b] (%)
Case I							
CS	312	2.52 ± 0.11	3.27 ± 0.14	6.09	5.84	0.56	10.2
HS	382	2.67 ± 0.11	3.61 ± 0.14	7.40	6.46	0.56	-
PS	290	3.10 ± 0.25	7.11 ± 0.53	12.88	6.49	1.09	- 49.3
PJS	621	1.74 ± 0.06	2.37 ± 0.08	4.15	3.85	0.62	52.2
Case II							
CS	626	2.72 ± 0.08	3.50 ± 0.10	7.47	6.46	0.54	6.5
HS	782	2.68 ± 0.08	3.73 ± 0.11	9.18	6.46	0.58	-
PS	643	2.54 ± 0.07	3.32 ± 0.09	10.08	6.34	0.52	12.2
PJS	1127	2.21 ± 0.05	2.85 ± 0.07	4.95	4.72	0.60	30.9
Case III							
CS	965	2.36 ± 0.05	3.02 ± 0.07	6.09	5.88	0.51	1.2
HS	461	2.39 ± 0.08	3.05 ± 0.10	5.55	5.27	0.58	-
PS	794	2.29 ± 0.06	3.05 ± 0.08	7.00	6.37	0.48	0
PJS	555	1.78 ± 0.07	2.48 ± 0.09	4.09	3.91	0.63	23.1
Case IV							
HS	339	2.72 ± 0.09	3.21 ± 0.10	5.77	5.42	0.59	-
CS	339	2.55 ± 0.09	3.13 ± 0.11	5.83	5.42	0.58	-
Case V							
HS	476	2.34 ± 0.06	2.62 ± 0.07	4.27	3.94	0.66	-

[a] The uncertainty is based on a 95% confidence interval.

[b] Difference is defined as $\frac{d_{32HS} - d_{32}}{d_{32}} \times 100\%$

Summary of the bubble size results.

Table 5.2

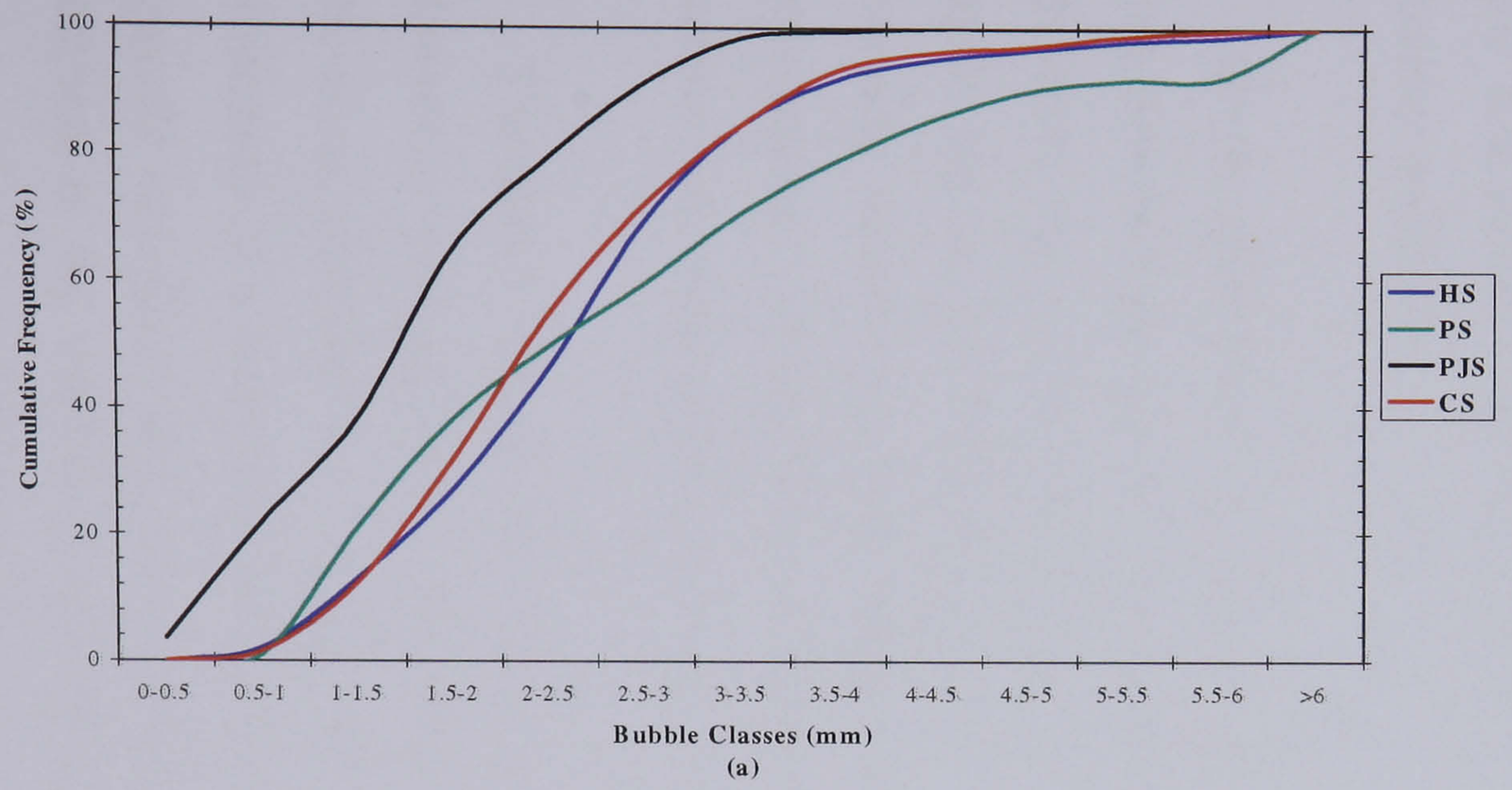

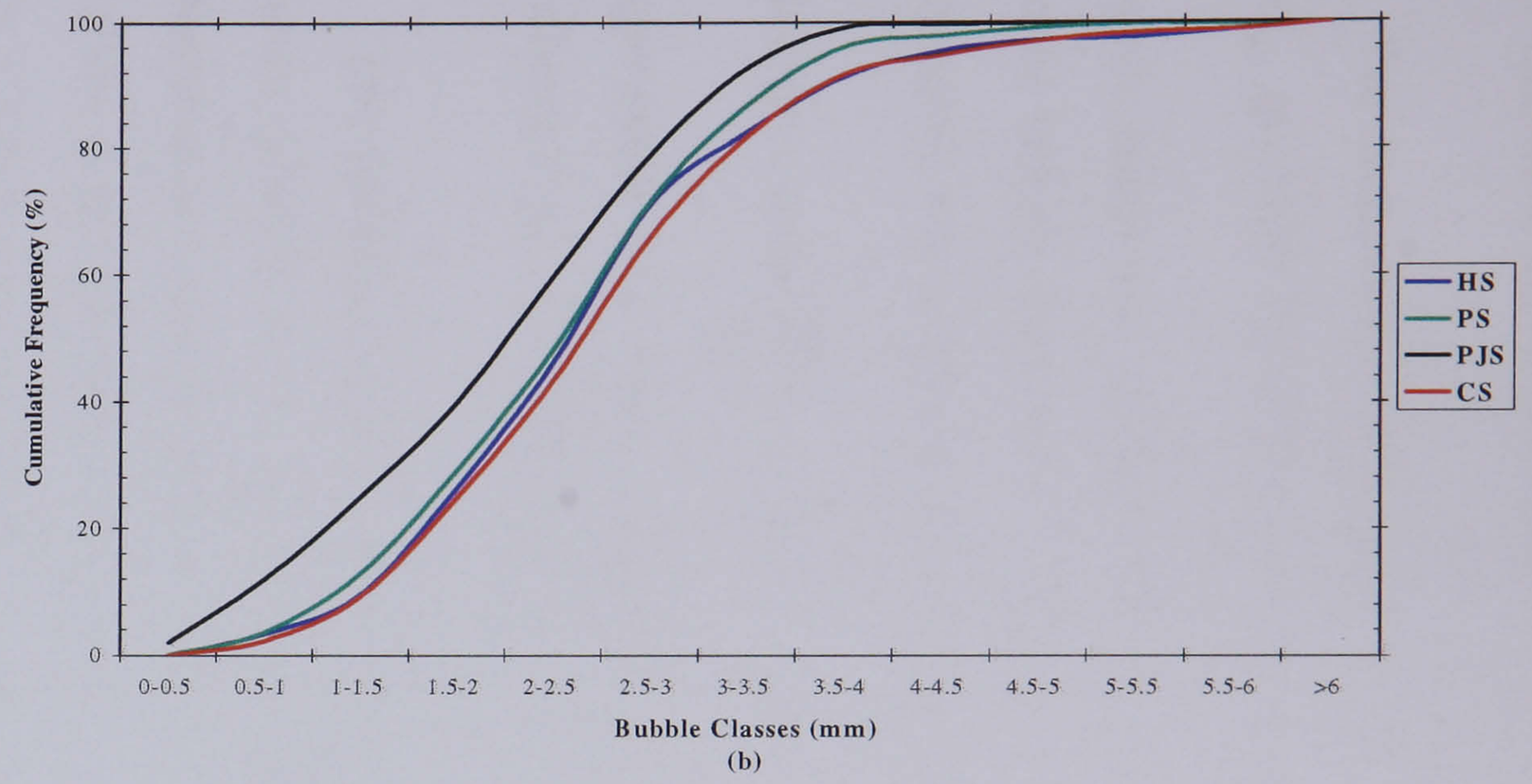

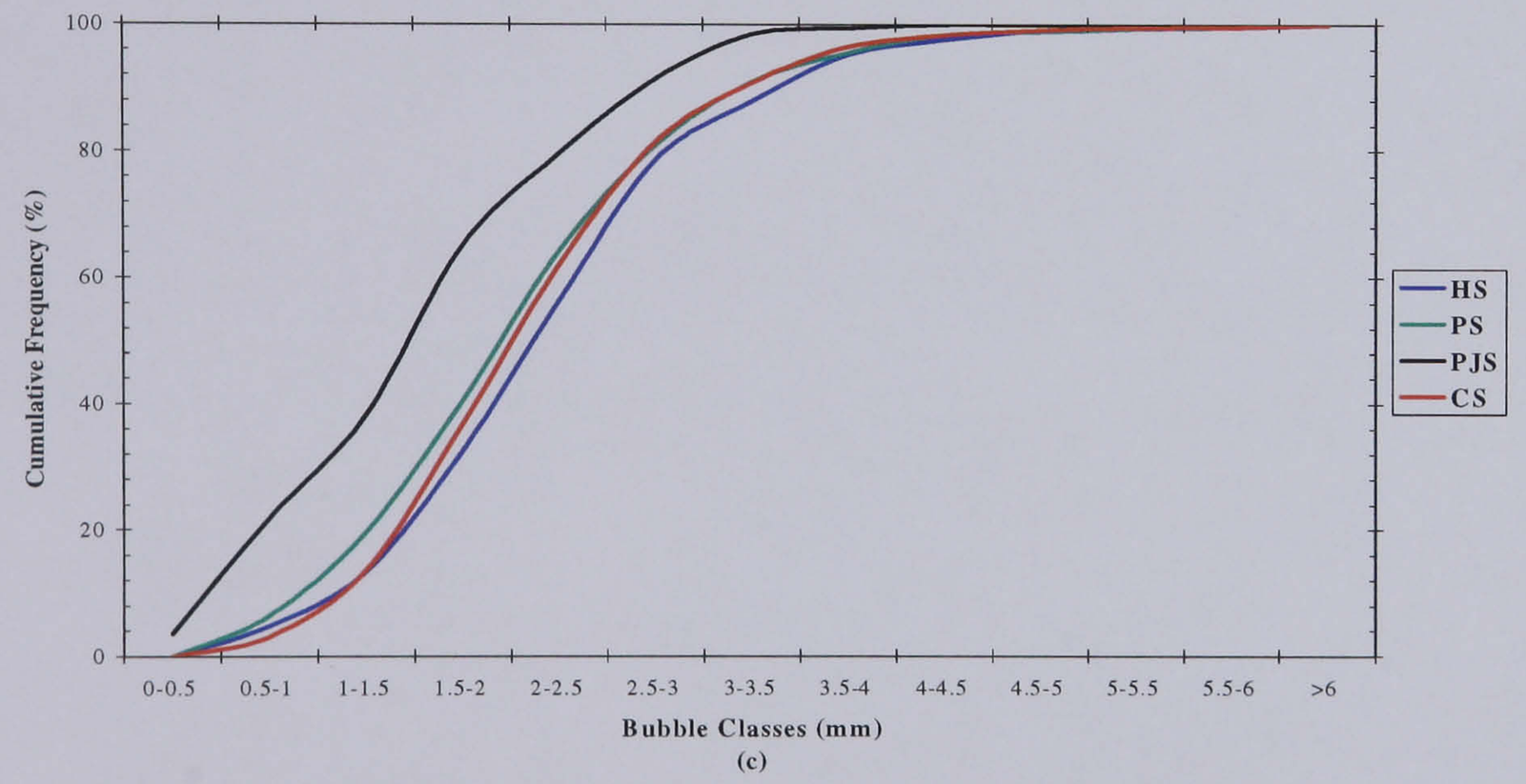

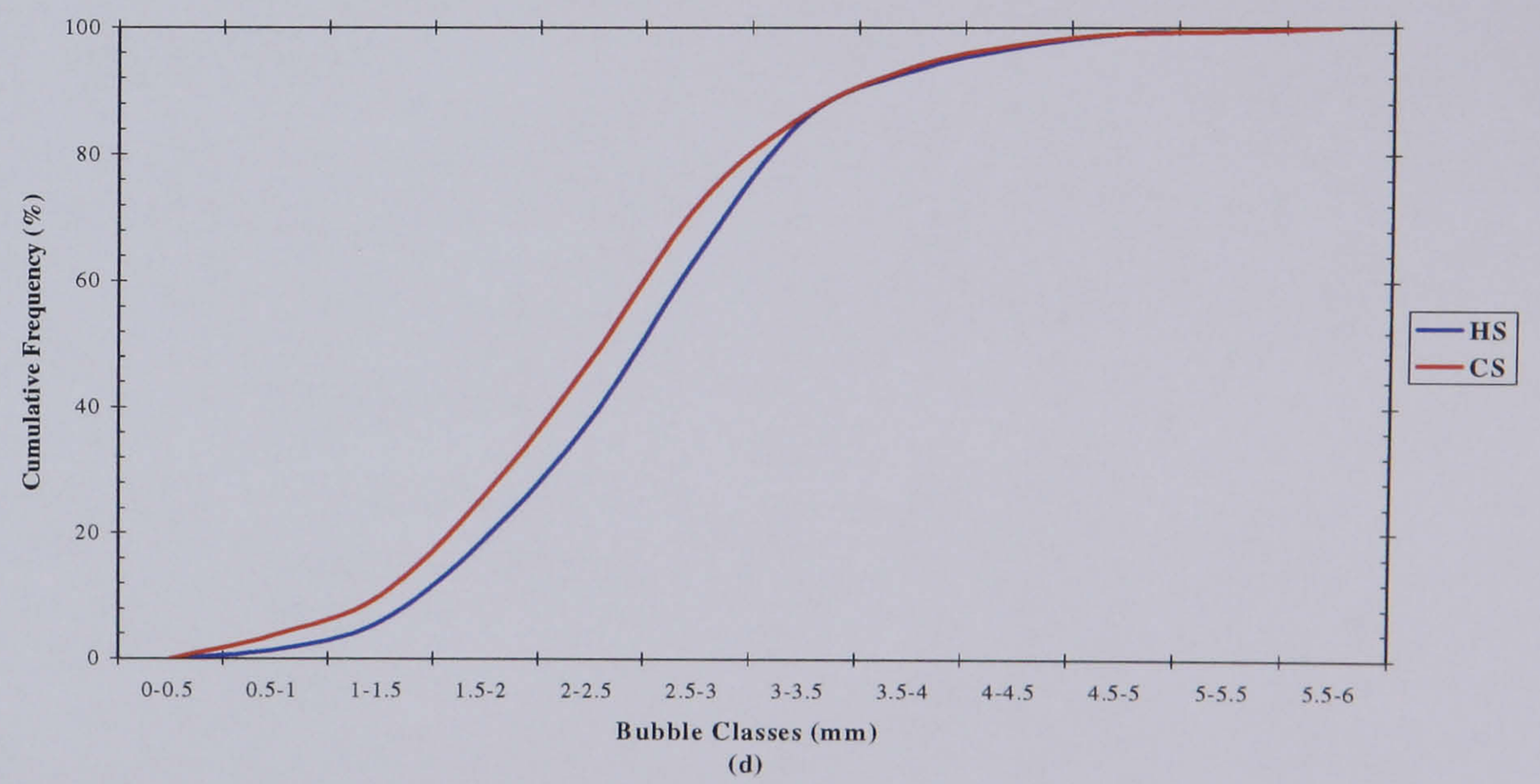

Cumulative distribution curve of the mean bubble diameter (d_b) for (a) Case I, (b) Case II, (c) Case III and (d) Case IV.

Figure 5.2

For comparison with other studies in the literature the results were normalised with respect to $d_{99.9}$ given by Eq. (5.5). In Case I the PS had the largest value of $\frac{d_{32}}{d_{99.9}}$ (Table 5.2) because of the cyclic behaviour discussed in the above paragraph. Due to this anomaly the measured Sauter mean bubble diameter for Case I for the PS was larger than the 99.9% percentile (Table 5.2) and therefore the normalised ratio $\frac{d_{32}}{d_{99.9}}$ was larger than unity. The average value for the bubble diameter ratio $\frac{d_{32}}{d_{99.9}}$ from all of the experiments was found to be 0.61. This result is in excellent agreement with other published values in the literature, which are in the range of 0.6 - 0.62 (Zhang et al., 1985; Hesketh et al., 1987; Calabrese et al., 1986; Evans et al., 1992).

The bubble diameter distributions for all Cases for the HS, CS and PS were unimodal and when plotted on a log-probability scale almost followed a straight line. Such a typical distribution curve is presented in Fig. 5.3a for the HS for Case III. The data in this figure almost follow a straight line implying that the bubble size distribution could be reasonably represented by a log-normal distribution. The log-normal distribution might be the result of the breakup of the less stable larger bubbles by the shearing liquid forces in preference to the more stable smaller bubbles.

On the other hand, the results for all Cases for the PJS were different as shown in Fig. 5.3b. It can now be seen that the resultant curve can be approximated by two straight lines each having different slope. The observation that the plot is linear suggests that the bubble distribution is again log-normal, but the change in slope confirms the presence of a bimodal distribution. The bimodal distribution suggests that the resulting bubble size was the outcome of two different mechanisms. Evans (1990) reported similar bimodal bubble distributions for a plunging liquid aerator, which he attributed to the two different gas entrainment mechanisms (see section 2.2.1).

The above results show that the bubble size produced by a sparger in a vertical pipe in downflow depends on the operating conditions and the sparger design. The PJS is shown to be the most effective way of distributing gas in the downcomer pipe since it did not allow the formation of a ventilated cavity and also produced smaller bubbles with a significantly higher specific interfacial area for mass transfer than the other three spargers. The estimated average increase in the volumetric gas-liquid mass transfer coefficient, $k_L a$, due to the smaller bubble size produced by the PJS was by a factor of 1.35 (Table 5.2).

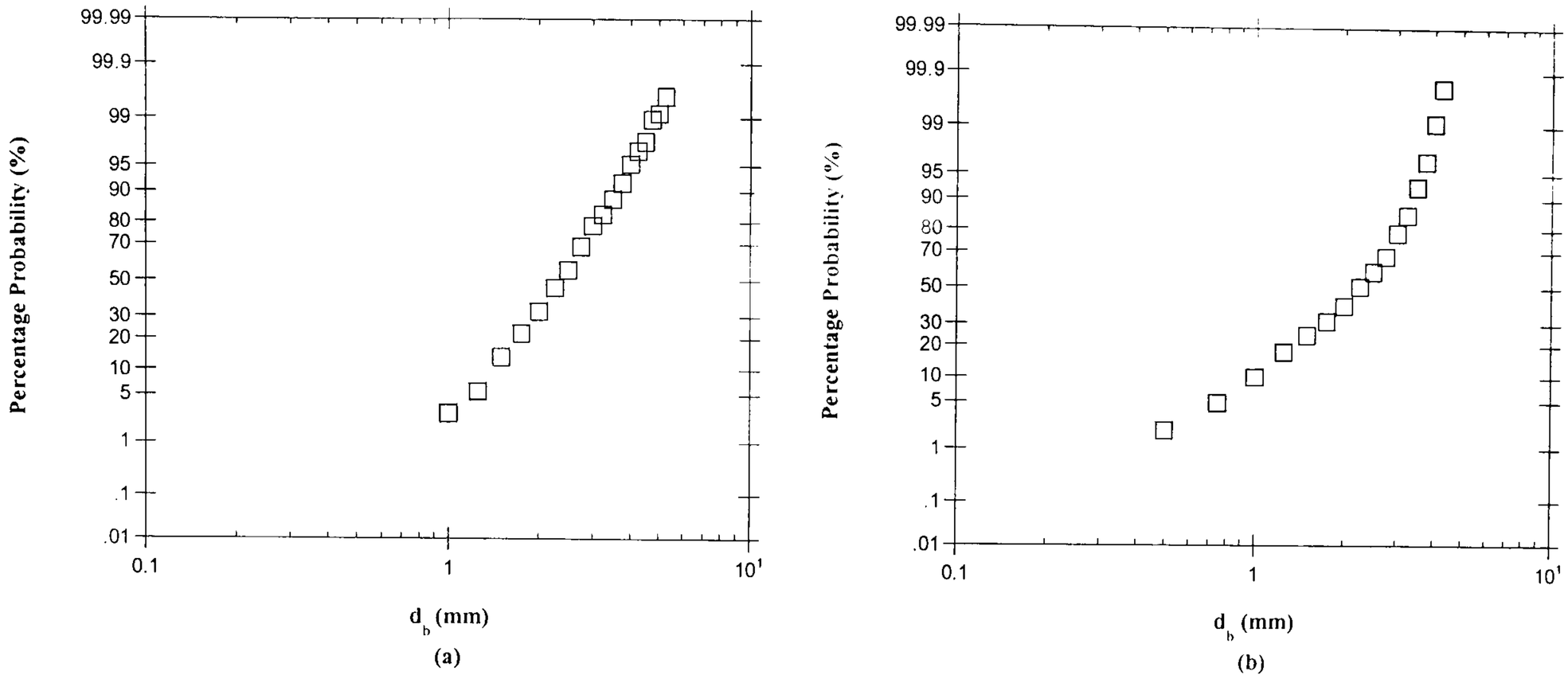

Log-probability plots of the cumulative bubble diameter distribution
(a) HS for Case III and (b) PJS for Case II.
Figure 5.3

However is should be noted that the power consumption was larger when the current version of the PJS[5.1] was used instead of the HS (Appendix D). This is doubly problematic; first the excess power consumption negates the advantage of the PJS of shorter cavity length. Secondly higher energy dissipation rates are known to lead to a smaller bubble size and therefore to larger interfacial area (and therefore $k_L a$) and so the comparison of bubble sizes is not like for like. Hence the bubble size adjusted for the same energy losses as the HS, d'_{32}, needed to be calculated. The energy losses were also important to quantify in order to be able to make direct comparisons with widely accepted empirical correlations in the literature that relate power consumption per unit volume with bubble size. The next section provides a brief account of how these losses were calculated in this work.

5.3 ENERGY LOSSES

The formation of ventilated cavities attached to spargers leads to pressure losses that are characteristic of the sparger used. Lee et al. (2000) determined the losses associated with the presence of a HS from the pressure profile measured along a cavity attached to the sparger. The

---

[5.1] Plunging jet spargers with low energy consumption can be designed (see Appendix A). The PJS in this work was manufactured before the significance of the energy consumption was fully appreciated.

losses were found to be the same order of magnitude as the total frictional losses in the whole column and were approximately equal to $0.7 \times L_B$ (70 % of the cavity length). Lee et al. (2000) also developed a theoretical model that was found to agree within only 15 % of the experimental loss. The model was based on a momentum balance and a Bernoulli equation taking into account the losses due to the presence of the ventilated cavity. Lee's et al. model is also expected to apply to the case of the CS used in this work since both spargers have been shown to have similar entrainment characteristics (Bacon, 1995).

The energy losses associated with the presence of the different spargers were not measured in the present work but were theoretically calculated. The energy losses associated with the presence of the HS or the CS were estimated from the equations developed by Lee et al. (2000). A similar approach to Lee's et al. (2000) was adopted here to calculate the energy losses due to the PJS (Appendix D). The losses due to the PS were not quantified because Lee's et al. (2000) approach is not suitable to the case of the PS. However this did not undermine the completeness of the present work; the focus was mainly on the PJS since it was the only sparger that produced considerable smaller bubble size against the HS and for this reason was also expected to give the highest $k_L a$.

The aim of this section is not to determine just the losses due to sparger design but also to estimate the dissipation rate that corresponded to the whole aerated volume in the system. This approach mimics that used in the literature for stirred tanks and bubble columns for which information is available on the relation between d_{32} and ε_G. The total aerated volume, V_a, was taken as the sum of the volumes of the bubble cloud dispersion in the downcomer (including the ventilated cavity region) and in the disengagement zone in the tank. The volume of the disengagement zone was estimated as the volume of a cylinder defined by the maximum depth that the bubbles travelled as they entered the tank and the maximum radial distance from the point of entry at which they disengaged at the free surface. The volume of the bubble cloud dispersion in the pipe was always greater that the volume of the disengagement zone, but of the same order of magnitude.

Subsequently and bearing in mind that the gas was simply used for sparging at sub-atmospheric conditions in this work the total power consumption per unit of aerated volume $\left(P/V_a\right)$ was calculated as the sum of four different components: (1) energy losses associated with the presence of the sparger, ℓ_1, (2) energy losses due to the bubbly flow inside the pipe, ℓ_2,

(3) energy losses due to friction at the wall, ℓ_3 and (4) energy losses due to the total loss of the kinetic head at the exit of the downcomer pipe, ℓ_4.

The last three terms (ℓ_2, ℓ_3, ℓ_4) are roughly the same for the HS, CS and PJS since the bubble cloud dispersion height in the pipe (taken from the point of injection to the end of the downcomer – see Fig. 3.1) and the gas void fractions (Table 5.1) were almost the same for all three spargers for all the cases examined. These losses could be easily estimated according to the following equations:

$$\ell_2 = g\varepsilon_G L_c \qquad \text{[loss due to bubble drag]} \qquad (5.6)$$

$$\ell_3 = \frac{2C_f L_c}{D} V_L^{\,2} \qquad \text{[frictional loss at pipe wall]} \qquad (5.7)$$

$$\ell_4 = \frac{V_L^{\,2}}{2} \qquad \text{[loss kinetic energy at exit]} \qquad (5.8)$$

where L_c is the length of the bubble cloud dispersion in the downcomer, C_f is the wall friction factor, and V_L is the interstitial liquid velocity defined as:

$$V_L = \frac{j_L}{(1-\varepsilon_G)} \qquad (5.9)$$

Lee et al. (2000) identified two main sources of energy losses as the liquid flowed round a ventilated cavity attached to a HS as a liquid film: (i) losses due to shear stress at the wall and (ii) losses due to turbulence in the bubble wake. The following equations were used to estimate these losses:

$$\ell_w = \frac{j_L^2}{2}\left(\frac{1-2\varepsilon_G}{(1-\varepsilon_G)^2} + \frac{A^2}{\alpha_2^{\,2}} - \frac{2A}{\alpha_2}\right) \qquad (5.10)$$

$$\ell_s = gL_B - \frac{j_L^2}{2}\left(\frac{A^2}{\alpha_2^{\,2}} - \frac{A^2}{\alpha_1^{\,2}}\right) \qquad (5.11)$$

$$\ell_1 = \ell_w + \ell_s \qquad (5.12)$$

where ℓ_w are the predicted energy losses per unit mass due to the turbulent cavity wake, ℓ_s are the predicted energy losses per unit mass due to wall shear around the ventilated cavity, L_B is the length of the ventilated cavity attached to the HS or the CS, α_2 is the falling film flow area at the base of the ventilated cavity attached to the HS or the CS and α_1 is the falling film flow area at the top of the ventilated cavity attached to the HS or the CS. The analysis behind Eq. (5.10) ignored the effects of gravity because it was difficult to determine the length of the recirculating region in the wake of the ventilated cavity. In the previous chapter it was shown that the toroidal vortex extended up to $1.32D$ beneath the ventilated cavity. Photographs of the recirculating wake of the cavities attached to the HS and to the CS for the experimental conditions of Table 5.1 showed that the length of the recirculation zone was around 1.4 - 1.45D. A value of $L_w = 1.4D$ is taken as the length of the recirculating zone beneath all of the ventilated cavities of Table 5.1. Then the effects of gravity can be included and Eq. (5.10) becomes:

$$\ell_w = \frac{j_L^2}{2}\left(\frac{1-2\varepsilon_G}{(1-\varepsilon_G)^2}+\frac{A^2}{\alpha_2{}^2}-\frac{2A}{\alpha_2}\right)+gL_w\left(1-\frac{\alpha_2}{A}\right) \tag{5.13}$$

Combining Eq. (5.6), Eq. (5.7), Eq. (5.8), Eq. (5.9), Eq. (5.11) and Eq. (5.13) and multiply them by $\rho_L Q_L$, gives the total power consumption per unit of aerated volume of liquid for the HS or CS in W m^{-3}:

$$\frac{P_{HS}}{V_a} = \rho_L Q_L\left[\frac{j_L^2}{2}\left(\frac{1-2\varepsilon_G}{(1-\varepsilon_G)^2}+\frac{A^2}{\alpha_2{}^2}-\frac{2A}{\alpha_2}\right)+g\left[L_B+(L_c-1.4D)\varepsilon_G+1.4D\left(1-\frac{\alpha_2}{A}\right)\right]-\frac{j_L^2}{2}\left(\frac{A^2}{\alpha_2{}^2}-\frac{A}{\alpha_1{}^2}\right)+\frac{j_L^2}{2(1-\varepsilon_G)^2}+\frac{2C_f L_c}{D}\frac{j_L^2}{(1-\varepsilon_G)^2}\right] \tag{5.14}$$

Taking a similar approach to Lee et al. (2000) the total power consumption per unit of aerated volume for the PJS is given by (Appendix D):

$$\frac{P_{PJS}}{V_a} = \rho_L Q_L\left[\frac{j_L^2}{1-\varepsilon_G}-j_L\sqrt{V_N{}^2+2gL_B}+\frac{1}{2}V_N{}^2+g(L_B+L_c)+\frac{2C_f L_c}{D}\frac{j_L^2}{(1-\varepsilon_G)^2}\right] \tag{5.15}$$

where V_N is the liquid velocity at the rim of the sparger.

The results from Eq. (5.14) and Eq. (5.15) are shown in Table 5.3 where the excess amount of energy consumed by the PJS compared to the HS is clearly shown. On the other hand the power consumption per unit of aerated volume of liquid was almost the same for both the CS and HS.

	P_{HS}/V_a $\left(Wm^{-3}\right)$	P_{CS}/V_a $\left(Wm^{-3}\right)$	P_{PJS}/V_a $\left(Wm^{-3}\right)$	$\left[\frac{P_{CS}}{V_a}\right]\Big/\left[\frac{P_{HS}}{V_a}\right]$	$\left[\frac{P_{PJS}}{V_a}\right]\Big/\left[\frac{P_{HS}}{V_a}\right]$
Case I	259	243	1107	0.94	4.28
Case II	421	398	1185	0.95	2.81
Case III	498	524	3015	1.05	6.05
Case IV	533	456	-	0.86	-
Case V	1448	-	-	-	-

Power consumption per unit of aerated volume for the PJS, HS and CS.

Table 5.3

The published correlations in the literature relating the power consumption per unit volume of liquid with Sauter mean bubble diameter are usually of the form:

$$d_{32} = C\left(\frac{P}{V_a}\right)^n \tag{5.16}$$

where C is an empirical constant. Using the form of the above equation the variation of the bubble Sauter diameters versus the power consumption per unit of aerated volume of liquid is shown in Fig. 5.4 for the HS for all five Cases in Table 5.1. The data are reasonably correlated by the expression (the correlation coefficient is 0.81):

$$d_{32} = 11.4\times10^{-3}\left(\frac{P}{V_a}\right)^{-0.21} \tag{5.17}$$

There are not enough data in Fig. 5.4 to establish a strong relation between Sauter mean bubble diameter and power consumption since that was not one of the aims in this work. Nevertheless the data in Fig. 5.4 can provide a crude approximation of the order of magnitude of the exponent n in Eq (5.16).

The bubble diameter decreased with an increase in the power dissipated (Fig. 5.4), which is in agreement with the Hinze (1955) equation obtained in a bubble column equipped with a perforated plate. However, the exponent on $\frac{P}{V_a}$, of $n = -0.21$ does not agree with considerations

from turbulence theory where the bubble breakage scales with $n = -0.4$ (Hinze, 1955). This suggests that the effect of turbulence on bubble formation may had been diluted by other factors and that the bubble size may had been influenced by coalescence. The latter is supported by a comparison with the widely accepted empirical correlation of Calderbank (1958). This correlation was developed for a six bladed disk turbine in a baffled tank, a system much different to the one here, but has been recommended by Joshi and Sharma (1979) also for diffused air systems.

$$d_{32} = 4.15 \frac{\sigma^{0.6}}{\left(\frac{P}{V}\right)^{0.4} \rho_L^{0.2}} \sqrt{\varepsilon_G} + 9 \times 10^{-4} \tag{5.18}$$

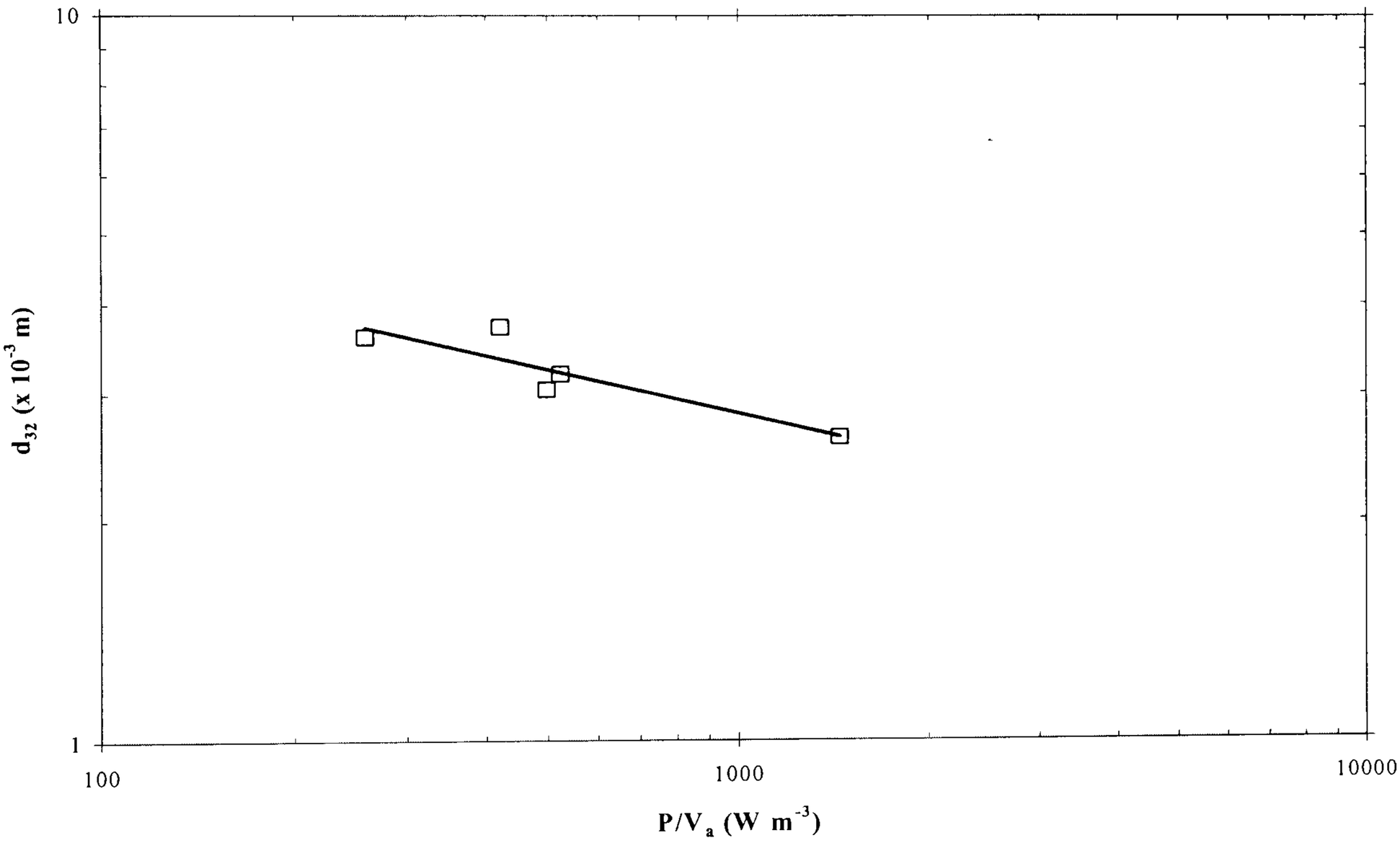

Sauter mean bubble diameter versus the power consumption for the HS.

Figure 5.4

where $\left(\frac{P}{V}\right)$ is the energy dissipation rate per unit volume of dispersion. It can be seen that the power consumption exponent obtained was $n = -0.4$ and not around $n = -0.21$ as in this work. The difference is attributed to the fact that the correlation was developed for a different system and also in Eq. (5.18) the gas void fraction is introduced which in turn might influence the bubble size through coalescence and this then might influence the best fit in Eq. (5.18). Also note

the constant of 9×10^{-4} in Eq. (5.18), which is dimensional with units in m. This prohibits the applicability of the Calderbank correlation at small bubble sizes, i.e. at $d_{32} \leq 9\times10^{-4}$ m.

Alves et al. (2002) correlated his data with those of various authors regarding tap water-air systems in stirred tanks and suggested an exponent of $n=-0.14$. Bouaifi et al., (2001), worked also with tap water and air and proposed $n=-0.23$, for a perforated plate sparger in a bubble column and $n=-0.21$ for dual impeller reactors. If the average of these experiments exponents $n=-0.19$ is taken, then the estimation of the adjusted Sauter mean bubble diameter, d'_{32PJS}, is shown in Table 5.4. In the same Table the estimated d'_{32PJS} using the exponent $n=-0.4$ suggested by the Calderbank correlation is also shown, as is the value for $n=-0.21$, the value obtained for the HS.

	d_{32HS} (mm)	d'_{32PJS} (mm) $n=-0.19$	d'_{32PJS} (mm) $n=-0.21$	d'_{32PJS} (mm) $n=-0.4$	*Difference*[a] (%) $n=-0.19$	*Difference*[a] (%) $n=-0.21$	*Difference*[a] (%) $n=-0.4$
Case I	3.61	3.13	3.22	4.24	+ 15.4	+ 12.1	- 17.5
Case II	3.73	3.47	3.54	4.31	+ 7.5	+ 5.3	- 15.5
Case III	3.05	3.49	3.62	5.09	- 12.5	- 15.6	- 66.9

[a] Difference is defined as $\frac{d_{32HS}-d'_{32PJS}}{d'_{32PJS}}\times100\%$ and therefore the numbers suggest that at equal energy consumption the PJS produces smaller bubbles than HS.

Adjusted Sauter mean diameter for the PJS for equal energy consumption compared to the HS.

Table 5.4

It can be seen that the PJS produced essentially the same Sauter mean diameter with the HS when the empirical exponents of $n=-0.19$ or $n=-0.21$ are used. The only discrepancy is Case III, which corresponded to the highest liquid volumetric flow rate used in the present work, where the adjusted value, d'_{32PJS}, is an average 17% higher than d_{32HS} and almost the same to the one estimated in Case II. On the other hand if $n=-0.4$ is considered then d'_{32PJS} is much higher than d_{32HS} suggesting that the PJS at comparable power consumption rates produces much larger bubble diameters than the HS. The latter implies that the HS has a better mass transfer performance than PJS, which would be a disappointing conclusion. However, the results when

$n = -0.4$ should be treated with some scepticism since that exponent was developed for a different system.

The results from the Sauter mean bubble diameters made it instructive to examine the mass transfer capacity of the PJS and HS for even higher gas volumetric flow rates (and hence gas void fractions) when the two spargers have comparable operating power consumptions (i.e. when the ventilated cavity attached to the HS is much longer) in order to see if the above differences persist. But first, for the sake of completeness, a comparison is given of the bubble size results with widely used empirical correlations and theoretical models from the literature of gas-liquid flows.

5.4 COMPARISON WITH THE LITERATURE

Much effort has been devoted to modelling of the breakup rate of bubbles and droplets in turbulent two-phase flows. Much of the published literature is based on work of Hinze (1955). Sevik and Park (1973) extended the work of Hinze (1955) to air bubbles in turbulent water jets. The aim was to establish a critical value of a Weber number for a bubble beyond which bubble breakup occurs. Breakup occurs when cohesive forces (surface tension) are smaller than local shear forces exerted by the surrounding fluid. The non-dimensional critical Weber number is used to characterize this competition. It is defined by the ratio of shear forces caused by turbulent fluctuations (eddies) and superficial forces:

$$We_{ct} = \frac{\rho_L \left\langle u'^2 \right\rangle d_{\max}}{\sigma} \tag{5.19}$$

where $\left\langle u'^2 \right\rangle$ is the average value of the fluctuating velocity acting over a length scale equivalent to the maximum stable bubble diameter, $d_{\max}$ and σ is the surface tension. A critical maximum bubble diameter is obtained from Eq. (5.19) by considering that breakup occurs for a critical Weber number larger than one.

Hinze (1955) developed a model and gave a value of 1.18 for the critical Weber number based on the breakup of a droplet or bubble in viscous shear flow. Sevik and Park (1973) extended Hinze's model and gave a value of 1.24 based on the assumption that a bubble would oscillate violently and broke up when the characteristic frequency of the turbulence was equal to one of

the resonant frequencies of the bubble. Lewis and Davidson (1982) based on their experimental results found that a cylindrical bubble became unstable in an axisymmetric inviscid shear flow at a critical Weber number of 4.7.

There are three main different theoretical approaches in the literature for bubbly flow in a pipe that are based on the concept of the critical Weber number. The measured bubble sizes (Table 5.2) are compared with these three models and also with two empirical correlations from the literature in the following paragraphs.

5.4.1 The model of Thorpe et al. (2001)

As already mentioned in the previous chapter, Thorpe et al. (2001) modelled the recirculation region beneath a ventilated cavity as a Hill's vortex. The bubble breakup was modelled using a critical Weber number that was defined differently than Eq. (5.19). The Weber number used by Thorpe et al. (2001) is shown below:

$$We_C = \frac{\rho_L \Delta u^2 d_{\max}}{\sigma} \tag{5.20}$$

where Δu^2 was the square of the velocity difference across the diameter of the bubble and was estimated based on the predicted velocity profile within the recirculation region. Thorpe et al. (2001) found that the prediction of bubble size was in general agreement with experimental observations when a critical Weber number of 4.7 was assumed. The value of 4.7 seemed more appropriate than the values in the range of 1.1 - 1.24 reported in the literature, given that the Hill's vortex velocity profile was very similar to that by Lewis and Davidson (1982) who also found a value of 4.7. Lewis and Davidson (1982) investigated the break up of bubbles in a shear field above an orifice; a system with many similarities to the shear field beneath a porous sparger currently investigated in this work. Thorpe et al. (2001) estimated the average maximum stable bubble size by:

$$d_{\max} = 3\sqrt[3]{\frac{We_C \sigma (R-\delta)^4}{128 \rho_L (KV_F)^2} \frac{1}{\left(R-\delta-\frac{d_{\max}}{2}\right)^2}} \tag{5.21}$$

where K is the proportionality constant given by Eq. (4.2) and found fairly good agreement with their measurements.

Eq. (5.21) is not applicable to the PJS results since they were taken for a system much different to the one described by Thorpe et al. (2001). Therefore only the results from the CS and the HS are compared with Eq. (5.21) in Fig. 5.5. It can be seen that the agreement between the predictions and the experiments is very good with almost all of the data falling within 20% of the model. It seems that the understanding of the flow field at the base of the ventilated cavity had enabled Thorpe et al. (2001) to provide also a satisfactory prediction of the resulting bubble size based on a value of the critical Weber number of 4.7. This amplifies even more the significance and success of their model.

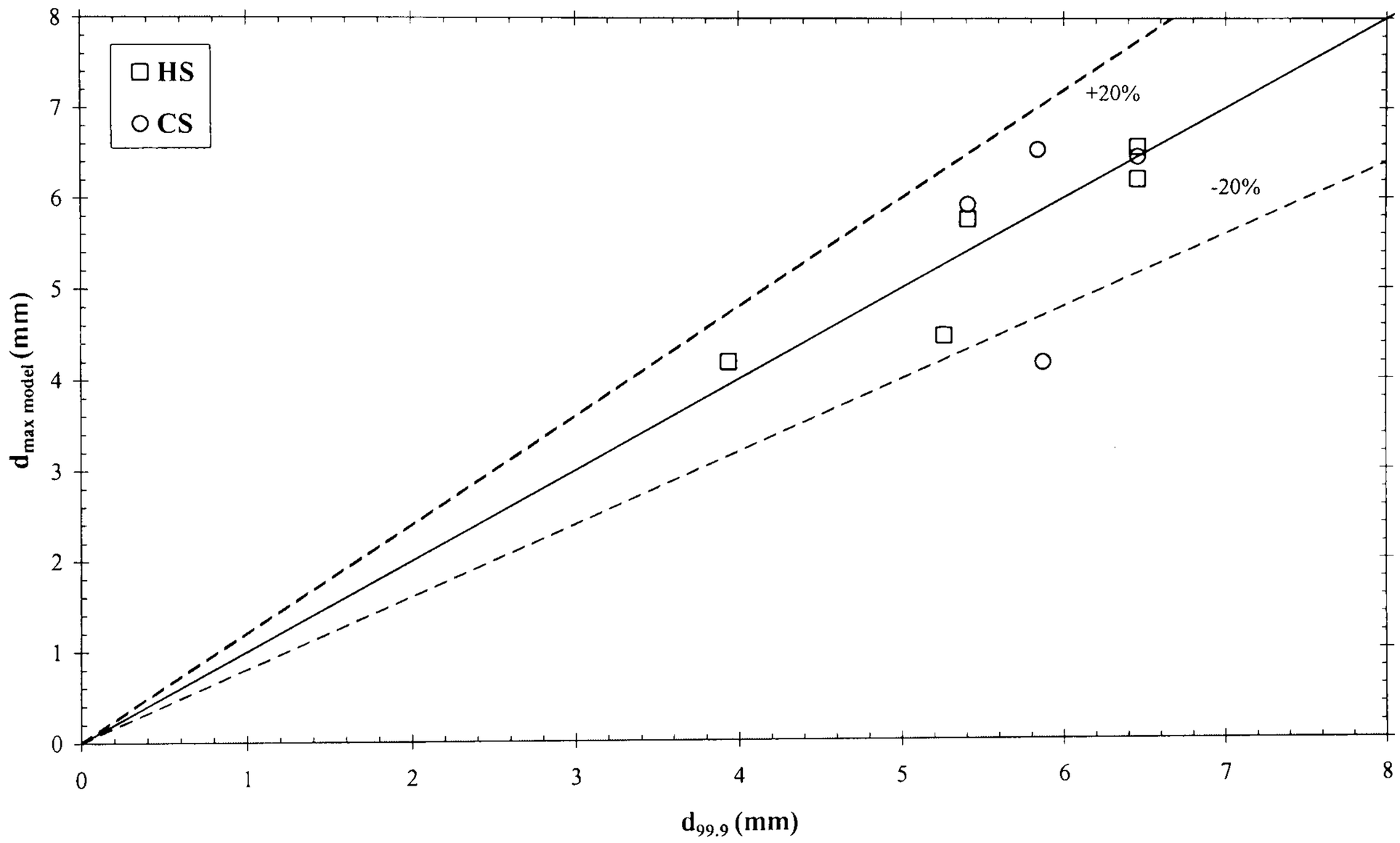

Comparison between measured and predicted max bubble diameters for the HS and CS using the model of Thorpe et al. (2001). The critical Weber number is 4.7.

Figure 5.5

5.4.2 The model of Evans et al. (1992)

Evans et al. (1992) presented a model based on a critical Weber number to predict the maximum stable size generated within the mixing zone of a confined plunging liquid jet (CPLJ). They used the Kolmogoroff energy distribution law to calculate $\langle u'^2 \rangle$. In isotropic homogeneous turbulence this velocity term is a function of the energy dissipation rate.

They derived the following expression for the maximum stable bubble diameter:

$$d_{\max} = \left(\frac{We_{ct}}{2}\sigma\right)^{3/5} \rho_L{}^{-1/5} e^{-2/5} \tag{5.22}$$

$$e = \frac{\rho_L b V_N{}^3}{2L_w}(1-2b) \tag{5.23}$$

where e was the average energy dissipation rate per unit volume derived from the theory of liquid jet gas ejectors, V_N was the jet velocity at the nozzle exit, L_w was the length of the mixing zone (defined as the point where the wall axial pressure profile became constant with respect to axial distance) and b is the jet/column area ratio. Their results were correlated within 20% of Eq. (5.22) when a critical Weber number of 1.2 was used.

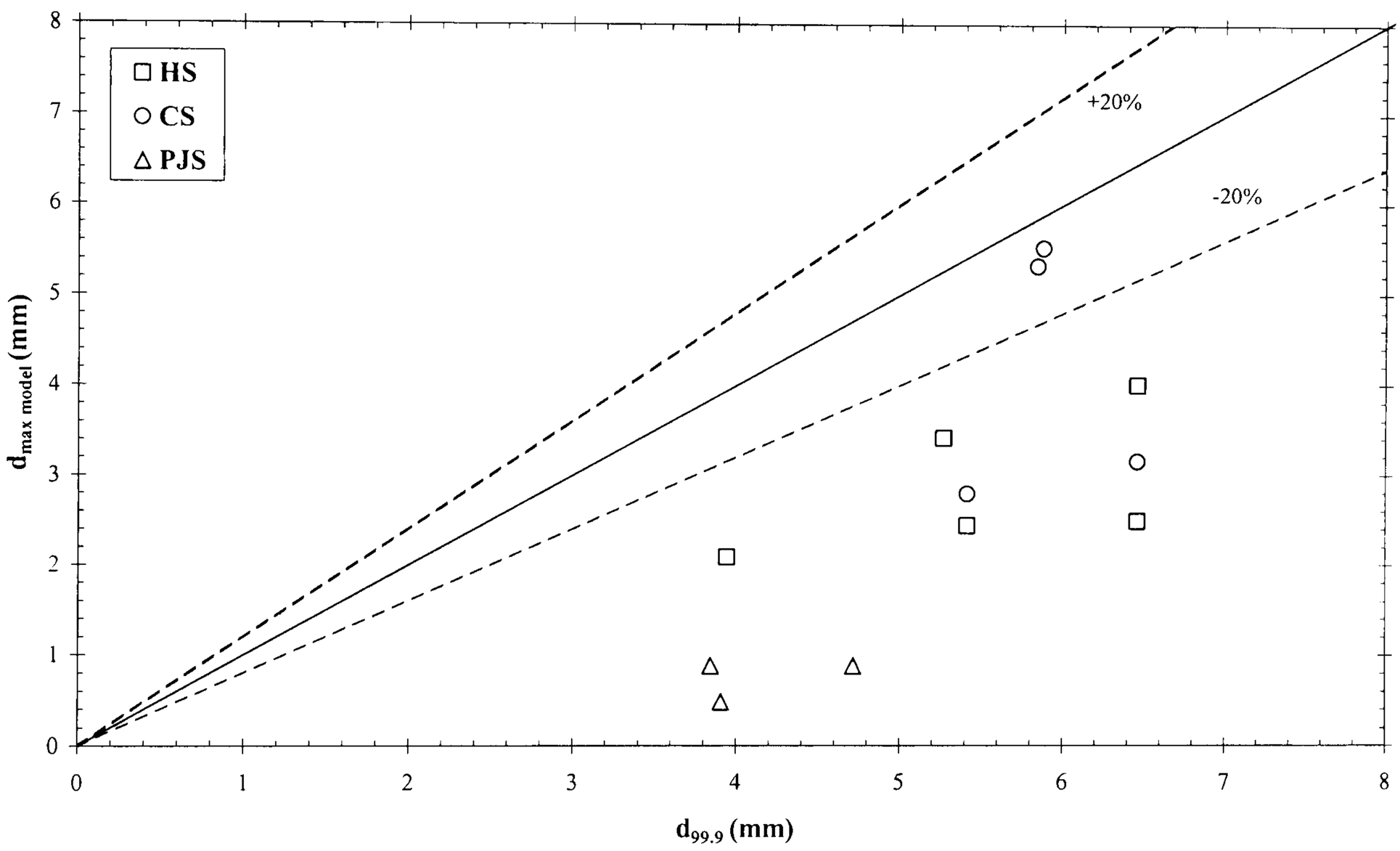

Comparison between measured and predicted max bubble diameters for the HS, CS and PJS using the model of Evans et al (1992). The critical Weber number is 1.2.

Figure 5.6

A comparison of the measured and predicted maximum bubble diameters for the HS and CS using the model of Evans et al. (1992) with a $We_{ct} = 1.2$ is given in Fig. 5.6. An average value of $3.5D$ was taken as the mixing length, L_w, in Eq. (5.23) based on the mixing length definition given by Evans et al. (1992). The accuracy of this value is further supported by the detailed pressure measurements of Lee et al. (2000) (their figures 4 and 5). It can be seen that the agreement between measured and predicted maximum bubble diameters is very poor for all three

spargers with deviations far in excess of 20%. These deviations are somewhat surprising at a first glance, mainly for two reasons: (i) Eq. (5.22) was developed for a CPLJ, a system that has identical characteristics to the PJS and also some similarities to the HS and CS and (ii) Evans et al. (1992) have tested their model against their experimental results and found good agreement within 20%.

The above discrepancy prompted a thorough look on the data Evans et al. (1992). Fortunately Evans et al. (1992) provided Tables with their experimental conditions, methodology and results. A careful test to reproduce their data using exactly the same equations, i.e. Eq. (5.22) and Eq. (5.23), showed that the final results they presented in their paper (their Table 2) did not correspond to the experimental conditions they quoted (their Table 1). Therefore their comparison with the model (their Fig. 4) was flawed. This highly unexpected result is also supported by a quick literature review on bubble size prediction. There is a wealth of papers referencing the approach of Evans et al. (1992) in predicting bubble size but none was actually testing their measured bubble size with Eq. (5.22). The correct calculated data based on the experimental conditions they quote in their paper are now presented in Fig. 5.7 together with the Evans et al. (1992) original data. It is seen that the agreement is no longer within 20% when a critical Weber number of 1.2 is used and that the model over predicts significantly their data. Instead a critical Weber number of around 0.9 provides the best agreement between measured and predicted maximum bubble diameters.

5.4.3 The model of Hesketh et al. (1987)

Levich (1962) postulated a similar force balance to Eq. (5.22) but he considered the balance of the internal pressure of the bubble with the capillary pressure of the deformed bubble. He hypothesised that a deformed bubble would break up when the internal pressure force overcomes the surface tension force. Considering a force-balance between these two forces he obtained the following critical Weber number:

$$We_{ct} = \frac{\rho_L \left\langle u'^2 \right\rangle d_{\max}}{\sigma} \left(\frac{\rho_G}{\rho_L} \right)^{1/3} \tag{5.24}$$

Hesketh et al. (1987) taking into account the Levich Weber number expression and calculating $\left\langle u'^2 \right\rangle$ from the Kolmogoroff energy distribution law, as Evans et al. (1992) did afterwards, derived the following equation for $d_{\max}$ in horizontal fully developed pipe flows:

$$d_{\max} = \left(\frac{We_{cl}\sigma}{2}\right)^{0.6} \frac{1}{\left(\rho_L{}^2 \rho_G\right)^{0.2}} e'^{-0.4} \tag{5.25}$$

where e' is the energy dissipation rate per unit mass defined by Hesketh et al. (1987) as:

$$e' = \frac{2 f j_L{}^3}{D} \tag{5.26}$$

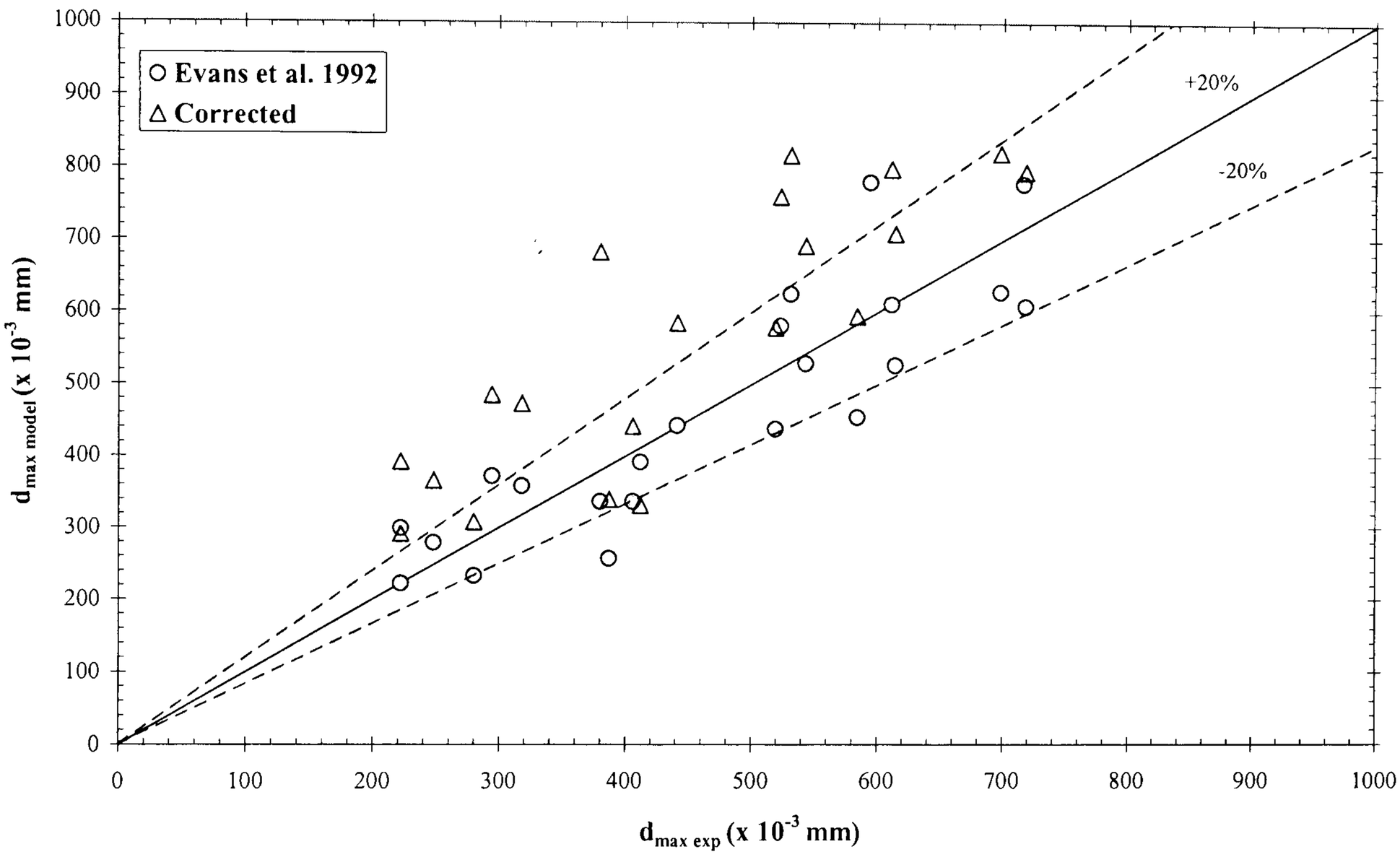

Comparison between meàsured and predicted maximum bubble diameters for the data of Evans et al. (1992). The circles represent the flawed points as plotted by Evans et al. (1992). The triangles represent the corrected calculated data based on the conditions quoted in their paper and are also plotted to show the poor agreement between model and experiment. The critical Weber number is 1.2.

Figure 5.7

The model by Hesketh et al. (1987) predicted successfully the measured maximum stable bubble or drop diameter in gas-liquid or liquid-liquid dispersions when a critical Weber number of 1.1 was used. However huge deviations were found (up to 500%) between the model and the measured bubble sizes in the present study. This is hardly surprising because the model by Hesketh et al. (1987) was developed for a fully developed horizontal flow and was validated

with data that were taken approximately $220D$ downstream of the gas entry point. Whereas in this work the flow was vertical, the data were taken at approximately $18D$ (the experimental setup for bubble size measurements did not allow the successful and safe capture of photographs at lower distances) and there was a toroidal vortex downstream of the gas entry point.

Therefore to check the applicability of Hesketh's model to this work an alternative definition for the energy dissipation rate was sought that would account for the differences in geometry and give better predictions. The most suitable way to define the energy dissipation rate per unit mass was by converting the inlet water flow rates for each sparger to energy dissipation rates. The following equations were used:

$$e' = \frac{P_j}{\rho_L L_w A} \tag{5.27}$$

$$P_j = Q_L \rho_L \frac{V_j^{\,2} - j_L^{\,2}}{2} \tag{5.28}$$

where P_j is the power of the jet at the nozzle exit in the case of the PJS or at the base of the ventilated cavity in the case of the HS and CS, L_w is the length of the recirculation region below the ventilated cavities taken as $1.4D$ (see section 5.3) and j_L is the superficial liquid velocity in the pipe. The comparison between the measured and predicted maximum bubble sizes is given in Fig. 5.8. for a critical Weber number of 1.1. It can be seen that even when modifying the model of Hesketh et al. (1987) by using Eqs. (5.27) and (5.28) to define the energy dissipation per unit mass the model still under predicts significantly the measured bubble sizes for all three different spargers.

5.4.4 The correlation by Calderbank (1958)

The bubble size results are compared in Fig. (5.9) with the empirical correlation of Calderbank (1958) shown in Eq. (5.18). This correlation was developed for a six bladed disk turbine in a baffled tank, a system much different to the one here, but has been recommended by Joshi and Sharma (1979) also for diffused air systems (see section 5.3). Surprisingly there is a rather good agreement for most of the data between measured and predicted Sauter mean bubble diameters with deviations up to 20%. In Fig. 5.9 the shaded area corresponds to the region of $d_{32} \leq 9\times10^{-4}$ m, i.e. the region where the Calderbank correlation is not applicable (see also section 5.3).

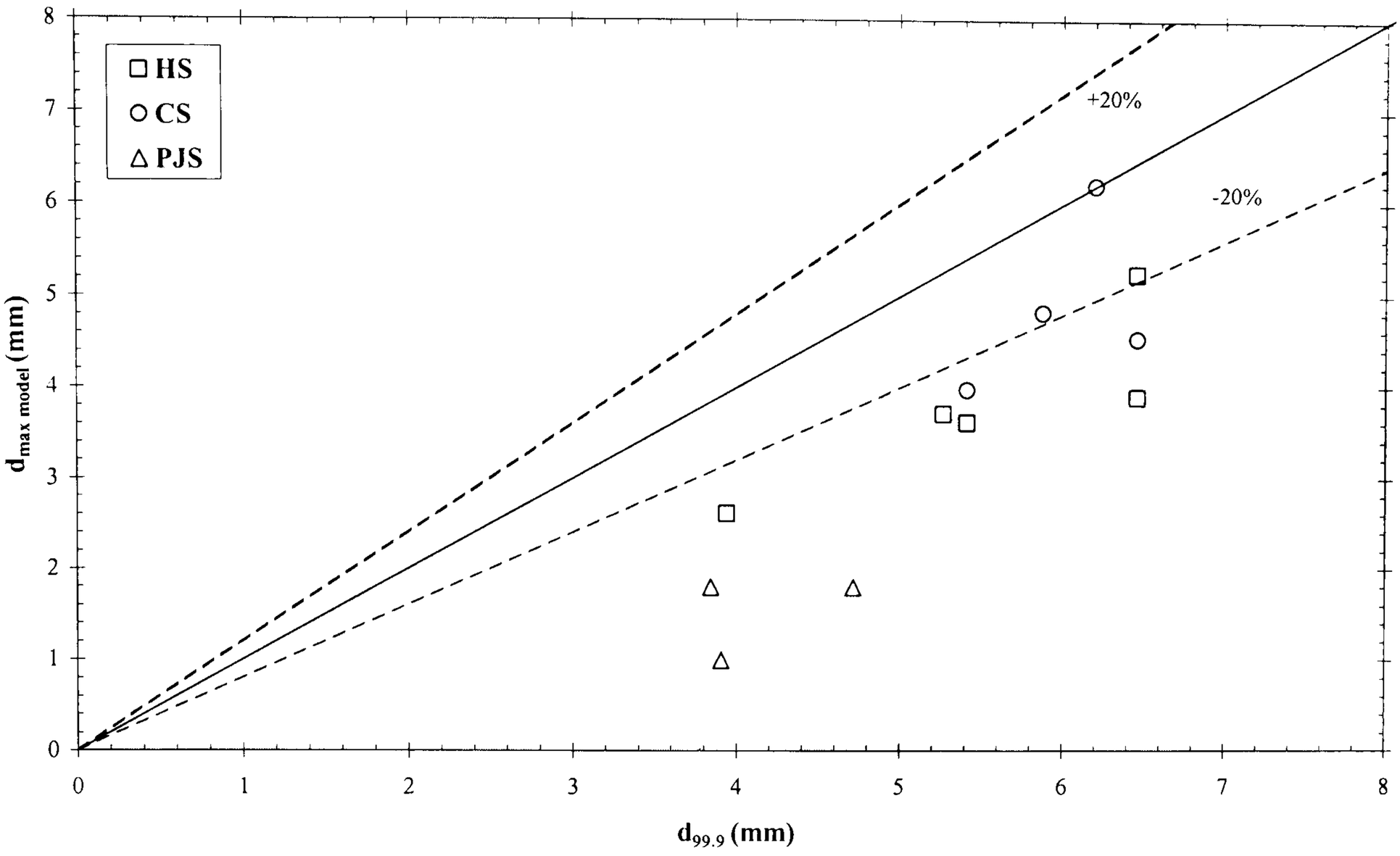

Comparison between measured and predicted max bubble diameters for the HS, CS and PJS using the model of Hesketh et al. (1987). The critical Weber number is 1.1.

Figure 5.8

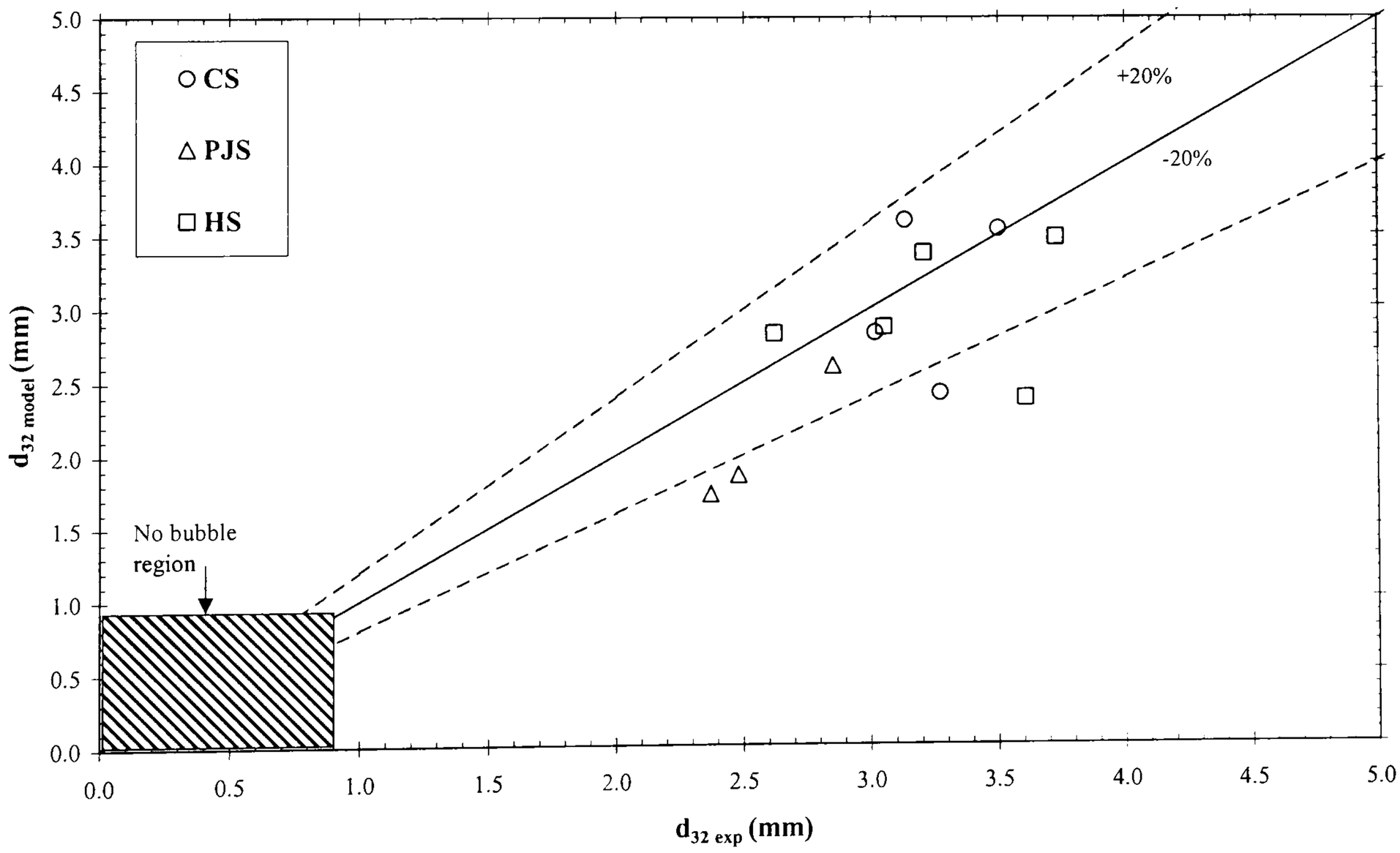

Comparison between measured and predicted Sauter mean bubble diameters for the HS, CS and PJS using the correlation of Calderbank (1958).

Figure 5.9

5.4.5 The correlation by Varley (1995)

Varley (1995) measured using photography mean bubble sizes and bubble size distributions in the fully developed region downstream of a nozzle in a submerged jet reactor. The nozzle she used had many similarities to one used by Bando et al. (1989), (1988). Varley fitted her results to a correlation using a similar form to Calderbank's equation:

$$d_{32} = 0.215 \frac{\sigma^{0.6}}{\left(\frac{P}{V_a}\right)^{0.29} \rho_L} \frac{Q_G}{Q_L} 100 \qquad (5.29)$$

Interestingly Varley (1995) replaced the gas void fraction term in the Calderbank equation (Eq. 5.18) with $\frac{Q_G}{Q_L}100$ in her correlation because only a small volume of the bulk liquid was entrained into the two-phase jet at the point of measurement and very few bubbles escaped in that region. The comparison of the measured Sauter mean bubble diameters with the empirical correlation of Varley (1995) is shown in Fig. 5.10. It can be seen that the agreement is poor with deviations exceeding 20% in all cases of the measured data.

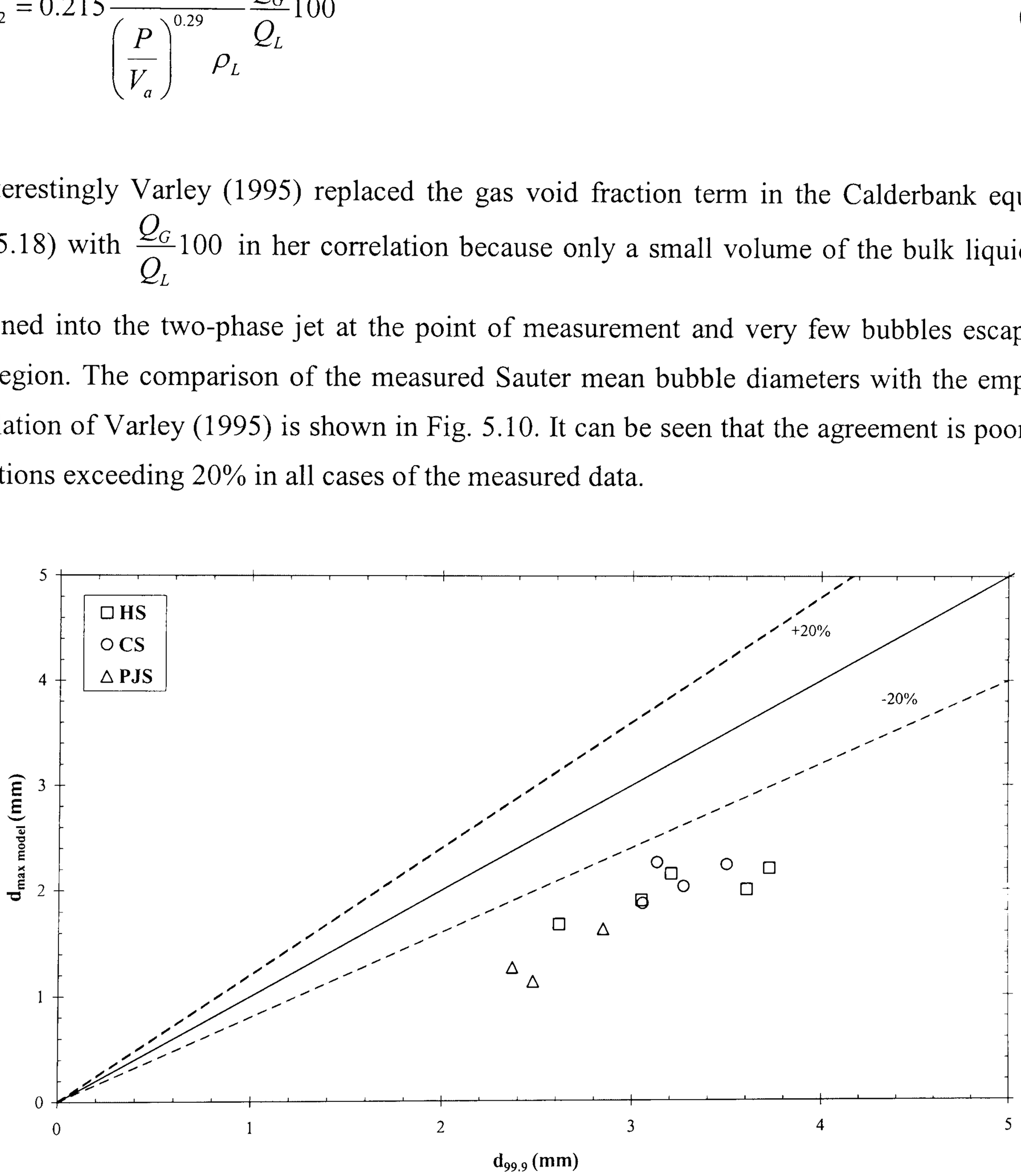

Comparison between measured and predicted max bubble diameters for the HS, CS and PJS using the correlation of Varley (1995).

Figure 5.10

The conclusion of this section is that the model by Thorpe et al. (2001) gave the best and most accurate bubble size predictions followed by the Calderbank correlation. However, the application of the Calderbank equation is still questionable since it was developed for a system much different to one in the present work. Some more experimental bubble size data are needed at even higher void fractions than the ones in Table 5.1 to provide a more detailed assessment of this correlation.

The model of Evans et al. (1992), the model of Hesketh et al. (1987) and the correlation of Varley (1995), all under predicted the resulting bubble size significantly. This suggests that they are not applicable to a geometry where a ventilated cavity is attached to a sparger in a downflowing liquid.

5.5 MASS TRANSFER RESULTS

For the mass transfer measurements, the water in the whole system was de-aerated by sparging with nitrogen until the DO concentration had fallen to a very low value. The nitrogen was then stopped, the bubbles were allowed to disengage in the tank and a continuous airflow was injected into the downcomer. The changes of the DO concentration with time were recorded until the water became saturated with air (see section 3.7). DO measurements with no air or nitrogen flow showed that the cover above the tank prohibited significant transfer from the room to the tank. The method of the DO measurement is described in detail in Appendix B.

The results from the bubble size distributions suggested that the PJS would display the best mass transfer characteristics. The estimated increase in the $k_L a$ due to the smaller bubble size when compared to the industrial design (HS) was around 30% for Case II (Table 5.2). The $k_L a$ was measured for all spargers for the operating conditions in Case II (Table 5.1) and in order to get a more conclusive assessment of the PJS mass transfer performance the $k_L a$ of the HS and PJS was determined for Cases VI and VII (Table 5.5). Both spargers had almost the same operating power consumption in Case VII (Table 5.5). The liquid physical properties and the bubble length were measured according to the methods outlined in chapter 3 and the void fraction was estimated using the correlation suggested by Wallis (1969) (see section 4.4).

To evaluate the mass transfer coefficient from the unsteady DO response curve a number of assumptions had to be made. The model assumed that (i) the mass transfer rate, $k_L a$, was

controlled by liquid phase resistance (i.e. all resistance to interfacial mass transfer of the gas is localised in the liquid film at the mass transfer, which is true for air as showed by Chisti (1989), (ii) a well-mixed liquid in the bubble cloud and the tank with no radial variations of concentration or other properties (i.e. uniform C_L), (iii) no change in the gas phase composition (i.e. a constant C^*) and (iv) absence of any oxygen consumption in the physical system. When dynamic measurements are used care is taken to keep the hydrodynamics constant and hence the void fraction independent of time. The gas was assumed to establish very rapidly on admitting air to the system and consequently the aerated volume could be considered constant with time. Chisti (1989) gives a thorough account with examples on the understanding and importance of these assumptions. A discussion is given further below that justified the use of the dynamic method in the present geometry.

	Q_L (m^3s^{-1})	Q_G (m^3s^{-1})	j_L (ms^{-1})	j_G (ms^{-1})	Q_G/Q_L	ε_G (%)	L_B (mm)	P/V_a (Wm^{-3})	$\left[\frac{P}{V_a}\right]\Big/\left[\frac{P_{HS}}{V_a}\right]$
Case II									
	0.00825	0.00016	0.95	0.0185	0.0194				
CS						1.8	80	398	0.95
HS						1.8	100	421	1
PS						1.8	100	-	-
PJS						1.8	0	1185	2.81
Case VI									
	0.00825	0.00062	0.95	0.0720	0.0750				
HS						5.8	370	997	1
PJS						5.8	55	1484	1.49
Case VII									
	0.00825	0.00088	0.95	0.1020	0.0107				
HS						8.1	500	1380	1
PJS						8.1	100	1677	1.22

Summary of the operating conditions for the mass transfer measurements.

Table 5.5

A mass balance on the dissolved oxygen in the liquid contained within the bubble cloud gives the relation between the rate of oxygen transfer, the overall volumetric mass transfer coefficient and the concentration driving force:

$$V\frac{dC(t)}{dt} = k_L a V_a \left(C^* - C(t)\right) \tag{5.30}$$

where C^* and $C(t)$ were the instantaneous and saturation concentration of dissolved oxygen in the water, V was the total volume of water (1 m^3) and V_a was the aerated volume. Integration of Eq. (5.30) yields:

$$\ln\left(\frac{C^* - C_o}{C^* - C(t)}\right) = k_L a \frac{V_a}{V} t \tag{5.31}$$

where C_o was the initial dissolved oxygen concentration at time, t_0, when a hydrodynamic steady state had been re-established upon commencement of aeration. The $k_L a$ was calculated as the slope of the graph $\ln\left(\frac{C^* - C_o}{C^* - C(t)}\right)$ vs $\frac{V_a}{V} t$. In order to compare $k_L a$ values, all of the $k_L a$ obtained at different temperatures were corrected to $k_L a$ at 20°C, because there are some physical properties that are dependent on temperature, such as viscosity, density, surface tension and molecular diffusivity. For convenience the subscript (20°C) will not be utilized in this work. The relationship is as follows:

$$k_L a_{(20^\circ C)} = k_L a_{(T^\circ C)} \times 1.024^{(20-T)} \tag{5.32}$$

The use of a single DO probe during the actual measurements could lead to problems if the tank was not perfectly mixed. For example a small amount of bypassing within the tank could lead to a change in the measured DO history, which eventually would be reflected in the fitted $k_L a$. Thus the influence of the quality of mixing in the tank on the measurements had to be checked. A residence time distribution (RTD) experiment was therefore conducted to determine the mixing characteristics and liquid flow patterns present in the tank. A pulse of concentrated salt (very close to saturation) was injected into the tank and a conductivity probe inserted in the tank detected the transient response. The results showed that the liquid mixing time was around 25 s and that the tank was stirred and well mixed with no dead zones present. 25 s is more than a factor 20 shorter than the time period of the $k_L a$ experiment and therefore for practical purposes, the tank etc. is well mixed.

Preliminary mass transfer experiments showed that (at flow rates similar to Case II) there was no measurable difference in DO concentration with probe position. This further justified the use of Eq. (5.31). Preliminary measurements also showed that two DO probes (positioned at the back and front sides in the tank) gave very similar response curves for all the spargers used. According to Paulson (1989) (referenced in Chisti, 1987) because the $k_L a$ values are reproducible within ±10%, agreement of $k_L a$ values between two or more sampling points within ±10%, can be taken as an indication of a fully mixed behaviour. This is even more pronounced in systems with low $k_L a$ values, $k_L a \leq 0.1$ s^{-1}, as in the present work. Furthermore the surface of the tank was seen to be turbulent. The flows in the system were so large that the fluid in the tank was never quiescent. The above together with the existence of the two baffles (which acted as crude mixers – Fig. 3.2) in the tank and the high rate of recirculation (a plug flow system with large recirculation acts like a well mixed system) confirmed the validity of the initial assumption, that the whole system in most of the experiments was well mixed at long times (but also see the discussion below).

A typical DO concentration profile $\left(E = \frac{C_L - C_o}{C^* - C_o} \right)$ is shown in Fig. 5.11 where the long time scale of the measurement is clear. The parameter E is essentially the ratio of the instantaneous mass transfer rate to the maximum possible rate of mass transfer. This profile corresponds to Case VII for the HS, i.e. the case with highest void fraction that was expected to reach saturation levels faster than Case II or Case VI. Only a handful researchers have published similar graphs in the literature (Chisti, 1989; Moppett et al., 1997).

Care was taken to ensure that the response time of the probe did not affect the measured $k_L a$. The response time of the polarographic probe for a 63% of the full-scale reading was about 5 sec. Van't Riet (1979) showed that the ultimate error in $k_L a$ to be $\leq 6\%$ as long as the DO electrode response time (63% of the full scale) was $\leq 1/k_L a$. The present study satisfied the requirements of Van't Riet (1979). Subsequently and in keeping with other investigators (Chisti, 1989 for more references on probe dynamics) the effects of the DO electrode were neglected in the $k_L a$ calculations. Notwithstanding the above, the experiments ran for 1000 seconds or more (Fig. 5.11), which meant that simply shifting in the analysis by 5 sec would not make any considerable difference.

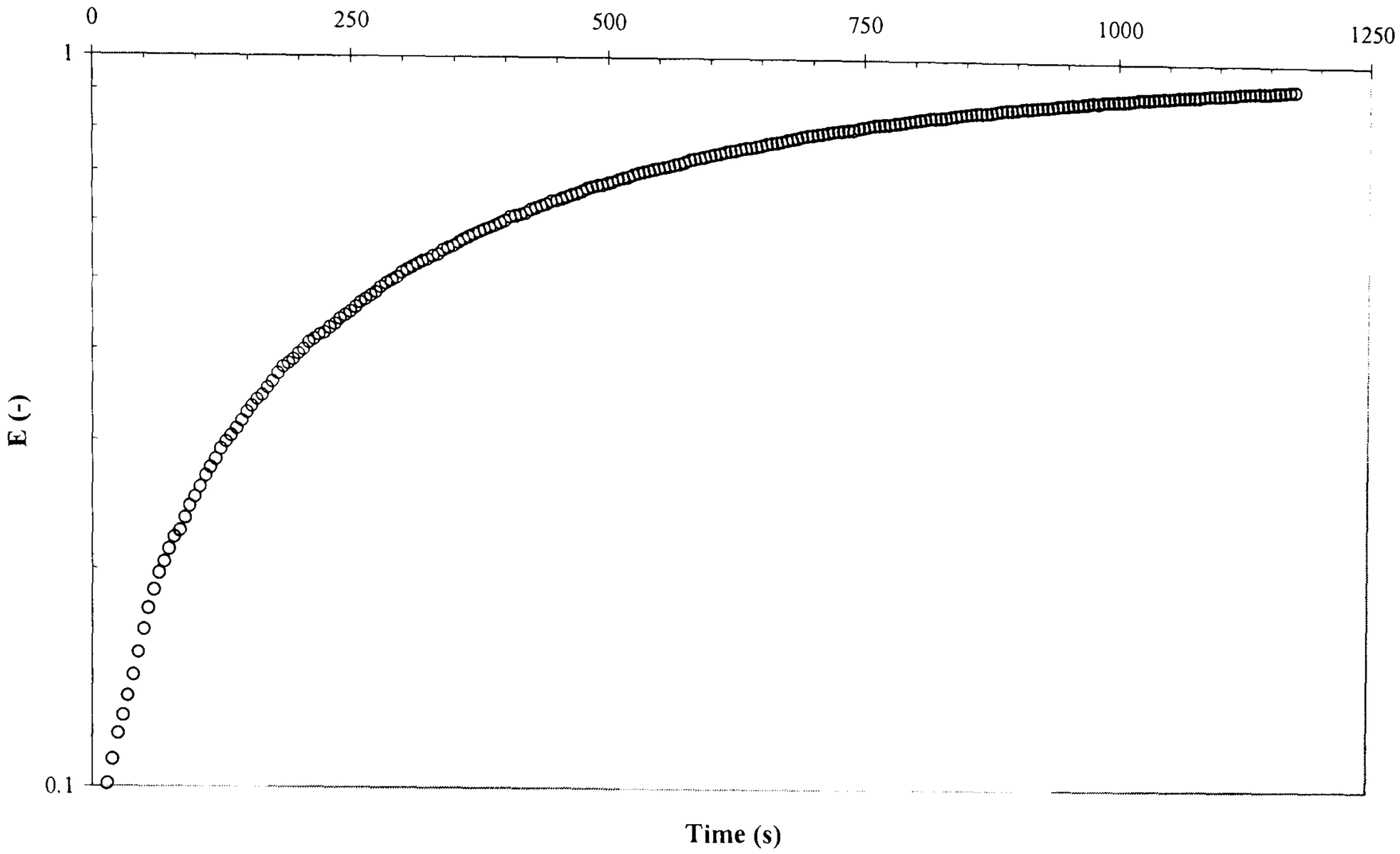

A typical DO concentration profile versus time. This profile corresponds to Case VII for the HS.

Figure 5.11

Eq. (5.31) could be used successfully for the determination of the $k_L a$ as long as the DO measured by the probe and elsewhere in the bubble cloud was approximately equal to the DO concentration in the tank, C_{Tank}. In order to check this, a model was created that estimated the DO concentration in the tank in which the riser and the downcomer of the experiments were modelled as plug flow elements. Details of this model can be found in Appendix E. The model showed that for the experimental conditions of Case II the differences between the experimental DO concentration at the probe location and the one in the tank were negligible (within 3%) (Fig. 5.12a). This is clearly shown in Fig. 5.12 where both profiles for the HS are plotted together. Similar results were found for all spargers for Case II. Hence Eq. (5.31) was used to derive the $k_L a$ for Case II. Thus is concluded that for the experimental conditions of Case II the effects of the bubble cloud on the derivation of a correct $k_L a$ for the whole system were not that important.

However for higher gas void fractions as in Cases VI and VII a change of concentration with position in the downcomer was apparent in the bubble cloud. The DO concentration in the tank was no longer the same as the DO concentration in the probe location. This is clearly seen in Fig. 5.12b where the calculated DO concentration in the tank for the PJS for Case V was different

from the DO concentration at the probe location. Hence the driving force for mass transfer for the DO experimental values at the probe location and elsewhere in the bubble cloud was no longer $C^* - C_{Tank}$. Calculating the logarithmic mean concentration driving force between the probe location and the exit of the downcomer should then approximate the concentration driving force for mass transfer. The latter implies that the system may show some elements of plug flow behavior. This is built in the model described in Appendix E. Therefore the $k_L a$ values that are presented here for the Cases VI and VII were estimated based on the model and not taken from the slope of a log plot. A description of the model and the procedure followed to determine the $k_L a$ for the HS and PJS for Cases VI and VII (with the raw data) are given in Appendix E.

The superiority of the PJS is clearly seen in Fig. 5.13 (The experimental data points for the CS are so close to the PS ones for clarity they have not been plotted in Fig. 5.13). The data lines of the PJS and PS are above the one of the HS suggesting a higher $k_L a$. The PJS had the highest $k_L a$ value followed by the PS. The increase in the $k_L a$ value compared with the HS is around 25% (Table 5.6), which agrees pleasingly with the 30% increase implied by the bubble size distributions (Table 5.2). The rest of the spargers showed similar $k_L a$ values again within 10% of the HS, a result that is consistent with the bubble size distributions for Case II (Table 5.2).

The superiority of the PJS against HS persisted at even higher void fractions as it is clearly shown in Fig. 5.14 where the results for Cases II, VI and VII are plotted for each sparger. The average increase in the $k_L a$ for all three cases when the PJS was used instead of the HS was around 19 % (Table 5.6).

As it is obvious in Figs. 5.13 - 5.14 the PJS enhanced the $k_L a$ relative to the HS. However it must be checked if the enhancement in $k_L a$ is due to the increased power demand of the PJS[5.2] used in these experiments. Hence the adjusted $k_L a'$, which allows for the difference in energy consumption between the PJS and HS, needed to be calculated. The adjusted $k_L a'$ values are shown in Table 5.7 using the same exponents as in Table 5.4 for the Sauter mean bubble diameters and the all the results are plotted in Fig. 5.15. It is shown that for higher void fractions and comparable power dissipation rates as in Cases VI and VII the PJS produced essentially the same $k_L a$ (within 10%) even when using the theoretical exponent of $n = 0.4$. Especially in Case VII, where the ventilated cavity attached to the HS was long, the losses were almost the same for both spargers (Table 5.3) the PJS had a slightly better $k_L a$. Evans et al. (1999) measured $k_L a$

[5.2] It is possible to design PJS with lower power demand

values for a plunging jet aerator and found that $k_L a \propto \left(\frac{P}{V}\right)^{0.2}$ for tap water – CO_2. Clearly to get a more conclusive comparison the dependence of each sparger on power consumption, the exponent n should be determined accurately.

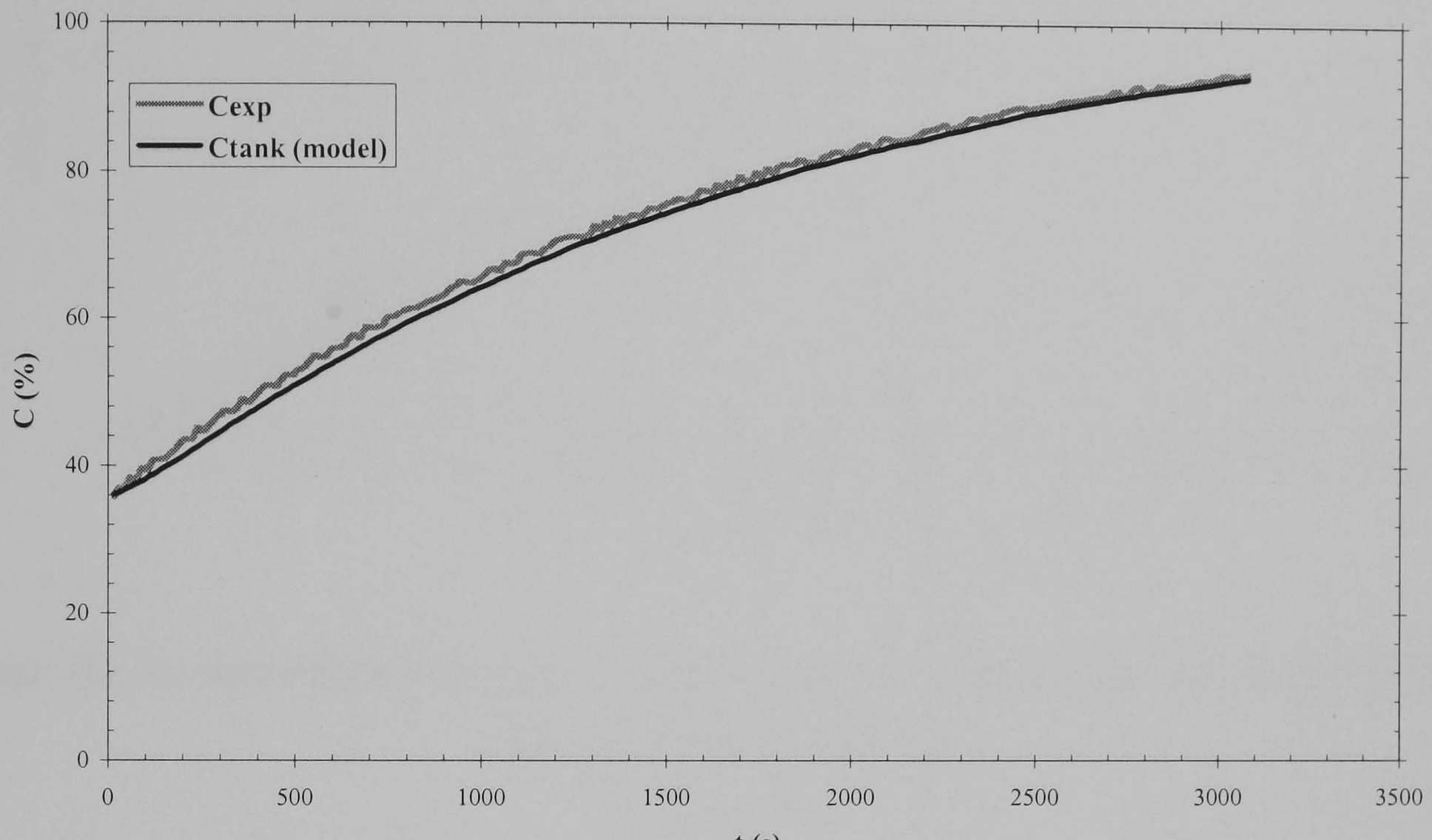

(a)

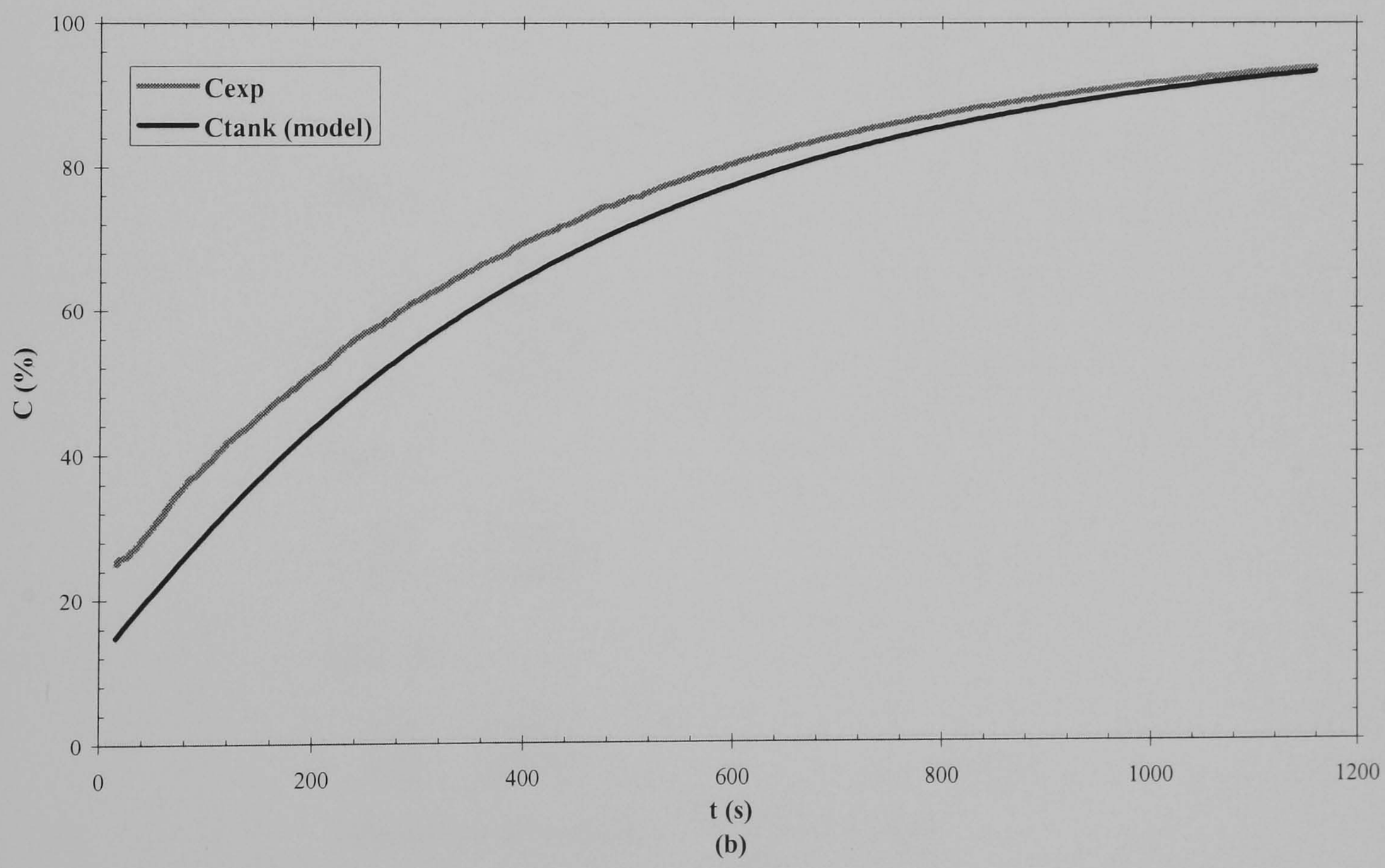

(b)

Experimental and model DO profiles (a) for the HS for Case II and (b) for the PJS for Case VII.

Figure 5.12

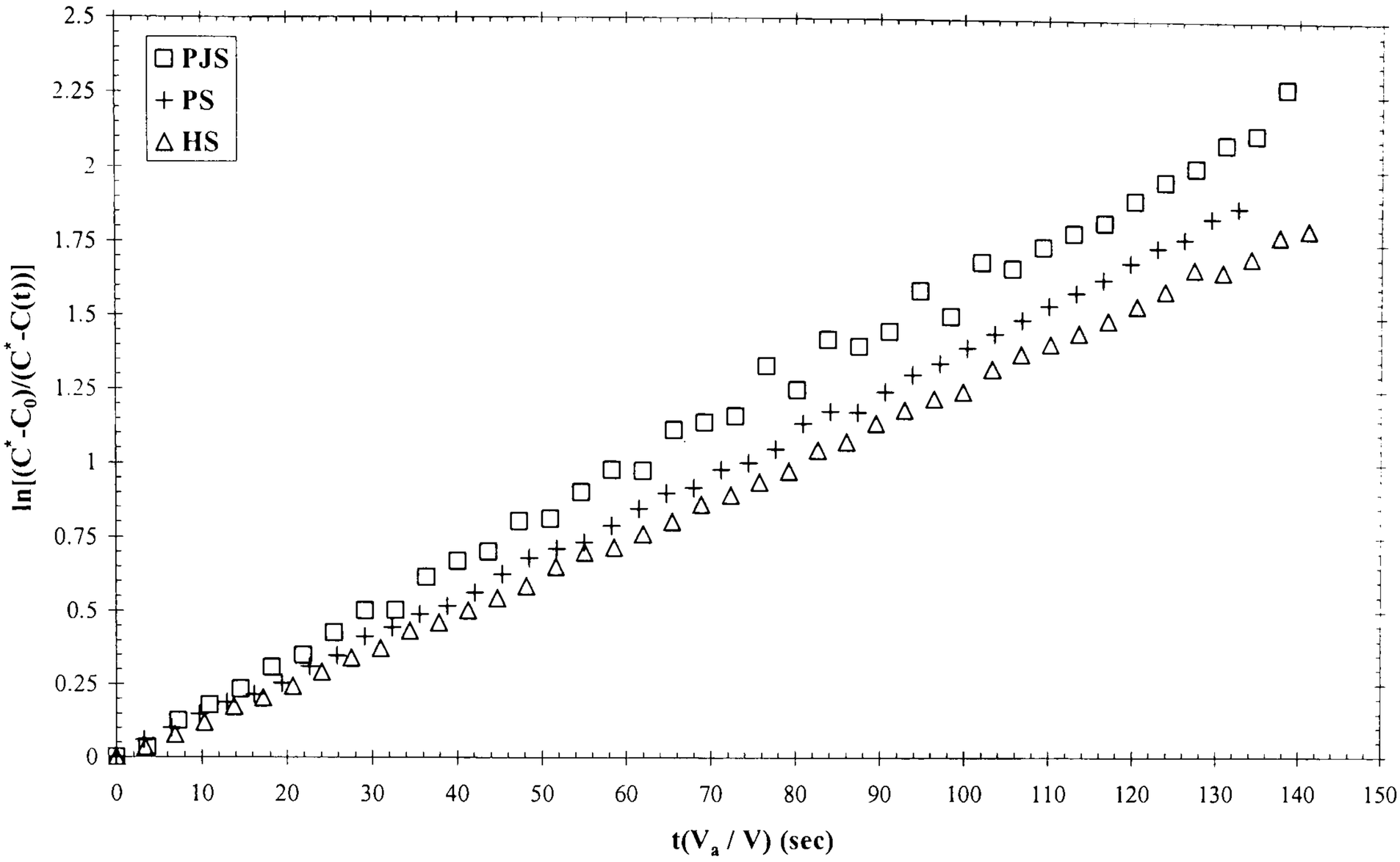

Graph for the determination of gas – liquid volumetric mass transfer coefficients for the PJS, PS and HS for Case II.

Figure 5.13

	$k_L a$ $\left(s^{-1}\right)$	k_L $\left(x10^{-3} ms^{-1}\right)$	*Difference*[a] $(\%)$
Case II			
CS	0.0137	0.436	7.90
HS	0.0127	0.430	-
PS	0.0139	0.420	9.40
PJS	0.0160	0.414	25.9
Case VI			
HS	0.0389	-	-
PJS	0.0453	-	16.5
Case VII			
HS	0.0525	-	-
PJS	0.0603	-	14.9

[a] Difference is defined as $\frac{k_L a - k_L a_{HS}}{k_L a_{HS}} \times 100\%$

Summary of the mass transfer results.

Table 5.6

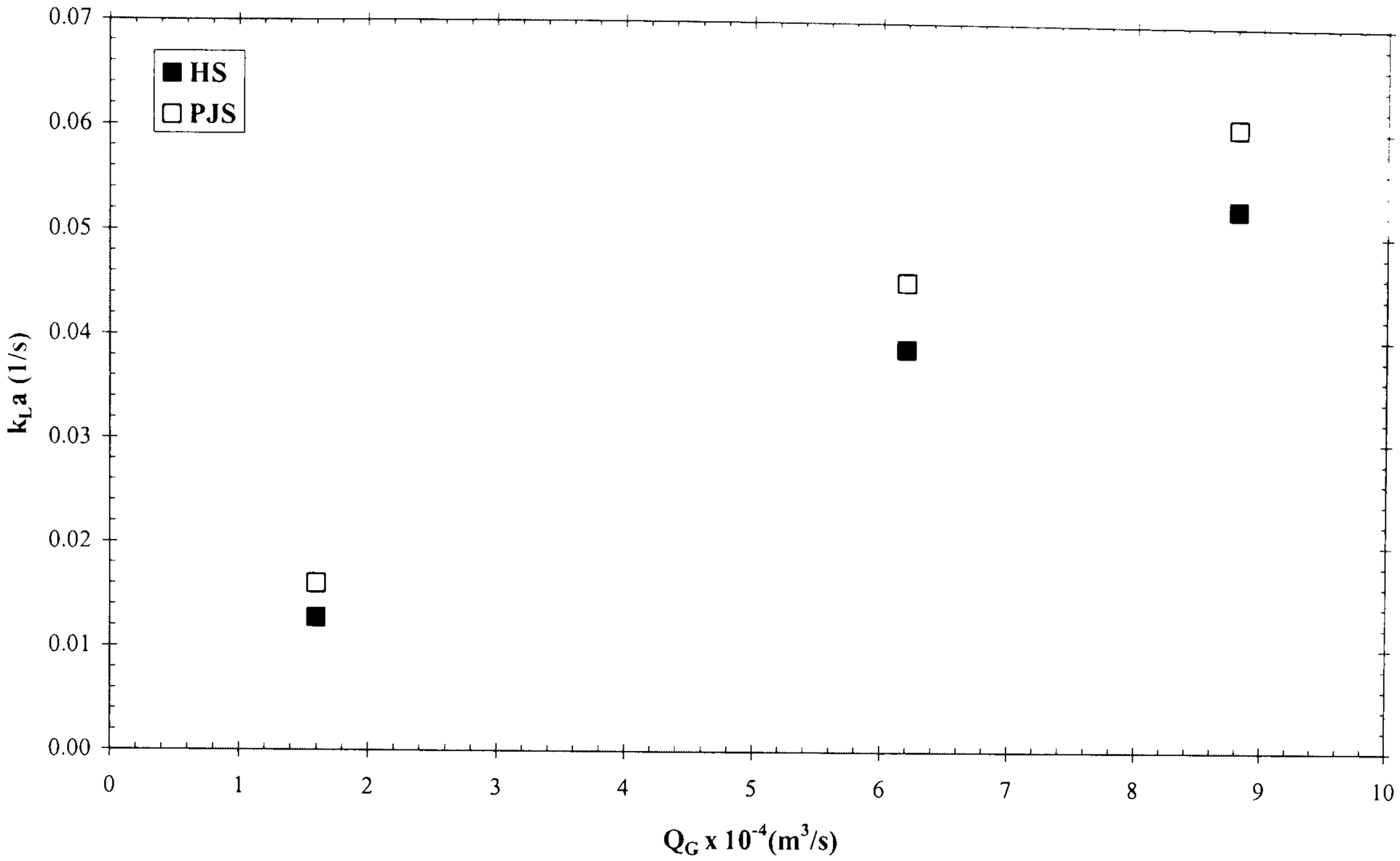

Overall gas – liquid volumetric mass transfer coefficients for the PJS and HS for Cases II, VI and VII.

Figure 5.14

	k_La_{PJS} (s^{-1})	$k_La'_{HS}$ (s^{-1}) $n=0.19$	$k_La'_{HS}$ (s^{-1}) $n=0.21$	$k_La'_{HS}$ (s^{-1}) $n=0.40$	*difference*[a] (%) $n=0.19$	*difference*[a] (%) $n=0.21$	*difference*[a] (%) $n=0.40$
Case II	0.0160	0.0155	0.0158	0.0192	3.51	1.39	16.70
Case VI	0.0453	0.0420	0.0423	0.0456	7.97	7.11	0.69
Case VII	0.0603	0.0545	0.0547	0.0568	10.68	10.25	6.24

[a] Difference is defined as $\frac{k_La_{PJS}-k_La'_{HS}}{k_La'_{HS}}\times 100\%$

Adjusted gas – liquid volumetric mass transfer coefficient, k_La, for the PJS for equal energy consumption to the HS.

Table 5.7

Assuming spherical bubble shape then the gas-liquid mass transfer coefficient k_L for all spargers was estimated from the measured values of k_La and gas void fraction using the published procedure based on Eq. (5.32). The results are shown in Table 5.6 where it can be

observed that the k_L is roughly the same irrespective of sparger design. The (constant) value of k_L is 4×10^{-4} m s^{-1}, which is independent of $\frac{P}{V}$ and j_G proposed by Calderbank and Moo-Young (1961) and derived for large circulating bubbles and liquid drops with diameter larger than 2.5 mm.

$$k_L = k_L a \frac{d_{32}\left(1-\varepsilon_G\right)}{6\varepsilon_G} \tag{5.33}$$

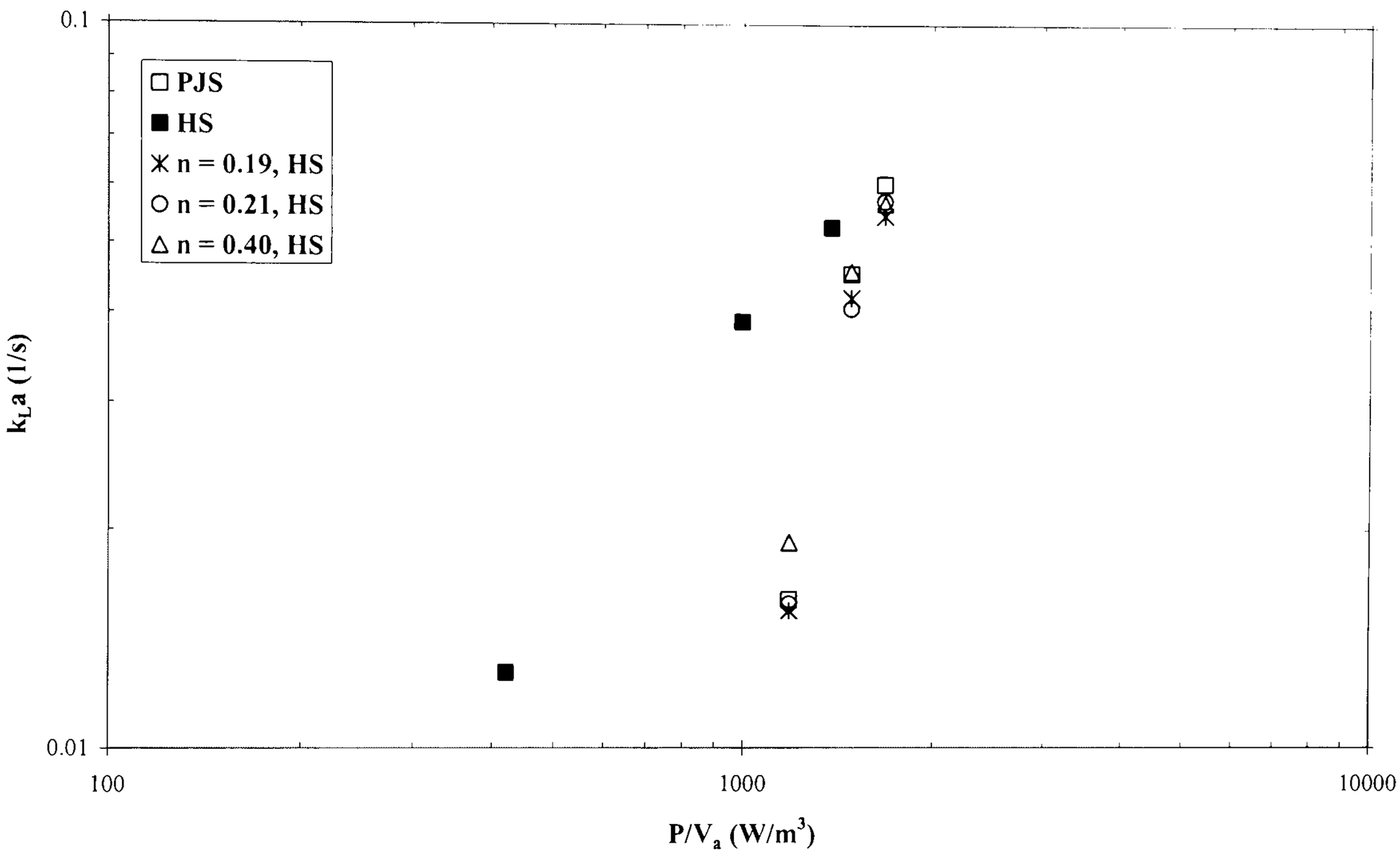

Overall gas – liquid mass transfer coefficients versus power consumption for the PJS and HS for Cases II, VI and VII. The adjusted k_La values of the HS for equal energy consumption are also shown.

Figure 5.15

5.6 ALTERNATIVE INTERPRENTATION

In this section a tentative alternative interpretation regarding the general mass transfer performance of this PJS against the HS is suggested. The experimental k_La data for this PJS and the HS are plotted in Fig. 5.16 against the power consumption per unit of aerated volume, i.e. in the same coordinates as in Fig. 5.15. However, in Fig. 5.16 the trendlines (based on least squares fitting) of the experimental data for both spargers are also plotted (solid thick lines).

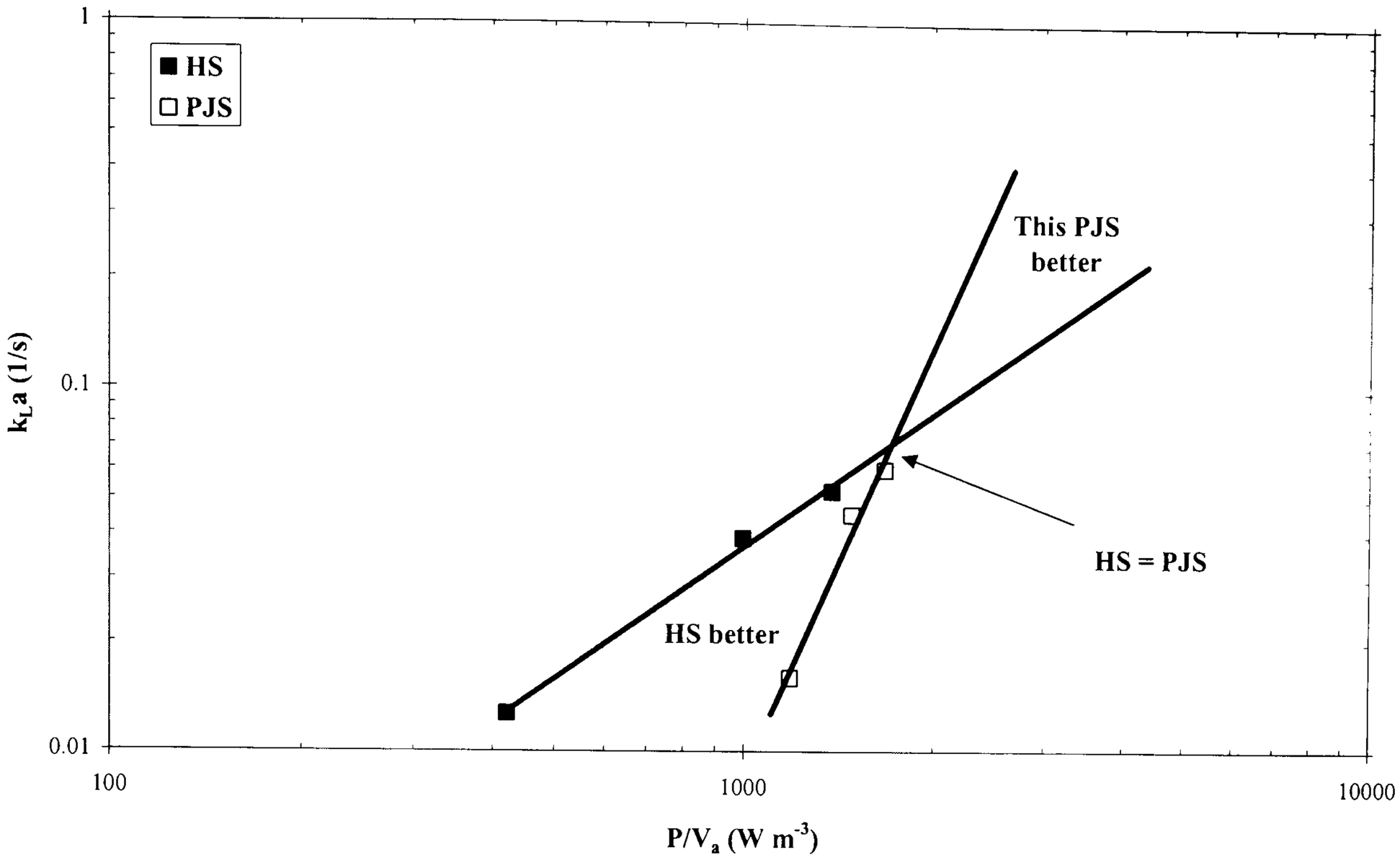

Overall gas – liquid mass transfer coefficients versus power consumption for the PJS and HS for Cases II, VI and VII. The trendlines (based on least squares fitting) in each case are also shown in the graph as solid thick lines.

Figure 5.16

It is seen that the HS performs better than this PJS in the range of $0.01 \le k_L a \le 0.07$ s^{-1} since it can produce the same $k_L a$ as this PJS but for with lower energy dissipation rates. The region of $0.01 \le k_L a \le 0.07$ s^{-1} corresponds to low mass transfer rates and low gas flow rates (see Table 5.5 – Cases II and VI) where the ventilated cavity attached to the HS is short and therefore the energy losses associated with it low (see section 5.3). This region where the HS performs better than this PJS is clearly shown in Fig. 5.16.

On the other hand, at approximately around $k_L a \simeq 0.07$ s^{-1} both spargers exhibit the same mass transfer performance (for the same energy dissipation rate they produce the same $k_L a$). For higher mass transfer rates, i.e. when a value of $k_L a \ge 0.07$ s^{-1} is required, the advantages of this PJS start to show. As it is seen in Fig. 5.16 this PJS outperforms the HS since it can produce the same $k_L a$, but with lower energy dissipation rates. This region corresponds to intermediate and high gas flow rates. The ventilated cavity that is attached to the HS grows long (e.g. in Case VII – Table 5.5), which contributes to an increase in the overall energy losses.

5.7 SUMMARY

The results presented in this chapter show that the bubble size produced by a sparger in a vertical pipe in downflow depended on the operating conditions and the sparger design. The PJS was shown to be the most effective way of distributing gas in the downcomer pipe since it did not allow the formation of a ventilated cavity and also produced a significantly higher specific interfacial area for mass transfer than the PS, CS and HS. The average increase in the $k_L a$ when the PJS was used instead of the industrial design (HS) was 19 %. The average bubble size and the $k_L a$ magnitude was essentially the same (differences within 10%) for the PS, CS and HS. The PS created the largest bubble in all cases examined.

When the 19 % average enhancement in $k_L a$ produced by the particular design of the PJS used in the present work was corrected for power consumption, then the PJS and HS had the same mass transfer performance. The PJS still had the important operational advantages of producing shorter cavities (i.e. no pressure loss) and having the greater resistance to stall at high gas flow rates (see section 2.4.3).

*CHAPTER 6

SLUGS IN VERTICALLY DOWNWARDS TWO-PHASE FLOW

6.1 INTRODUCTION

Upward vertical gas-liquid two-phase slug flow in pipes occurs in many industrial situations (see section 2.5). The pressing need for reliable design methods has triggered a very large research activity in this type of flow over the past several decades. Following the widely accepted semi-empirical approach suggested by Nicklin et al. (1962) it is possible to represent the propagation velocity of the long slug bubbles, V_s as the sum of two terms:

$$V_s = C_0\left(j_L + j_G\right) + V_d \tag{6.1}$$

where V_d is the Taylor bubble velocity in a quiescent liquid, j_G and j_L are the superficial gas and liquid velocities respectively. C_0 is a distribution parameter that reflects the liquid velocity ahead of the slug nose. The value of the constant C_0 is based upon the assumption that the propagation velocity of the Taylor bubble follows the maximum local velocity V_{cl} in front of the nose tip. It can be seen as the ratio of the maximum to the mean velocity in the profile ahead of the slug. Thus:

$$C_0 = \frac{j_L}{V_{cl}} \tag{6.2}$$

---

* Some of the results of this chapter have been published in:

Sotiriadis, A. A., Thorpe, R. B. and Cheung, C., (2003), Slugs in Vertically Downward Two-Phase Flow, *Anglo Japanese Conference on Two Phase Flow,* Guildford, Surrey, UK, April, pp10.

Sotiriadis, A. A. and Thorpe, R. B., (2005), Critical Weber numbers for the existence of wall slugs in vertical pipes, *Anglo Japanese Conference on Two Phase Flow,* Osaka, Japan, September, pp.8.

The value of C_0 therefore equals approximately 1.2 for fully developed turbulent upward flow and 2 for fully developed laminar upward flow. Bendiksen (1984) conducted extensive experiments with individual slug bubbles in a vertical tube with a flowing liquid, confirming that $C_0 = 1.2$ in the range of $\mathrm{Re} = 5000 - 100000$.

The slug bubble velocity in a quiescent liquid is given by:

$$V_d = C_1 \sqrt{gD \frac{\rho_L - \rho_G}{\rho_L}} \tag{6.3}$$

where C_1 is a factor that depends upon the fluid properties through two dimensionless numbers, namely the inverse viscosity number $\left(N_f = \frac{\sqrt{gD}\rho_L}{\mu_L} \right)$ and the Eotvos number $\left(Eo_D = \frac{gD^2(\rho_L - \rho_G)}{\sigma} \right)$. When $N_f \geq 300$ and $Eo_D \geq 100$, viscosity and surface tension effects are negligible and the bubble rise velocity depends primarily on the force that creates the drift, i.e. gravity; this is the case in most practical applications (Fabre and Line, 1992). Air Taylor bubbles rising at atmospheric pressure in pipes of $D \geq 27$ mm id filled with water fall within these conditions. The factor C_1 acquires under these conditions the limiting value of 0.351 as theoretically specified by Dimitrescu (1943). The agreement of this value with various experimental results in the literature is quite impressive.

The influence of surface tension $\left(Eo_D \leq 3.37\right)$ on the slug bubble velocity was studied by Bendiksen (1985) first in stagnant liquid and then in upward flow. An increase in surface tension was found to decrease the bubble rise velocity in both cases. A comprehensive discussion of the influence of the liquid physical properties on C_1 can be found elsewhere (Fabre and Line, 1992).

A remarkable feature of Eq. (6.3) is that the bubble rise velocity is independent of its length, L_B. Barr (1926) was the first one to point out that the slug velocity and nose geometry were independent of the length of the bubble as long as the length to pipe diameter ratio was in excess of 5 $\left(\frac{L_B}{D} \geq 5 \right)$. However, the teaching of fluid mechanics would lead one to believe that a bubble rising steadily in a liquid is in a balance of buoyant weight and drag and that the buoyant weight is proportional to the volume of gas. On the contrary, the accurate formula of Eq. (6.3) does not depend on the length of the bubble. Another related paradoxical property is that the

Taylor bubble velocity does not depend on the way gas is introduced into the pipes. In the Davies and Taylor (1950) experiments the column was open to the gas. In other experiments the gas was injected into a column whose bottom was closed. Batchelor (1967) also stated: "*the remarkable feature of [equations like (6.3)] and its extensions is that the speed of the bubble is derived in terms of the bubbles shape, without any need for consideration of the mechanism of the retarding force which balances the effect of the buoyancy force on a bubble in a steady motion.*" However despite the above discrepancies, Eq. (6.3) gives a very accurate prediction of the drift velocity.

On the other hand vertical downward slug flow has received little attention in the literature and its analysis has been restricted to only a handful publications. Single slug bubbles in downflowing liquids have been reported in the vertical shaft of the hydraulic air compressor (Schulze, 1954), in nuclear reactors during transient situations (Martin, 1976; Yamazaki and Yamaguchi, 1979) and as a deflooding mechanism in caissons on offshore production platforms (Moon et al., 1987; Thorpe et al., 1989). Annular flow is desirable in offshore disposal caissons to prevent cavitation either in the pipe or at upstream control valves and to avoid vibrations of the equipment. Single rising slugs rising in the caissons can create the desired annular flow pattern. Also problems encountered in the downcomers of airlift reactors (Sodeberg, 1980) and deep shaft wastewater treatment facilities (Irwin et al, 1989) have been associated with the development of large rising bubbles.

On the subject of vertical flow patterns the vast majority of data collected for vertical multiphase flows has been confined to upwards cocurrent flow. Predictive flow maps for downward two phase flow are available in the literature (Golan and Stenning, 1970; Oshinowo and Charles, 1974; Speding and Nguyen 1980 and Barnea et al., 1982) mainly for liquid Froude numbers larger than unity $(Fr \geq 1)$. Unfortunately the work in this area is very limited and the question of accuracy of predictions in downwards cocurrent flow remains the subject of considerable speculation. Despite all the above four studies being based on experiments in pipes of 0.025 – 0.051 mm id, there are major differences between them, both in the flow pattern definitions and in predicted areas.

Griffith and Wallis (1961) were probably the first to report the unstable motion of slug bubbles in downward liquid flow. They reported that in contrast to upward flow, where bubbles are symmetrical with respect to the pipe axis, in downward flow they are eccentrically located, with surface tension acting to restore the symmetry. Thorpe et al. (1989) commented that the

slug bubbles in downflow tended to rise as fast as possible. They stated that because of the differences in the velocity profile far of the bubble nose the bubble chose to rise using the path of least resistance in the pipe i.e. near the wall in direct contrast to co-current upwards slug flow (Fig. 6.1 and Figs. 6.8-6.11). Martin (1976) showed that Eq. (6.1) was not valid for downward slug flow due to this bubble instability, except for the case of the smallest pipe diameter examined $(D = 26mm \ \& \ Eo = 100)$ where his results did not display any significant deviations from Eq. (6.1).

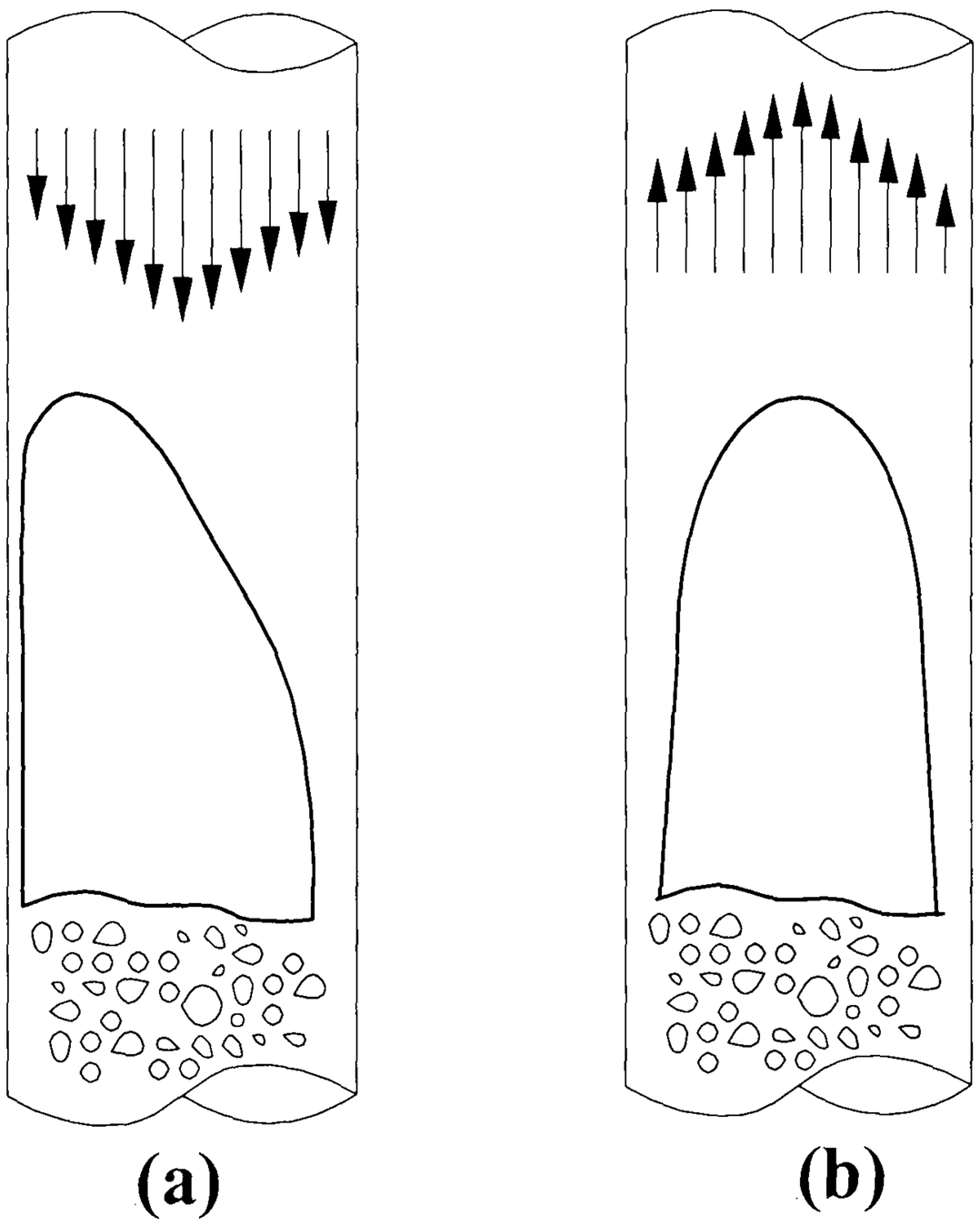

The liquid velocity profile inside a pipe far upstream the bubble nose in a frame of reference with the stationary pipe wall, differs by the sign of the vorticity (after the suggestion of Thorpe et al., 1989): (a) slug bubble rising in downflow and (b) in upflow.

Figure 6.1

The deviation from the Nicklin law, a well established and widely used correlation, proscribes any information on the slug bubble rise velocity. Knowledge of this velocity is critical to the determination of the flow field pressure drop. Yet, to date there are no predictive models

or enough experimental data on the bubble rise velocity that can provide sufficient information towards a more accurate design of systems where downward slug flow is observed. Therefore the aim of this chapter is to provide additional measurements on the dynamics of downward slug flow with respect to the slug bubble velocities. The experiments presented henceforth were conducted for low Froude numbers $(0 \le Fr \le 1.21)$ because of the limited amount of data in the literature regarding this region.

6.2 RESULTS

The measurement procedure for the slug velocity has been described in section 3.10. The slug bubble velocity[6.1] V_s was measured for the operating conditions of Table 6.1.

Operating System	D (mm)	$\mathrm{Re} = \frac{\rho_L j_L D}{\mu_L}$	$Fr = \frac{j_L}{\sqrt{gD}}$	μ_L $\left(kgm^{-1}s^{-1}\right)$	ρ_L $\left(kgm^{-3}\right)$	σ $\left(Nm^{-1}\right)$
Tap Water	105	0 - 126714	0 - 1.21	0.00101	995	0.0725
Salt Water	105	0 - 122832	0 - 1.20	0.00107	1026	0.0741
2% w/w IPA	105	0 - 114275	0 - 1.20	0.00111	992	0.0575
8% w/w IPA	105	0 - 95152	0 - 1.09	0.00120	983	0.0417
Tap Water	50	0 - 72838	0 - 0.69	0.00101	991	0.0725
Salt Water	50	0 - 65443	0 - 0.61	0.00107	1026	0.0741

Range of experimental programme.

Table 6.1

The results reported in the literature (Martin, 1976; Thorpe et al., 1989) are for water, whereas in the present work the slug velocity was measured for four different liquids. These liquids were tap water, salt water and 2% and 8% w/w of aqueous solutions of isopropanol (IPA). The salt

[6.1] The value of V_s corresponded to the tip of the bubble relative to a fixed datum.

water solution was made from tap water plus 3.5% w/w of sodium chloride (NaCl) with 99.5% quality and was used to simulate the mock sea water which exists in offshore disposal caissons. The addition of IPA in water reduced significantly the surface tension without changing much the viscosity of the solution. Following Griffith and Wallis (1961) who commented that the surface tension acting to restore the symmetry in downwards flow, it was then possible to quantify the stabilising effects of the surface tension on the slug bubble rise velocity. The liquid physical properties were measured according to the methods outlined in Chapter 3 and are also shown in Table 6.1.

The vertical positioning of the slug nose at the each plane had an uncertainty of ± 0.015 m. The slug velocity was measured using a stopwatch. The timing had an uncertainty of ± 0.1 s. The error in the estimation of the liquid velocity from the magnetic flow meter was ± 0.03 m s^{-1}. These errors were quantified and are shown as error bars in the Figs 6.2 – 6.7. The shape of the slugs in downwards flow was determined for qualitative analysis from photographs. The aim was to emphasise the variations of the specific slug shape in the nose region with changes of the superficial liquid velocity. As already mentioned the slug bubble velocity that was measured corresponded to the tip of the bubble i.e. at the nose.

6.2.1 Slug velocity

The measured values of the slug velocity are plotted against the liquid superficial velocity[6.2], j_L after the suggestion of Nicklin et al. (1962) and the results are shown in Figs. 6.2 - 6.7. The downward superficial liquid velocities have been defined as positive (in agreement with the rest of the thesis – e.g. in Chapter 4). The velocity of ascending slugs, i.e. the slugs that rose in the downflowing liquids (countercurrent two phase flow) have also been defined as positive whereas the velocity of descending slugs, i.e. the slugs that descended in the downflowing liquids (concurrent two phase flow) as negative.

6.2.1.1 Wall slugs

There are three main trends in each figure that correspond to a specific slug shape and position inside the pipe. The majority of the data in all figures concerned *wall* slugs, which have already been reported in the literature (Martin, 1976; Thorpe et al., 1989). These were rising or

---

[6.2] For the experiments reported in this work there is no gas in the region in front of the generated slugs and therefore the superficial gas velocity is zero $\left(j_G = 0\right)$ in Eq. (1).

descending slugs that did not propagate along the axis of the pipe but rather migrated to the pipe wall. This behaviour resulted in a much sharper slug nose than a conventional slug. Wall slugs have a greater speed than a conventional one that rises at the centre of the pipe for two reasons: (1) the nose is sharper and (2) the liquid near the wall has a lower downwards velocity.

The shape of the wall slugs is clearly shown for three different cases in the photographs of Fig. 6.8. The only ones that have produced photographs of wall slugs are Martin (1976) (his Figs. 6 and 7) and Moon et al. (1987) (their Fig. 23). However the quality of their photographs was bad and the region of interest for the slug rise velocity i.e. the slug nose was barely distinguishable. On the other hand, the photographs presented in this work (Figs. 6.8 - 6.11) are clear and revealing (because of advances in cameras in the last 20 years) in allowing for the first time a successful qualitative view of the slug nose region in downwards flow.

The shape of the slug nose changed for all test liquids as the downward liquid flow rate was increased. A typical example is shown in Fig. 6.9 where two wall slugs are rising in water. It can be seen that as the water downward flow rate was increased the slug nose was distorted and large ripples appeared on its main body. The slug was moving around the circumference of the pipe wall trying to find the quickest way to rise. The pipe diameter also had an effect on the slug shape. The distortion of the bubble in the 50 mm id pipe was not as severe as that observed in the 105 mm id pipe (Fig. 6.8).

6.2.1.2 Central slugs

The second specific slug type was observed when the superficial liquid velocity was close to zero. The slugs were not located in the wall any more and their nose had become nearly spherical. The slugs were very stable and remained almost concentric within the pipe (Fig. 6.10). The velocity of these *central* slugs was described adequately by Eq. (6.1) valid for upflow i.e. $C_0 = -1.2$ and $C_1 = 0.35$ as is shown in Figures 6.2 - 6.7.

6.2.1.3 Transition region slugs

For a minority of the data, at low superficial liquid velocities, but still in turbulent flow (for example at $j_L = 0.225$ m s^{-1} in Fig. 6.2), there was an apparent change from the central slug behaviour in all of the experimental cases. The slug velocity was slightly higher than the velocity of central slugs and lower than that indicated by following the trend of the wall slugs. This was associated with observation that the bubbles were not situated near the wall. Indeed, photographs showed that they were rising close to the pipe centre and that their shape had drastically changed

(Fig. 6.11). These slugs were oscillating across the pipe's centreline and their nose was much less distorted compared to wall slugs. Their shape distinctly resembled the one of upward flow. For those lower superficial liquid velocities the experimental data show a jump of the slug velocity (from central to wall slug), which marks the boundaries of a *transition region* between central and wall slugs. This region is clearly depicted in Figs. 6.2 – 6.7. There is no report in the literature of the transition region or the jump in the slug velocity observed in this study.

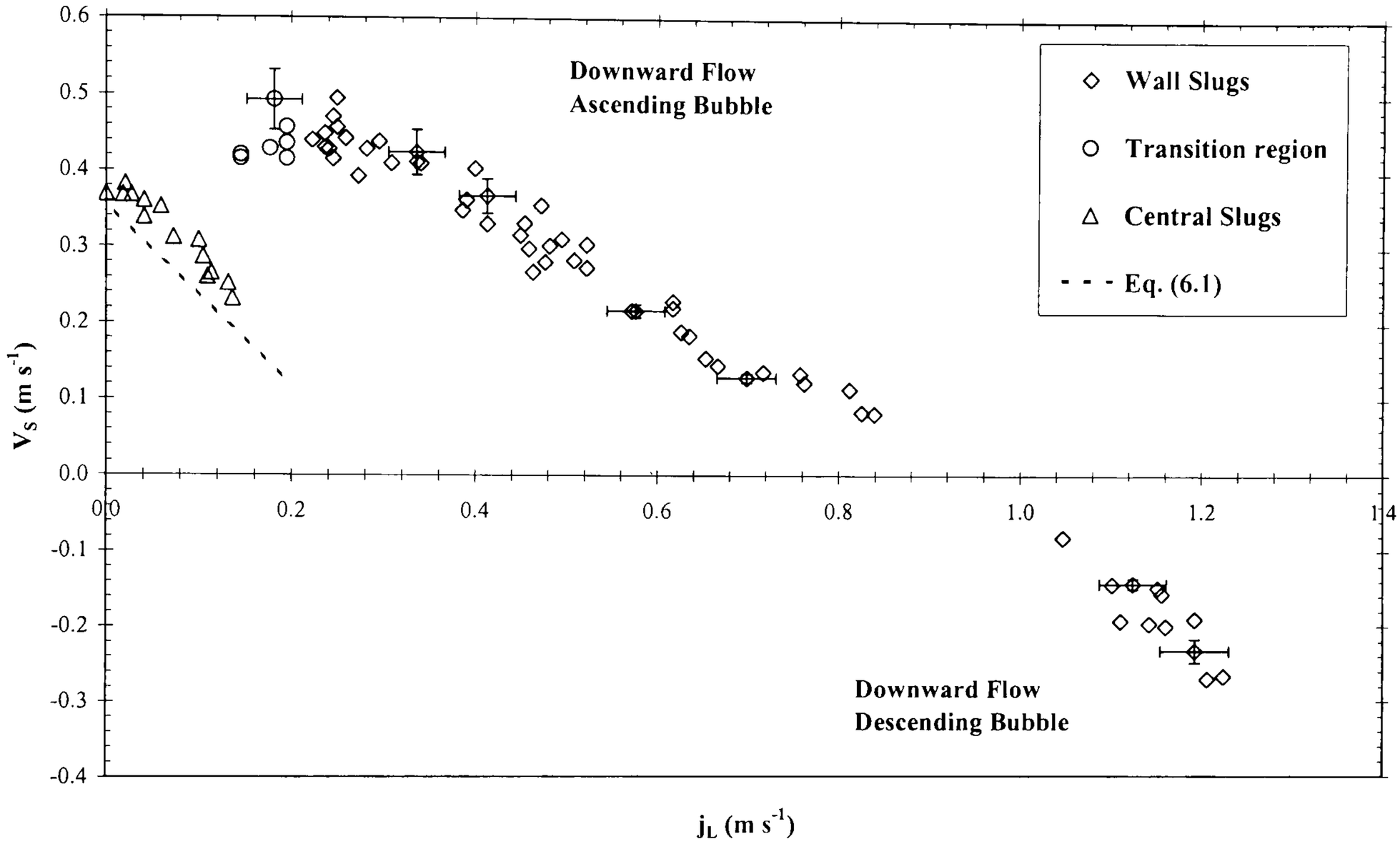

Slug velocity plotted against the superficial liquid velocity for $D = 105$ mm in water. Note that $j_G = 0$ m s^{-1} in Eq. (1).

Fig. 6.2

The results for all test liquids (see Figs. 6.2 to 6.7) suggest that the transition region depends on both the pipe diameter and the surface tension. The jump in the velocity is more pronounced for the 105 mm id pipe rather than the 50 mm id pipe where the data for both test liquids illustrate a smoother transition. Moreover the boundaries of the transition region are influenced by the surface tension. It seems that a reduction in the surface tension shifts the transition region closer to zero, e.g. from $j_L = 0.225$ m s^{-1} in Fig. 6.2 to $j_L = 0.17$ m s^{-1} in Fig. 6.5. Also as the interfacial surface tension is reduced (Table 6.1) then its stabilising effect on the slug nose becomes reduced, which allows the slug bubble to flee the pipe's centerline at lower downward superficial liquid velocity and thus rise faster (Fig. 6.5 at $j_L = 0.05$ m s^{-1}). Certainly this is

shown in the data regarding the IPA solution. One can observe that central slugs were only formed when the liquid was almost quiescent ($j_L \simeq 0$ m s^{-1}). On the other hand, this was not the case for the data shown in Figs 6.2 and 6.3 where central slugs were observed for downward liquid superficial velocities up to 0.16 m s^{-1}.

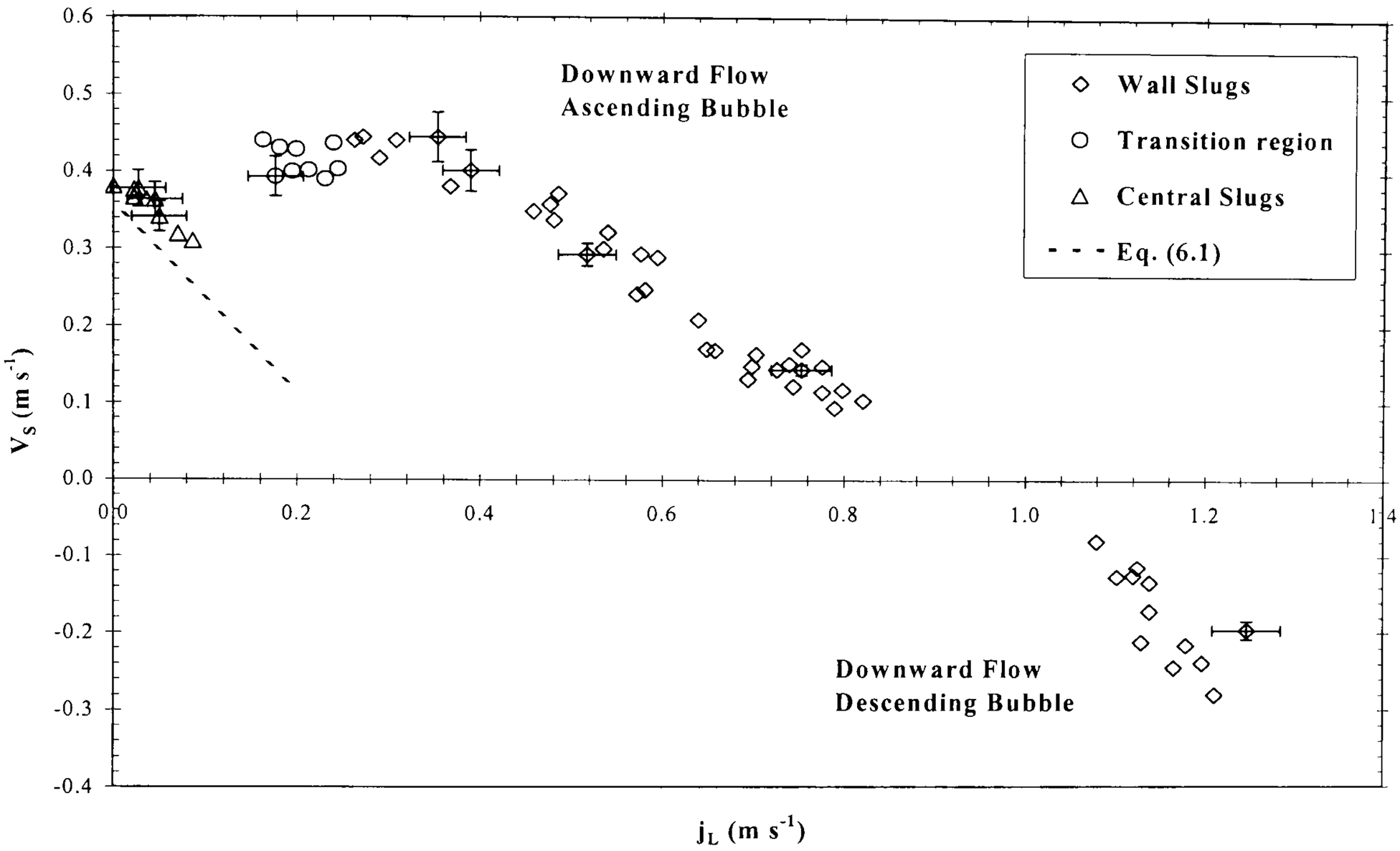

Slug velocity plotted against the superficial liquid velocity for $D = 105$ mm in salt water.

Fig. 6.3

The effects of pipe diameter and surface tension on the boundaries of the transition zone are quantified using the dimensionless Weber number shown below and the results are presented in Table 6.2:

$$We_T = \frac{\rho_L j_{L,T}^2 D}{\sigma} \tag{6.3}$$

where $j_{L,T}$ is the superficial liquid velocity that marks the onset of wall slugs, i.e. a wall slug would be formed inside the pipe for every superficial liquid velocity that is higher than $j_{L,T}$.

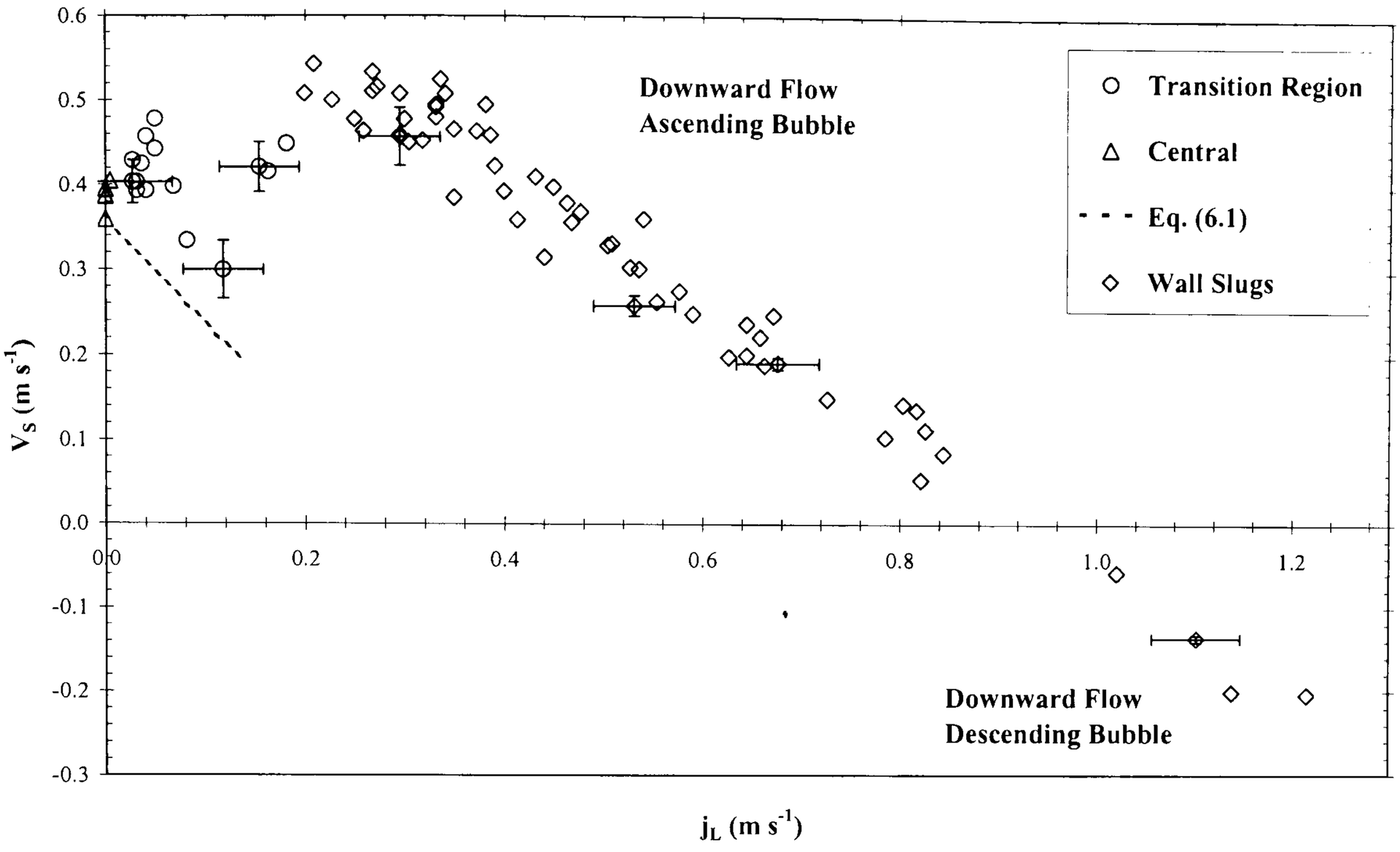

Slug velocity plotted against the superficial liquid velocity for $D = 105$ mm in 2% w/w aqueous solution of IPA.

Fig. 6.4

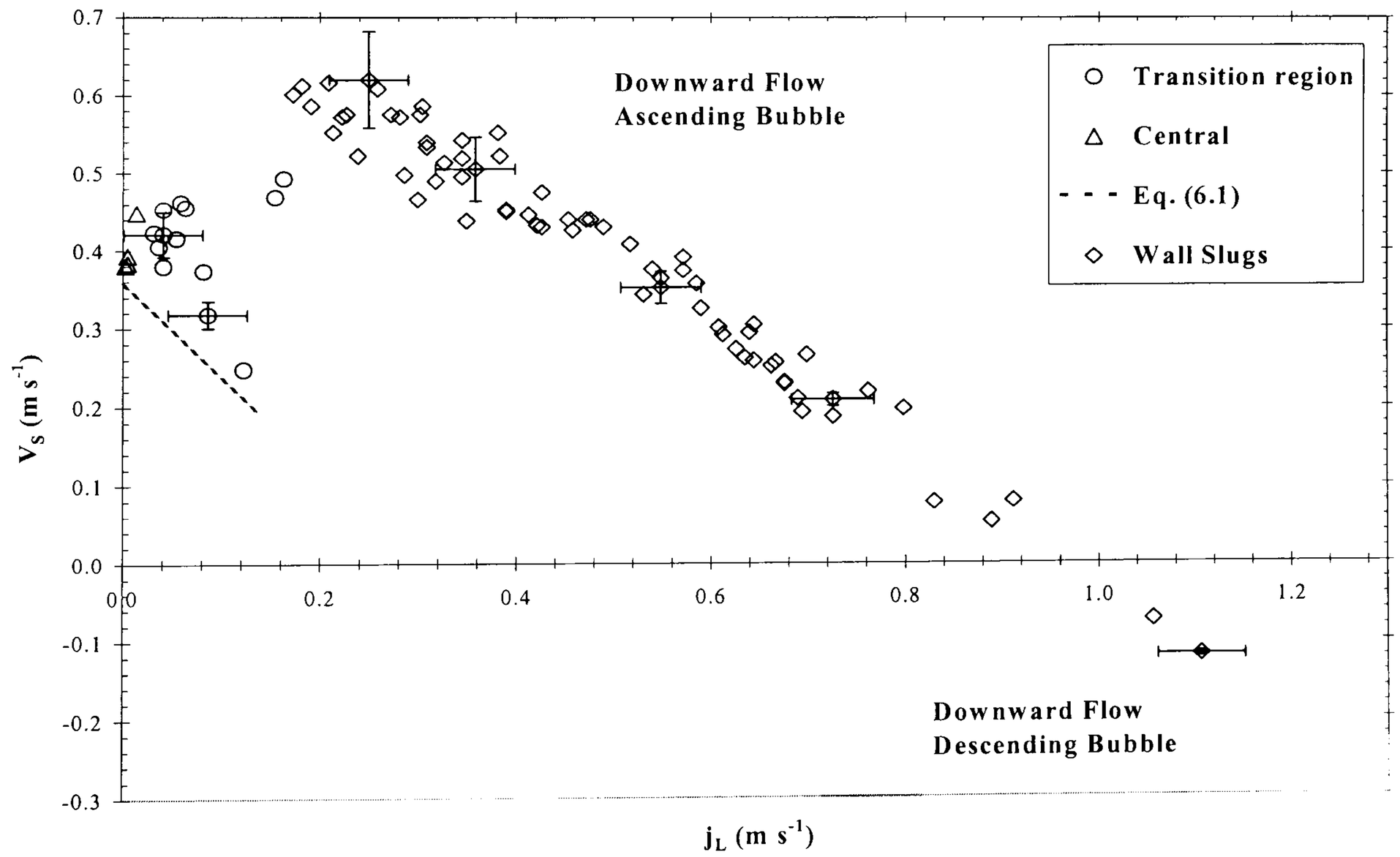

Slug velocity plotted against the superficial liquid velocity for $D = 105$ mm in 8% w/w aqueous solution of IPA.

Fig. 6.5

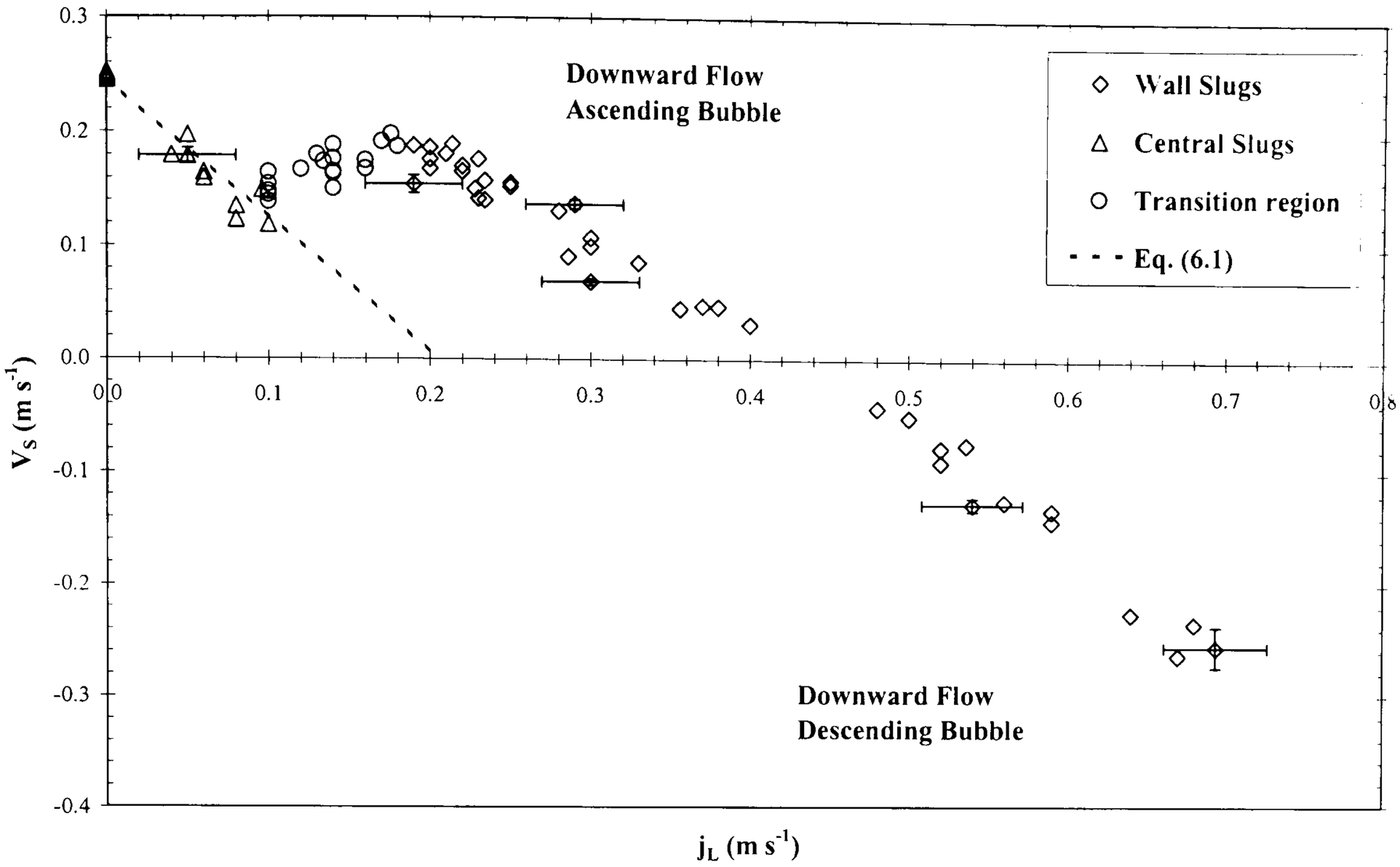

Slug velocity plotted against the superficial liquid velocity for $D = 50$ mm in water.

Fig. 6.6

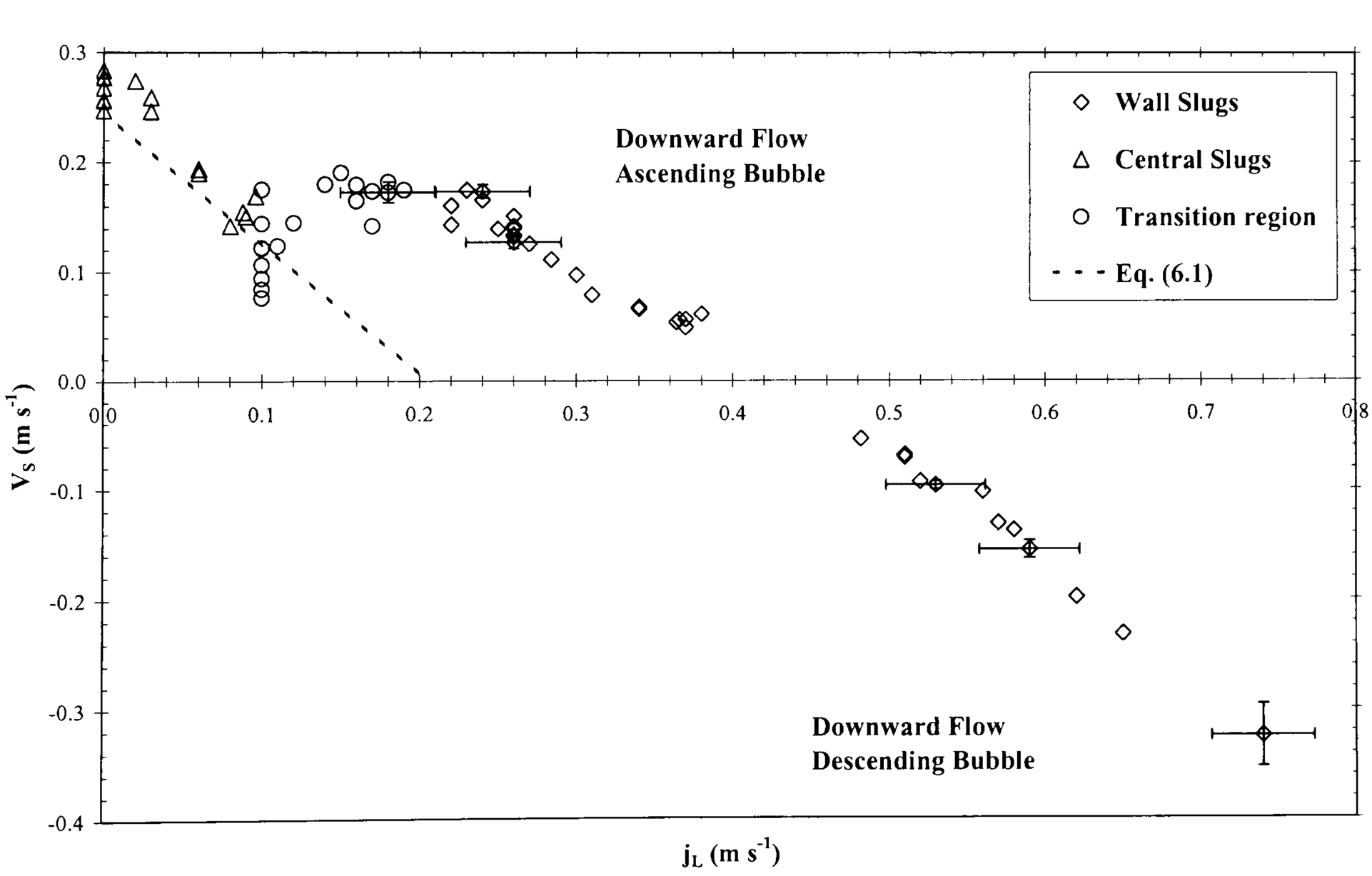

Slug velocity plotted against the superficial liquid velocity for $D = 50$ mm in salt water.

Fig. 6.7

(a) (b) (c)

Ascending wall slugs (a) in water, $D = 105$ mm and $j_L = 0.43$ m s^{-1} (b) in salt water, $D = 50$ mm and $j_L = 0.38$ m s^{-1} and (c) in 8% w/w IPA solution, $D = 105$ mm and $j_L = 0.36$ m s^{-1}.

Figure 6.8

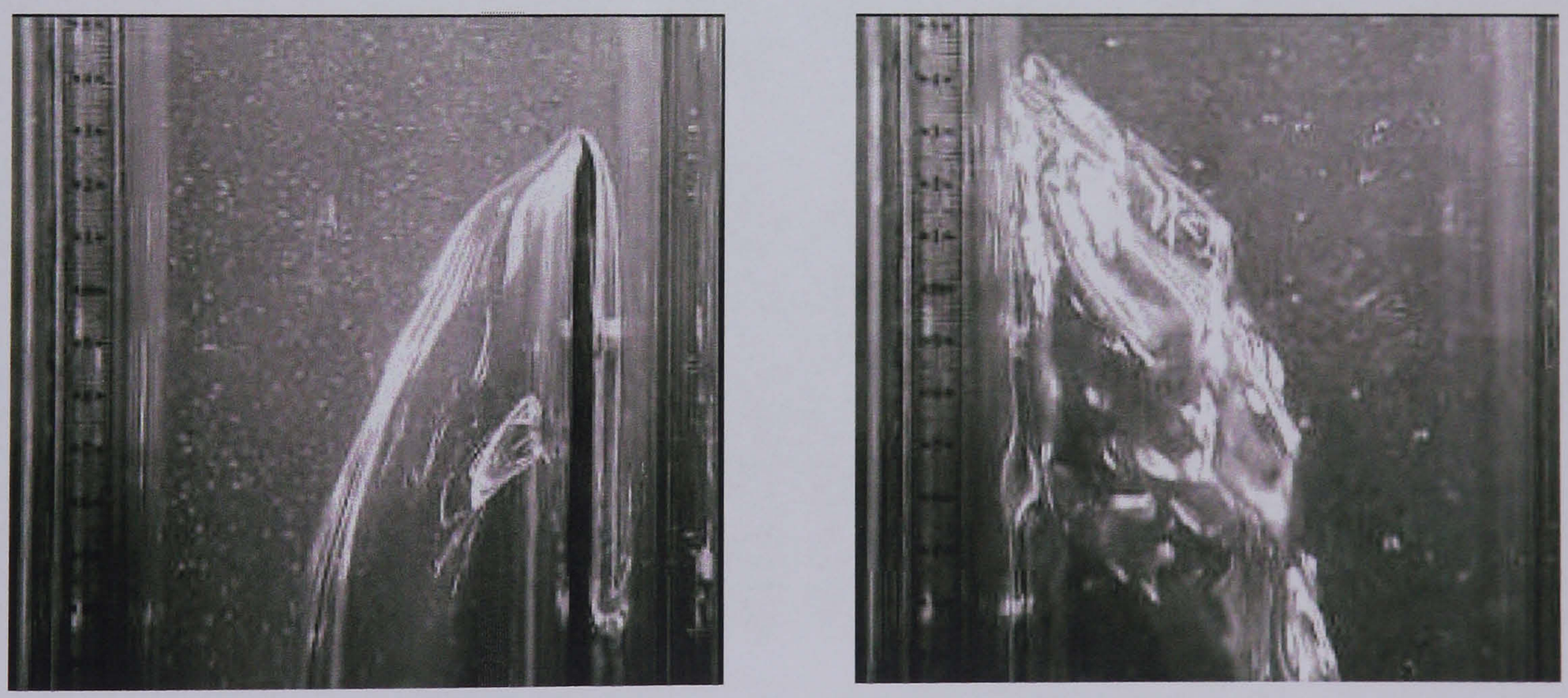

Effect of the water flow rate on the shape of rising wall slugs in $D = 105$ mm:

(a) $j_L = 0.43$ m s^{-1} and (b) $j_L = 0.75$ m s^{-1}.

Figure 6.9

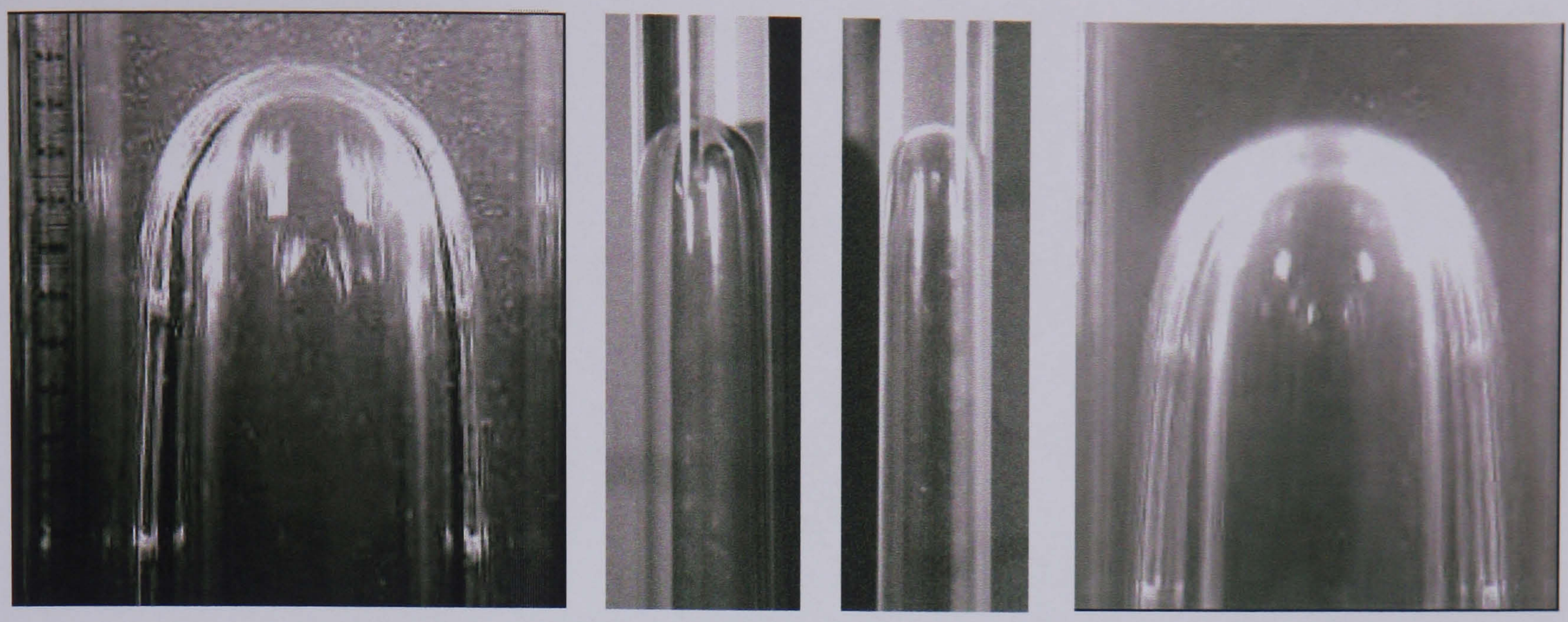

(a) (b) (c) (d)

Central slugs (a) central slug in water $D = 105$ mm and $j_L = 0.056$ m s^{-1} (b) central slug in water, $D = 50$ mm and $j_L = 0.06$ m s^{-1} (c) central slug in salt water, $D = 50$ mm and $j_L = 0.08$ m s^{-1} & (d) central slug in 8% w/w IPA solution, $D = 105$ mm and $j_L = 0.01$ m s^{-1}.

Figure 6.10

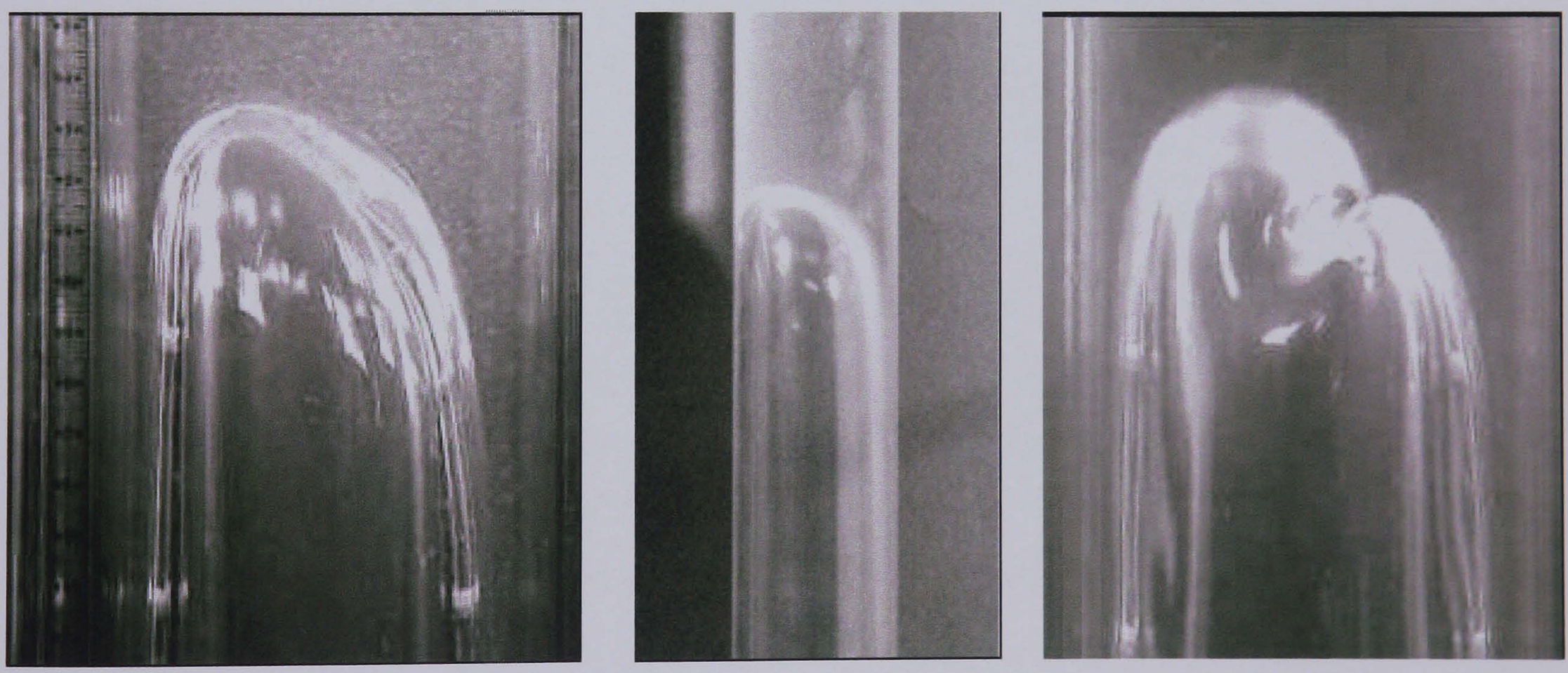

(a) (b) (c)

Slugs in the transition region (a) Slug in water, $D = 105$ mm and $j_L = 0.165$ m s^{-1} (b) slug in salt water, $D = 50$ mm and $j_L = 0.125$ m s^{-1} & (c) slug in 8% w/w IPA solution, $D = 105$ mm and $j_L = 0.065$ m s^{-1}.

Figure 6.11

The agreement for the onset of wall slugs of the Weber number between the different test liquids in each case is astonishing. It is seen that there is a critical value for the Weber number in Eq. (6.3) thát marks the onset of wall slugs. The constant value of the Weber number for each pipe diameter suggests that the onset of wall slugs does not depend primarily on the liquid physical properties, but rather has a specific value depending on the pipe diameter[6.3]. Interestingly there is a difference by a factor of 3 in the We_T with a doubling of the pipe diameter (Table 6.2).

Operating System	D (mm)	$j_{L,T}$ (ms^{-1})	We_T
Tap Water	105	0.225	73.0
Salt Water	105	0.23	76.9
2% w/w IPA	105	0.20	72.5
8% w/w IPA	105	0.17	71.5
Tap Water	50	0.19	24.7
Salt Water	50	0.19	25.0

Weber number of transition for all the test liquids used.

Table 6.2

An attempt was made to resolve the above pipe dependence for the onset of wall slugs. The dimensionless correlation shown in Eq. (6.4) is proposed to predict the end of the transition region. The results for all the test liquids and the two pipe diameters are shown in Table 6.3. It can be seen that the dependence of the pipe diameter has been alleviated since the onset of the wall slugs takes place at around 4.7×10^5 irrespective of the pipe diameter.

$$\frac{\sigma g}{\mu_L j_{T,L}^2}\left(\frac{D}{y^*}\right)=4.\cdot\times10^5 \qquad (6.4)$$

[6.3] A similar result was obtained for the onset of gas entrainment from ventilated attached to spargers (see section 2.3.2).

where y^* is the dimensionless friction distance from the pipe wall $\left(\frac{\mu_L}{\sqrt{\rho_L \tau_0}}\right)$.

Operating System	D (mm)	$j_{L,T}$ (ms^{-1})	$\frac{\sigma g}{\mu_L j_{T,L}^2}\left(\frac{D}{y^*}\right)\times 10^5$
Tap Water	105	0.225	5.05
Salt Water	105	0.23	4.65
2% w/w IPA	105	0.20	4.19
8% w/w IPA	105	0.17	3.94
Tap Water	50	0.19	4.75
Salt Water	50	0.19	4.32

Onset of wall slugs based on Eq. (6.4) for all the test liquids used.

Table 6.3

6.2.2 Sensitivity analysis – Comparison with the literature

Martin (1976) and Thorpe et al. (1989) observed that wall slugs in downward flow can also be represented by Eq. (6.1), but the values of the coefficients C_0 and C_1 differ from those of upward flow (see Table 6.4). Thorpe et al. (1989) studied only few rising wall slugs, created by natural aeration in downward flow in a 101.6 mm id pipe. On the other hand, the data of Martin (1976) are more plentiful; he studied ascending and descending wall slugs created by forced or natural aeration in downward flow for 140 mm, 101.6 mm id pipes and only descending slugs created by forced aeration for a 2.6 mm id pipe.

A sensitivity analysis based on the least squares fitting method was carried out for the experimental data in Figs 6.2 – 6.7. The aim was to determine the values of C_0 and C_1 as well as the uncertainties in V_S, C_0 and C_1 that corresponded to a 68% confidence interval. This will allow direct comparisons to other results found in the literature. The analysis was carried out for three different cases. In the first case the transition zone data were taken into account in order to investigate the effects on C_0 and C_1. In the second case only the wall slug data were considered (both counter-current and co-current flow data) to enable comparison to Martin's data. Finally, in

the third case only rising wall slugs were considered (co-current flow) to compare to Thorpe's et al. (1989) data. The analysis is shown in Table 6.5.

Literature Data	D (mm)	C_0	C_1	$\sigma_{V_S}{}^{a}$ (ms^{-1})	$\sigma_{C_0}{}^{a}$	$\sigma_{C_1}{}^{a}$
Martin (1976)	140	-0.860	0.680	0.100	0.052	0.040
Martin (1976)	101.6	-0.900	0.660	0.053	0.030	0.020
Martin (1976)	26	-0.930	-	-	-	-
Thorpe et al. (1989)	101.6	-0.710	0.493	0.055	0.110	0.040

[α] The uncertainties are based on a 68% confidence interval

Literature data.

Table 6.4

It is obvious from Table 6.5 that exclusion of the transition zone increased both the slope (C_0) and the intercept (C_1) of the experimental fitting and the uncertainties in the estimation of V_S, C_0 and C_1 were reduced. For the 50 mm id pipe, a reduction by a factor of 2 is observed in the values of σ_{V_S}, σ_{C_0} and σ_{C_1} (Table 6.5). This is attributed to the fact that the transition zone was more gradual for both test liquids and the distortion of the bubble was not as severe as that observed for the larger pipe (Fig. 6.11).

There is no report in the literature of the transition region or the jump in the slug velocity observed in this study. In Martin's (1976) and Thorpe's et al. (1989) results, there was a lack of experimental data for superficial liquid velocities below $j_L \leq 0.25$ m s^{-1}. However in both of these studies there are measurements for $j_L = 0$ m s^{-1}. Martin reported that initially the slugs rose in the pipe centre having a spherical nose (central slugs) but frequently moved and rode up the pipe wall resulting in a distorted nose (wall slugs). After a while the slugs returned to the pipe centre and their nose changed back to a spherical. This unstable behaviour is depicted by the great scatter observed in Martin's experimental data for $j_L = 0$ m s^{-1} and resulted in measuring a higher slug velocity than that given by the Eq. (6.1). Thorpe et al. (1989) also measured higher

slug velocity for $j_L = 0$ m s^{-1} than the one given by Eq. (6.1) indicating that they must have also observed the same unstable behaviour. In the present study, only central slugs were observed for $j_L = 0$ m s^{-1} and their velocity was described well by the Eq. (6.1) (Figs 6.2 – 6.7).

The differences between the results of Thorpe et al. (1989) and Martin (1976) for $D = 101.6$ mm are mainly due to three reasons: (1) Thorpe et al. studied only rising wall slugs; the results in this study show that if only rising slugs are taken into account both C_0 and C_1 are reduced (Table 6.5); (2) Martin's experiment had a continuous flow which included small bubbles present in the flow. That is reason why the distribution parameter $(C_0 = -0.9)$ of Martin for $D = 101.6$ mm is between results for slugs (Thorpe et al., 1989; this work) $(C_0 = -0.7)$ and that for homogeneous bubbly flow $(C_0 = -1)$ and (3) Martin (1976) plotted his experimental data as slug velocity vs. mixture velocity $(j_L + j_G)$ since the superficial gas velocity in his experiments was not zero (there was gas in the region in front of the slugs). On the other hand, Thorpe et al. (1989) conducted similar experiments to this work where the superficial gas velocity was zero.

6.3 FURTHER DISCUSSION

In the present work a lot of experimental data have been presented. The uncertainties in V_s, C_0 and C_1 are less by a factor of 2 than the results of Martin and Thorpe et al. (see Tables 6.3 and 6.4), which proves that the data presented in this chapter data are more precise.

The effect of surface tension on the wall slug velocity is evident when all the wall slug data are plotted together. This is done in Fig. 6.12 for the 105 mm id pipe. The bubble velocity in water and saltwater was almost the same. On the other hand, the wall slugs rose faster in the IPA solution for both concentrations than water or saltwater. Especially in the 8% w/w solution where the surface tension was reduced by a factor of 1.74 comparing to water (Table 6.1) the wall slugs rose almost with a velocity approximately of 0.15 - 0.25 m s^{-1} faster than water. This is depicted in the analysis of Table 6.5 where the intercept of $C_1 = 0.77$ is by far the highest than the rest, when only the wall slugs are taken into account.

It is clear from Table 6.4 that there is some dependence in the slug velocity on pipe size. If the results for the water-air system are considered (Fig. 6.2 and Table 6.5) then:

$$V_S = -0.70 j_L + 0.63\sqrt{gD}\text{ , for } D = 105 \text{ mm and} \qquad (6.5)$$

$$V_S = -0.86 j_L + 0.36\sqrt{gD}\text{, for } D = 50 \text{ mm} \tag{6.6}$$

Operating System	C_0	C_1	$\sigma_{V_s}\left(ms^{-1}\right)$	σ_{C_0}	σ_{C_1}
Water: $D = 105$ mm					
Transition data & Wall Slugs	-0.68	0.61	0.034	0.011	0.008
Wall Slugs	-0.70	0.63	0.027	0.011	0.008
Ascending Wall Slugs	-0.65	0.61	0.024	0.020	0.010
Salt Water: $D = 105$ mm					
Transition data & Wall Slugs	-0.66	0.61	0.048	0.019	0.014
Wall Slugs	-0.74	0.68	0.032	0.016	0.013
Ascending Wall Slugs	-0.68	0.65	0.027	0.028	0.016
2% w/w IPA: $D = 105$ mm					
Transition data & Wall Slugs	-0.51	0.56	0.086	0.036	0.018
Wall Slugs	-0.76	0.71	0.071	0.039	0.022
Ascending Wall Slugs	-0.74	0.70	0.062	0.046	0.023
8% w/w IPA: $D = 105$ mm					
Transition data & Wall Slugs	-0.50	0.61	0.097	0.043	0.021
Wall Slugs	-0.77	0.77	0.075	0.042	0.023
Ascending Wall Slugs	-0.75	0.76	0.070	0.045	0.023
Water: $D = 50$ mm					
Transition data & Wall Slugs	-0.73	0.30	0.036	0.026	0.009
Wall Slugs	-0.86	0.36	0.017	0.016	0.007
Ascending Wall Slugs	-0.76	0.33	0.015	0.046	0.012
Salt Water: $D = 50$ mm					
Transition data & Wall Slugs	-0.66	0.27	0.055	0.040	0.014
Wall Slugs	-0.90	0.37	0.014	0.017	0.007
Ascending Wall Slugs	-0.77	0.33	0.011	0.046	0.013

Sensitivity Analysis.

Table 6.5

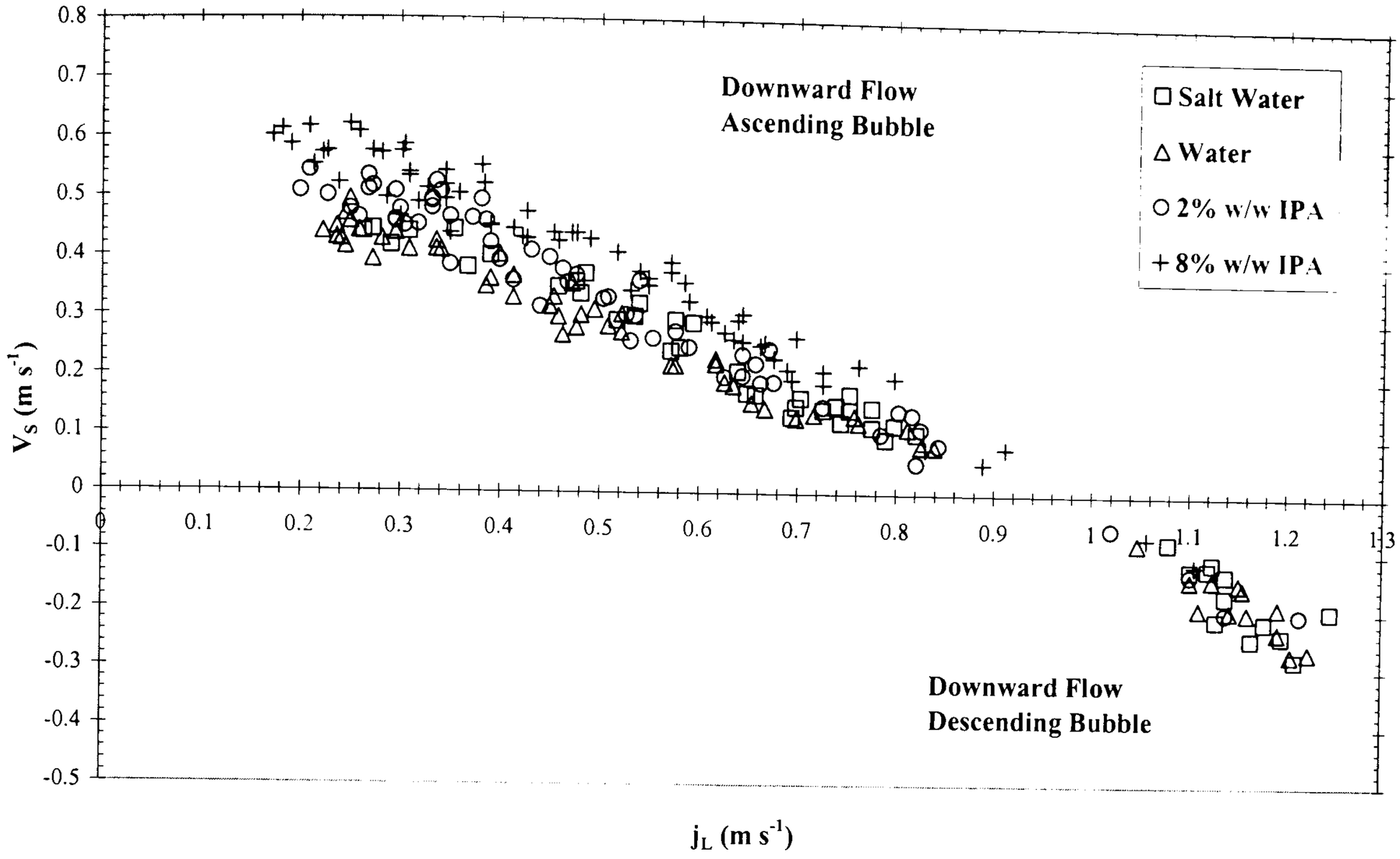

Wall slugs in the 105 mm pipe. Data for all test liquids.

Figure 6.12

By comparison with Eq. (6.1) is noted that the drift parameter C_1 does not have a constant value, as it does in upflow $(C_1 = 0.35)$. The same also holds for the results for the salt water – air system (Table 6.5). This variation in C_1 is a new result in that Martin (1976) did not observe major change in C_1 with change in D (Table 6.4).

In Fig. 6.13 the wall slug data presented in this chapter, the literature data of Martin (1976) and Thorpe et al. (1989) are plotted against the slip velocity[6.4]. The literature data that corresponded to $j_L = 0$ m s^{-1} are also included because as mentioned in the previous section regarded slugs that were not central. A fit based on least squares method is applied to all the data. The results show the following remarkable trend. The slope is almost the same for all the data with a constant value of around 0.45. This is somehow surprising because the data correspond to different pipe diameters and different liquids. In contrast, the intercept is different for all the different cases, ranging from 0.19 (50 mm id pipe and water) to 0.44 (105 mm id pipe

---

[6.4] Slip velocity is the difference between the average velocities of two different fluids flowing together in a pipe. In vertical ascending flow, the lighter fluid flows faster than the heavier fluid. The slip velocity depends mainly on the difference in density between the two fluids, and their holdups.

and 8% w/w IPA). The intercept is increasing with increasing pipe diameter and decreasing surface tension. It has already been shown that the slugs rise faster both in larger pipe diameters and in liquids with lower surface tension. This is clearly depicted in Fig.6.13.

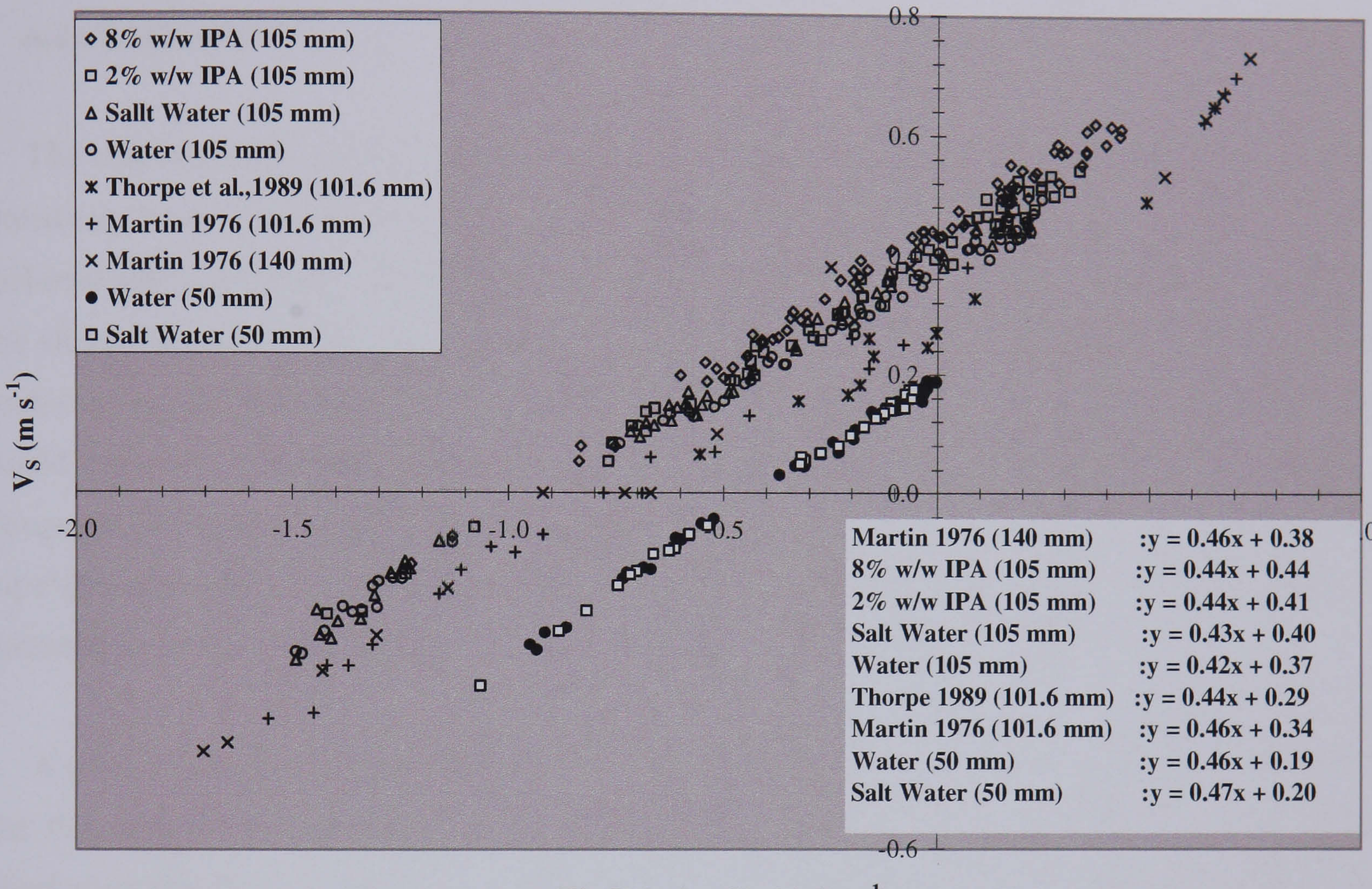

Wall slugs versus slip velocity.

Figure 6.13

The value of the distribution parameter C_0 found in the experiments also increases as the pipe diameter decreases and again does not hold the value found in upflow ($C_0 = 1.2$, which is independent of pipe diameter) but is smaller and less than one. Lower values than one of the distribution parameter, C_0 were observed by Martin (1976) and by Thorpe et al. (1989). This agrees with the theoretical considerations based on drift flux analysis of Zuber and Findlay (1967) who showed that $C_0 < 1$ if the wall void fraction is greater than that on the pipe axis. For the case of the wall slugs most of the void fraction is located towards the pipe wall and therefore is expected that $C_0 < 1$. For the smaller pipe, surface tension forces are stronger so the distortion of the bubble is not as great as that observed in the larger pipe (Figs 6.8 and 6.11). This explains why the values of C_0 and C_1 for the 50 mm pipe lie between the values for upflow and those for

the 105 mm pipe in which the slugs seem able to get somewhat closer to the wall. The closer the slug can get to the wall the slower the liquid ahead of it and therefore the faster it can rise relative to the wall of the pipe.

6.4 SUMMARY[6.5]

The characteristics of gas slugs in co-current and downward flow, only briefly reported in the literature, have been investigated more extensively and more precisely than before for four different test liquids and two different pipe diameters. For very low downward liquid velocities the slugs rose near to the pipe centre (central slugs) and so their drift velocity was close to that predicted by the Nicklin et al. (1962) equation (Eq. 1). On the other hand, at higher downward liquid velocities the slugs did not propagate along the axis of the pipe but instead ascended or descended close to the pipe wall (wall slugs). The velocity of these slugs was dependent on the pipe diameter and surface tension; a reduction of the surface tension or an increase in the pipe diameter increased their speed.

A transition region with respect to the slug velocity from central to wall slug behaviour is for the first time reported. This transitional behaviour is because the stabilising effects of surface tension on the shape of the slugs were overcome, which caused the slugs to migrate towards the pipe wall. A constant Weber number accurately describes the onset of the wall slugs for each pipe diameter.

The distribution parameter for the wall slugs C_0 is confirmed to much less than the value of 1.2, found by Nicklin et al. for co-current upflow, and the coefficient C_1 is greater than the value of 0.35 found in upflow (Taylor bubble theory), in both diameter pipes. The reason for this is that the slug bubble rose near to the pipe wall.

[6.5] A semi-empirical model is presented in Appendix F that predicts the slug bubble velocity in downwards flow. The model is not included in this Chapter because its predictions are dependent on pipe size.

CHAPTER 7

CONCLUSIONS & RECOMMENDATIONS

This final chapter of this thesis presents the main contributions of the present work and provides some suggestions for further research. The main contributions on the various subjects covered are outlined in the first part, followed by some few suggestions on future work on both theoretical and experimental extensions of the current work.

7.1 CONCLUSIONS

The novelty of the present work can be summarised in the following paragraphs. The main conclusions drawn are briefly mentioned and discussed.

7.1.1 Wake velocity field

The velocity characteristics of the turbulent flow field in the wake of a cylindrical bluff body (blockage ratio 82%) and beneath two ventilated cavities attached to a central sparger (blockage ratios of 80% and 82% respectively) in turbulent flow were measured using LDV. This velocity flow field has never been measured for turbulent conditions, i.e. the conditions that exist in most practical situations. The results confirmed the existence of a toroidal vortex with very similar characteristics below both the bluff body and the ventilated cavities. The bluff body has proved to be a convenient experimental substitute for the study of the flow pattern beneath the ventilated cavity.

The axial boundary of the vortex was defined to be the position of the stagnation point on the centreline, which was found at around $z \simeq 1.32D$ for all cases. The results revealed a re-circulation region of intense turbulence followed by dissipation further downstream. A detailed presentation of all the measured velocity profiles beneath the bluff body and the ventilated cavities can be found in Chapter 4. These results would provide valuable assistance in any future attempts to model the entrainment rate at the base of a ventilated cavity or a slug bubble.

It was confirmed by the LDV experiments that the geometry (i.e. size) of the toroidal vortex formed below a cavity did not depend on the liquid volumetric flow rate or the speed of the vortex. On the other hand, the speed of the vortex was directly proportional to the film velocity. The film velocity at the base of a ventilated cavity was the parameter that determined the velocity field in the near wake and the driving force of the vortex. The speed of rotation was approximately 40% of that in the film at the base of the cavity. Away from the boundaries of the vortex the presence of the entrained bubbles started to influence the flow pattern by flattening the flow velocity profile.

The LDV results were used to assess the model of Thorpe et al. (2001). The model accurately described the velocity flow field in the wake of a ventilated cavity, but only towards the centre of the vortex. It seems that the flow in the wake of a ventilated cavity evolves into a spherical vortex ring where the velocity distribution is close to the theoretical solution of the Hill-type vortex. The Hill-type vortex is a potential vortex (inviscid vortex). That means that the vortex in the wake of a cavity does not need a lot of energy to drive and thus little or no energy is dissipated inside it. Therefore most of the entrained bubble breakup processes that determine the resulting bubble size and void fraction further downstream, takes place at the outer boundaries of the vortex, in the channel defined by the high downward axial liquid velocities.

The accurate measurements of the velocity flow field can lead to some conclusions in the subject of the slug (Taylor) bubble coalescence in undeveloped two phase slug flow. The work by Hasanein et al. (1996) indicated that the deformation of the trailing slug nose and the bubble acceleration started at about 6 D below the tail of the leading bubble, which is far below the wake length as measured in the presented work (of $1.32D$). Therefore the short liquid film penetration depth and the rapid decay of the turbulent eddies with axial distance in the wake of a ventilated cavity suggest that the acceleration of the trailing bubble is not directly related to the effect of film penetration and large scale eddies in the wake of the leading bubble. Another mechanism must be responsible for the coalescence of two gas slugs.

7.1.2. Bubble size & Mass transfer

The local average bubble size in the bulk two-phase flow region below the ventilated cavity was determined using photography for three combinations of liquid and gas volumetric flow rates for the HS, CS, PS and PJS. The results showed that the bubble size produced depended on the gas and liquid volumetric flow rates and the sparger design. The average bubble size was

essentially the same (differences within 10%) for the PS, CS and HS. The PS created the largest bubble in all cases examined. The PJS was shown to be the most effective way of distributing gas in the downcomer pipe since it created smaller bubbles than all the other spargers and did not allow the formation of cavities. The estimated increase in $k_L a$ due to the smaller bubble size for the PJS was by a factor of 1.35.

In order to check this result, the effects of sparger type on the volumetric mass transfer coefficient $k_L a$ were also measured. The results confirmed the apparent superiority of PJS over the other spargers. An average increase of 19% in the $k_L a$ was observed when the PJS was used instead of the industrial design (HS). The CS and PS showed similar $k_L a$ values again within 10% of the HS.

However the power consumption is larger when the PJS is used instead of the industrial design HS. Hence the measured bubble sizes and mass transfer coefficients of the PJS were corrected to account for the differences in energy consumption. When this is done the PJS and HS produce roughly the same bubble size and have the same mass transfer performance. Still the PJS had the important operational advantages of producing shorter cavities and having the greater resistance to stall at high gas flow rates.

7.1.3 Slugs in downwards flow

The characteristics of gas slugs in co-current and downward flow, only briefly reported in the literature, have been investigated more extensively and more precisely than before for four different test liquids and two different pipe diameters. For very low downward liquid velocities the slugs rose near to the pipe centre (central slugs) and so their drift velocity was close to that predicted by the Nicklin et al. (1962) equation. On the other hand, at higher downward liquid velocities the slugs did not propagate along the axis of the pipe but instead ascended or descended close to the pipe wall (wall slugs). The velocity of these slugs was dependent on the pipe diameter and surface tension; a reduction of the surface tension or an increase in the pipe diameter increased their speed.

A transition region with respect to the slug velocity from central to wall slug behaviour is for the first time reported. This transitional behaviour is because the stabilising effects of surface tension on the shape of the slugs were overcome, which caused the slugs to migrate towards the

pipe wall. A constant Weber number accurately describes the onset of the wall slugs for each pipe diameter.

The distribution parameter for the wall slugs C_0 is confirmed to much less than the value of 1.2, found by Nicklin et al. for co-current upflow, and the coefficient C_1 is greater than the value of 0.35 found in upflow (Taylor bubble theory), in both diameter pipes. The reason for this is that the slug bubble rose near to the pipe wall.

7.2 RECOMMENDATIONS FOR FUTURE WORK

Thus far the main contributions of the present work have been presented. The next paragraphs give a few suggestions for further research on both theoretical and experimental extensions of this work. Based on the current work the following areas of research are identified:

i.) In this work information has been presented on the vortex flow associated with the entrainment rate at the base of ventilated cavities and slug bubbles. It was discussed in section 2.4.5 that a model that will predict this entrainment rate (or a model that will predict the ventilated cavity or slug length) should take account of the rotation of this vortex. It is thus proposed that such a model become the main aim of future studies. This model should also account for the re-coalescence flux of the gas. The author believes that now there is enough information to initiate some feasible attempts of modelling this phenomenon.

ii.) There is not doubt that downward slug flow is an important issue that raises several questions that are mainly linked to flow instability and to the balance between surface tension and inertia. It is proposed that numerical simulation techniques be used in order to understand this very complex problem. All the published numerical methods to model slug flow in vertical tubes assumed either the shape of the bubble or a functional form of the shape (for instance in Dimitrescu). These solutions constrain the nature of the solution while the approach adopted based on a Volume of fluid method (VOF) lays no such a priori foundations. Advances in Computational Fluid Dynamics (CFD) in recent years have provided the basis for further insight into the dynamics of multiphase flows. The objective of the proposed CFD model would be to calculate the shape and velocity of slugs in downward two phase slug flow.

Application of the VOF technique to track the gas liquid interface requires only a single set of equations common to both phases to be solved (rather than solving separate conservation equations for each phase as in the conventional approaches in the literature). The CFD results can then be compared with the results presented in Chapter 6.

iii.)An important factor governing the entrainment rate beneath the ventilated cavity is believed to be the falling liquid film. It is proposed that both PIV/LIF and high-speed video camera be applied to the falling liquid film to provide information about the nature of the film. The main interest would be on the turbulence intensity and the amplitude of waves of the falling liquid film that are believed to affect the entrainment rate. In a recent paper by Kockx et al. (2005) some initial results on this subject have been presented. Clearly more information in needed to reach some solid conclusions. Also in the literature of the plunging liquid jets many researchers have shown that the rate of gas entrainment is also a function of the magnitude of disturbances on the surface of the jet. (McKeogh and Ervine (1981), amongst others). In an analogy in vertical slug flow, the falling liquid film's surface roughness grows as it recedes from the nose of the Taylor bubble (Mao and Dukler (1991) and then it plunges at its base as a circular wall jet. The results would then be related to the measured velocity profile below the ventilated cavity presented in this work.

iv.)To measure the volumetric mass transfer coefficient for the PJS and the HS for void fractions in excess of 10% in water. The results of Chapter 5 showed that when the energy losses between the two spargers were the same, then they exhibited same mass transfer performance. However for higher void fractions and hence longer cavity lengths the energy losses associated with the HS would be larger than the PJS (see the Equations that predict the losses in Chapter 5). It would be interesting to see then if the trends that are presented in Chapter 5 persist.

v.) To measure the volumetric mass transfer coefficient and the resulting bubble size for all four spargers (HS, CS, PS and PJS) in different liquids (e.g. surfactants, viscous liquids etc.). This would provide a better assessment of the effects of liquid physical properties on the system's mass transfer performance and direct comparisons can be made with the results presented in Chapter 5.

vi.)To measure the resulting bubble size in different liquids (e.g. surfactants, viscous liquids etc.) for all four spargers at different axial positions below the base of the ventilated cavity. This measured then bubble size gradient would allow:

- The determination of the breakage and coalescence phenomena that are taking place in the downcomer.
- Direct comparisons of the results between different liquids (for instance the presence of a surfactant would suppress coalescence).
- The definition of the various hydrodynamic zones (vortex, shedding, bubbly flow) in terms of the measured bubble size e.g. divided into different bubble classes.
- The influence of the liquid physical properties on bubble size. The latter can be related to the mass transfer measurements.
- The measurements can be used to assess if standard bubble population models are applicable in a geometry where a ventilated cavity is attached to a sparger.

REFERENCES

American Institute of Aeronautics and Astronautics Standard (AIAA), (1995), *Assessment of wind tunnel data uncertainty*, AIAA S071-1995.

Alfredsson, P. H. and Johansson, A. V., (1983), Effects of imperfect spatial resolution on measurements of wall-bounded turbulent shear flows, *Journal of Fluid Mechanics*, **137**, 409-421.

Alves, S., S., Maia, C., I., Vasconelos, J., M., T. & Serralheiro, A., J., (2002), Bubble size in aerated stirred tanks, *Chemical Engineering Journal*, **89**, 109-117.

Asalor, T. D. and Whitelaw, J. H., (1976), The influence of combustion-induced particle concentration variations on laser Doppler anemometry, *In Proceedings LDA Symposium Copenhagen 1975*, Copenhagen, Skovlunde, Denmark, 151-137.

Batchelor, G. K., (1967), *An introduction to fluid dynamics*, (1st Edition), Cambridge University Press, Section 6.11.

Bacon, R., (1995a), *Large bubbles in downwards two phase flow*, PhD Thesis, Department of Chemical Engineering, University of Cambridge, UK.

Bacon, R. P., Scott, D. M. and Thorpe, R. B., (1995b), Large bubbles attached to spargers in downward two-phase flow, *International Journal of Multiphase Flow,* **21**, 949-959.

Bacon, R. P., Scott, D. M. and Thorpe, R. B., (1995c), Large bubbles in downwards two-phase flow, *Chemical Engineering Research and Design,* **73**(A), 228-233.

Bando, Y., Nishimura, M., Ichikawa, C., Takeshita, I. and Kuraishi, M., (1989), Gas-liquid contactor using gas entrainment by liquid flowing downward into downcomer, *Journal of Chemical Engineering of Japan*, **22**, 660-664.

Bando, Y., Kuraishi, M., Nishimura, M., Hattori, M. and Asada, T., (1988), Cocurrent downflow bubble column with simultaneous gas-liquid injection nozzle, *Journal of Chemical Engineering of Japan*, **21**, 607-612.

Barr, G., (1926), *Phil. Mag.*, **1**, 395.

Bauer, T, Roy, S., Lange, L. and Al-Dahhan, M., (2005), Liquid saturation and gas-liquid distribution in multiphase monolithic reactors, *Chemical Engineering Science*, **60**, 3101-3106.

Becker, S., De Bie, H. and Sweeney, J., (1999), Dynamic flow behaviour in bubble columns, *Chemical Engineering Science*, **54**, 4929-4935.

Bendiksen, K H., (1985), On the motion of long bubbles in a vertical tube, *International Journal of Multiphase Flow,* **11**, 797-812.

Bendiksen, K H., (1984), An experimental investigation of the motion of long bubbles in inclined tubes, *International Journal of Multiphase Flow,* **10**, 467-483.

Bertic, G. and Pintar, A., (1997), The role of gas bubbles and liquid slug lengths on mass transport in the Taylor flow through capillaries, *Chemical Engineering Science*, **52**, 3709-3719.

Bin, A. K., (1993), Gas entrainment by plunging liquid jets: A review, *Chemical Engineering Science*, **48**, 3585-3630.

Bin, A. K., (1988), Minimum air entrainment velocity of vertical plunging liquid jets, *Chemical Engineering Science*, **43**, 379-389.

Bin, A. K. and Smith J. M., (1982), Mass transfer in a plunging liquid jet absorber, *Chemical Engineering Communications,* **15**, 367-383.

Boneto, F. and Lahey, R. T., (1993), An experimental study on air carryunder due to a plunging liquid jet, *International Journal of Multiphase Flow,* **19**, 281-294.

Bouaifi, M., Herbrard, G., Bastoul, D. & Roustan, M., (2001), A comparative study of gas hold up, bubble size, interfacial area and mass transfer coefficients in stirred gas-liquid reactors and bubble columns, *Chemical Engineering and Processing*, **40**, 97-111.

Brattberg, T. & Chanson, H., (1998a), Air entrapment and air bubble dispersion at two-dimensional plunging water jets, *Chemical Engineering Science*, **53**, 4113-4127.

Brattberg, T. & Chanson, H., (1998b), Entrainment, Dispersion and diffusion of air bubbles by plunging water jet, *Third International Conference on Multiphase Flow 98*, Lyon, France, June 8-12.

Bugg, J. D. & Saad G. A., (2001), The velocity field around a Taylor bubble rising in stagnant viscous liquid, numerical and experimental results, *International Journal of Multiphase Flow*, **28**, 791-803.

Burgess J. M., Molloy, N. A. & McCarthy, M. J. (1972), A note on the plunging jet reactor, *Chemical Engineering Science*, **27**, 442-445.

Calabrese, R. V., Chang, T. P. K. and Dang, P. T., (1986), Droplet breakup in turbulent stirred tank contactors. Part I: Effect of dispersed phase viscosity, *A. I. Ch. E. Journal,* **32**, 657-666.

Calderbank, P. H. and Moo-Young, M., (1961), The continuous phase heat and mass transfer properties of dispersions, *Chemical Engineering Science*, **16**, 39-54.

Calderbank, P. H., (1958), The interfacial area in gas liquid contacting with mechanical agitation, *Transactions Institution of Chemical Engineers*, **36**, 443-448.

Camarasa, E., Vial, C., Poncin, S., Wild, G., Midoux, N and Bouillard, J, (1999), Influence of coalescence behaviour of the liquid and of the gas sparging on hydrodynamics and bubble characteristics in a bubble column, *Chemical Engineering and Processing*, **38**, 329-344.

Campos, J. B. L. M. and. Guedes de Carvalho, J. R .F., (1988a), An experimental study of the wake of gas slugs rising in liquids, *Journal of Fluids Mechanics*, **196**, 27-37.

Campos, J. B. L. M. and. Guedes de Carvalho, J. R .F., (1988b), Mixing induced by air slugs rising in narrow columns of water, *Chemical Engineering Science*, **43**, 1569-1582

Chisti, Y., (1989), *Airlift Bioreactors*. Elsevier, London.

Ciroboski, J. and Bin, A., (1972), Minimum entrainment velocity for free liquid jets, *Inzyniera Chem.*, **2**, 453-469, (in Polish).

Couvert, A., Roustan, M. and Chatellier, P., (1999)., Two-phase hydrodynamic study of a rectangular airlift loop reactor with an internal baffle, *Chemical Engineering Science*, **54**, 5245-5252.

Cramers, P. H. M. R., Beenackers, A. A. C. M. and van Dierendonck, L. L., (1992), Hydrodynamics and mass transfer characteristics of a loop venture reactor with a downflow liquid jet ejector, *Chemical Engineering Science*, **47**, 3557-3564.

Cummings, P. D. and Chanson, H., (1999), An experimental study of individual air bubble entainment at a planar plunging jet, *Transactions Institution of Chemical Engineers,* **77**, 159-164.

Cummings, P., D. and Chanson, H., (1997), Air entrainment in the developing flow region of plunging jets –Part 1: Theoretical Development, *Journal of Fluids Engineering,* **119**, 597-602.

Cummings, P. D. and Chanson, H., (1994), Experimental study on air carryunder due to a plunging liquid jet, *International Journal of Multiphase Flow,* **20**, 667-670.

Cumming, I., W., (1975), *The impact of falling liquids with liquid surfaces*, Ph.D Thesis, Department of Chemical Engineering, Loughborough University of Technology, UK.

Davidson, J. F. and Harisson, (1963), *Fluidisation*, Academic Group Publishing Corporation, London, UK.

Davies, R. M. and Taylor, G., (1950), The mechanics of large bubbles rising through extended liquids and through liquids in tubes, *Proceedings Royal Society A*, **200**, 375.

Davoust, L., Achard, J., L. and El Hammoumi, M., (2002), Air entrainment by a plunging jet:the dynamical roughness concept and its estimation by a light absorption technique, *International Journal of Multiphase Flow,* **28**, 1541-4564.

De Frate, L. A. and Rush, F. E., (1969), Preprint 39D, *Symposium on selected papers, Part II, 64th National Meeting of AICHE*, New Orleans, Louisiana, March 16-20.

Degraaf, B. D., (1999), *Reynolds number scaling of the turbulent boundary layer on a flat plate and on swept and unswept bumps*, PhD Thesis, Department of Mechanical Engineering, Stanford University, USA.

Delfos, R., Wisse, C. J. and Oliemans, R. V. A., (2001a), Measurement of air-entrainment from a stationary Taylor bubble in a vertical tube, *International Journal of Multiphase Flow,* **27**, 1769-1787.

Delfos, R., Rops, C. M., Kockx, J. P. and Nieuwstadt, F. T. M., (2001b), Measurement of the recoalescence flux into the rear of a Taylor bubble, *Physics of Fluids*, **13**, 1141-1150.

Dimitrescu, D. T., (1943), Stromung an einer Luftblase in senkrechten Rohr., *Z.Angew. Math. Mech.,* **23**, 139-149, (In German).

Durst, F., Fischer, M., Jovanovic, J. and Kikura, H., (1998), Methods to set up and investigate low Reynolds number, fully developed turbulent plane channel flows. *Journal of Fluids Engineering*, **120**, 496–503.

Durst, F., Jovanovic, J. and Sender, J., (1995), LDA measurements in the near-wall region of a turbulent pipe flow, *Journal Fluid Mechanics,* **295**, 305–335.

Durst, F., Melling A., & Whitelaw, J. H., (1981), *Principles and Practice of Laser Doppler Anemometry* (2nd ed.), London: Academic Press Inc., UK.

Edwards, R. V., (1987), Report of the special panel on statistical particle bias problems in laser anemometry, *Journal of Fluids Engineering*, **109**, 89-93.

Elmore, P. A., Chahine, G. L. and Oguz, H. N., (2001), Cavity and flow measurements of reproducible bubble entrainment following drop impacts, *Experiments in Fluids,* **31**, 664-673.

Ervine, D. A., McKeogh, E. J. and Elsawy, E. M., (1980), Effect of turbulence intensity on the rate of air entrainment by plunging water jets, *Proceedings of the Institution of Civil Engineers,* Part 2, June, 425-445.

Evans, G. M., Machniewski, P. M. & Bin, A. K., (2004), Bubble size distribution and void fraction in the wake region below a ventilated gas cavity in downward pipe flow, *Chemical Engineering Research and Design*, **82,** 1095-1104.

Evans, G. M. and Machniewski, P. M., (1999), Mass transfer in a confined plunging liquid jet bubble column, *Chemical Engineering Science*, **54**, 4981-4990.

Evans, G. M., Jameson., G. J. and Rielly, D. C., (1996), Free jet expansion and gas entrainment characteristics of a plunging liquid jet, *Experimental Thermal and Fluid Science,* **12**, 142-149.

Evans, G. M., Jameson, G. J. and Atkinson, B. W., (1992), Prediction of the bubble size generated by a plunging liquid jet bubble column, *Chemical Engineering Science*, **47**, 3265-3272.

Evans, G. M., (1990), *Hydrodynamics of a plunging liquid jet column*, Ph. D. Thesis, Department of Chemical Engineering, University of Newcastle, Australia.

Fabre, L. and Line, A., (1992), Modelling of two phase slug flow, *Annual Review of Fluid Mechanics,* **24**, 21-46.

Fernades, R. C., Semiat, R. and Duckler, A. E., (1983), Hydrodynamic model for gas-liquid slug flow in vertical pipes, *A. I. Ch. E. Journal*, **29**, 981-989.

Golan, L. P. and Stenning, A. H., (1970), Two phase vertical flow maps, *Proceedings of the Institution of the Mechanical Engineers*, **184**, 108.

Gould, R. D. and Loseke, K. W., (1993), A comparison of four velocity biased techniques for laser Doppler velocimetry, *Trans. ASME*, **115,** 508-514

Griffith, P. and Wallis, G. B., (1961), Two phase slug flow, *Journal of Heat Transfer,* **83**, 307-320.

Guet, S., Oooms, G., Oliemans, R. V. A. and Mudde, R. F., (2004), Bubble size effect on low liquid input drift-flux parameters, *Chemical Engineering Science*, 59, 3315-3329.

Hamarthy, T. Z., (1960), Velocity of large drops and bubbles in media of infinite or restricted extent, *A. I. Ch. E. Journal*, **6**, 281.

Hasasein, H. A., Tudose, G. T., Wong, S., Malik, M. and Kawaji, M., (1996), Slug flow experiments and computer simulation of slug length distribution in vertical pipes, *31st National Heat Transfer Conference*, Houston, August, 211-219.

Havelka, P., Linek, V., Sinkule, J., Zahradnik, M. and Fialova, M., (2000), Hydrodynamics and mass transfer characteristics of ejector loop reactors, *Chemical Engineering Science*, **55**, 535-549.

Hepworth, N., J., Hammond, J., R., M. & Varley, L., (2004), Novel application of computer vision to determine bubble size distributions in beer, *Journal of Food Engineering*, 61, 119-124.

Hesketh, R. P., Russell, T. W. F. and Etchells, A. W., (1987), Bubble size in horizontal pipelines, *A. I. Ch. E. Journal*, **33**, 663-667.

Hill, T. J. and Wood, D. G., (1994), Slug flow: Occurrence, consequences and prediction, *Contonial Petroleum Engineering Symposium,* Tulsa, OK, USA, August.

Hill, M. J. M., (1894), On a spherical vortex, *Philosophical Transactions of the Royal Society*, **185**, 213-222.

Hinze, J. O., (1955), Fundamentals of the hydrodynamic mechanisms of splitting dispersion processes, *A. I. Ch. E. Journal,* **1**, 289.

Hyde, M., (2003), *Private communication*, TSI Inc., Guildford, Surrey, UK.

Joshi, J. B., Ranade, V. V., Gharat, S. D. and Lele, S. S., (1990) Sparged loop reactors: A Review, *The Canadian Journal of Chemical Engineering*, **68**, 705-741.

Joshi, J B. and Sharma, M., M., (1979), A circulation model for bubble columns, *Trans. Inst. Chem. Engrs*, **57**, 244-251.

Irwin A. R., Brignal, W. J. and Biss, M. A., (1989), Experiences with Deep Shaft Process at Tilbury, *Journal of Industrial Waste Experience Management*, **3**, 280-287.

Kapteijn, F., Nijhuis, T. A., Heiszwolf, J. J. and Moulijn, J., (2005), New non-traditional multiphase catalytic reactors based on monolithic structures, *Catalysis Today*, **66,** 133-144.

Kashinsky, O. N. & Randin, V. V., (1999), Downward bubbly gas-liquid flow in a vertical pipe, *International Journal of Multiphase Flow*, **25**, 109-138.

Kay, J., M. & Nedderman, R., M., (1985), *Fluid mechanics and transfer processes* (1st Edition), Cambridge: Cambridge University Press.

Kockx, J. P., Nieuwstadt, F. M. T., Oliemans, R. V. A. and Delfos, R., (2005), Gas entrainment by a liquid film falling around a stationary Taylor bubble in a vertical tube, *International Journal of Multiphase Flow*, **31**, 1-24.

Kumagai, M. and Endoh, K., (1982), Effects of kinematic viscosity and surface tension on gas entrainment rate of an impinging liquid jet, *Journal of Chemical Engineering of Japan*, **15**, 427-433.

Kundu, G., Mukherjee, D. and Mitra, A., (1994), Gas entrainment and depth of penetration in a co-current gas-liquid downflow bubble column, *Journal of Chemical Engineering of Japan*, **27**(5), 621-656.

Kusabiraki, D., Niki, H., Yamagiwa, K. and Ohkawa, A., (1990a), Gas entrainment rate and flow pattern of vertical plunging liquid jets, *The Canadian Journal of Chemical Engineering,* **68**, 893-903.

Kusabiraki, D., Murota, M., Ohno, S., Yamagiwa, K., Yasuda, M. and Ohkawa, A., (1990b), Gas entrainment rate and flow pattern in a plunging liquid jet aeration system using inclined nozzles, *Journal of Chemical Engineering of Japan,* **23**, 704-710.

Lara, P., (1979), Onset of air entrainment for a water jet impinging vertically on a water surface, *Chemical Engineering Science,* **34**, 1164-1165.

Lee, S. L. and Durst, F., (1982), On the motion of particles in turbulent duct flows, *International Journal of Multiphase Flow*, **8**, 125-146.

Lee, Y. H., Scott, D. M. and Thorpe, R., B., (2000), Energy losses due to large bubbles beneath spargers in circulating bubble columns, *Chemical Engineering Science,* **55**, 97-112.

Lee, Y. H., Scott, D. M. and Thorpe, R., B., (1999), The scale up of large bubbles attached to spargers in downward two-phase flow, *Chemical Engineering Science,* **54**, 3893-389.

Lee, Y. H., (1998), *Large bubbles beneath spargers in gas-liquid downflow*, PhD Thesis, Department of Chemical Engineering, University of Cambridge, UK.

Lee, Y. H., Scott, D. M. and Thorpe, R. B., (1997a), The scale up of large bubbles attached to spargers in downward two-phase flow, *Chemical Engineering Science,* **52**, 3797-3809.

Lee, Y. H., Scott, D. M. and Thorpe, R. B., (1997b), Large bubbles in downwards two-phase flow, *Proceedings of the 1997 of the Institution of the Chemical Engineers Jubilee Research Event,* Nottingham, UK, 221-224.

Lewis, D. A., and Davidson, J. F., (1982), Bubble splitting in shear flow, *Transactions of Institution of Chemical Engineers*, **60**, 283-291.

Lin, T. J. and Donelly, H. G., (1966), Gas bubble entrainment by plunging laminar jets, *A. I. Ch. E. Journal*, **12**, 563-571.

Mao, Z. and Dukler, A. E., (1991), The motion of Taylor bubbles in vertical tubes –II. Experimental data and simulation for laminar and turbulent flow, *Chemical Engineering Science*, **46**, 2055-2064.

Marie, J. L., (1983), Investigation of two-phase bubbly flows using laser Doppler anemometry, *Physico Chemical Hydrodynamics*, **4**, 103-118.

Martin, P. M., Pugliese, G. J. and Leisman, G. J., (2000), Laser Doppler velocimetry uncertainty analysis for rotor blade tip vortex measurements, *Meeting of the American Institute of Aeronautics and Astronautics*, AIAA 2000-0263, 1-15.

Martin, S., (1976), Vertically downward two phase slug flow, *Journal of Fluids Engineering,* **98**, 715-722.

McCarthy, M., J., (1972), *Entrainment by Plunging Liquid Jets*, Ph.D Thesis, Department of Chemical Engineering, University of Newcastle, Australia.

McKeogh, E. J. and Ervine, D. A., (1981), Air entrainment rate and diffusion pattern of plunging liquid jets, *Chemical Engineering Science*, **36**, 1161-1981.

McLaughlin, D. K. and Tiederman, W. G., (1973), Biasing correction for individual realisation laser anemometer measurements in turbulent flows, *Physics of Fluids*, **16**, 2083-2088.

Mendelson, H. D., (1967), The prediction of bubble terminal velocities from wave theory, *A. I. Ch. E. Journal,* **13**, 250.

Mertes, A. T., (1938), U.S. Patent 2 128 311.

Moon, R. K, Moore, R. M., Thorpe, R. B. and Verghese, T. M., (1987), Two Phase Downflow, 3th *International Conference on Multiphase Flow*, The Hague, Netherlands, 18-20 May 1987.

Moppett, G. D., Rielly, C. D. and Davidson, J. F., 1997, Waste-water treatment using a plunging jet oxygenator issuing into a downflowing liquid, *Proceedings of the 4th International Conference on Bioreactor and Bioprocess Fluid Dynamics (Edinburgh)*, 1-3 July, 151-161.

Moppett, G. D., Rielly, C. D. and Davidson, J. F., (1995), An oxygenator for waste water treatment using a stationary bubble cloud in a downflowing liquid, *Trans. I. Chem. E*, **73(A)**, 685-689.

Mudde, R. F., Groen, J. S. and Van Den Akker, H E. A., (1998), Application of LDA to bubbly flows, *Nuclear Engineering and Design*, **184**, 329-338.

Muller, F. L. and Davidson, J. F., (1992), On the contribution of small bubbles to mass transfer in bubble columns containing highly viscous liquids, *Chemical Engineering Science*, **47**, 3525-3532.

Nakoryakov, V. E., Kashinski, O. N., Petukhov A. V. and Gorelik, R. S. (1989), Study of local hydrodynamics characteristics of upward slug flow, *Experiments in Fluids*, **7**, 560-566.

Nicklin, D. J., Wilkes, J. O. and Davidson, J. F., (1962), Two phase flow in vertical tubes. *Transactions of the Institution of Chemical Engineers,* **40**, 61-68.

Nicol, R. S. and Davidson, J. F., (1988), Effect of surfactants on the gas hold-up in circulating bubble columns, *Chemical Engineering Research and Design,* **66**, 159-164.

Nogueira, S, Riethmuller, M. L., Campos, J. B. L. M. and Pinto, A. M. F. R., (2004), Flow in the annular film around a Taylor bubble rising through vertical column of liquids, *3rd International Symposium on Two-Phase Modelling and Experimentation*, Pisa, Italy, September, ISBN 88-467-1075-4.

Nogueira, S., Sousa, R. G., Pinto, A. M. F. R., Riethmuller, M. L. & Campos, J. B. L. M., (2003), Simultaneous PIV and pulsed shadow technique in slug flow: a solution for optical problems, *Experiments in Fluids*, **35**, 598-609.

Nogueira, S., Dias, I., Pinto, A. M. F. R. & Riethmuller, M. L., (2000), Liquid PIV measurements around a single gas slug rising through stagnant liquid in vertical pipes, *10th International Symposium of Laser Techniques to Fluid Mechanics*, Lisbon, Portugal, July 10-13.

Oguz, H. and Prosperetti, A., (1994), Mechanics of air entrainment by a falling liquid, *American Society of Mechanical Engineers, Fluids Engineering Division (Publication) FED,* **187**, 13-20.

Ohba, K, Kishimoto, I. and Ogasawara, M., (1976), Simultaneous measurement of local liquid velocity and void fraction in bubbly fraction using a gas laser – part I: principle and measuring procedure, *Technology Rep. Osaka Univ.*, **26**, 547-556.

Ohkawa, A., Kawai, Y., Kusabiraki, D. and Sakai, N., (1987a), Flow characteristics of an air-entrainment type aerator having a long downcomer, *Chemical Engineering Science,* **42**, 2788-2790.

Ohkawa, A., Kawai, Y., Kusabiraki, D., Sakai, N. and Endoh, K., (1986), Some flow characteristics of a vertical liquid jet system having downcomers, *Chemical Engineering Science*, **41**, 2347-2361.

Ohkawa, A., Shiokawa, Y., Nobuyuki, S. and Endoh, K., (1985a), Gas holdup in downflow bubble columns with gas entrainment by a liquid jet, *Journal of Chemical Engineering of Japan*, **18**(2), 172-174.

Ohkawa, A., Shiokawa, Y., Nobuyuki, S. and Imai, H., (1985b), Flow characteristics of downflow bubble columns with gas entrainment by a liquid jet, *Journal of Chemical Engineering of Japan*, **18**(5), 466-469.

Oshinowo, T. and Charles, M. E., (1974), Vertical two-phase flow. I. Flow pattern correlations. *Canadian Journal of Chemical Engineering.*, **49**, 25-35.

Perry, H. R., & Green D. W., (1999), *Perry's Chemical Engineer's Handbook*, 16th Ed., New York: McGraw-Hill.

Perry, R. T., (1967), *Fluid mechanics of entrainment through liquid-liquid and solid-liquid junctures*, PhD Thesis, University of Minnesota, U.S.A.

Pinto, A. M. F. R. and Campos, J. B. L. M., (2004), *Private Communication*, Pisa, Italy, September.

Pinto, A. M. F. R. and Campos, J. B. L. M., (1996), Coalescence of two gas slugs rising in a vertical column of liquid, *Chemical Engineering Science,* **51**, 45-54.

Polonsky, S., Barnea, D. and Shemer, L., (1999a), Averaged and time dependent characteristics of the motion of an elongated bubble in vertical pipe, *International Journal of Multiphase Flow*, **25**, 795-812.

Polonsky, S., Shemer, L. and Barnea, D., (1999b), The relation between the Taylor bubble motion and the velocity field ahead of it, *International Journal of Multiphase Flow*, **25**, 957-975.

Richardson, J. F. and Zaki, W. N., (1954), Sedimentation and fluidisation, *Transactions of the Institute of Chemical Engineers*, **32**, 55.

Riiser, K., Fabre, J. and Suzanne, C., (1992), Gas entrainment at the rear of Taylor-bubble, *29th Meeting of the European Two-Phase Flow Group,* Stockholm, Sweden.

Saffman, (1992), *Vortex dynamics*, (1st Edition), Cambridge University Press, UK.

Schlichting, H., (1979), *Boundary layer-theory*, (7th Edition), McGraw-Hill Series in Mechanical Engineering, USA.

Schugerl, K., (1991), *Bioreactor engineering: characteristics features of bioreactors, Volume 2,* John Wiley & Sons, UK.

Schulze, L. E., (1954), *Hydraulic air compressors*, Information circular 7683, US Department of the Interior, Bureau of Mines.

Sene, K. J., (1988), Air entrainment by plunging liquid jets, *Chemical Engineering Science,* **43**, 2615-2623.

Sevik, M. and Park, H. S., (1973), The splitting of drops and particles by turbulent fluid flow, *Journal of Fluids Engineering Transactions of ASME*, **95**, 53-60.

Sheridan, A. T., (1966), Surface entrainment of air by water jets, *Nature*, **209**, 799-800.

Smith, J. M., (2004), *Private communication*, University of Surrey, Guildford, Surrey, UK.

So, S., Morikita, H., Takagi, S. and Matsumoto, Y., (2002), Laser Doppler velocimetry measurement of turbulent bubbly channel flow, *Experiments in Fluids*, **33**, 135 – 142.

Sodeberg, D. J., (1980), The stability of circulation in bubble columns, *Ph.D. Thesis*, University of Cambridge, UK.

Soler, J. G., Marques, J. J. P. and Caicedo, G. R., (2003), Calibration of the method to measure bubble properties in 2D fluidised beds, *Chemical Engineering Communications*, **190**, 285-298.

*Sotiriadis, A. A., Thorpe, R. B. and Smith J. M., (2005), Bubble size and mass transfer in sparged downwards two-phase flow, *Chemical Engineering Science*, **60**, 5917-5925.

*Sotiriadis, A. A. and Thorpe, R. B., (2005), Liquid re-circulation in turbulent vertical pipe behind a cylindrical bluff body and a ventilated cavity attached to a sparger, *Chemical Engineering Science*, **60**, 981-994.

*Sotiriadis, A. A., Thorpe, R. B., Kirkby, N. F. and Rockliff, N., (2004), Liquid re-circulation beneath a ventilated cavity in a vertical pipe, *3rd International Symposium on Two-Phase Modelling and Experimentation*, Pisa, Italy, September, pp 8.

*Sotiriadis, A. A. and Thorpe, R. B., (2005), Critical Weber numbers for the existence of wall slugs in vertical pipes, *Anglo Japanese Conference on Two Phase Flow,* Osaka, Japan, September, pp.8.

*Sotiriadis, A. A., Thorpe, R. B. and Cheung, C., (2003), Slugs in Vertically Downward Two-Phase Flow, *Anglo Japanese Conference on Two Phase Flow,* Guildford, Surrey, UK, April, pp10.

---

* These references are based on the research of this study.

Spedding, P. L. and Nguyen, V. T., (1980), Regime maps for air water two phase flow, *Chemical Engineering Science,* **35**, 779.

Su, C., (1995), *Gas entrainment at the bottom of a Taylor bubble in vertical gas-liquid slug flows*, PhD Thesis, Department of Chemical Engineering, University of Houston, USA.

Sun, X., Paranjape, S., Ishii, M. and Uhle, J., (2004a), LDA measurement in air-water downward flow, *Experimental and Fluid Science*, **28**, 317-328.

Sun, X., Paranjape, S., Kim, S., Ozar, B. and Ishii, M., (2004b), Liquid velocity in upward and downward air water flows, *Annals of Nuclear Energy*, **31**, 357-373.

Sun, X., Paranjape, S., Kim, S., Goda, H., Ishii, M. and Kelly, J. M., (2003), Local liquid velocity in vertical air-water downward flow, *Proceedings of the 8th International Symposium on Gs-Liquid Flows, 4th ASME/JSME Joint Fluids Engineering Division Summer Meeting,* Honolulu, Hawaii, USA, July 6-10, Paper No.: FEDSM2003-45548.

Szekely, J., (1969), *Trans. Met. Soc. A.I.M.E.*, **245**, 341.

Taha, T. and Cui, Z. F., (2002), Hydrodynamics analysis of upward slug flow in tubular membranes, *Desalination*, **145**, 179-182.

Taylor, A. M. K. P. and Whitelaw, J. H., (1984), Velocity characteristics in the turbulent near wakes of confined axisymmetric bluff bodies, *Journal of Fluid Mechanics,* **139**, 391-416.

Thorpe, R. B., Evans, G. M., Zhang, K. and Machniewski, P. M., (2001), Liquid circulation and bubble breakup beneath ventilated gas cavities in downward pipe flow, *Chemical Engineering Science*, **56**, 6399-6409.

Thorpe, R. B., Jemsby, B., Fairhust, R., Lee, Y. H. and Scott, D. M., (1997), A plunging jet sparger for injecting gas into downflowing liquids, *Proceedings of the 4th International Conference on Bioreactor and Bioprocess Fluid Dynamics,* ed. A., W., Nienow, Edinburgh, UK, 163-181.

Thorpe, R. B., Beresford-Peirse, J. D., Giancola, F. L., McVay, J. and Tabberer, R. J., (1989), Two phase Downflow, *4th International conference on multiphase flow*, Nice France, Paper K4.

TSI Inc., (1993), *Instruction Manual: Model 9800 series fiberoptic probes*, TSI Inc., Saint Paul, MN 55164, USA.

Tudose, E. T. and Kawaji, K., (1999), Experimental investigation of Taylor bubble acceleration mechanism in slug flow, *Chemical Engineering Science*, **54**, 5761-5775.

Van de Donk, J. A., C., (1981), *Water aeration with plunging jets*, PhD Thesis, Delft University of Technology, The Netherlands.

Van de Sande, E. and Smith, M. J., (1976), Jet break up and air entrainment by low velocity turbulent water jets, *Chemical Engineering Science*, **31**, 219-224.

Van de Sande, E. and Smith, M., J., (1973), Surface entrainment of air by high velocity water jets, *Chemical Engineering Science,* **28**, 1161-1168.

Van Hout, R., Gulitski, A., Barnea, D. & Shemer, L. (2002), Experimental investigation of the velocity field induced by a Taylor bubble rising in stagnant water, *International Journal of Multiphase Flow*, **28**, 579-596.

Velidandla, V., Putta, S. and Roy, R. P., (1996), Velocity field in isothermal turbulent bubbly gas-liquid flow through a pipe, *Experiments in Fluids*, **21**, 347-356.

Wallis, G. B., (1969). *One dimensional two-phase flow*, McGraw-Hill, New York, USA.

Watrasiewicz, B. M. & Ruud, M. J. (1976), *Laser Doppler Measurements*, (1st Ed.). London: Butterworth & Co Ltd.

Wendt, G., Mickan, B., Kramer, R. and Dopheide, D., (1996), Systematic investigation of pipe flows and installation effects using Laser Doppler Anemometry – Part I. Profile measurements downstream of several pipe configurations and flow conditioners, *Flow Meas. Instr.*, **7**, 141-149.

West, C. J. and Hull, C. (1933), *International critical tables of numerical data*, Physics, Chemistry and Technology, I-V, III, McGraw-Hill Publishing C. Inc.

Wongsuchoto, P., Charinpanitkul, T. and Pavasant, P., (2003), Bubble size distribution and gas-liquid mass transfer in airlift reactors, *Chemical Engineering Journal*, **92**, 81-90.

Yamagiwa, K., Ito, A., Kato, Y., Yoshida, M. and Ohkawa, A., (2001), Effects of liquid property on air entrainment and oxygen transfer rates of a plunging jet reactor, *Journal of Chemical Engineering of Japan*, **34**, 506-512.

Varley, J., (1995), Sub-merged gas-liquid jets, Chemical Engineering Scienc, 50(5), 901-905.

Yamagiwa, K., Mashima, T., Kadota, S. and Ohkawa, A., (1993), Effect of liquid property on gas entrainment behaviour in a plunging liquid jet aeration system using inclined nozzles, *Journal of Chemical Engineering of Japan*, **26**, 333-336.

Yamagiwa, K., Kusabiraki, D. and Ohkawa, A., (1990), Gas holdup and gas entrainment rate in downflow bubble column with gas entrainment by a liquid jet operating at high liquid throughput, *Journal of Chemical Engineering of Japan*, **23**, 343-348.

Yamazaki, Y. and Yamaguchi, K., (1979), Characteristics of cocurrent two-phase downflow in tubes, *Journal of Nuclear Science and Technology*, **16**, 24-255.

Yeh, Y. AND Cummings, H., (1964), Localised fluid flows measurements with a He – Ne laser Spectrometer, *Appl. Phys. Lett.*, **4**, 176-178.

Van Hout, R., Gulitski, A., Barnea, D. & Shemer, L., (2002), Experimental investigation of the velocity field induced by a Taylor bubble rising in stagnant water, *International Journal of Multiphase Flow*, **28**, 579-596.

Van Hout, R., Shemer, L. and Barnea, D., (1992), Spatial distribution of void fraction within a liquid slug and some other related slug parameters, *International Journal of Multiphase Flow*, **18**, 831-845.

Varley, J., (1995), Submerged gas-liquid jets: bubble size prediction, *Chemical Engineering Science*, **50**, 901-905.

Velidandla, V., Putta, S. and Roy, R. P., (1996), Velocity field in isothermal turbulent bubbly gas-liquid flow through a pipe, *Experiments in Fluids*, **21**, 347-356.

Vial, Ch., Poncin, S., Wild, G. and Midoux, N., (2005), Experimental and theoretical analysis of axial dispersion in the liquid phase in external-loop airlift reactors, *Chemical Engineering Science*, (In Press).

Zhang, S. H., Yu, S. C., Zhou, Y. C. and Su, Y. F., (1995), A model for liquid-liquid extraction column performance – the influence of drop size distribution on extraction efficiency, *Canadian Journal of Chemical Engineering*, **63**, 212-226.

Zhu, Y., Oguz, H. and Prosperetti, A., (2000), On the mechanism of air entrainment by liquid jets at a free surface, *Journal of Fluid Mechanics*, **404**, 151-177.

Zuber, N. and Findlay, J. A., (1965), Average volumetric concentration in two-phase flow. *Journal of Heat Transfer, Transactions of ASME Series C,* **83**, 453-468.

Zukoski, E. E., (1966), Influence of viscosity, surface tension and incination angle on motion of long bubbles in closed tubes, *Journal of Fluid Mechanics*, **25**, 821-837.

Zu, B., Zheng, B., Lin. C. X., Pena, O. J. and Ebadian, M. A., (2003), Laser Doppler anemometer of laminar flow in helical pipe, *Experimental Thermal and Fluid Science*, **27**, 855-865.

APPENDIX A

HS & PJS DESIGNS

A.1 INTRODUCTION

The HS design is designed to generate even air-flow through each of the air holes. Therefore a careful choice of the number of air holes, hole diameter and sparger pipe diameter is important (Bacon, 1995). The PJS is designed to create a stable free plunging jet at its exit. The following design criteria and methodology can be found in Bacon (1995) for the HS and in Thorpe et al. (1997) for the PJS, but have been repeated here for completeness.

A.2 HS DESIGN

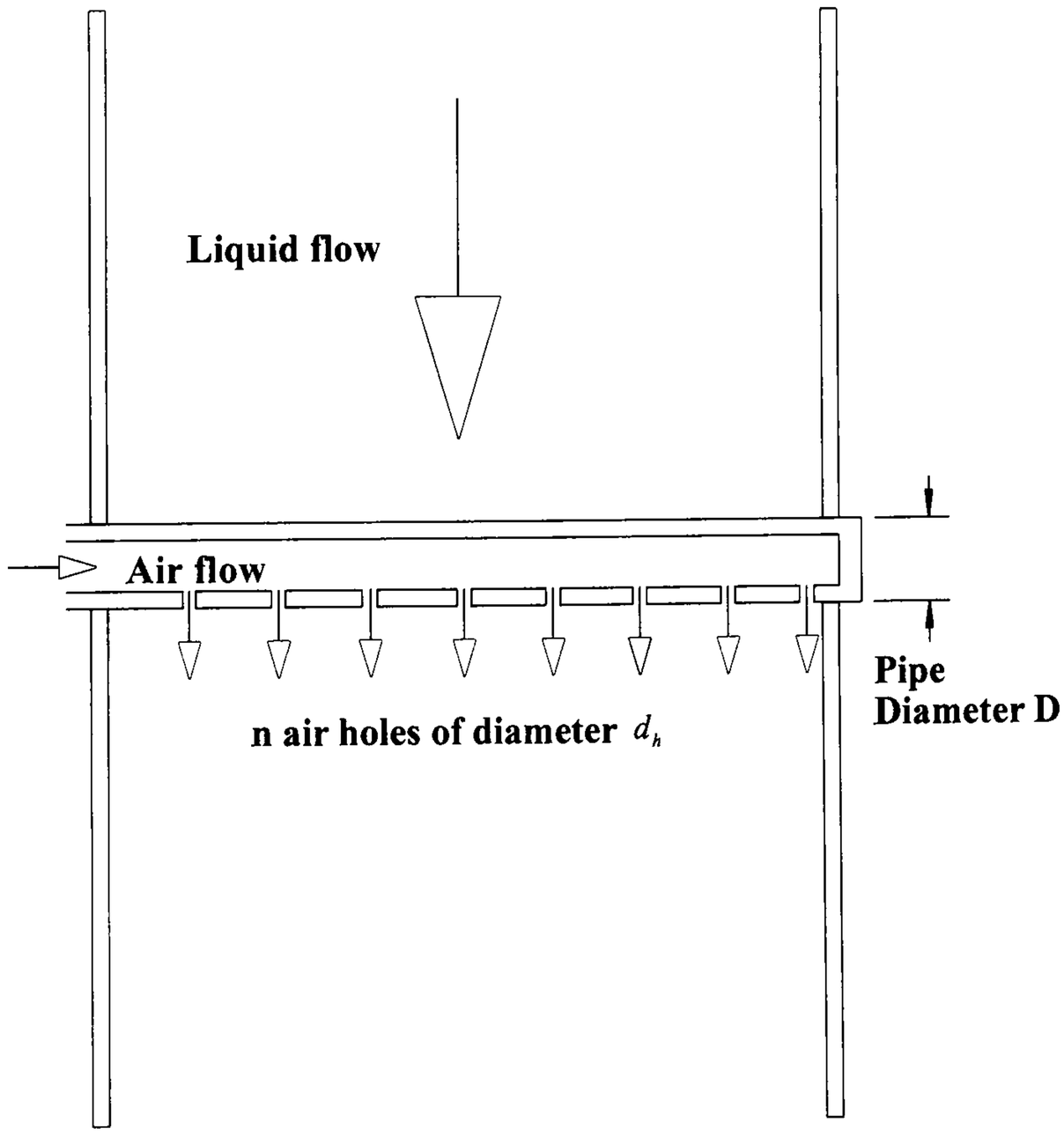

Schematic diagram of the horizontal sparger (HS).

Figure A.1

Figure A.1 represents a horizontal sparger with n air holes of diameter d in a pipe of diameter D. Perry and Green (1999) suggested that for even air distribution across the entire length of the sparger pipe the pressure drop across the holes of the sparger must be significantly greater than the pressure rise along the length of the sparger. They recommended an order of magnitude difference, shown below:

$$\Delta P_{orifice} \geq 10 \Delta P_{sparger} \tag{A.1}$$

where $\Delta P_{orifice}$ is the pressure drop across the holes in the sparger pipe and $\Delta P_{sparger}$ is the pressure rise along the sparger pipe.

A.2.1 Pressure drop across the holes in the sparger pipe, $\Delta P_{orifice}$

The average air velocity in the sparger pipe, $u_{G,HS}$ is:

$$u_{G,HS} = \frac{4Q_G}{\pi D^2} \tag{A.2}$$

where Q_G is the air volumetric flowrate. Similarly the air velocity in the vena contracta of a hole, $v_{G,HS}$ is:

$$v_{G,HS} = \frac{Q_G}{n} \frac{4}{\pi d^2 C_c} \tag{A.3}$$

where C_c is the contraction coefficient due to the flow through the air holes. Assuming that the gas density, ρ_G remains constant, application of Bernoulli yields:

$$\Delta P_{orifice} = \frac{\rho_G \left(v_{G,HS}^2 - u_{G,HS}^2 \right)}{2} \tag{A.4}$$

A.2.2 Pressure rise along the sparger pipe, $\Delta P_{sparger}$

The pressure inside the sparger will increase because the end of the sparger is blocked off. The kinetic energy is converted to pressure energy, shown below:

$$\Delta P_{sparger} = \frac{\rho_G u_{G,HS}^2}{2} \tag{A.5}$$

where ρ_G is the gas density and u is the air velocity in the sparger pipe. Simplification of equation (A.1) by introducing eqs. (A.4) and (A.5) gives:

$$d_h \leq 0.55 \frac{D}{\sqrt{nC_c}} \tag{A.6}$$

Equation (A.6) is used to determine the number and size of holes in the horizontal sparger used.

A.3 PJS DESIGN

A schematic diagram of the PJS is shown in Fig. 3.7. It consists of a carefully tapered section with the inlet having the same diameter as the downcomer and exit in the form of a protruding lip section. The design of the PJS embodies the following features:

1) The lower lip of the sparger is sharp eliminating any random diversions due to the effects of surface tension.
2) The air is introduced through a number of ports and directed onto the outside of the sparger lip. These jets are diverted vertically downwards as well as being spread around the periphery of the liquid jet. Thus the air does not disturb the smoothness of the liquid jet and is incapable of breaking it up.
3) There is a long conical entry and a large rim diameter to minimise energy losses due to turbulence. As shown in Chapter 5 the energy losses associated with the sparger are an important design feature.
4) The angle of the cone is such that at the exit of the sparger, the acceleration of the liquid due to convergence with a flat velocity profile is the gravitational acceleration, g, that is[A.1]:

$$V_r \frac{dV_r}{dr} = -g \tag{A.7}$$

[A.1] This criterion was not satisfied in this work with the particular design of the PJS used.

where V_r is the radial velocity in spherical polar coordinates (r,θ,ϕ). The thinking behind design criterion 4) i.e. matching the acceleration at the lip, is that just below the lip, the liquid jet will be on free fall (Appendix D) and the only natural force which can give rise to an acceleration in a free jet is that due to gravity. The result should be a smooth jet for the liquid from the nozzle resulting in a smooth surface to a stable jet. It is important that the jet is stable because it defeats the object of the PJS for the jet to touch the wall of the downcomer and thus be slowed by friction.

The velocity of the liquid within the sparger can be estimated, in turbulent flow, by assuming that the velocity profile is flat (uniform), i.e. V_r depends only on the radial co-ordinate r. Hence continuity yields:

$$Q_L = 2\pi(1-\cos\theta_w)r^2V_r \tag{A.8}$$

Thus the velocity gradient can be obtained as:

$$\frac{dV_r}{dr} = \frac{-Q_L}{\pi(1-\cos\theta_w)r^3} \tag{A.9}$$

A suitable value of r may be obtained from the geometry of the system because the sparger rim diameter, D_N, is given by the relation to the hald angle of the cone, θ_w:

$$D_N = 2r\tan\theta_w \tag{A.10}$$

The combination of all the above equations gives the angle of the cone in terms of other parameters, which are otherwise determined or chosen:

$$\frac{16Q_L^2\tan^5\theta_w}{\pi^2D_N^5(1-\cos\theta_w)^2} = g \tag{A.11}$$

APPENDIX B

DO PROBES

B.1 DISSOLVED OXYGEN (DO)

Dissolved oxygen (DO) is the term commonly used in liquid analytical work for the measurement of the amount of oxygen dissolved in a unit volume of water. A volume of water in contact with air will absorb air, and hence oxygen, until the pressure the absorbed oxygen exerts at the air-water interface equals the pressure exerted at the same interface by the oxygen in the air. At this point, the water is said to be *saturated with oxygen*. The amount of oxygen actually absorbed is quite small (about five to ten parts of oxygen to one million parts of water). Since the oxygen content is important in many biological and chemical processes, measurements of the amount of oxygen actually dissolved in a water sample is of great importance.

B.2 CLARK POLAROGRAPHIC OXYGEN ELECTRODE

Membrane oxygen electrodes are the most widely used and accepted method for real-time measurements of oxygen in water. These electrodes are known as "Clark type" after their inventor, Dr. Leland Clark and they measure the partial pressure of the oxygen in solution, and not the concentration. The concentration of oxygen in solution (in mg/L) or ppm (parts per million) cannot be easily inferred because dissolved salts will reduce the concentration of oxygen without changing its partial pressure in the solution. The Clark probe can measure directly at the source without having to take a sample and risking that the sample will either absorb or lose oxygen from the atmosphere. Since the oxygen electrode measurement does not depend on any change in colour, this measurement is free of any interference from other colour bearing components in the water or from any effect of turbidity. Furthermore, the electrode method does not involve any introduction of reagents, which are dependent on operator error and reagent aging.

B.3 PRINCIPLES OF ELECTRODE OPERATION

The oxygen electrode used in this work is shown in Fig. B.1. It is a commercial oxygen electrode manufactured by the Data Harvest Group Ltd (Model 3131). The oxygen electrode was based on a simple electrochemical reaction that occurred in water when oxygen was present. The anode and cathode were immersed in electrolyte[B.1] and separated from the sample by a semi-permeable membrane. The job of the membrane was to prevent most components present in water except for oxygen from entering the electrode interior. The membrane was what gave the electrode great selectivity for oxygen with hardly any interferences. The anode was made out of silver and the cathode of gold. When oxygen passed through the membrane, the cathode was depolarized and electrons were consumed. The anode was necessary to complete the electrical circuit so that electrons were available at the cathode to reduce the oxygen. The cathode electrochemically reduced the oxygen to hydroxyl ions in the reaction:

$$O_2 + 2H_2O + 4e^- \rightarrow 4OH^- \qquad \text{(B.1)}$$

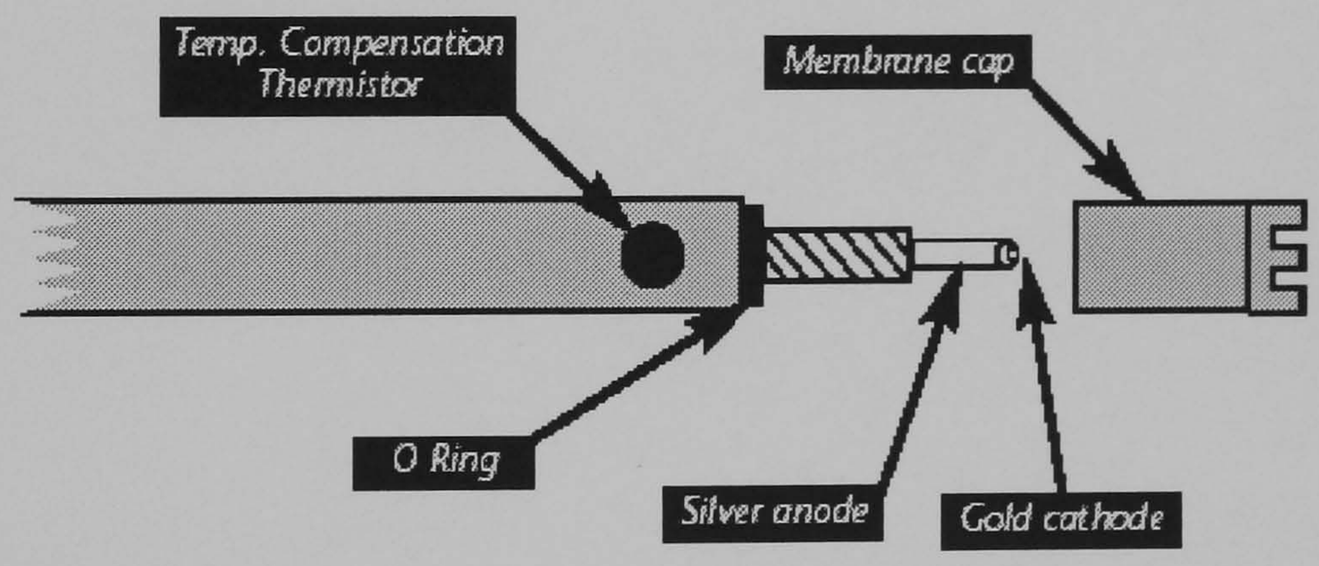

The DO electrode.

Figure B.1

In order to prevent other electrochemical reactions from interfering with the oxygen reaction and giving a false signal at the cathode, the anode and the cathode were inside the electrode body, which was covered by the membrane (Fig. B.1). The consumption of electrons at the cathode during the oxygen reaction resulted in a small current between the anode and the

---

[B.1] The electrolyte was composed of 1.28m Potassium Chloride (KCl) made up with de-ionised water.

cathode. Provided that diffusion through the membrane was the rate-controlling step in the path of the oxygen to the cathode, the signal current that flowed from the anode to the cathode was proportional to the concentration (partial pressure) of oxygen in the sample. This current, of the order of 1nA (one billionth of an amp) was converted by an adaptor (model 3130) into a voltage and allowed the output to be calibrated and scaled appropriately.

A thermistor was used to compensate the output for changes in the oxygen permeability of the membrane with temperature over the range 5 to 45°C. The thermistor was located under the metal disk on the side of the electrode about 35mm from the end (Fig, B.1). The thermistor was immersed in water at the same temperature as the membrane.

The oxygen consumption by the electrode as it measured the DO concentration produced a depletion of oxygen at the membrane surface as compared to the oxygen level in the water sample. In other words, the oxygen concentration found at the membrane, which was in direct contact with the oxygen electrode could be lower than the oxygen level in the sample itself. However this was not the case in this work because the water was flowing in the pipe and the layer of water that was in contact with the membrane was continuously renewed.

APPENDIX C

LASER DOPPLER VELOCIMETRY

C.1 BASIC PRINCIPLES

C.1.1 The Doppler effect

The Doppler effect plays an important role in LDA, since the technique is based on Doppler shift of the light reflected (and/or refracted) from a moving seeding particle. The principle is illustrated in Fig. C.1 where the vector $\vec{U}$ represent the velocity of a seeding particle and the unit vectors $\vec{I}_1$ and $\vec{I}_2$ describe the motion of incoming and scattered light respectively. The incoming light source has velocity c (i.e. speed of light) and angular frequency f_1. The observed frequency change (Doppler shift), f_D would then be:

$$f_D = f_1 \frac{\vec{U}}{c} \tag{C.1}$$

The term f_1/c can be grouped together as a wavelength λ, so that Eq. (C.1) becomes:

$$f_D = \lambda \vec{U} \tag{C.2}$$

Taking the seeding particle to act as an observer, the observed frequency will be shifted due to the particle movement relative to the source. If the incident beam light is then reemitted from the moving particle to a stationary observer, the total frequency shift observed by the stationery observer can be expressed as the dot product:

$$f_D = \left(\vec{I}_2 - \vec{I}_1\right) \bullet \vec{U} \tag{C.3}$$

Since the frequency shift is inevitable much smaller than the frequency of the light, this lead to the following approximation:

$$f_D = 2\lambda U_x \sin\kappa \tag{C.4}$$

As shown in Eq. (C.4) the Doppler frequency is directly proportional to the x-component of the particle velocity and the half angle between the incoming and scattering direction.

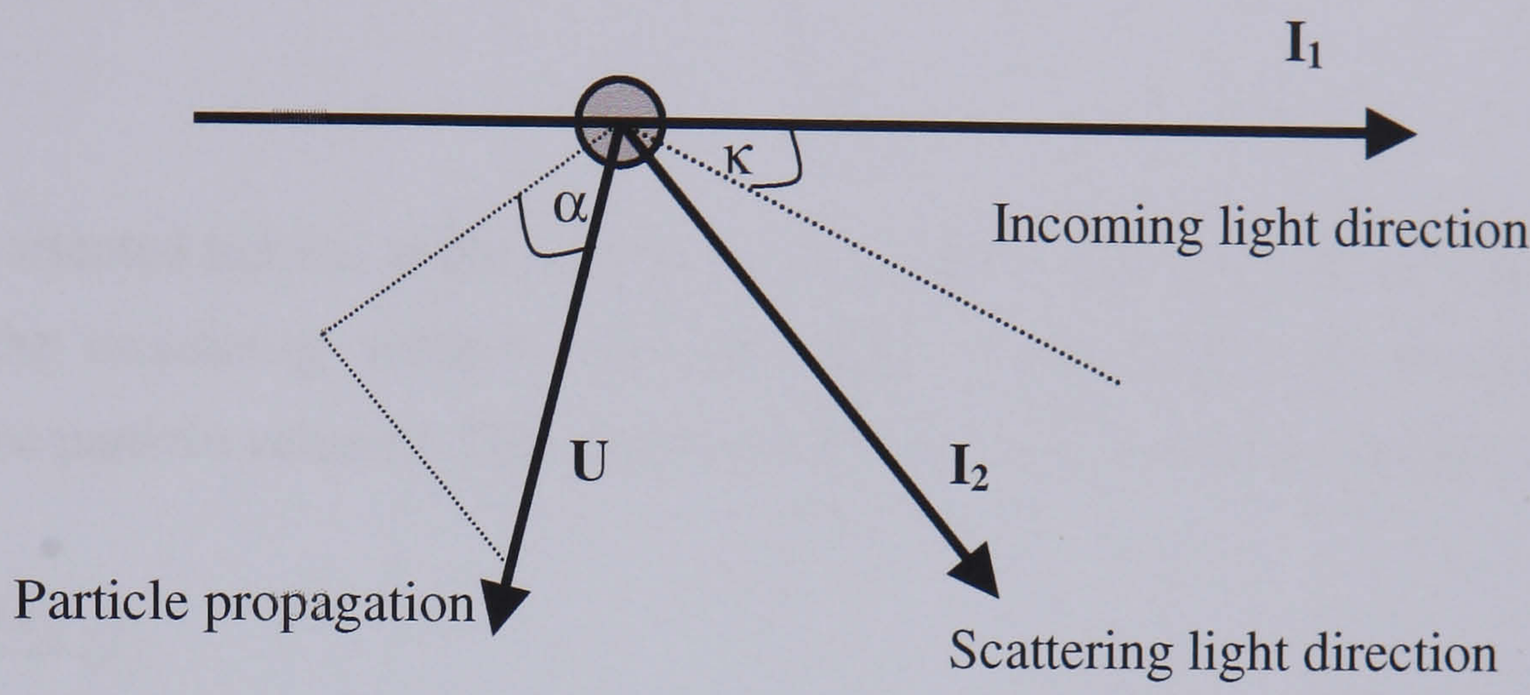

Vector diagram showing the light scattering from a moving seeding particle.

Figure C.1

C.1.2 The fringe model

While there are several ways to describe the features of the dual beam LDV system used in this work, the description based the fringe model is the simplest. When two coherent laser beams intersect, they interfere in the volume of intersection. Fringes will be formed by the interference between the two laser beams. Where the interfering light waves are in phase (peak aligned with peak) they add up creating a bright fringe. Where the light waves are out of phase (peak aligned with trough) they cancel creating a dark fringe. The bright and dark fringes form in lines parallel to the bisector of the beams (Fig. C.2).

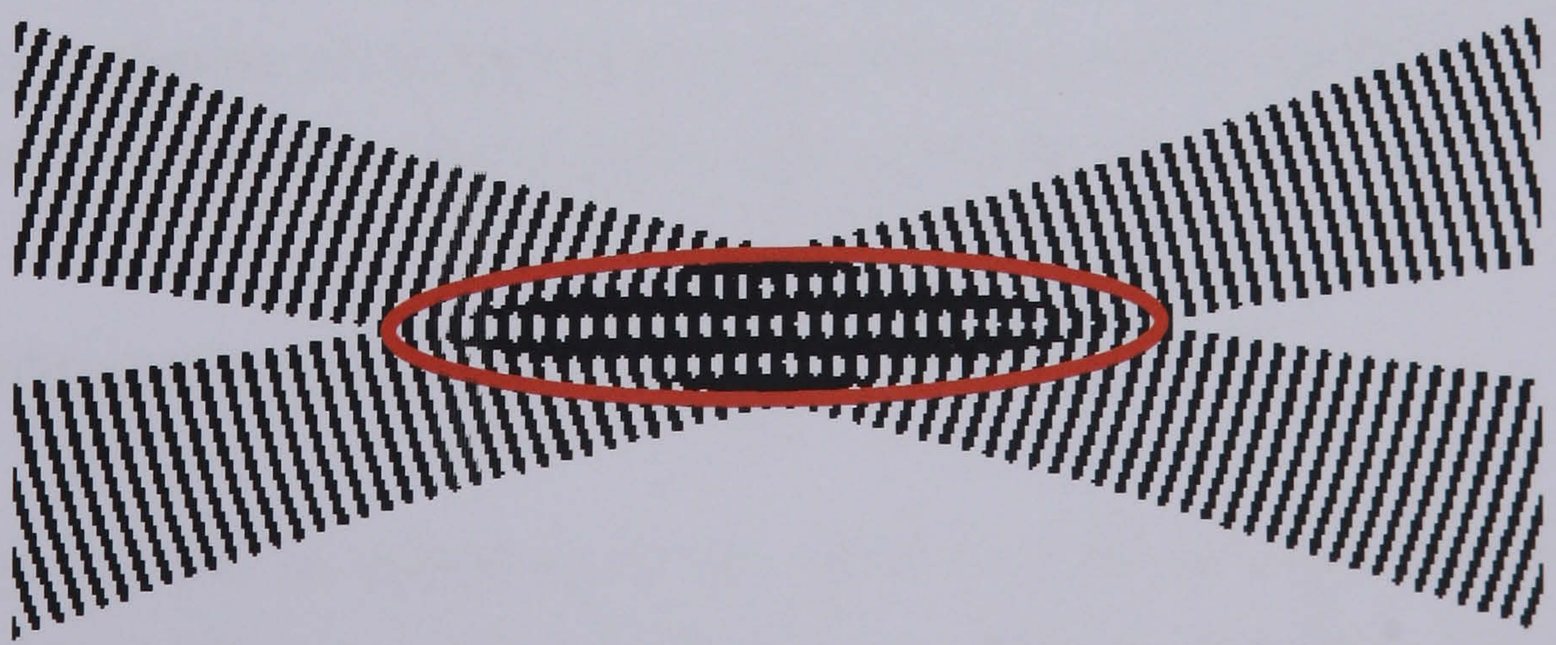

Fringes form where two coherent laser beams cross.

Figure C.2

The distance between the fringes depends on the wavelength and the angle between the incident beams. Using trigonometry the fringe spacing is found:

$$\delta_{fa} = \frac{\lambda_a}{2\sin\kappa_a} \tag{C. 5}$$

The fringes are oriented normal to the x-axis, so the intensity of light reflected from a particle moving through the measuring volume will vary with a frequency proportional to the x-component U_x of the particle velocity. This can be described by the following equation:

$$f_D = \frac{\vec{U}}{\delta_{fa}} = \frac{2\sin\kappa_a}{\lambda_a} U_x \tag{C.6}$$

which is identical to Eq. (C.4). Therefore the fringe model produces the correct relationship between velocity and Doppler frequency and may be used to describe the dual beam LDV mode.

C.2 PMT - THE DETECTOR

The PMT used to detect the scattered light in this work, was a quantum detector that depended upon the absorption of quantum of radiant energy. It consisted of a photodiode (a piece of material that emits electrons when exposed to light) with a very high gain amplifier included in a vacuum tube. Many electrodes called dynones manufactured the amplifier. The photodiode emitted electrons when exposed to scattered light, which were then accelerated in an electric field towards sequence of dynodes. When these high energy electrons collided with the first dynode it emitted more electrons which were then accelerated into another dynode, and so on. The resulting avalanche of electrons greatly amplified the original signal, which was fed into the counter signal processor for additional filtering and processing.

C.3 FREQUENCY SHIFTING – BRAGG CELL

The Bragg cell was an acousto-optic cell, which used the interaction of laser light and high frequency ultrasound in a transparent medium to shift the frequency (Fig. C.3). A carrier frequency (40MHz) supplied by a crystal controlled oscillator was amplified and applied to the transducer attached to the front of a glass block. This generated a travelling acoustic wave in the

glass. At the peaks and troughs of the acoustic waves, variations of the index of refraction occurred, which appeared to the incident beam as a moving diffraction grating. When the incident beam stroke the grating at the Bragg angle *a* the diffraction was mainly confined to the 1st order direction, which appeared at *2a* angle from the incident beam. The diffracted beam was frequency shifted over 40MHz ± 3KHz. Since it was difficult to resolve small Doppler frequencies relative to 40MHZ, downmixing of the electrical signal was mostly used to obtain more suitable shift values. The down-mixed shift frequency was referred to as the effective shift frequency.

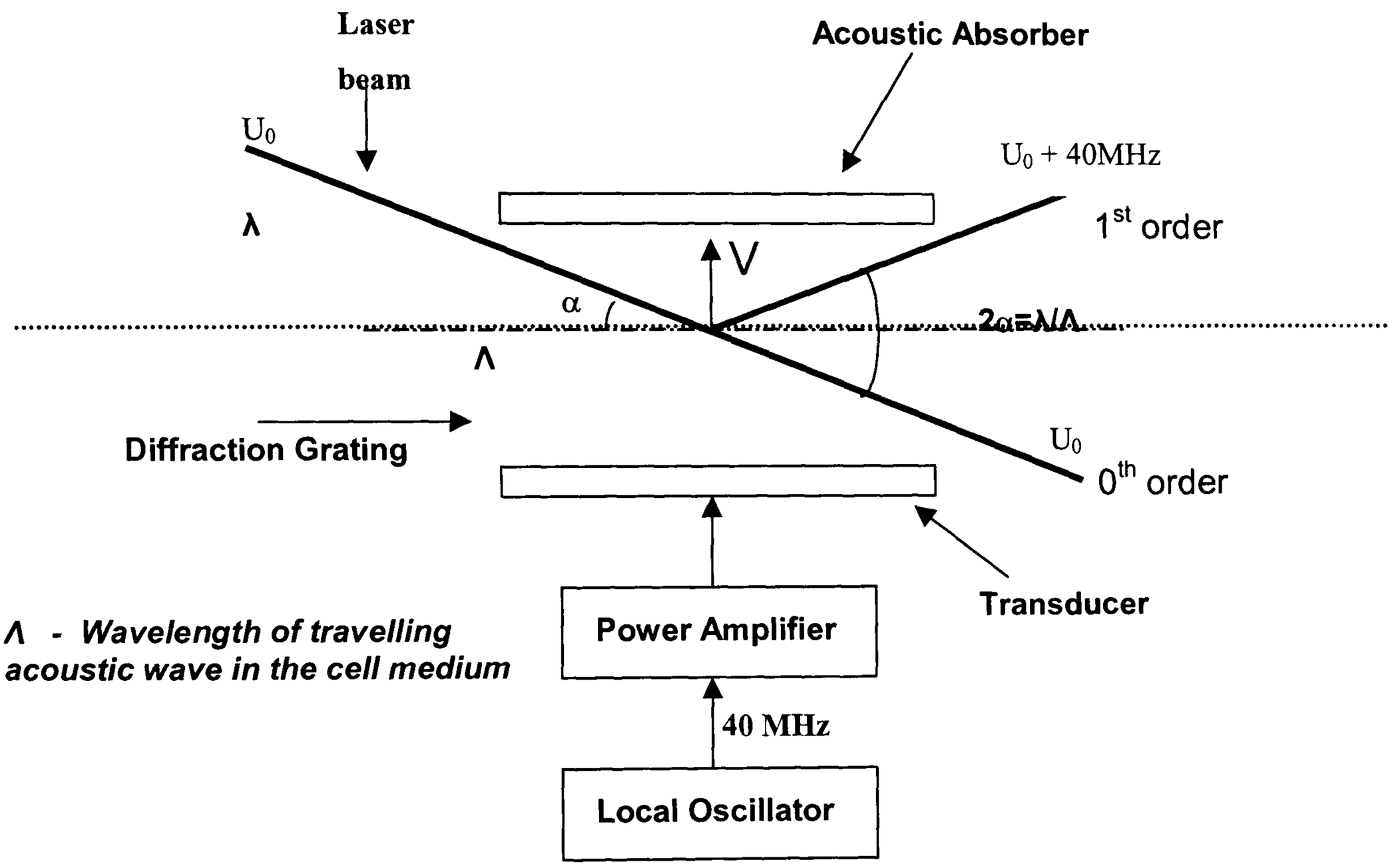

The Bragg cell.

Figure C.3

C.4 COUNTER TYPE SIGNAL PROCESSOR

The IFA 650 was a digital counter type signal processor that was designed specifically to process signals produced by a LDV system. The IFA 650 received signals from the receiving optics and/or electronics such as the Colourlink in the form of electrical signals. It extracted information such as frequency, phase, burst transit time and burst arrival time, from these signals

and sent it to the DMA board in the computer. The data was analysed using the FIND software running on the computer, which displayed the detailed analysis.

The IFA 650 signal processor consisted of an input conditioner (bandpass filter and amplifier), a burst detector and sampler and finally an autocorrelator. In general, the signal received from the PMT consisted of the Doppler signal, the pedestal and the broadband noise (burst) (Fig. C.4). The overall shape of the burst was a consequence of the fact that the laser beams, producing the measurement volume, were inevitably stronger at their centre than at their edges. As the particle passed through the edge of the measurement volume where the fringes were weakly illuminated, the signal fluctuations were also weak. As the particle passed through the measurement volume centre the signal fluctuations became larger and then decayed again. A high-pass filter was used to remove the pedestal, setting an upper limit to the pedestal amplitude rejecting large particle or particles, which may not follow the flow correctly. Furthermore, a low-pass filter was used to reduce high-frequency noise (Doppler shifted component). A fixed-gain amplifier then amplified the signal.

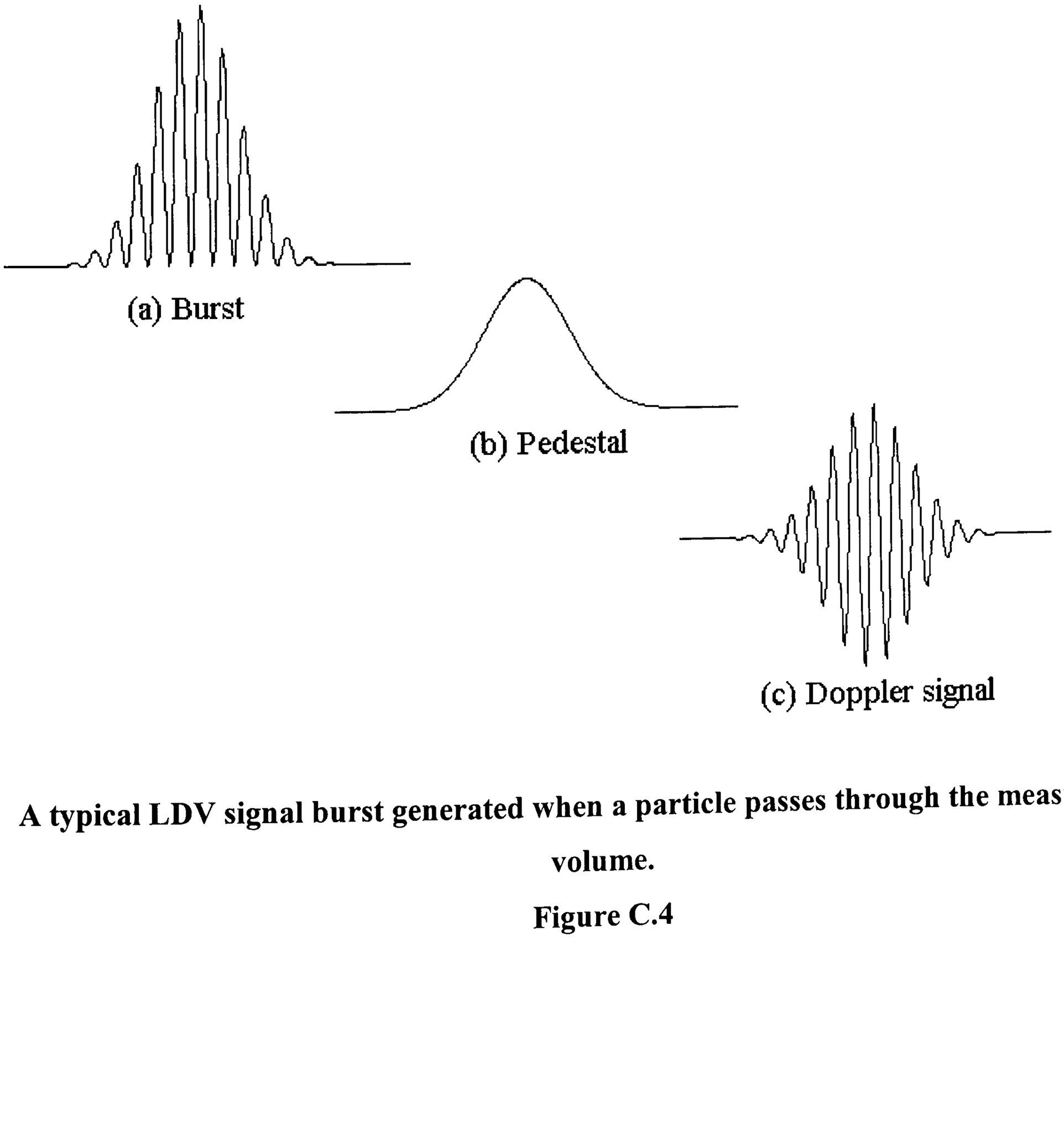

A typical LDV signal burst generated when a particle passes through the measurement volume.

Figure C.4

The basic functions of the counter signal processor are shown by the scheme in Fig. C.5. The burst detector detected when the burst started and stopped and also provided an estimate of the Doppler frequency. Activating two Schmitt triggers did the discrimination between the Doppler signal and the noise. One Schmitt trigger was activated for each zero crossing of the signal and the second Schmitt trigger was activated when the signal exceeds a 50mV threshold. To prevent false triggering of the zero-crossing detector by random noise, the zero-level was provided with a hysteresis amplitude of 10mV. When the signal exceeded the threshold value, a burst timer measured the length of the signal burst. At the same time the signal was monitored by the burst detector and it was sampled at multiple-sampling frequencies. At the end of the signal burst (at the first zero-crossing after the signal stopped exceeding the threshold value) the sampled information was placed in the buffer memory and the measured burst duration was used to determine the centre of the burst. The estimate of the Doppler frequency provided by the burst detector was used to determine which of the multiple sampling rates was the optimum for individual burst of the incoming signal. Once the optimum sampling rate of the signal was determined (at least 10 samples per cycle), 256 samples per burst from the centre and outward were transferred to an autocorrelator.

The autocorrelator performed a double-clipped autocorrelation function on the 256 samples. Once the autocorrelation function for the individual signal burst was calculated, multiple validation tests were performed to determine the signal-to-noise ratio (SNR) of the signal. If these tests were successful the frequency of the incoming signal was calculated by determining the number of delays that occurred between validated cycles of the autocorrelation function. Then, by knowing the sampling time period and the number of time delays and the number of cycles in the correlation function, the frequency was determined and sent to the computer.

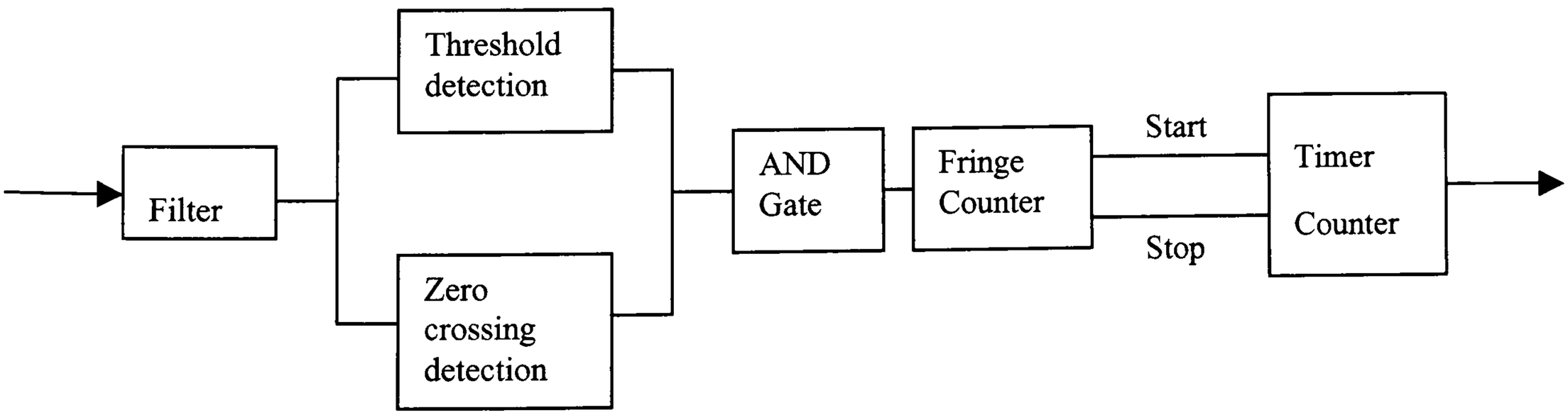

Scheme for the frequency counter type processor IFA 650.

Figure C.5

APPENDIX D

TOTAL ENERGY LOSSES FOR THE PJS

The energy losses due to the presence of the PJS were calculated following a similar approach to Lee et al. (2000). Their model was based on a momentum balance and a Bernoulli equation taking into account the losses due to the presence of the ventilated cavity attached to a HS.

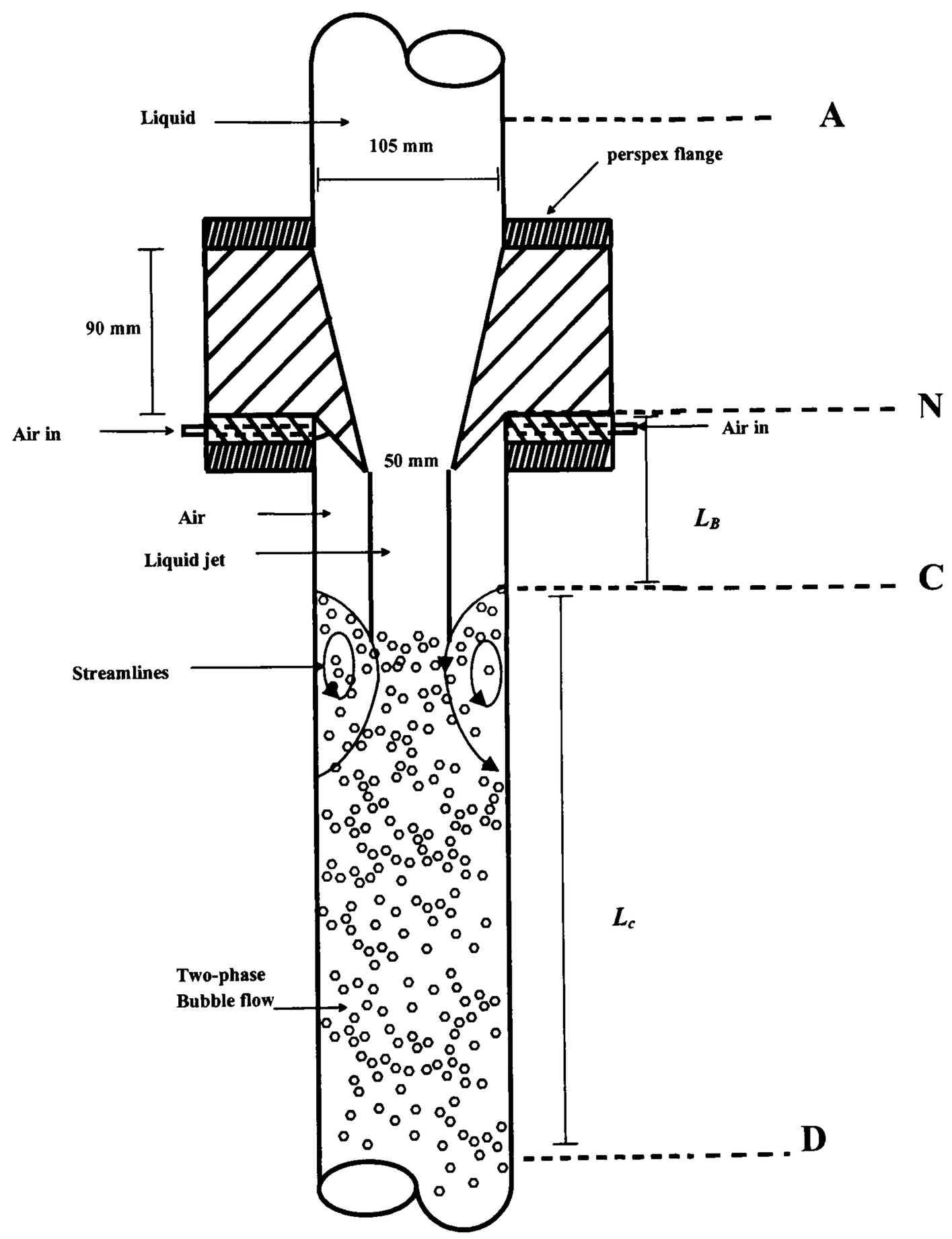

Schematic diagram of the PJS.

Fig. D.1

By taking the continuity from A to N (Fig. D.1) the nozzle velocity of the PJS is estimated as:

$$V_N = j_L \left(\frac{D}{D_N} \right)^2 \tag{D.1}$$

The liquid jet is in free fall between N and C (This is a good approximation). Therefore:

$$P_C = P_N \tag{D.2}$$

By applying the Bernoulli equation from N to C and taking into account Eq. (D.2) the liquid velocity at point C is calculated as:

$$V_C = \sqrt{V_N{}^2 + 2gL_B} \tag{D.3}$$

By applying the momentum equation from C to D and ignoring gas momentum the pressure difference between C and D is estimated:

$$\frac{P_C - P_D}{\rho_L} = j_L \left(\frac{j_L}{1-\varepsilon_G} - \sqrt{V_N{}^2 + 2gL_B} \right) - (1-\varepsilon_G) gL_c \tag{D.4}$$

Finally by applying the Bernoulli equation from C to D incorporating the losses per unit mass:

$$\frac{P_C - P_D}{\rho_L} + \frac{V_C{}^2}{2} - \frac{j^2}{2(1-\varepsilon_G)^2} + gL_c = l \tag{D.5}$$

Combining Eqs. (D.1), (D.3), (D.4) and (D.5) the losses per unit mass due to the PJS are:

$$\frac{j_L^2}{(1-\varepsilon_G)} + \frac{V_N^2}{2} + gL_B - j_L \sqrt{V_N^2 + 2gL_B} + \varepsilon_G gL_c - \frac{j_L^2}{2(1-\varepsilon_G)^2} = l \tag{D.6}$$

Combining Eqs. (D.6), (5.6), (5.7) and (5.8) gives the total energy losses per unit mass for the PJS (Eq. 5.15).

APPENDIX E

MASS TRANSFER MODEL

The model presented in this Appendix was created to deal with the presence of the DO concentration gradient in the bubble cloud for Cases VI and VII that resulted in a change of the driving force for mass transfer (see discussion in section 5.5). The model is a simple approach and is not expected to be exact or to apply to systems with different geometry, but does contain sufficient complexity to capture the features of interest.

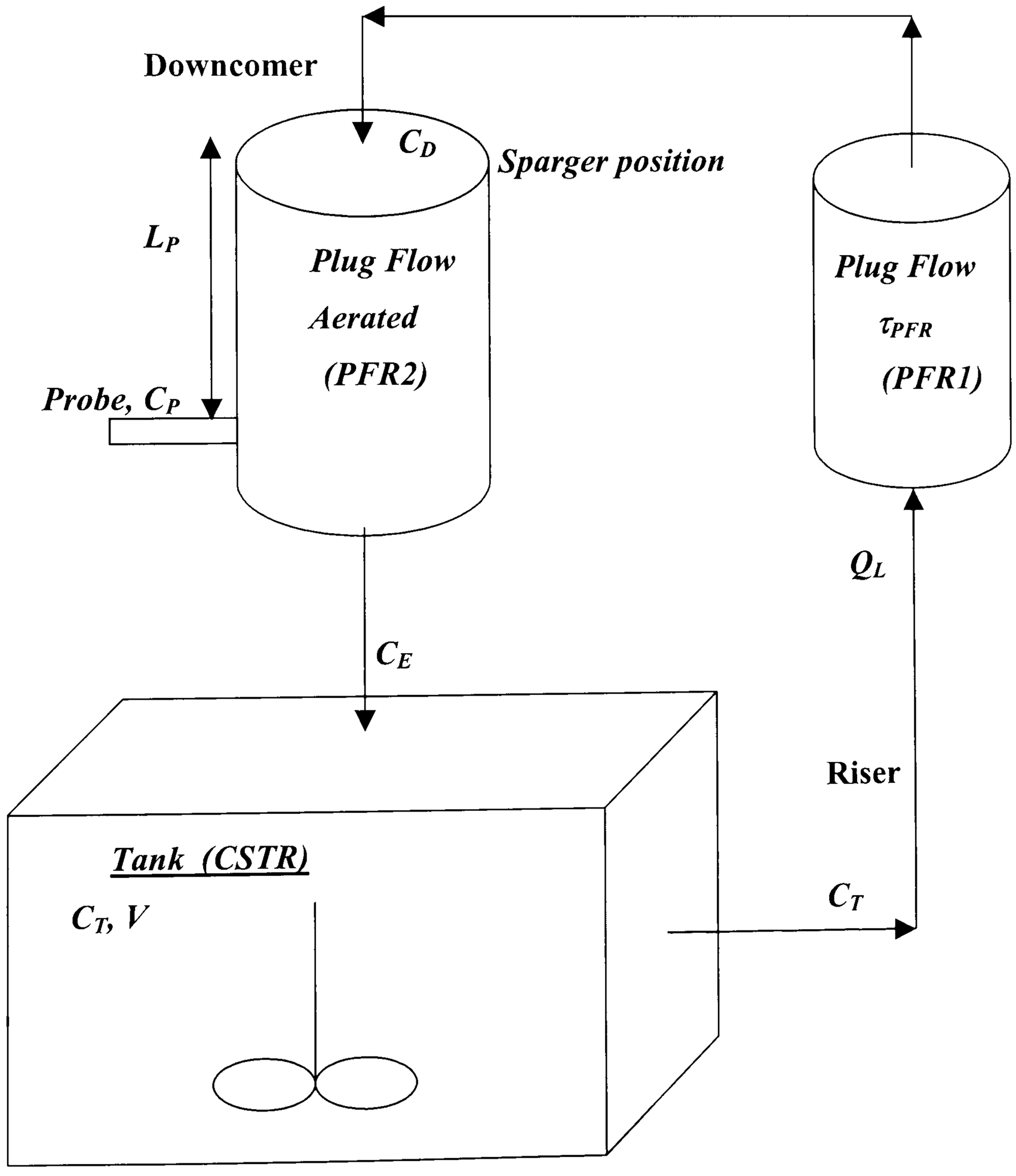

Schematic diagram of the proposed model.

Fig. E.1

The Residence time distribution (RTD) study had shown that the reservoir tank can over long enough time scales be modeled successfully as a Continuous Stirred Tank Reactor (CSTR). On the other hand the clear liquid in the riser etc. and the aerated part (two-phase mixture) in the downcomer were modeled as Plug Flow Reactors (PFR), i.e. PFR1 and PFR2 (notwithstanding the mixing zone).

A mass balance on the DO concentration, C_T, in the liquid contained in the reservoir tank gives:

$$V\frac{dC_T}{dt} = Q_L\left(C_E - C_T\right) \tag{E.1}$$

where C_E was the DO concentration leaving the downcomer and C_T is the DO concentration leaving the tank at time t. At $t = 0$ when a hydrodynamic equilibrium was reached before the commencement of aeration with oxygen $C_T = C_P$ where C_P was the experimental DO concentration at the probe location. C_T at $t = 0$ is therefore measured and known. The riser etc. and aerated downcomer sections were modeled as PFRs with a residence times estimated as:

$$t = \tau_{PFR} = \frac{V_{pipe}}{Q_L} \tag{E.2}$$

where V_{pipe} was the liquid volume contained in the relevant pipe sections of the experimental apparatus (tank exit, riser, top cross pipe and downcomer to the sparger position):

$$C_D = C_T\left(t - \tau_{PFR}\right) \tag{E.3}$$

For $Q_L = 0.00825$ m^3 sec^{-1} used in the present work the residence time in the riser etc. PFR1 was $\tau_{PFR} \approx 12$ sec. Thus according to Eq. (E.3), C_D which was the DO concentration before the sparger would be equal to the DO concentration that was in the tank, C_T, 12 sec before.

The DO concentration in the bubble cloud inside the pipe is not uniform. A mass balance in an infinitesimal vertical slice of the PFA (Fig. E.2) assuming no axial dispersion and no depletion of the oxygen content of the bubbles across the slice gives the change of the DO concentration:

$$Q_L \frac{dC}{dz} dz = k_L a A dz \left(C^* - C(t) \right) \tag{E.4}$$

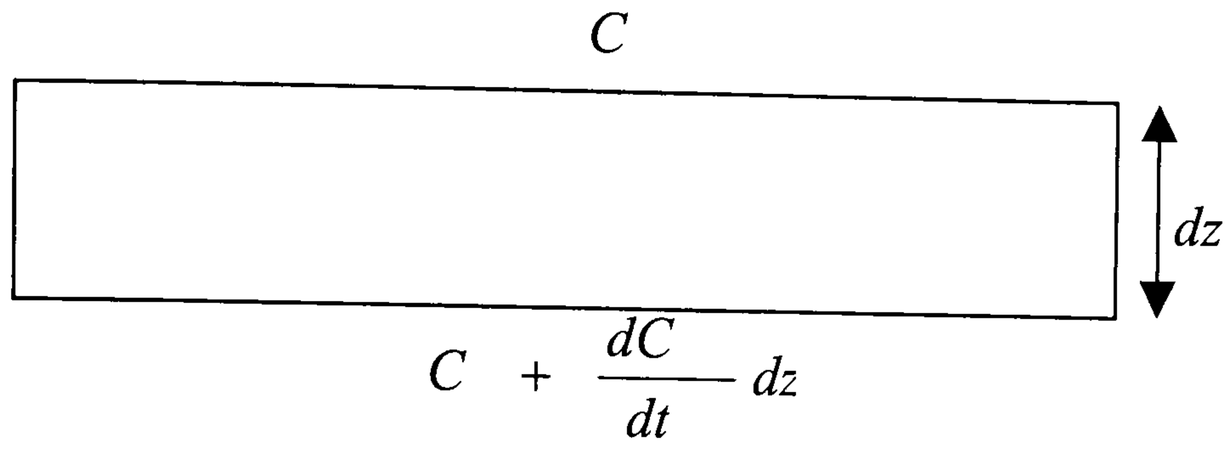

Vertical slice of the PFA.

Fig. E.2

where A is the pipe's cross section. C^* is the DO saturation concentration based on gas in bubbles and $C(t)$ the DO concentration at time t. Integration of Eq. (E.4) between the limits C_D to C_P and zero to L_P gives:

$$\ln\left(\frac{C^* - C_D}{C^* - C_P} \right) = k_L a \frac{A L_P}{Q_L} \approx k_L a \frac{V_P}{Q_L} \tag{E.5}$$

where L_P was the vertical distance from the sparger to the probe and V_P was the aerated volume contained between the sparger and the probe.

The mass balance may also be taken to the downcomer exit but also including the small aerated section inside the tank. Then integration of Eq. (E.4) between the limits C_D to C_E gives:

$$\ln\left(\frac{C^* - C_E}{C^* - C_D} \right) \approx k_L a \frac{V_a}{Q_L} \tag{E.6}$$

where V_a was the total aerated volume in the system.

The best value of $k_L a$ for a set of experimental data was determined using a golden section search method described below. For a guessed $k_L a$ value:

i C_D was calculated from Eq. (E.5)

ii C_E was calculated from Eq. (E.6)

iii C_T was calculated from Eq. (E.3)

iv C_T was calculated from Eq. (E.1)

v The guessed $k_L a$ value was changed until both C_T profiles (calculated in steps iii and iv) agreed within 5%.

vi The result was accepted if the fit between model and data was satisfactory.

A typical example of $k_L a$ determination using the model outlined above is given in Table E.1. The example corresponds to CASE VII for the PJS. The best value of $k_L a$ for this set of experimental data was 0.0603 (see Table 5.6). The data from the last two columns of Table E.1, corresponding to the DO concentration in the tank, C_T, determined using Eqs. (E.1) and (E.3), are plotted with the experimental data at the probe location, C_P, in Fig. (E.3). It can be seen that the fit between the two lines that correspond to the DO concentration in the tank, C_T, is excellent (see also Fig. 5.11).

t (s)	C_P (%)	C_D (%)	C_E (%)	$t-\tau_{PFR}$ (s)	C_T (%) Eq. (E.3)	C_T (%) Eq. (E.1)
0	12.6	-2.4	26.6	-13.8	12.3	12.6
5	16.8	2.5	30.1	-8.8	13.1	13.2
10	23.4	10.3	35.7	-3.8	13.3	13.9
15	25.1	12.3	37.1	1.2	14.3	14.8
20	25.8	13.1	37.7	6.2	15.1	15.7
25	26	13.3	37.9	11.2	16.1	16.6
30	26.8	14.3	38.5	16.2	17.2	17.5
35	27.5	15.1	39.1	21.2	18.2	18.3
40	28.4	16.1	39.9	26.2	19.4	19.2
45	29.3	17.2	40.6	31.2	20.3	20.1
50	30.2	18.2	41.4	36.2	21.7	20.9
55	31.2	19.4	42.2	41.2	22.9	21.8
60	32	20.3	42.9	46.2	23.9	22.6
65	33.2	21.7	43.9	51.2	24.9	23.4
70	34.2	22.9	44.7	56.2	26.0	24.3
75	35	23.9	45.4	61.2	26.6	25.1
80	35.9	24.9	46.2	66.2	27.4	26.0
85	36.8	26.0	46.9	71.2	28.3	26.8
90	37.3	26.6	47.3	76.2	28.9	27.6

95	38	27.4	47.9	81.2	30.1	28.4
100	38.8	28.3	48.6	86.2	30.9	29.2
105	39.3	28.9	49.0	91.2	31.8	30.0
110	40.3	30.1	49.9	96.2	32.5	30.8
115	41	30.9	50.5	101.2	33.2	31.6
120	41.8	31.8	51.1	106.2	33.8	32.4
125	42.4	32.5	51.6	111.2	34.4	33.2
130	43	33.2	52.1	116.2	35.2	33.9
135	43.5	33.8	52.6	121.2	36.0	34.7
140	44	34.4	53.0	126.2	36.7	35.4
145	44.7	35.2	53.6	131.2	37.6	36.1
150	45.4	36.0	54.1	136.2	38.3	36.9
155	46	36.7	54.7	141.2	38.9	37.6
160	46.7	37.6	55.2	146.2	39.4	38.3
165	47.3	38.3	55.7	151.2	40.1	39.0
170	47.8	38.9	56.2	156.2	40.7	39.7
175	48.3	39.4	56.6	161.2	41.5	40.3
180	48.9	40.1	57.1	166.2	42.1	41.0
185	49.4	40.7	57.5	171.2	42.8	41.7
190	50.1	41.5	58.1	176.2	43.5	42.3
195	50.6	42.1	58.5	181.2	44.0	43.0
200	51.2	42.8	59.0	186.2	44.7	43.6
205	51.8	43.5	59.5	191.2	45.5	44.3
210	52.2	44.0	59.9	196.2	46.3	44.9
215	52.8	44.7	60.4	201.2	47.1	45.5
220	53.5	45.5	61.0	206.2	47.8	46.1
225	54.2	46.3	61.5	211.2	48.5	46.7
230	54.8	47.1	62.0	216.2	48.9	47.3
235	55.4	47.8	62.5	221.2	49.5	47.9
240	56	48.5	63.1	226.2	49.9	48.5
245	56.4	48.9	63.4	231.2	50.4	49.1
250	56.9	49.5	63.8	236.2	50.8	49.7
255	57.2	49.9	64.1	241.2	51.5	50.3
260	57.7	50.4	64.5	246.2	51.9	50.9
265	58	50.8	64.7	251.2	52.7	51.4
270	58.6	51.5	65.2	256.2	53.3	52.0
275	58.9	51.9	65.5	261.2	53.8	52.5
280	59.6	52.7	66.1	266.2	54.4	53.1
285	60.1	53.3	66.5	271.2	54.8	53.6
290	60.6	53.8	66.9	276.2	55.3	54.1
295	61.1	54.4	67.3	281.2	55.8	54.7
300	61.4	54.8	67.6	286.2	56.2	55.2
305	61.8	55.3	67.9	291.2	56.7	55.7
310	62.3	55.8	68.3	296.2	57.1	56.2
315	62.6	56.2	68.6	301.2	57.7	56.7
320	63	56.7	68.9	306.2	58.3	57.2
325	63.4	57.1	69.3	311.2	58.6	57.7
330	63.9	57.7	69.7	316.2	59.2	58.2
335	64.4	58.3	70.1	321.2	59.6	58.6
340	64.7	58.6	70.4	326.2	60.1	59.1
345	65.2	59.2	70.8	331.2	60.6	59.6
350	65.5	59.6	71.0	336.2	61.0	60.0
355	65.9	60.1	71.4	341.2	61.3	60.5

360	66.4	60.6	71.8	346.2	61.7	60.9
365	66.7	61.0	72.0	351.2	62.0	61.4
370	67	61.3	72.3	356.2	62.5	61.8
375	67.3	61.7	72.5	361.2	63.2	62.3
380	67.6	62.0	72.8	366.2	63.7	62.7
385	68	62.5	73.1	371.2	64.2	63.1
390	68.6	63.2	73.6	376.2	64.5	63.5
395	69	63.7	74.0	381.2	64.9	63.9
400	69.4	64.2	74.3	386.2	65.3	64.3
405	69.7	64.5	74.6	391.2	65.7	64.8
410	70	64.9	74.8	396.2	65.9	65.2
415	70.4	65.3	75.1	401.2	66.3	65.6
420	70.7	65.7	75.4	406.2	66.8	65.9
425	70.9	65.9	75.6	411.2	67.0	66.3
430	71.2	66.3	75.8	416.2	67.3	66.7
435	71.7	66.8	76.2	421.2	67.8	67.1
440	71.8	67.0	76.3	426.2	68.1	67.5
445	72.1	67.3	76.6	431.2	68.6	67.8
450	72.5	67.8	76.9	436.2	69.1	68.2
455	72.8	68.1	77.2	441.2	69.4	68.6
460	73.2	68.6	77.5	446.2	69.9	68.9
465	73.6	69.1	77.8	451.2	70.1	69.3
470	73.9	69.4	78.1	456.2	70.1	69.6
475	74.3	69.9	78.4	461.2	70.6	70.0
480	74.5	70.1	78.6	466.2	70.9	70.3
485	74.5	70.1	78.6	471.2	71.3	70.7
490	74.9	70.6	78.9	476.2	71.7	71.0
495	75.2	70.9	79.2	481.2	71.7	71.3
500	75.5	71.3	79.4	486.2	72.1	71.6
505	75.8	71.7	79.7	491.2	72.5	72.0
510	75.8	71.7	79.7	496.2	72.8	72.3
515	76.2	72.1	80.0	501.2	73.2	72.6
520	76.5	72.5	80.3	506.2	73.5	72.9
525	76.8	72.8	80.5	511.2	73.8	73.2
530	77.1	73.2	80.8	516.2	74.0	73.5
535	77.4	73.5	81.0	521.2	74.3	73.8
540	77.6	73.8	81.2	526.2	74.6	74.1
545	77.8	74.0	81.4	531.2	74.9	74.4
550	78.1	74.3	81.6	536.2	75.3	74.7
555	78.3	74.6	81.8	541.2	75.5	75.0
560	78.6	74.9	82.0	546.2	75.8	75.2
565	78.9	75.3	82.3	551.2	76.0	75.5
570	79.1	75.5	82.4	556.2	76.3	75.8
575	79.3	75.8	82.6	561.2	76.5	76.1
580	79.5	76.0	82.8	566.2	76.9	76.3
585	79.8	76.3	83.0	571.2	77.0	76.6
590	79.9	76.5	83.1	576.2	77.4	76.9
595	80.3	76.9	83.5	581.2	77.6	77.1
600	80.4	77.0	83.5	586.2	77.9	77.4
605	80.7	77.4	83.8	591.2	78.1	77.6
610	80.9	77.6	84.0	596.2	78.3	77.9
615	81.1	77.9	84.1	601.2	78.6	78.1
620	81.3	78.1	84.3	606.2	78.8	78.4

625	81.5	78.3	84.5	611.2	79.0	78.6
630	81.7	78.6	84.6	616.2	79.3	78.9
635	81.9	78.8	84.8	621.2	79.5	79.1
640	82.1	79.0	85.0	626.2	79.6	79.4
645	82.3	79.3	85.1	631.2	80.0	79.6
650	82.5	79.5	85.3	636.2	80.2	79.8
655	82.6	79.6	85.4	641.2	80.3	80.0
660	82.9	80.0	85.6	646.2	80.6	80.3
665	83.1	80.2	85.8	651.2	80.8	80.5
670	83.2	80.3	85.9	656.2	81.0	80.7
675	83.4	80.6	86.1	661.2	81.3	80.9
680	83.6	80.8	86.2	666.2	81.4	81.1
685	83.8	81.0	86.4	671.2	81.6	81.3
690	84	81.3	86.6	676.2	81.7	81.5
695	84.1	81.4	86.6	681.2	82.0	81.8
700	84.3	81.6	86.8	686.2	82.2	82.0
705	84.4	81.7	86.9	691.2	82.3	82.2
710	84.6	82.0	87.1	696.2	82.7	82.4
715	84.8	82.2	87.2	701.2	82.8	82.5
720	84.9	82.3	87.3	706.2	83.0	82.7
725	85.2	82.7	87.6	711.2	83.1	82.9
730	85.3	82.8	87.7	716.2	83.4	83.1
735	85.5	83.0	87.8	721.2	83.5	83.3
740	85.6	83.1	87.9	726.2	83.7	83.5
745	85.8	83.4	88.1	731.2	83.8	83.7
750	85.9	83.5	88.2	736.2	84.0	83.9
755	86.1	83.7	88.3	741.2	84.2	84.0
760	86.2	83.8	88.4	746.2	84.4	84.2
765	86.3	84.0	88.5	751.2	84.5	84.4
770	86.5	84.2	88.7	756.2	84.5	84.6
775	86.7	84.4	88.8	761.2	84.8	84.7
780	86.8	84.5	88.9	766.2	84.9	84.9
785	86.8	84.5	88.9	771.2	85.1	85.1
790	87	84.8	89.1	776.2	85.4	85.2
795	87.1	84.9	89.2	781.2	85.5	85.4
800	87.3	85.1	89.3	786.2	85.6	85.5
805	87.5	85.4	89.5	791.2	85.8	85.7
810	87.6	85.5	89.6	796.2	85.9	85.8
815	87.7	85.6	89.7	801.2	86.2	86.0
820	87.9	85.8	89.8	806.2	86.3	86.2
825	88	85.9	89.9	811.2	86.4	86.3
830	88.2	86.2	90.1	816.2	86.4	86.5
835	88.3	86.3	90.2	821.2	86.6	86.6
840	88.4	86.4	90.3	826.2	86.8	86.8
845	88.4	86.4	90.3	831.2	86.9	86.9
850	88.6	86.6	90.4	836.2	87.1	87.0
855	88.7	86.8	90.5	841.2	87.1	87.2
860	88.8	86.9	90.6	846.2	87.3	87.3
865	89	87.1	90.8	851.2	87.5	87.4
870	89	87.1	90.8	856.2	87.5	87.6
875	89.2	87.3	90.9	861.2	87.7	87.7
880	89.3	87.5	91.0	866.2	87.8	87.8
885	89.3	87.5	91.0	871.2	87.9	88.0

890	89.5	87.7	91.2	876.2	88.1	88.1
895	89.6	87.8	91.3	881.2	88.2	88.2
900	89.7	87.9	91.4	886.2	88.3	88.4
905	89.8	88.1	91.4	891.2	88.4	88.5
910	89.9	88.2	91.5	896.2	88.5	88.6
915	90	88.3	91.6	901.2	88.6	88.7
920	90.1	88.4	91.7	906.2	88.9	88.8
925	90.2	88.5	91.8	911.2	88.9	89.0
930	90.3	88.6	91.9	916.2	89.1	89.1
935	90.5	88.9	92.0	921.2	89.1	89.2
940	90.5	88.9	92.0	926.2	89.2	89.3
945	90.7	89.1	92.2	931.2	89.3	89.4
950	90.7	89.1	92.2	936.2	89.5	89.5
955	90.8	89.2	92.3	941.2	89.6	89.6
960	90.9	89.3	92.4	946.2	89.7	89.8
965	91	89.5	92.4	951.2	89.8	89.9
970	91.1	89.6	92.5	956.2	89.8	90.0
975	91.2	89.7	92.6	961.2	90.0	90.1
980	91.3	89.8	92.7	966.2	90.0	90.2
985	91.3	89.8	92.7	971.2	90.3	90.3
990	91.5	90.0	92.9	976.2	90.3	90.4
995	91.5	90.0	92.9	981.2	90.4	90.5
1000	91.7	90.3	93.0	986.2	90.4	90.6
1005	91.7	90.3	93.0	991.2	90.5	90.7
1010	91.8	90.4	93.1	996.2	90.6	90.8
1015	91.8	90.4	93.1	1001.2	90.7	90.9
1020	91.9	90.5	93.2	1006.2	90.9	91.0
1025	92	90.6	93.3	1011.2	91.0	91.1
1030	92.1	90.7	93.4	1016.2	91.0	91.1
1035	92.2	90.9	93.4	1021.2	91.1	91.2
1040	92.3	91.0	93.5	1026.2	91.2	91.3
1045	92.3	91.0	93.5	1031.2	91.3	91.4
1050	92.4	91.1	93.6	1036.2	91.2	91.5
1055	92.5	91.2	93.7	1041.2	91.4	91.6
1060	92.6	91.3	93.8	1046.2	91.4	91.7
1065	92.5	91.2	93.7	1051.2	91.6	91.8
1070	92.7	91.4	93.9	1056.2	91.7	91.9
1075	92.7	91.4	93.9	1061.2	91.8	91.9
1080	92.8	91.6	94.0	1066.2	91.9	92.0
1085	92.9	91.7	94.0	1071.2	92.0	92.1
1090	93	91.8	94.1	1076.2	92.0	92.2
1095	93.1	91.9	94.2	1081.2	92.0	92.3
1100	93.2	92.0	94.3	1086.2	92.2	92.3
1105	93.2	92.0	94.3	1091.2	92.3	92.4
1110	93.2	92.0	94.3	1096.2	92.3	92.5
1115	93.3	92.2	94.4	1101.2	92.4	92.6
1120	93.4	92.3	94.5	1106.2	92.5	92.6
1125	93.4	92.3	94.5	1111.2	92.5	92.7
1130	93.5	92.4	94.5	1116.2	92.6	92.8
1135	93.6	92.5	94.6	1121.2	92.6	92.9
1140	93.6	92.5	94.6	1126.2	92.7	92.9
1145	93.7	92.6	94.7	1131.2	92.7	93.0
1150	93.7	92.6	94.7	1136.2	92.7	93.1

1155	93.8	92.7	94.8	1141.2	93.0	93.1
1160	93.8	92.7	94.8	1146.2	93.0	93.2

Typical example of determining the value of $k_L a$ using the golden section search method.

The data are for Case VII for the PJS.

Table E.1

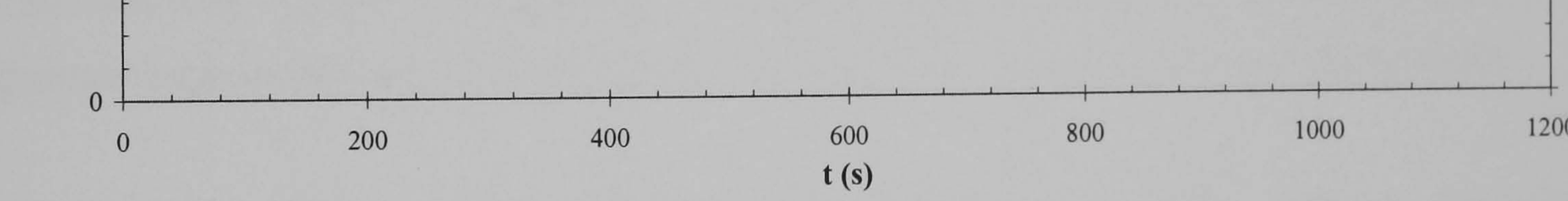

Experimental and model DO profiles for the PJS for Case VII. The agreement between the results from Eqs. (E.1) and Eq. (E.3) is excellent.

Fig. E.3

APPENDIX F

SLUG SEMI-EMPIRICAL MODEL

F.1 INTRODUCTION

In this Appendix a semi-empirical model is presented that predicts the velocity of ascending or descending slugs in downwards flow (an experimental investigation of such bubbles has been presented in Chapter 6 for four different test liquids and two different pipe diameters). There are no reports in the literature of a model that predicts the velocity of slugs in downwards flow. The model is not included in the main text of this thesis because its predictions are dependent on pipe size, when every attempt has been made to allow for this parameter. A similar problem of pipe size dependency was encountered for the onset of air entrainment at the base of ventilated cavities and the onset of the transition region for slugs rising in downflowing liquids but both were successfully solved (see sections 2.3.2 and 6.2.1.4). A brief description of the model and a comparison against the experimental results of Chapter 6 is given in the next paragraphs.

According to the theory of Davies and Taylor (1950) give for the rise velocity of a spherical cap bubble is given by:

$$V_B = \frac{2}{3}\sqrt{g\Re} \tag{F.1}$$

where $\Re$ was the radius of the curvature of the frontal of the bubble. Davidson and Harrison (1963) calculated the rise velocity, V_B, of a conventional slug bubble (i.e. with round nose) relative to the liquid velocity ahead of its tip (based on Bernoulli equation) as:

$$V_B = \sqrt{2gz} \tag{F.2}$$

where z was the distance between the stagnation point at the tip of the slug bubble and an arbitrary point. In both different curved bubbles surfaces the curvature of the bubble scales with the pipe diameter. However, in the case of wall slugs the curvature of the slug bubble is unknown. Thinking of a wall slug nose, the principal radius in the radial direction is of the order

of y, where y is the distance of the bubble nose from the pipe wall; the radius in the circumferential direction is of the order of R, where R is the pipe radius. The velocity, V_B, of an ascending or descending slug in a downflowing liquid relative to the liquid velocity ahead of its tip, is defined here as:

$$V_B = 0.35\left[\left(\frac{y}{R}\right)\sqrt{g\left[\left(1-\left(\frac{2y}{D}\right)^{1/7}\right)10R+2y\right]}+\left(1-\frac{y}{R}\right)\left(\sqrt{2gy}+\sqrt{g\left[\left(1-\left(\frac{2y}{D}\right)^{1/7}\right)10R+2y\right]}\right)\right] \qquad \text{(F.3)}$$

where the constant 0.35 is the same as in Eq. (6.3) for rising slugs in stagnant liquids. Eq. (F.3) satisfies the following boundary conditions:

(i) At the centre of the pipe where $y = R \rightarrow V_B = \sqrt{2gR}$, which agrees with Eq. (F.1).

(ii) At the pipe wall $y = 0 \rightarrow V_B = 0$, which agrees with common sense for an infinitely small bubble.

Eq. (F.3) is essentially the sum of two different terms that both depend on the distance y, from the pipe wall. When the slug rises close to the pipe's centreline (central slug and slug in the transition region) then $\left(\frac{y}{R}\right)\sqrt{g\left[\left(1-\left(\frac{2y}{D}\right)^{1/7}\right)10R+2y\right]}$ becomes the dominant term and essentially determines the bubble velocity. On the other hand, if the slug rises close to the pipe wall (wall slug) the second term $\left(1-\frac{y}{R}\right)\left(\sqrt{2gy}+\sqrt{g\left[\left(1-\left(\frac{2y}{D}\right)^{1/7}\right)10R+2y\right]}\right)$ mainly determines the bubble velocity.

Following the linear dependence of the slug velocity, V_s, suggested by Nicklin et al. (1962) (Eq. 6.1), the slug velocity of an ascending or descending slug in a downflowing liquid relative to the pipe wall is calculated as:

$$V_s = V_B\left[1-\frac{Eo_{crit}}{Eo_{\Re}}\right]-u(y) \qquad \text{(F.4)}$$

where, $u(y)$ is the liquid velocity profile ahead of the tip of the slug bubble, Eo_{crit} is a tunable constant representing a critical Eotvos number that determines the onset of wall slugs and $Eo_{\Re}$ is an Eotvos number that approximates the curvature of the bubble's tip defined as:

$$Eo_{\Re} = \frac{\rho_L g (\Re)^2}{\sigma} \tag{F.5}$$

where ρ_L is the liquid density and $\Re$ is a term defined as:

$$\frac{5}{\Re} = \frac{1}{y} + \frac{4}{\sqrt{Ry}} \tag{F.6}$$

The term $\left[1 - \frac{Eo_{crit}}{Eo_{\Re}}\right]$ is a correction factor in Eq. (F.4) that is included in the model in an effort to find an $\Re$ that works for the wall slug case.

The liquid velocity profile in Eq. (F.3) is determined using the universal velocity profile (UVP). Therefore the following three different cases are examined depending on the distance from the pipe's centreline where the slug nose is located. Note that u^* is the friction velocity, μ_L the liquid viscosity and τ_o the wall shear stress.

(I) For $y^+ > 30 \Leftrightarrow \frac{y\rho_L u^*}{\mu_L} > 30 \Leftrightarrow y > \frac{30\mu_L\sqrt{\rho_L}}{\rho_L\sqrt{\tau_o}}$, then the slug nose is located inside the turbulent layer. Then from the UVP, $u(y) = u^*\left[2.5\ln\frac{y\rho_L u^*}{\mu_L} + 5.5\right]$ and Eq. (F.4) becomes:

$$V_s = 0.35\left[\left(\frac{y}{R}\right)\sqrt{g\left[\left(1-\left(\frac{2y}{D}\right)^{1/7}\right)10R + 2y\right]} + \left(1-\frac{y}{R}\right)\left(\sqrt{2gy} + \sqrt{g\left[\left(1-\left(\frac{2y}{D}\right)^{1/7}\right)10R + 2y\right]}\right)\right]\left[1 - \frac{Eo_{crit}}{Eo_{\Re}}\right] +$$

$$-u^*\left[2.5\ln\frac{y\rho_L u^*}{\mu_L} + 5.5\right] \tag{Eq. F.7}$$

(II) For $5 < y^+ < 30 \Leftrightarrow \frac{y\rho_L u^*}{\mu_L} > 5 \Leftrightarrow y > \frac{5\mu_L\sqrt{\rho_L}}{\rho_L\sqrt{\tau_o}}$, then the slug nose is located inside the buffer layer. Then from the UVP, $u(y) = u^*\left[5\ln\frac{y\rho_L u^*}{\mu_L} - 3.5\right]$ (buffer layer) and Eq. (F.4) becomes:

$$V_s = 0.35\left[\left(\frac{y}{R}\right)\sqrt{g\left[\left(1-\left(\frac{2y}{D}\right)^{1/7}\right)10R+2y\right]}+\left(1-\frac{y}{R}\right)\left(\sqrt{2gy}+\sqrt{g\left[\left(1-\left(\frac{2y}{D}\right)^{1/7}\right)10R+2y\right]}\right)\right]\left[1-\frac{Eo_{crit}}{Eo_R}\right]+$$

$$-u^*\left[5\ln\frac{y\rho_L u^*}{\mu_L}-3.5\right] \qquad \text{(Eq. F.8)}$$

(III) For $0 < y^+ < 5 \Leftrightarrow \frac{y\rho_L u^*}{\mu_L} < 5 \Leftrightarrow y < \frac{5\mu_L\sqrt{\rho_L}}{\rho_L\sqrt{\tau_o}}$, then the slug nose is located inside the laminar viscous sub-layer. Then from the UVP, $u(y) = u^{*2}\frac{y\rho_L}{\mu_L}$ and Eq. (F.4) becomes:

$$V_s = 0.35\left[\left(\frac{y}{R}\right)\sqrt{g\left[\left(1-\left(\frac{2y}{D}\right)^{1/7}\right)10R+2y\right]}+\left(1-\frac{y}{R}\right)\left(\sqrt{2gy}+\sqrt{g\left[\left(1-\left(\frac{2y}{D}\right)^{1/7}\right)10R+2y\right]}\right)\right]\left[1-\frac{Eo_{crit}}{Eo_r}\right]+$$

$$-u^{*2}\frac{y\rho_L}{\mu_L} \qquad \text{(Eq. F.9)}$$

F.2 SOLUTION PROCEDURE

The solution procedure involves calculating the speed of the slug at various distances y, from the pipe's centreline. Therefore the tip of the slug is placed at various distances y, and then its speed is calculated from Eqs. (F.7)-(F.9). Such calculations for different superficial water velocities, j_L, in a 0.105 m id pipe are shown in Fig. F.1. Similar graphs were produced for all the other test liquids. The model takes account of the following two simple considerations for the determination of the slug velocity.

(i.) If the predicted slug velocity at the pipe's centreline is higher than the predicted slug velocity at the next adjacent location $\left(\frac{y}{R}=0.99\right)$ then the model assumes that the slug will rise at the pipe's centreline.

(ii.) If the predicted slug velocity at the pipe's centreline is lower than the predicted slug velocity at the next adjacent location $\left(\frac{y}{R}=0.99\right)$ then the model assumes that the slug will rise at the distance y from the pipe's centreline where it has the local maximum speed (Fig. F.1). This is in agreement with the physics outlined in

Chapter 6, i.e. that the slugs would rise as fast as possible using the path of least resistance.

The model predictions against the experimental results presented in Chapter 6 are shown in Figs. (F.2)-(F.7). It can be seen that the model is able to predict the onset of the transition region quite accurately. However, as already mentioned the model predictions are pipe dependent. The model predicts satisfactorily the experimental data of all different four liquids in the 105 mm pipe when $Eo_{crit} = 0.25$. On the other hand a value of $Eo_{crit} = 0.75$ for the data in the 50 mm id pipe. This shows a dependency of the tunable constant, Eo_{crit} by a factor of 3 on pipe diameter. Interestingly a same dependency by again a factor of 3 was found for the onset of the transition region (Table 6.2).

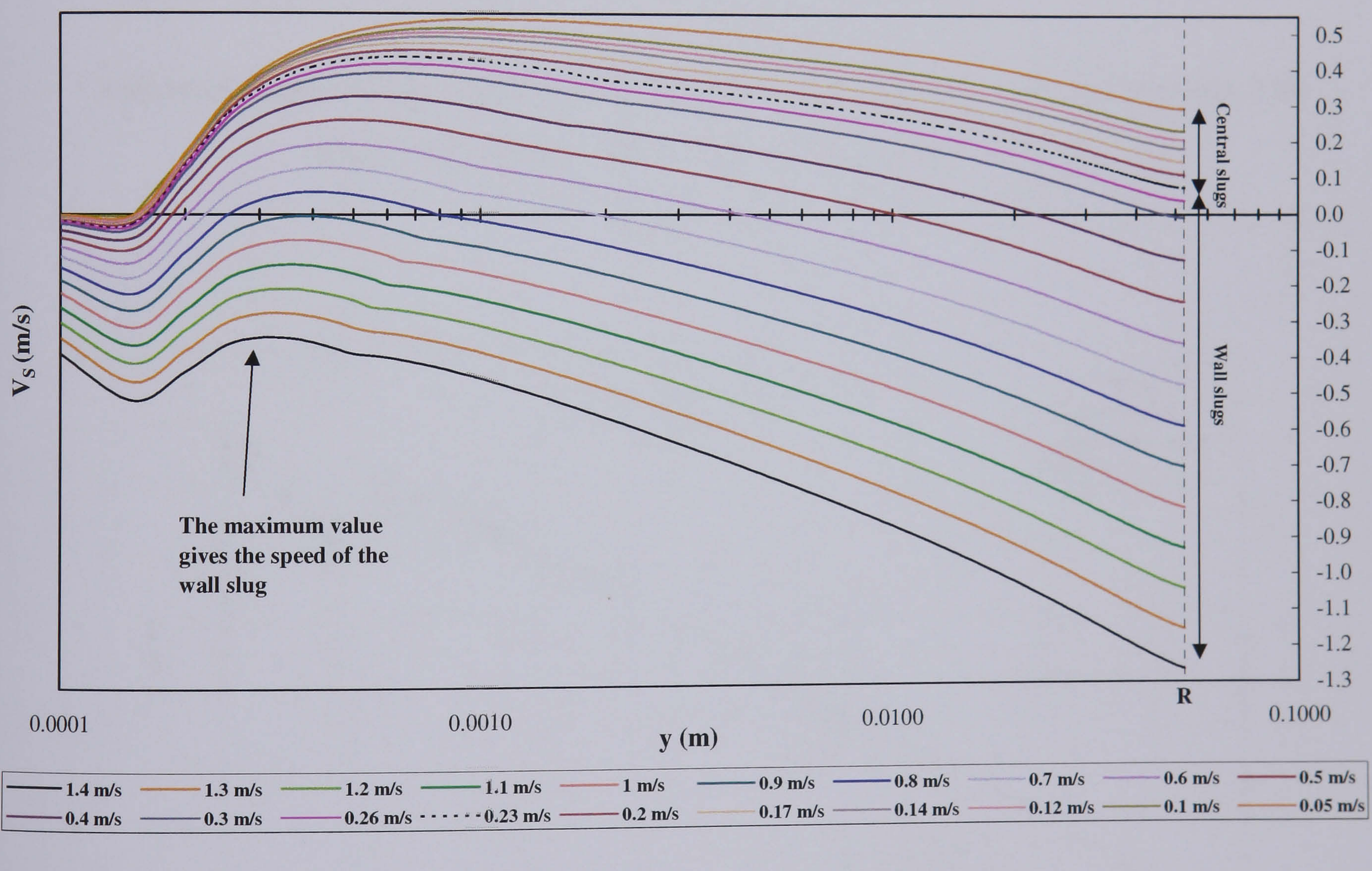

Predicted slug velocities for various superficial water velocities in $D = 105$ mm. The onset of wall slugs is predicted at $j_{T,L} = 0.23$ m s^{-1}, which agrees with the experimental results.

Figure F.1

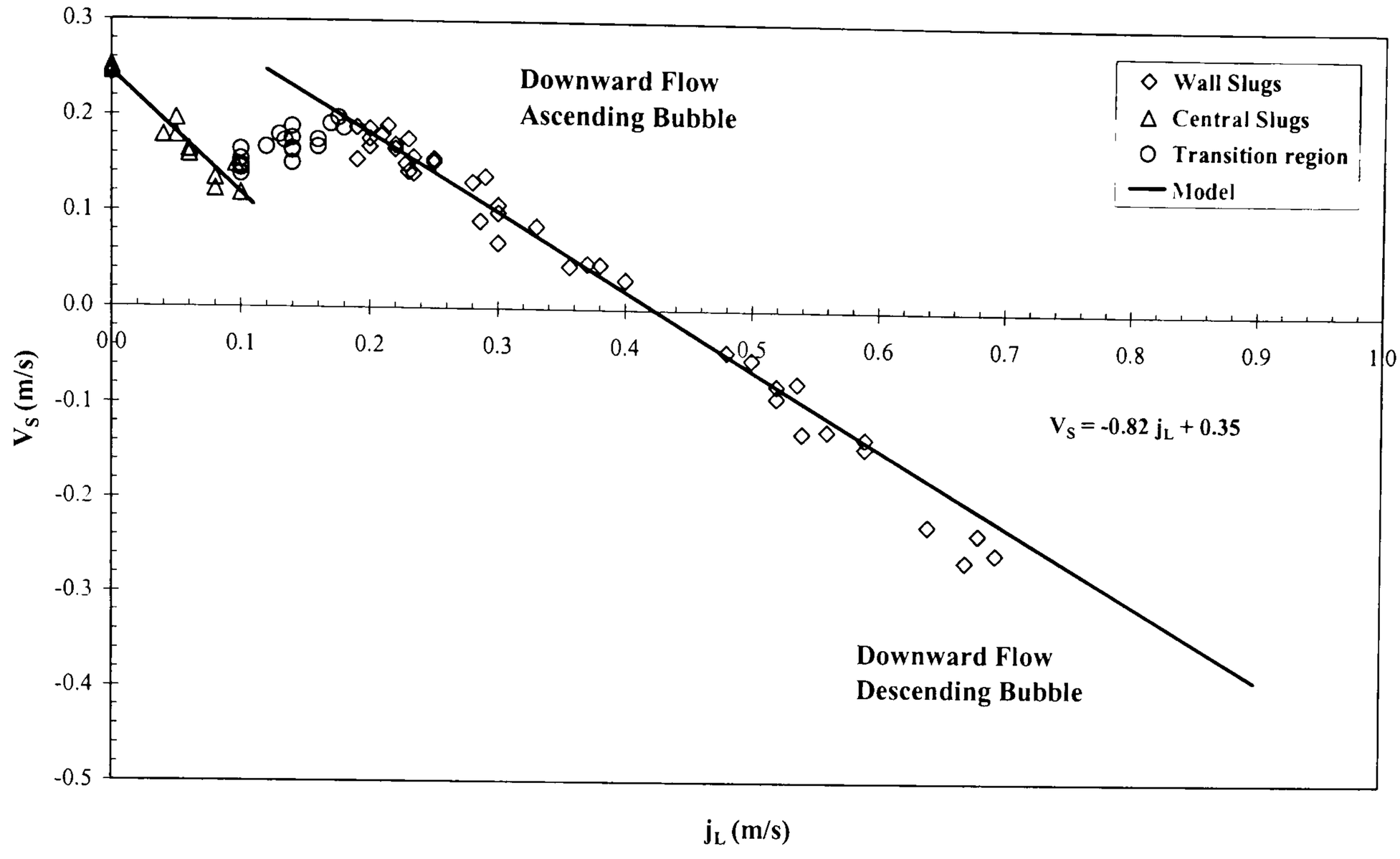

Comparison between the model and the experimental results in $D = 50$ mm in water. The value of the critical Eotvos number is 0.75 $\left(Eo_{crit} = 0.75\right)$.

Figure F.2

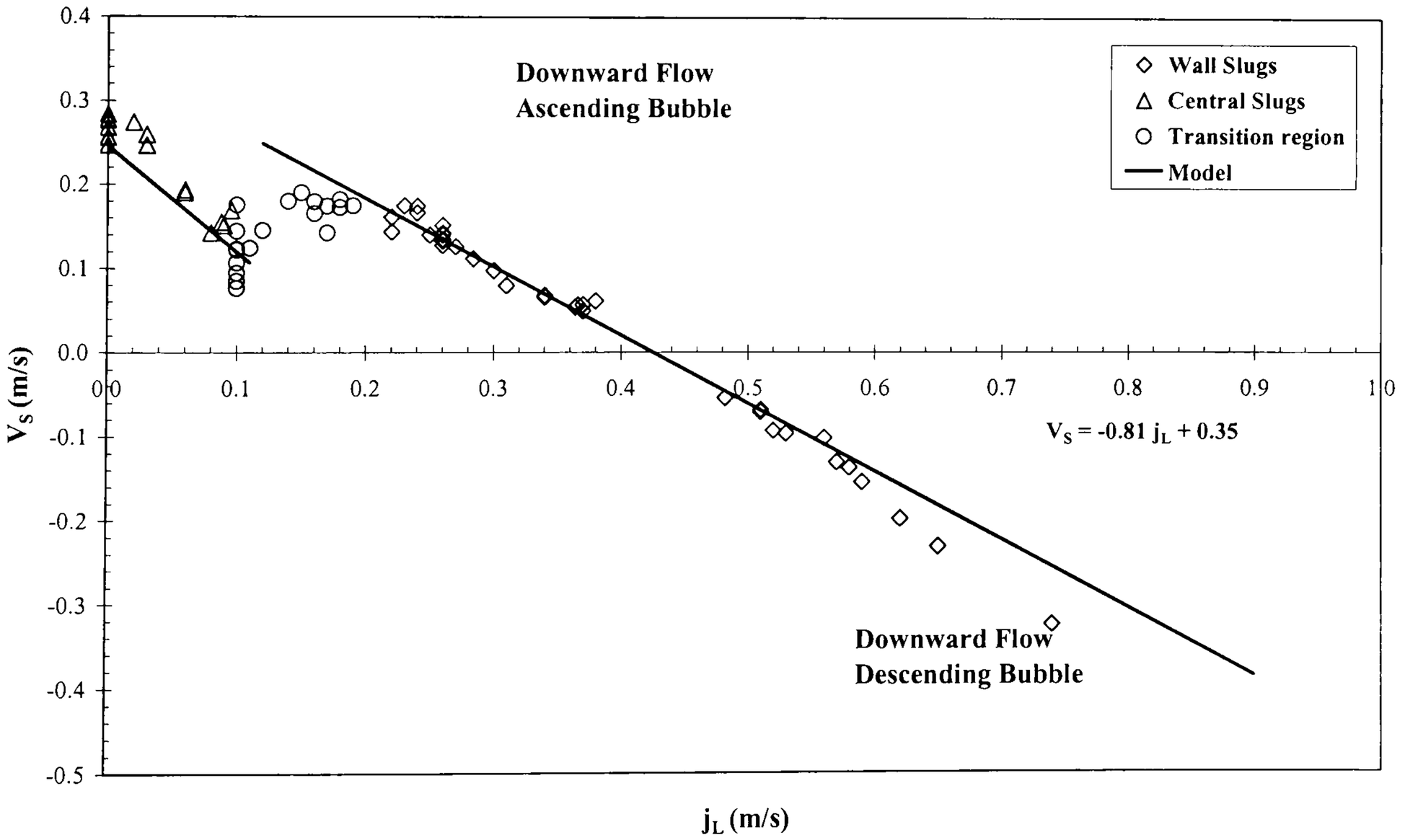

Comparison between the model and the experimental results in $D = 50$ mm in salt water. The value of the critical Eotvos number is 0.75 $\left(Eo_{crit} = 0.75\right)$.

Figure F.3

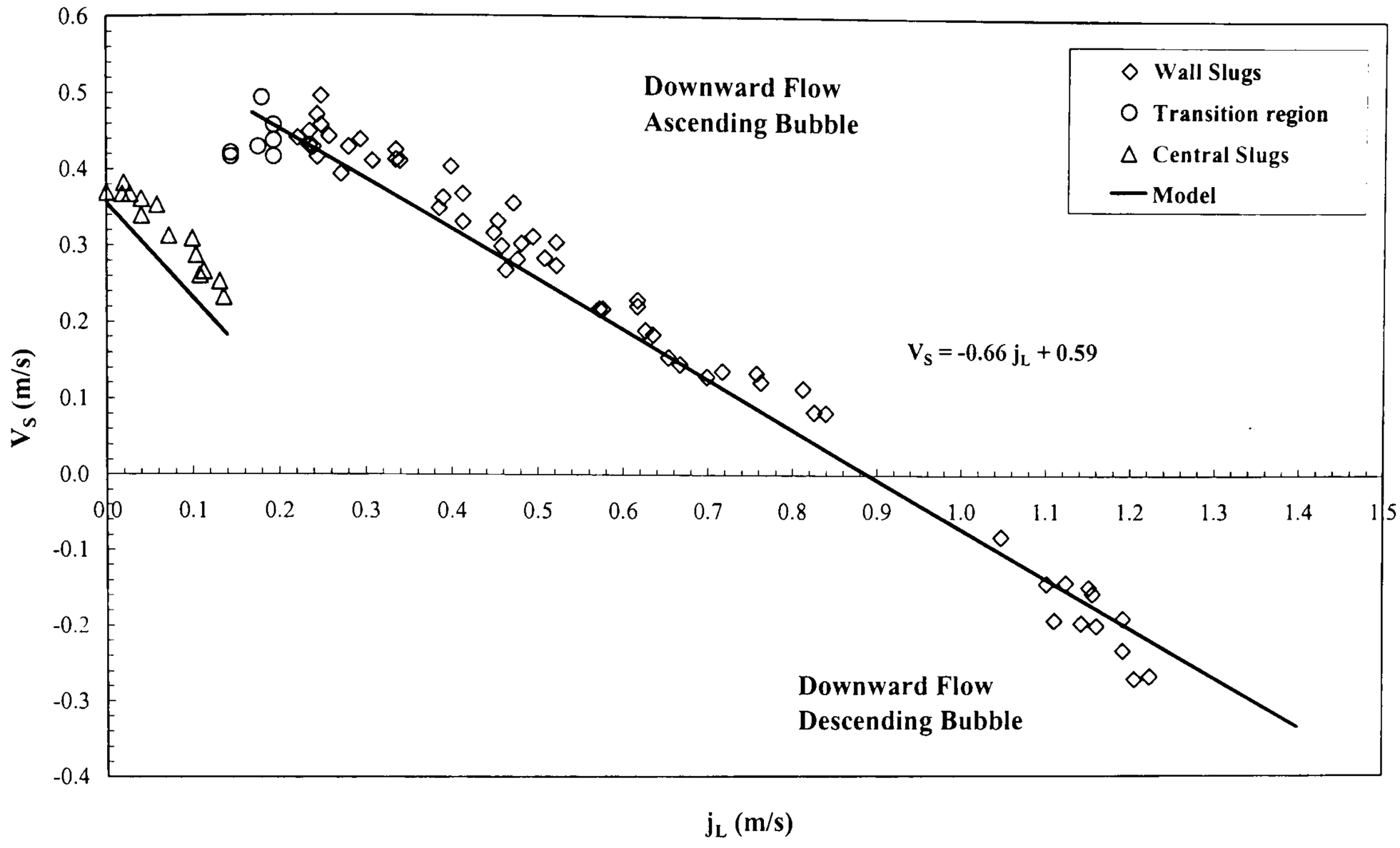

Comparison between the model and the experimental results in $D = 105$ mm in water. The value of the critical Eotvos number is 0.25 $\left(Eo_{crit} = 0.25\right)$.

Figure F.4

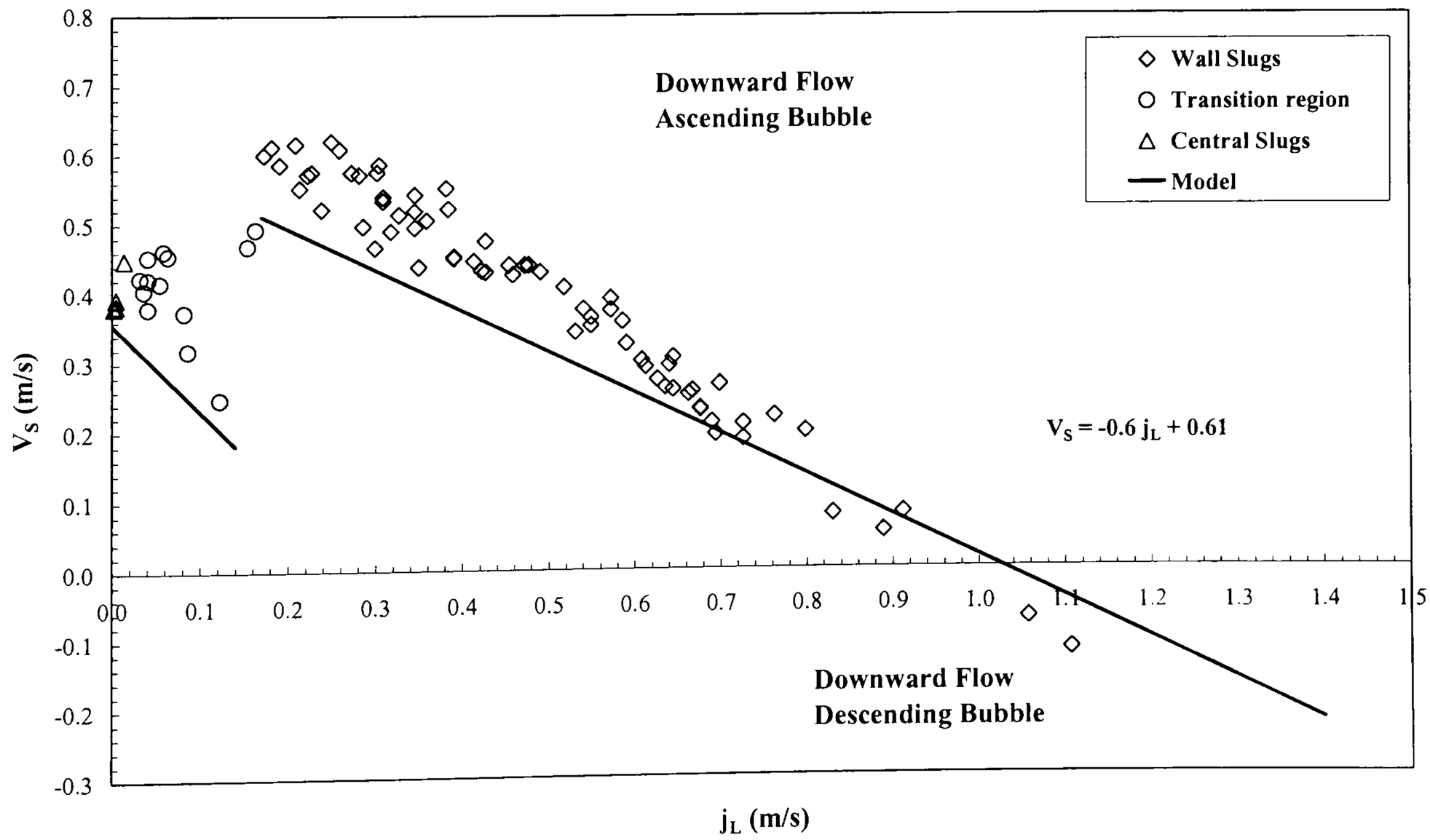

Comparison between the model and the experimental results in $D = 105$ mm in 8% w/w aqueous solution of IPA. The value of the critical Eotvos number is 0.25 $\left(Eo_{crit} = 0.25\right)$.

Figure F.5

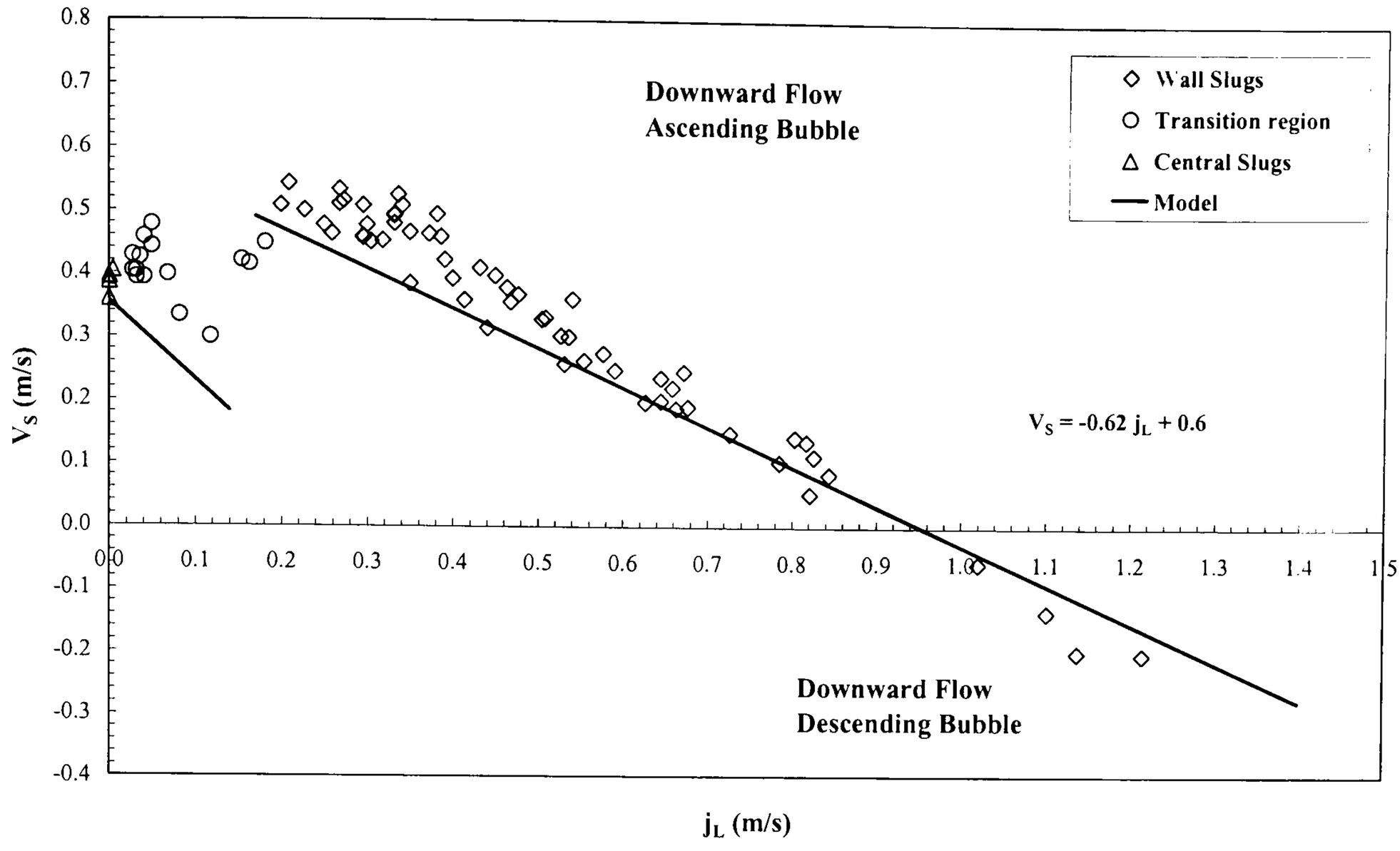

Comparison between the model and the experimental results in $D = 105$ mm in 2% w/w aqueous solution of IPA. The value of the critical Eotvos number is 0.25 $\left(Eo_{crit} = 0.25\right)$.

Figure F.6

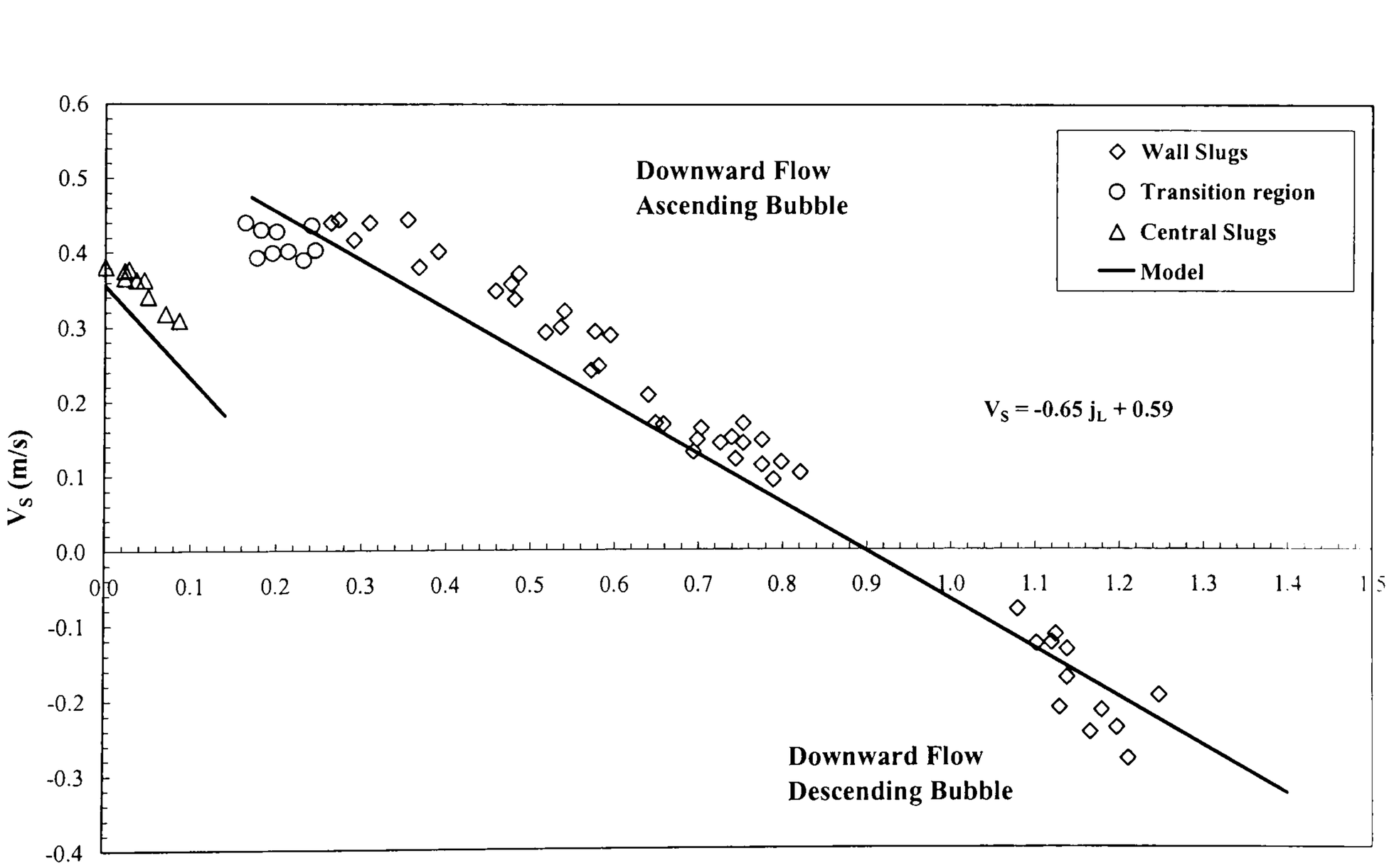

Comparison between the model and the experimental results in $D = 105$ mm in salt water. The value of the critical Eotvos number is 0.25 $\left(Eo_{crit} = 0.25\right)$.

Figure F.7